DTIC/TR-97-6 AD-A327 694

The DTIC Review

Microtechnologies and Microelectronics

Vol. 3, No. 3
September 1997

The DTIC Review is published by the
Defense Technical Information Center (DTIC),
DTIC-BRR, 8725 John J. Kingman Road, Suite 0944,
Ft. Belvoir, VA 22060-6218
Telephone: (703) 767-8266, DSN 427-8266
FAX: (703) 767-7070, DSN 767-9070
Email: bib@dtic-mil

Editorial Staff.
Editor: Christian M. Cupp
Compiler and Research Advisor: Phyllis Levine
Composition Editor: Sonya Webb
Composition Editor (Electronic): Sonya Webb

OFFICE OF THE UNDER SECRETARY OF DEFENSE (ACQUISITION & TECHNOLOGY)
DEFENSE TECHNICAL INFORMATION CENTER
8725 JOHN J KINGMAN RD STE 0944
FT BELVOIR VA 22060-6218

IN REPLY REFER TO DTIC-BR

Dear Subscriber/Reader:

Enclosed is your copy of "The DTIC Review", Vol. 3, No. 3. We noticed some errors that require further explanation.

Document 1 "A Technique for Achieving 4000 Microstrain from Hard PZT" begins on page 3. The illustrations and descriptions for Figure 1.a-1.c have been separated. You will find the descriptions on pages 21 and 22. The figures themselves are on the reverse side of page 29 on unnumbered pages. Beginning on the reverse of the last unnumbered page(showing Figure 1.c), Figure 1.d through Figure 8 are correct.

The cover sheet and title page of Document 2 "Microelectronic Radiation Hardening Process and Design" were placed two pages before the blue divider page.

We regret these errors and hope this explanation clarifies any confusion.

The Editorial Staff

REPORT DOCUMENTATION PAGE

Form Approved
OMB No. 074-0188

1. AGENCY USE ONLY (Leave blank)	2. REPORT DATE	3. REPORT TYPE AND DATES COVERED
	Sept. 1997	Final

4. TITLE AND SUBTITLE
The DTIC Review
Microtechnologies and Microelectronics
Vol. 3 No. 3

5. FUNDING NUMBERS

6. AUTHOR(S)
Christian M. Cupp, Editor
Phyllis Levine, Compiler

7. PERFORMING ORGANIZATION NAME(S) AND ADDRESS(ES)

Defense Technical
Information Center
DTIC -BRR, Suite 0944
8725 John J. Kingman Rd
Ft. Belvoir, VA 22060-6218

8. PERFORMING ORGANIZATION REPORT NUMBER

DTIC/TR-97/6

9. SPONSORING / MONITORING AGENCY NAME(S) AND ADDRESS(ES)

Def Technical Info Center
DTIC -BRR, Suite 0944
8725 John J. Kingman Rd
Ft. Belvoir, VA 22060-6218

10. SPONSORING / MONITORING AGENCY REPORT NUMBER

11. SUPPLEMENTARY NOTES
This publication is published irregularly by the Defense Technical Information Center

12a. DISTRIBUTION / AVAILABILITY STATEMENT
A - Approved for public release; distribution unlimited.

12b. DISTRIBUTION CODE
Statement A

13. ABSTRACT *(Maximum 200 Words)*

This compilation of reports on microtechnologies and microelectronics emphasizes new and innovative systems designs to materials science and applied mechanics using micrometer and nanometer dimensions. In addition to better efficiency and optimization, the research and design methodology will be used to solve a variety of engineering problems. Applications later find use in areas of communications, spectroscopy, remote sensing, nonlinear optics, projection displays and micromachining and provide the design framework for the future.

Research areas include principles of microstructural evolution in processing and in service and the design methodology for control of multilevel dynamic hierarchical microstructures, the mechanics of electro mechanical coupled materials and reports that explore fundamental concepts and formulas for designing and utilizing all classes of lasers specifically, miniature solid state lasers. The drive for increased device density in memory technologies demands smaller and closer packed future devices.

14. SUBJECT TERMS
Microelectronics, Nanotechnology, Micromachining, Miniature electronic equipment, Microtechnology

15. NUMBER OF PAGES
312

16. PRICE CODE

17. SECURITY CLASSIFICATION OF REPORT	18. SECURITY CLASSIFICATION OF THIS PAGE	19. SECURITY CLASSIFICATION OF ABSTRACT	20. LIMITATION OF ABSTRACT
UNCLASSIFIED	UNCLASSIFIED	UNCLASSIFIED	UL

The DTIC Review

Microtechnologies and Microelectronics

AD-A 327094

DTIC

Vol. 3, No 3
September 1997

TABLE OF CONTENTS

FOREWORD

This edition of The DTIC Review explores microtechnologies and microelectronics and applications in design framework for the future. The selected documents and bibliography are a representation of the information available on microtechnologies and microelectronics. The editorial staff hope you find this effort of value and always appreciate your comments.

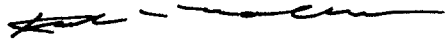

Kurt N. Molholm
Administrator

INTRODUCTION

This compilation of reports on microtechnologies and microelectronics emphasizes new and innovative systems designs to materials science and applied mechanics using micrometer and nanometer dimensions. In addition to better efficiency and optimization, the research and design methodology will be used to solve a variety of engineering problems. Applications later find use in areas of communications, spectroscopy, remote sensing, nonlinear optics, projection displays and micromachining and provide the design framework for the future.

Research areas include principles of microstructural evolution in processing and in service and the design methodology for control of multilevel dynamic hierarchical microstructures, the mechanics of electro mechanical coupled materials and reports that explore fundamental concepts and formulas for designing and utilizing all classes of lasers specifically, miniature solid state lasers. The drive for increased device density in memory technologies demands smaller and closer packed future devices.

Nanotechnology will bring new capabilities, giving us new ways to make things, heal our bodies, and care for the environment. Advanced molecular manufacturing will be able to make almost anything. The main reason to pay attention to nanotechnology now, before it exists, is to get a head start on understanding it and what to do about it.

Further information has been included at the end of the volume to help direct the interested reader to additional print and electronic references on microtechnologies and microelectronics.

DOCUMENT 1

A Technique for Achieving 4000 Microstrain from Hard PZT

AD-A322992

March 1997

Georgia Institute of Technology

Atlanta, GA

REPORT DOCUMENTATION PAGE

Form Approved
OMB No. 0704-0188

1. AGENCY USE ONLY (Leave Blank)	2. REPORT DATE	3. REPORT TYPE AND DATES COVERED
	3/30/97	4/1/96-3/30/97

4. TITLE AND SUBTITLE

A Technique for Achieving 4000 Microstrain from Hard PZT

5. FUNDING NUMBERS

Grant# N00014-96-1-0711

6. AUTHOR(S)

Christopher S. Lynch

7. PERFORMING ORGANIZATION NAME(S) AND ADDRESS(ES)

Christopher S. Lynch
School of Mechanical Engineering
Georgia Institute of Technology
Atlanta, GA 30332-0405

8. PERFORMING ORGANIZATION REPORT NUMBER

9. SPONSORING/MONITORING AGENCY NAME(S) AND ADDRESS(ES)

Roshdy Barsoum
ONR 334, Office of Naval Research
Ballston Center Tower One
800 North Quincy Street
Arlington, VA 22217-5660

10. SPONSORING/MONITORING AGENCY REPORT NUMBER

19970327 069

11. SUPPLEMENTARY NOTES COR:

12a. DISTRIBUTION/AVAILABILITY STATEMENT

DISTRIBUTION STATEMENT A
Approved for public release
Distribution Unlimited

12b. DISTRIBUTION CODE

13. ABSTRACT (Maximum 200 words)

The year 1 effort was split between laboratory development and research. A smart materials laboratory was developed for research on the mechanics of electro-mechanical coupled materials. The laboratory includes sample preparation, test facilities, and failure analysis tools as described below. There are presently four graduate students working on this research, one at the masters level and three at the Ph.D. level. There have been two conference proceedings articles and one journal article submitted. This will substantially increase in the coming year. The PI has made four presentations of research results and will make an invited presentation in July, 1997. The PI is presently working on several related programs described below. Departmental support from Georgia Tech is being used to perform work in excess of the original scope of this project.

14. SUBJECT TERMS	15. NUMBER OF PAGES
Piezoelectric, Ferroelectric, Reliability	5
	16. PRICE CODE

17. SECURITY CLASSIFICATION OF REPORT	18. SECURITY CLASSIFICATION OF THIS PAGE	19. SECURITY CLASSIFICATION OF ABSTRACT	20. LIMITATION OF ABSTRACT
unclassified	unclassified	unclassified	

Annual Report to the
Office of Naval Research

Due 3/30/97

A Technique for Achieving 4000 Microstrain from Hard PZT

PI:

Christopher S. Lynch
The G.W.W. School of Mechanical Engineering
The Georgia Institute of Technology
801 Ferst St. MRDC
Atlanta, GA 30332-0405

Grant No: N00014-96-1-0711
CFDA No: 12.300

Program Officer:

Roshdy Barsoum (703) 696-4306
ONR 334
Office of Naval Research
Ballston Center Tower One
800 North Quincy Street
Arlington, VA 22217-5660

Annual Report to the
Office of Naval Research

Due 3/30/97

A Technique for Achieving 4000 Microstrain from Hard PZT

Summary

The year 1 effort was split between laboratory development and research. A smart materials laboratory was developed for research on the mechanics of electro-mechanical coupled materials. The laboratory includes sample preparation, test facilities, and failure analysis tools as described below. There are presently four graduate students working on this research, one at the masters level and three at the Ph.D. level. There have been two conference proceedings articles and one journal article submitted. This will substantially increase in the coming year. The PI has made four presentations of research results and will make an invited presentation in July, 1997. The PI is presently working on several related programs described below. Departmental support from Georgia Tech is being used to perform work in excess of the original scope of this project.

Laboratory Development

Laboratory development occupied a substantial part of the contract period. Table 1 lists the smart materials laboratory equipment acquired from various sources (including this contract, $70k, test frame).

Table 1. Smart Materials Laboratory Equipment

Description	Cost
optical microscope w/DIC	$30k
scanning electron microscope	$30k
sample prep lab	$40k
test frame and associated equip.	$120k
Micro Moiré	$40k

The smart materials laboratory comprises equipment for sample preparation, testing, and failure analysis. The sample preparation equipment includes a diamond saw, grinding and polishing, an optical microscope, a vapor hood, and cabinetry/counters. Test equipment includes a load frame (purchased under this contract), a 20 kV power supply, an in-situ video based microscope with transmitted and reflected polarized light capability, fixtures for compression with electric field and compact tension with electric field, strain gauge amplifiers, and a computer based controller with multiple channel control and phased function generators. The failure analysis equipment includes a JOEL 840 scanning electron microscope, and an optical microscope with DIC.

Student/Post Doctoral Support

Four graduate students are working in this research area. Some of the student support is being provided by Georgia Tech as new faculty support. Will Stoll will complete a masters thesis on the non-linear and hysteretic behavior of commercial PZT in June 1997. Wei Chen has completed a micromechanics based modeling effort for tetragonal and rhombohedral structures. He is using the results in the development of continuum mechanics based constitutive laws using an internal

state variable approach. This model shows promise for implementation in commercial finite element codes, providing a design tool for both actuator developers and active structures designers. Don Upton is working on the masters portion of a Ph.D. program. He is measuring the time and temperature dependent response of commercially available actuator materials. Haihui Niu is working on the development of a J-integral test technique that uses the load-displacement and the voltage-charge curves from compact tension specimens to determine the energy release rate. J. Fan will be joining the project soon as a post doctor working on the implementation of the phenomenological constitutive laws in FEM codes.

Publications/Presentations

Journal articles submitted:

C.S. Lynch, "Fracture of ferroelectric and relaxor electro-ceramics: influence of electric field", submitted to Acta Materialia, 3/14/97

Book chapter written (partially related to this project)

Lynch, C.S., *Strain Measurement Techniques*, The Measurements, Instrumentation, and Sensors Handbook, A CRC Press, Inc. Publication, J.G. Webster ed., 1997

Proceedings articles submitted

Lynch, C.S. with W. Stoll, "Experimental Measurements of Electro-Mechanical Behavior of Four Compositions of PZT, Proceedings of the 1996 IEEE International Symposium on the Application of Ferroelectrics

Lynch, C.S. "J-Integral for Ferroelectric Compact Tension Specimens with Electric Field", SPIE 1997 Symposium on Smart Structures and Materials San Diego, Ca. Mar 1997

Presentations

3/19/96 Constitutive behavior of ferroelectric ceramics, Cambridge University, Cambridge U.K. (Invitation by Norman Fleck)

3/21/96 Constitutive behavior of ferroelectric ceramics, Leicester University, Leicester U.K. (Invitation by Alan Cocks)

7/18/96 Constitutive Behavior and Design Interrelations for PZT Actuators, Northrop Aircraft, Hawthorn CA (Invitation by Dr. Jay Kudva)

8/22/96 Poster Presentation, "Experimental Measurements of Electro-Mechanical Behavior of Four Compositions of PZT", Proceedings of the 1996 IEEE International Symposium on the Application of Ferroelectrics

12/2/96 "Stress/Strain/Electric Field Measurements on Hard and Soft PZT", Materials Research Society, Boston MA, Dec. 1996

7/97 Invited talk to be given at Banff, $500 honorarium, technology overview.

Two additional journal article manuscripts are near completion, one on the constitutive behavior of commercial compositions of PZT and a second on J-integral testing of electro-mechanically coupled ceramics.

Collaboration

The PI is involved in several related research projects outlined in Table 2.

Table 2. Related Research and Collaboration

Title	**Funding Agency**	**Amount**	**Period**
Smart Wing	ARPA/Northrop	$30,000	1/96 to 5/97
A Technique for Achieving 4000 microstrain from hard PZT	ONR Young Investigator	$370,000	4/96 - 3/99
Smart Wing Phase II*	DARPA/Northrop	$150,000	6/97-5/00
TRS/DARPA Actuator	DARPA/TRS	$105,000	6/97-5/99

*budget to be negotiated

In addition, the PI is negotiating a consulting arrangement with United Technologies, Pratt and Whitney to help with piezoelectric actuator characterization and qualification for aircraft applications.

University Support

Georgia Tech is continuing to provide support for graduate students and a light teaching load for the PI. The school of mechanical engineering is providing no cost machinist and shop time as well as no cost electrical engineer and electronics technician shop time.

Additional Information

Copies of articles are attached.

A Technique for Achieving 4000μStrain from Hard PZT

Office of Naval Research, Sponsor

Christopher S. Lynch
School of Mechanical Engineering
Georgia Institute of Technology

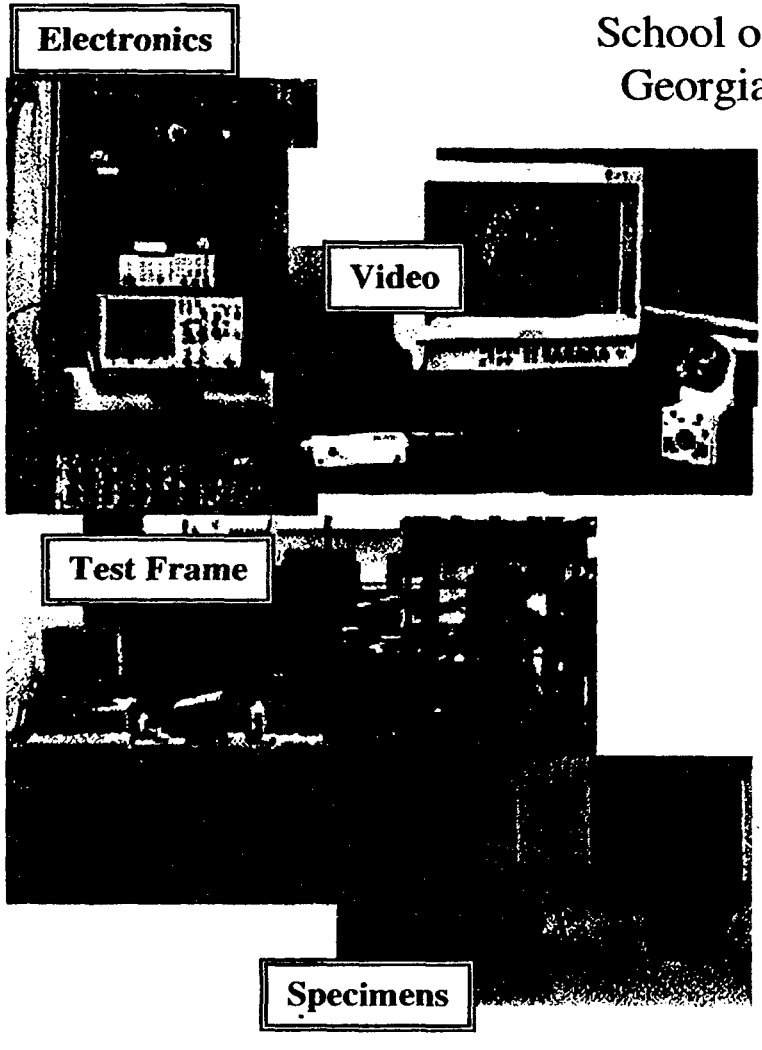

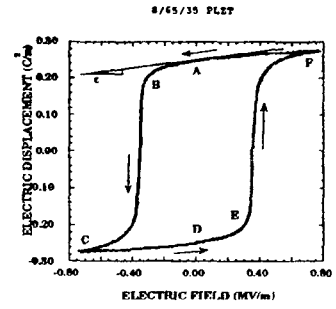

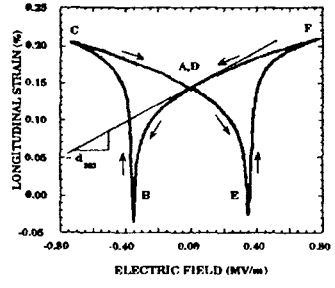

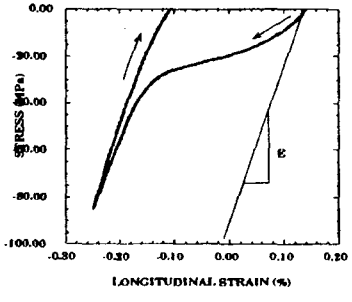

Approach:
Experimental Measurement of Polarization Switching Behavior

Impact:
Operation Across Switching Thresholds without Cracking. Much Larger Strain.

Preliminary Results:
1. Constitutive Measurements on Five Compositions of PZT, PLZT.
2. Toughness Measurements on Piezoelectric and Relaxor PLZT with E-Field.
3. Developed Internal State Variable Framework for Constitutive Models.
4. Extended Micromechanics Model to Rhombohedral and Orthorhombic Structures.

Fracture of Ferroelectric and Relaxor Electro-Ceramics: Influence of Electric Field

Christopher S. Lynch

The G.W. Woodruff School of

Mechanical Engineering

The Georgia Institute of Technology

Atlanta, Georgia 30332-0405

Submitted to

Acta Materialia

3/14/97

Fracture of Ferroelectric and Relaxor Electro-Ceramics: Influence of Electric Field*

Christopher S. Lynch

The G.W. Woodruff School of

Mechanical Engineering

The Georgia Institute of Technology

Atlanta, Georgia 30332-0405

ABSTRACT

Crack growth is studied in a ferroelectric and a relaxor composition of lead lanthanum zirconate titanate (PLZT) ceramic using Vicker's indentations with electric field. The polarized ferroelectric composition displays excess crack growth perpendicular to the polarization direction. This excess crack growth is increased by an electric field in the polarization direction. The relaxor composition does not display this excess crack growth. Results suggest that the excess crack growth perpendicular to the polarization is the result of intergranular residual stress.

---

* Work begun during a post doctoral appointment at the University of California Santa Barbara

I. INTRODUCTION

The Vicker's indentation test technique[1,2,3] involves pressing a square diamond pyramid into a sample with a known force. The resulting wedge force drives radial cracks. Polarized ferroelectric ceramics display increased radial crack growth[4-8] perpendicular to the polarization. A DC electric-field in the direction of the polarization enhances this effect[7,9]. The opposite effect has been observed in relaxor compositions. In quadratic electrostrictors, electric field hinders crack growth perpendicular to the applied field[10].

Several microstructural variables interact with crack growth in ceramics. Intergranular residual stress that arises from anisotropic strain of the crystal structure can result in microcracking, usually along grain boundaries[11]. Rice and Freiman[12,13] demonstrated that the fracture energy of a number of ceramics with anisotropic thermal expansion increases with grain size, reaches a peak, then falls with an additional increase in grain size. Pohanka, Freiman, and Rice[14] include these effects in their expression for the energy release rate of ferroelectric ceramics.

In ferroelectric ceramics, residual stress is associated with the phase transformation (from cubic to tetragonal, orthorhombic or rhombohedral) that occurs on cooling through the Curie temperature. In the absence of twinning (non-180° domain formation) the magnitude is independent of grain size and proportional to the transformation strain and the elastic modulus. At large grain sizes this residual stress is observed to induce spontaneous cracking[15]. At the Curie point, barium titanate (BT) spontaneously microcracks at a grain size of 100μm and lead titanate (PT) spontaneously microcracks and reduces to powder at a grain size of 1-10μm.

Dopants are used to harden or soften lead zirconate titanate (PZT)[16]. This affects both the mechanical and electrical properties by hindering or enhancing

twinning. Hard PZT shows less hysteresis and a greater resistance to polarization switching under stress or electric field loading[17,18] than does soft PZT.

Electric field is postulated to interact with the fracture toughness of ferroelectric ceramics altering the intergranular residual stress through removing twins and piezoelectrically or electrostrictively distorting the grains. This results in intergranular incompatible strains and stresses. Electric field also directly interacts with cracks due to the difference in the dielectric permittivity of the ceramic and the cracks' interiors[19-22]. This permittivity difference results in electric field concentrations.

Relaxor compositions in the quadratic electrostrictive state have little or no residual stress. Domains spontaneously nucleate and grow on the 100 nanometer size scale. Application of electric field preferentially grows domains in the direction of the applied field, but not sufficiently to induce a large component of residual stress.

II. EXPERIMENTS

The purpose of the experiments is to determine the necessary conditions for extended crack growth and find whether this extended crack growth can be explained by residual stress and electric field interactions. The material selected for these tests was PLZT, a relaxor ferroelectric[23,24]. Two compositions were selected, 8/65/35 and 9.4/65/35 (at%La/PZ/PT). At room temperature 8/65/35 is below the lower transition temperature and is ferroelectric, while 9.4/65/35 is at its dielectric maximum in the transition zone and is quadratic electrostrictive. The properties are listed in Table 1. Both have a rhombohedral crystal structure and an average 5 μm grain size.

A Vicker's indentation system was modified to accommodate application of electric field during the indentation process. Indentations were performed with and without electric field and at several temperatures on unpoled and poled ferroelectric samples and on quadratic electrostrictive samples. Tests were performed in immersion oil.

Indentations on unpoled samples of both compositions at several mechanical loads (with E=0) formed a reference data set. (Unpoled samples have no electro-mechanical coupling and have isotropic properties.) The indented samples were then subjected to electric field to determine the interaction between electric field, radial cracks, and the residual stress field left by the indentation process. Next, indentations were performed in the presence of a DC electric field to measure the effect of the interaction between the electric field, the stress field, and the radial cracks during crack growth. Finally, indentations were performed on a polarized ferroelectric specimen (piezoelectric in this state) at various electric field levels (applied in the direction of the polarization) ranging from zero to greater than the coercive field to assess the interaction of polarization, electric field, and the radial crack system.

III. RESULTS

Vicker's indentations in the unpoled ceramic resulted in symmetric radial crack growth (Fig. 1a). When the ferroelectric composition was polarized prior to indentation, increased crack growth perpendicular to the polarization direction was observed (Fig. 1b). When indentations were performed in the ferroelectric composition at twice the coercive field level, there was substantially more crack growth perpendicular to the field direction, and distributed damage in the vicinity of the indentation (Fig. 1c). In the unpoled state the indent diagonal and the radial crack lengths were labeled 2a and 2c (Fig. 1d). In the poled state, or in the presence

of electric field, the radial cracks were labeled with the angle relative to the polarization direction; 2c 0°, and 2c 90° (Fig. 1e).

A. Radial crack growth in non-polarized specimens

In the unpoled state the 8/65/35 specimen is ferroelastic and both the 8/65/35 and the 9.4/65/35 specimens have isotropic elastic properties. Indentations were performed using several indentation loads. Radial crack size increased with indentation load (Fig 2). The 8/65/35 and 9.4/65/35 displayed similar amounts of crack growth at low loads (short cracks) and the 8/65/35 displayed less crack growth than the 9.4/65/35 at higher loads (longer cracks). The indentation size, 2a, was the same for both compositions and increased with load.

B. Electric field applied to existing indentations

An 8/65/35 specimen was prepared with electrodes and lead wires. Indentations were performed in the face mid way between the electrodes at two different mechanical loads. The specimen was then subjected to a ramp in electric field. The field was increased to a fixed level then decreased to zero and the radial crack length measured. This electric field cycle was performed several times at increasing field levels and the radial crack length remeasured after each cycle (Fig. 3). When the electric field amplitude reached 0.3 MV/m, the radial cracks extended. This field level is approximately 75% of the coercive field. The cracks perpendicular to the field extended approximately 30%.

Similar tests were performed on the quadratic electrostrictive 9.4/65/35 composition (Fig. 4). The electric field induced a very small amount of crack extension.

C. Indentations performed in the presence of electric field

Indentations were performed in the ferroelectric 8/65/35 composition (initially in the unpoled state) with electric field present. A DC electric field was applied, the indentation performed, the indenter removed, the field reduced to zero, and the crack lengths measured (Fig. 5). Indentations were performed at various loads and electric field levels. Electric field had little or no effect until it was near the coercive field, at which point it induced additional crack growth. The maximum applied field of 0.3 Mv/m was below the coercive field. The additional crack growth induced by the electric field appears to be a function of the electric field and independent of indent load rather than a fixed percentage of the zero field crack length associated with that load.

Similar tests were performed on the quadratic electrostrictive 9.4/65/35 composition (Fig. 6). There was a slight decrease in crack growth in the presence of electric field.

D. Indentations performed in a pre-polarized ferroelectric composition with electric field present

Indentations were performed with a 4 kg load on the ferroelectric 8/65/35 specimens at several electric field levels. The specimens were first polarized by the application of several electric field cycles at twice the coercive field. Anisotropic crack growth was observed at zero electric field (Fig. 7). As the electric field was increased, the indentations produced radial cracks that were shorter parallel to the electric field direction and longer perpendicular to the field direction. This effect seemed to saturate at 0.5 Mv/m, about 1.2 times the coercive field.

When indented under high electric field, the ferroelectric composition developed a series of microcracks in the stress field of the indentation (Fig. 1.c). These were not extensions of the radial or lateral crack systems.

E. Indentations performed at various temperatures

Indentations were performed in unpoled specimens at various temperatures. The morphology of the cracks changed as the temperature was increased, with more microcracking around the indentation zone and less well developed radial cracks. In some of the indents, the radial cracks branched at odd angles relative to the indent axes. Only the data from symmetric radial cracks were plotted (Fig. 8). The indentation diagonals, 2a, were nearly independent of temperature. The crack length of the 8/65/35 composition increased as the temperature was increased to 100°C. At 100°C, the 8/65/35 composition has quadratic electrostrictive behavior, the same as the 9.4/65/35 composition at room temperature. The crack lengths in the 9.4/65/35 composition increased with temperature. At 100°C this composition is nearly cubic.

F. Other Tests

A series of tests were performed without the immersion oil. Radial crack lengths were comparable to those performed through a drop of oil. The samples indented in air were placed in a container of distilled water for 24 hours and then the radial crack lengths were remeasured. No additional crack growth was observed.

IV. DISCUSSION

Several variables affect crack growth in ferroelectric ceramics. The data from this study help to identify those that cause extended crack growth in polarized ferroelectric ceramics. The experimental results indicate that, at the field levels tested, extended crack growth is associated with approaching the coercive field in the ferroelectric composition. An additional observation of Mehta and Virkar[4] is

important to the following discussion. In their study, lead zirconate titanate was mechanically poled by application of compressive stress (ferroelastic switching). Specimens poled in this way were not piezoelectric, yet displayed the extended crack growth. This suggests piezoelectric coupling to the crack tip stress field is not a critical mechanism for extended crack growth.

The test results are discussed in terms of the energy release rate. This is the energy dissipated per unit advance of the crack per unit crack width. The energy release rate G, is written as the sum of contributions from several dissipative mechanisms that are active in the high stress, high electric field zone found at the tip of the crack, equation (1).

$$G = 2\gamma_s + \gamma_{\mu c} + \gamma_t + \gamma_r + \gamma_{pt} \qquad 1.$$

where $2\gamma_s$ is the surface energy needed to create the two crack surfaces, $\gamma_{\mu c}$ is the energy absorbed by microcrack formation, γ_t is the energy expended in ferroelastic twinning the crystal structure, γ_r is the energy the residual stress contributes to driving the main crack (a negative term), and γ_{pt} is the energy ~~contributed~~ by a dilational phase transformation. The crystal structure of the compositions used in this study is rhombohedral. Little or no stress induced phase transformation is expected, thus the last term is considered negligible.

Residual stress, microcracking, and twinning are coupled with electric field in ferroelectric ceramics. Residual stress arises from the anisotropic deformation of individual grains in the ceramic that is associated with the phase transformation as the ceramic is cooled through the Curie point. This anisotropic deformation is relieved by ferroelastic twining. In relaxors, a very fine domain structure forms as the material is cooled, leaving nearly zero residual stress in the as cooled state. Application of electric field in excess of the coercive field removes most or all of the

twins, resulting in single domain grains. In this state, the intergranular residual stress is large. When the intergranular residual stress is high enough and nucleation sites for grain boundary fracture are available, microcracking occurs along the tensile portion of the grain boundaries.

Residual stress, microcracking, and twinning influence crack propagation. Residual stress interacts with the fracture process in the following way: When a crack propagates through the ceramic, the stored strain energy density associated with residual stress is relieved on the crack face on the order of one grain diameter in depth. The strain energy released is proportional to the grain size. At small grain sizes there is little residual strain energy released as a crack propagates. At intermediate grain sizes the residual stress helps to propagate the main crack, and microcracks can form in the tensile crack tip field at grain boundaries that were under residual tension. If the residual strain energy released by a grain is not sufficient to source the surface energy required to form a microcrack, then the microcrack absorbs energy and the energy release rate is increased. At larger grain sizes, the residual strain energy released is sufficient to source the surface energy for the microcrack. In this case the contribution to the energy release rate is negative and the toughness is decreased. Microcrack formation is localized to a crack tip process zone when intrinsic flaws are small enough that the crack tip stress concentration is required to nucleate grain boundary flaws into microcracks. At even larger grain sizes, there is sufficient residual strain energy available to spontaneously microcrack the ceramic.

A relationship between residual stress and the contribution of microcracking to the energy release rate is developed by considering a main crack surrounded by a small scale microcrack cloud. Let $B\Delta a$ be the area increase of the main crack per crack advance Δa, where B is the width of the crack, and let $nB\Delta a$ be the area

increase of microcracks per crack advance Δa where n is the ratio of microcrack area formed to new crack surface formed.

The irreversible work done to advance the crack is equal to the work done to form the new crack surface less the residual stress contribution to the propagation of the main crack, plus the work done in creating microcrack surface in the crack tip process zone less the work done by releasing residual strain energy at each microcrack plus the work done in driving ferroelastic twinning. This energy balance is written as Equation (2).

$$W = 2\gamma_s B\Delta a - 2B\Delta a d\sigma_R^2/2E + 2\gamma_s nB\Delta a - 2nB\Delta a d\sigma_R^2/2E + \gamma_t B\Delta a \qquad 2.$$

where γ_s is the surface energy, B is the specimen thickness, n is the area increase of microcracks created per unit area increase of the main crack, d is the average grain diameter, σ_R is the magnitude of the tensile component of residual stress, E is the Young's modulus, and γ_t is the energy absorbed per unit crack advance per unit width by ferroelastic twinning. Dividing by BΔa gives an expression for the energy release rate in the presence of residual stress and twinning, equation (3).

$$G = (1+n)\left(2\gamma_s - d\sigma_R^2/E\right) + \gamma_t \qquad 3.$$

In equation (3), n is a function of σ_R, the size and distribution of grain boundary flaws, and the grain size. This function must be known to calculate G. The behavior of equation (3) describes observed material behavior. At small d, n tends toward zero (no microcracking) and the surface energy term is much larger than the intergranular stress term. As the grain size d, increases, n increases. This corresponds to the formation of microcracks near the primary crack tip. This increases G. As d further increases, the intergranular residual stress contribution

to fracture becomes larger. This term is negative and thus G begins to decrease. Further increase of grain size eventually leads to a negative energy release rate. This corresponds to spontaneous microcracking. Equation (3) captures the observed behavior of ceramics with anisotropic thermal expansion of the crystal structure. In these materials the energy release rate increases with grain size then decreases and goes to zero at a large grain size[12-15]. At sufficiently large d, there is enough residual strain energy available to spontaneous microcrack the ceramic. Laws could be developed relating the height of a microcrack zone to the residual stress and grain size, possibly taking the intrinsic flaw size proportional to d.

A sample calculation using equation (3) shows that the results are reasonable. The surface energy is determined from the fracture toughness of the unpoled material (K_{Ic} = 0.75 MPa$\sqrt{m}$) and the Irwin relation ($G=(1-\nu^2)/E\ K_{Ic}^2$) as γ_s = 6.2 J/m^2. The residual stress in the presence of a high electric field is estimated from the single crystal saturation strain ($\varepsilon^s \approx 3.5x10^{-3}$) and the Young's modulus (E=68 GPa). Taking n=0 (no microcrack cloud), γ_t=0 (no twin toughening at high electric field), and d=5x10^{-6} m, equation (3) predicts the energy release rate will be reduced from 12.4 to 8 J/m^2 by application of a strong electric field. Clearly a more rigorous analysis is needed to calculate the contribution of intergranular residual stress to the reduction in energy release rate. This order of magnitude calculation however, strongly supports the postulate that intergranular residual stress induced by remanent strain is the cause of the observed excess crack growth.

Intergranular residual stress is a function of electric field. When polarized, the residual stress is largest in the direction of polarization. Some of this residual stress is relieved by ferroelastic twinning (aging). Application of electric field in the direction of the polarizing field increases the intergranular residual stress and removes twins. At the grain sizes tested, the increase of intergranular residual stress with electric field reduces the energy release rate. The removal of twins also

removes the twin toughening component. An electric field in the opposite direction reduces residual stress and increases the amount of twinning available for toughening the ceramic.

When indentations were performed in the ferroelectric composition in the presence of a strong electric field, cracking occurred in the tensile stress field of the indenter but independent of the main crack (Fig 1.c). This is a spreading of the microcracking away from the crack tip zone. At high electric field this material is very near the threshold of spontaneous microcracking.

Other mechanisms interact with crack growth in electro-mechanically coupled ceramics. There is some twin toughening associated with the cracks that run parallel to the polarization. This slightly decreases crack growth in this direction in poled specimens. There is also a negative contribution to the energy release rate[19] caused by a jump in dielectric permittivity from the material to the crack interior. This accounts for the slight decrease in crack growth perpendicular to an applied electric field in the relaxor composition.

The reduction of toughness by intergranular residual stress also explains earlier observations of electric field driven fatigue crack growth by Cao and Evans[25] and by Lynch et al[26]. These cracks are observed to grow from Vicker's indentations perpendicular to the polarization in ferroelectric compositions driven by cyclic electric field above the coercive field. The cracks extend about 40 μm each half cycle, depending on electric field level. This type of fatigue crack growth does not occur in quadratic electrostrictors.

V. CONCLUDING REMARKS

The anisotropic crack growth observed when Vicker's indentations are performed in poled ferroelectric ceramics was discussed in terms of an intergranular

contribution to the energy release rate. The effect of residual stress is much larger than other mechanisms that interact with crack propagation. The results were not presented in terms of calculated toughness since the Vicker's indentation technique has not been calibrated for anisotropic materials. There is, however, a drop in fracture toughness perpendicular to the polarization direction that needs to be quantified for these materials. An equation was developed that describes the residual stress contribution to toughness by balancing the work of fracture with the energy absorbed in forming new surfaces less the residual strain energy released. The results indicate that smaller grain size ferroelectric ceramics will have a higher toughness perpendicular to the polarization, and that smaller grain size may reduce or eliminate the spontaneous cracking that can occur during polarization switching. It is also clear from the model that microcracking can be avoided by operating at field levels below the saturation level, and that it may be possible to increase the reliability of ferroelectric ceramic actuators by not fully polarizing the ceramic. If some twins are left in the crystal structure, they will relieve some of the intergranular residual stress.

VI. ACKNOWLEDGMENTS

This work was supported by ONR through contract N0014-93-1-0110 and N0014-931-0200 at the University of California at Santa Barbara, and through contract E-25-L-35/24-6-R8899-OAO at the Georgia Institute of Technology.

VII. REFERENCES

1. Anstis G.R., Chantikul, P., Lawn, B.R., Marshall, D.B., "A Critical Evaluation of Indentation Techniques for Measuring Fracture Toughness: I, Direct Measurements" *J. Am. Ceram. Soc*, **64** (9), 533-538, 1981

2. Braun L.M., S.J. Bennison, B.R. Lawn, "Objective Evaluation of Short Crack Toughness Curves Using Indentation Flaws: Case Study on Alumina-Based Ceramics", *J. Am. Ceram. Soc.*, 75[11] 3049-57 (1992)

3. Marshall D.B., B.R. Lawn, "An Indentation Technique for Measuring Stresses in Tempered Glass Surfaces", *J. Am. Ceram. Soc.* 60 [1,2] Jan-Feb (1977)

4. Mehta K., A.V. Virkar, "Fracture Mechanisms in Ferroelectric-Ferroelastic Lead Zirconate Titanate (Zr:Ti=0.54:0.46) Ceramics", J. Am. Ceram. Soc. 73[3] 567-74 (1990)

5. Esaklul K.A., W.W Gerberich, B.G. Koepke, "Stress relaxation in PZT", J. Am. Ceram. Soc. 63[1,2], 25-30, (1980)

6 Pisarenko, G.G., V.M. Chushko, and S.P. Kovalev, "Anisotropy of Fracture Toughness of Piezoelectric Ceramics", *J. Am. Ceram. Soc.*, **68** [5] 259-65, 1985

7. Tobin A.G., Y.E. Pak, "Effect of electric field on fracture behavior of PZT ceramics", Proceedings SPIE Vol. 1916/79, March (1993)

8. Okazaki K., "Mechanical behavior of ferroelectric ceramics", Ceramic Bulletin, 63[9] (1984)

9. Sun C.T., S.B. Pak, "Determination of fracture toughness of piezoelectrics under the influence of electric field using Vicker's indentation", School of Aeronautics and Astronautics, Purdue University, unpublished work

10. Raynes A.S., G.S. White, S.W. Freiman, B.S. Rawal, "Electric field effects in a lead magnesium niobate ceramic", NIST (need reference)

11. Evans A.G., "Microfracture from Thermal Expansion Anisotropy-I. Single Phase Systems", *Acta. Met.* 26, 1845-53 (1978)

12. Rice R.W., S.W. Freiman, P.F.Becher, "Grain-Size Dependence of Fracture Energy in Ceramics: I, Experiment", *J. Am Ceram. Soc,* 64[6], 345, June (1981)

13. Rice R.W., S.W Freiman, "Grain -Size Dependence of Fracture Energy in Ceramics: II, A Model for Noncubic Materials" *J. Am Ceram. Soc,* 64[6], 350, June (1981)

14. Pohanka R.C., S.W. Freiman, R.W. Rice, "Fracture Processes in Ferroic Materials", Ferroelectrics, 28, 337-342, (1980)

15. Rice R.W., R.C. Pohanka, "Grain Size Dependence of Spontaneous Cracking in Ceramics", *J. Am Ceram. Soc*, 61[11-12], 559, Dec (1979)

16. Jaffe B., W.R. Cook, H. Jaffe, "Piezoelectric Ceramics", Academic Press, London and N.Y. (1971)

17. Cao H.C., A.G. Evans, "Nonlinear Deformation of Ferroelectric Ceramics", J. Am. Ceram. Soc., 76[4] 890-96, (1993)

18. Lynch C.S., "The effect of uniaxial stress on the electro-mechanical response of 8/65/35 PLZT", Submitted to Acta. Met. (1995)

19. Suo Z., "Mechanics Concepts for Failure in Ferroelectric Ceramics", in *AD-Vol. 24/AMD-Vol. 123, Smart Structures and Materials, ASME Proceedings*, 1991

20. McMeeking, R.M., "Electrostrictive Stress near Crack-like Flaws," *J. Appl. Math. Phys.* **40**, 615-627 (1989)

21. Yang, W. and Z. Suo, "Cracking in Ceramic Actuators Caused by Electrostriction", *J. Mech. Phys. Solids*, 42[4], 649-63, (1994)

22. Suo, Z., "Models for Breakdown-Resistant Dielectric and Ferroelectric Ceramics," *J. Mech. Phys. Solids.* **41**, 1155-1176, 1993.

23. Cross, L.E., "Relaxor Ferroelectrics", *Ferroelectrics*, **76**, 241-267, 1987

24. Haertling, G.H., 1987, "PLZT Electrooptic Materials and Applications-A Review," *Ferroelectrics*, **75**, 25-55.

25. Cao H.C., A.G. Evans, "Electric Field Induced Fatigue Crack Growth in Ferroelectric Ceramics", *J. Am. Ceram Soc* (in press 1995)

26. Lynch C.S., W. Yang, L. Collier, Z. Suo, R.M. McMeeking, "Electric Field Induced Cracking in Ferroelectric Ceramics", Accepted for Publication in Ferroelectrics, (1994)

LIST OF FIGURES

Figure 6. Indentations are performed in the presence of electric field on the 9.4/65/35 quadratic electrostrictive composition. The presence of electric field may slightly hinder crack growth, but the amount is not significant.

Figure 7. Indentations in the polarized 8/65/35 composition in the presence of electric field. As the electric field is increased, the cracks perpendicular to the polarization direction become longer. This effect saturates just above the coercive field.

Figure 8. Crack length and indentation size produced by a 3 kg load are measured at various temperatures. The indentation size is independent of temperature. Crack growth increases with temperature. The 8/65/35 composition goes from ferroelectric to quadratic electrostrictive behavior over this temperature range. The 9.4/65/35 composition goes from quadratic electrostrictor to cubic paraelectric behavior over this temperature range. As the availability of twinning decreases, crack growth increases.

TABLE I. PROPERTIES OF PLZT

Composition (%La/Zr/Ti)	8/65/325	9.5/65/35
d_{33} (x10^{-12} C/N)	682	0
P^R (C/m^2)	.30	0
Ec (MV/m)	3.6	0
Tc (°C)	110	25
25°C Phase	Ferro. Rh.	
ε_r	3350	5500
tan δ (%)	2.5	5.5
resistivity (Ω-cm)	10^{13}	10^{13}
k	.648	0
S_{11} (x10^{-12} m^2/N)	12.4	12.4
Q_{11} (m^4/C^2)	.018	.021
Q_{12} (m^4/C^2)	-.008	-.009

Figure 1. a. Photograph of a symmetric indentation characteristic of an unpoled ferroelectric (width of field 500μm). b. Photograph of an asymmetric indentation characteristic of a ferroelectric composition poled in the vertical direction (width of field 1 mm). c. Photograph of an indentation in the ferroelectric composition 8/65/35 indented under an electric field of 0.8 Mv/m (width of field 3 mm). Note the peripheral microcracking that occurred in the stress field of the indentation. Back lighting gives the cracks the dark appearance.

Figure 1. d. Crack labeling for symmetric indentations. e. Crack labeling for asymmetric indentations.

Figure 2. Crack length and indentation size vs. indent load for 9.4/65/35 and unpoled 8/65/35PLZT. At higher loads the cracks are shorter in the ferroelectric composition.

Figure 3. Two indentations are monitored as electric field is increased to just below the coercive field, one produced with 1.5 kg load and one with 6 kg load. When the electric field nears the coercive field, the cracks perpendicular to the electric field grow and the cracks parallel to the polarization do not.

Figure 4. Three indents in 9.4/65/35 PLZT are monitored as electric field is applied. The electric field induces a small amount of crack growth.

Figure 5. Indentations are performed in the presence of electric field in the 8/65/35 unpoled ferroelectric composition. Crack growth is not affected by electric field until the coercive field is approached.

Figure 6. Indentations are performed in the presence of electric field on the 9.4/65/35 quadratic electrostrictive composition. The presence of electric field may slightly hinder crack growth, but the amount is not significant.

Figure 7. Indentations in the polarized 8/65/35 composition in the presence of electric field. As the electric field is increased, the cracks perpendicular to the polarization direction become longer. This effect saturates just above the coercive field.

Figure 8. Crack length and indentation size produced by a 3 kg load are measured at various temperatures. The indentation size is independent of temperature. Crack growth increases with temperature. The 8/65/35 composition goes from ferroelectric to quadratic electrostrictive behavior over this temperature range. The 9.4/65/35 composition goes from quadratic electrostrictor to cubic paraelectric behavior over this temperature range. As the availability of twinning decreases, crack growth increases.

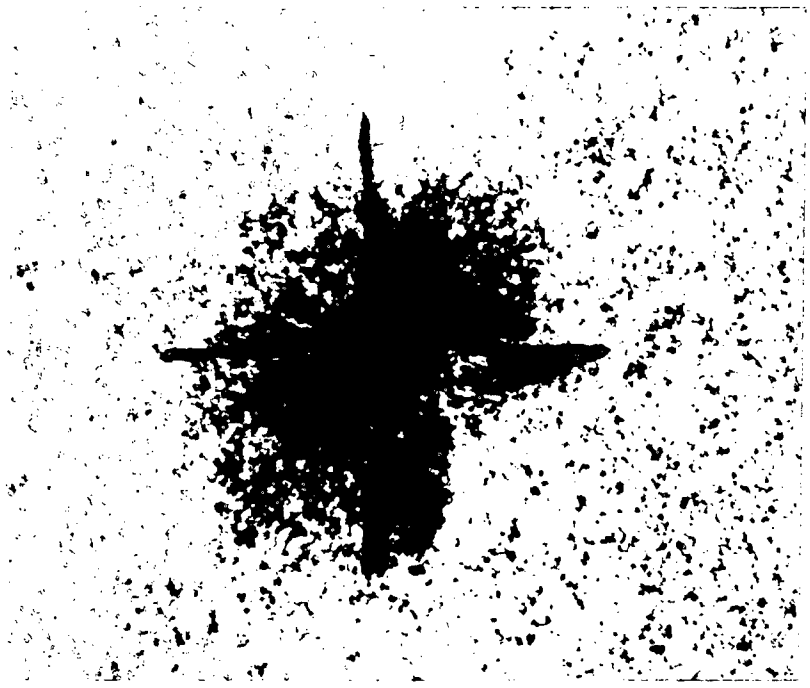

Figure 1.a

Figure 1.b

Figure 1.c

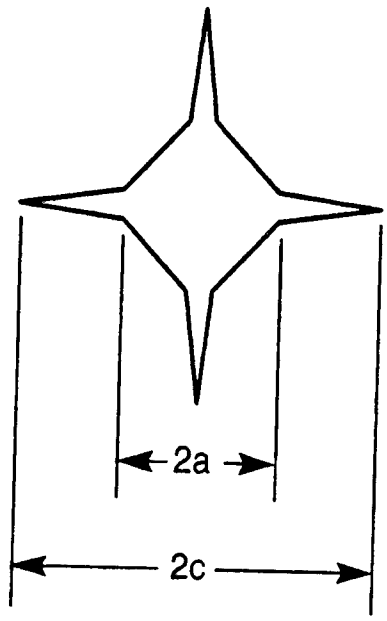

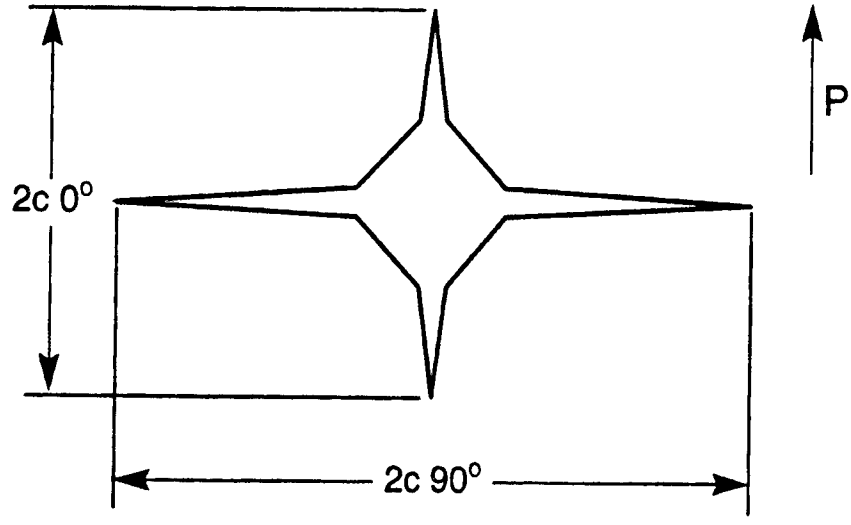

Figure 1. d. Crack labeling for symmetric indentations. e. Crack labeling for asymmetric indentations.

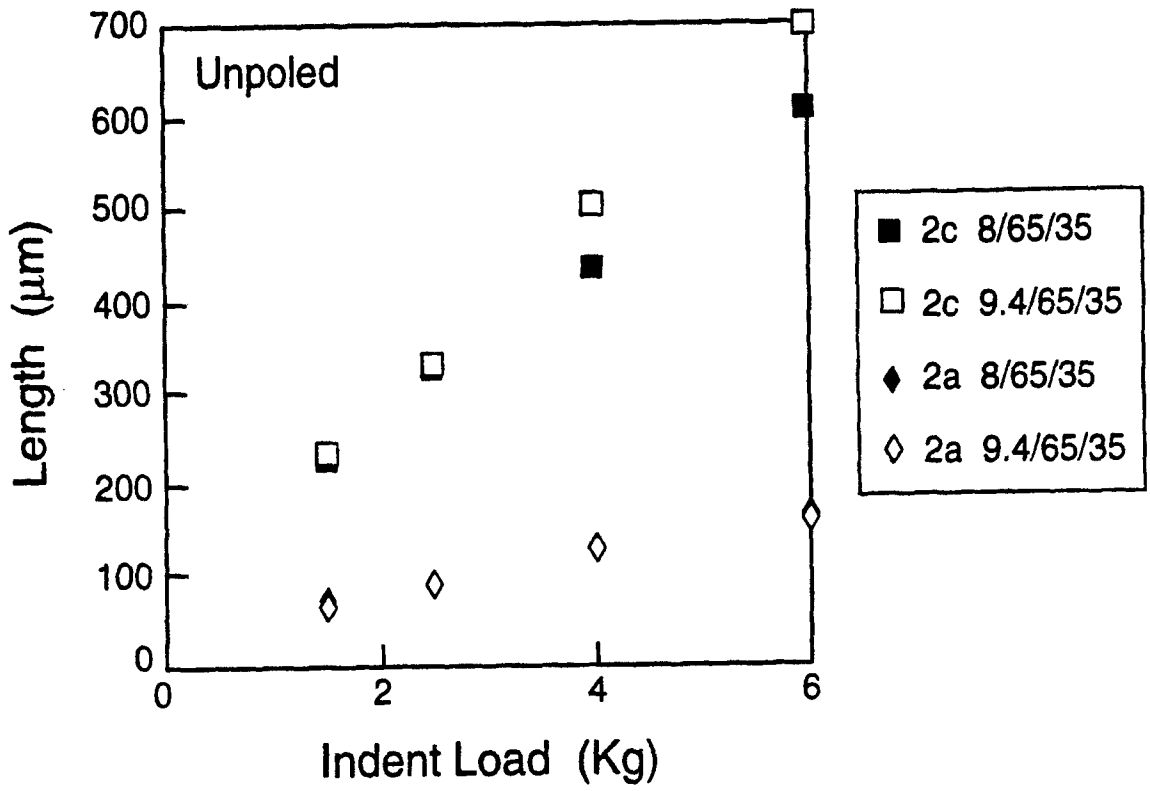

Figure 2. Crack length and indentation size vs. indent load for 9.4/65/35 and unpoled 8/65/35PLZT. At higher loads the cracks are shorter in the ferroelectric composition.

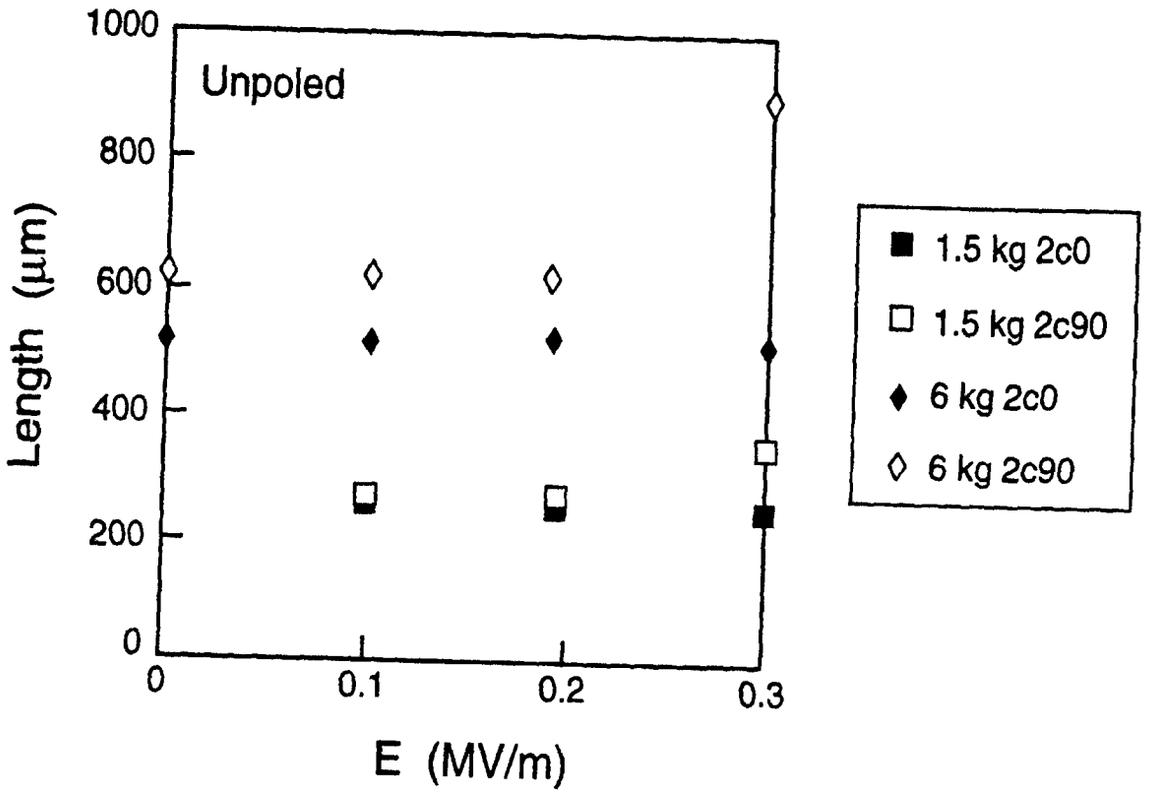

Figure 3. Two indentations are monitored as electric field is increased to just below the coercive field, one produced with 1.5 kg load and one with 6 kg load. When the electric field nears the coercive field, the cracks perpendicular to the electric field grow and the cracks parallel to the polarization do not.

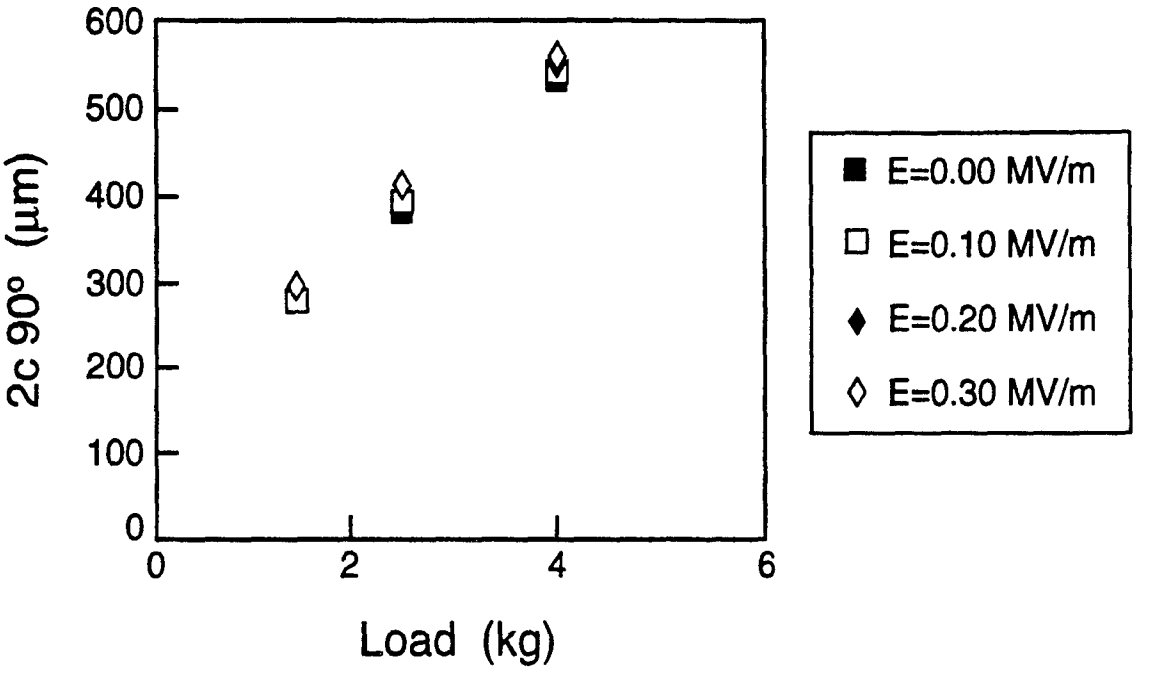

Figure 4. Three indents in 9.4/65/35 PLZT are monitored as electric field is applied. The electric field induces a small amount of crack growth.

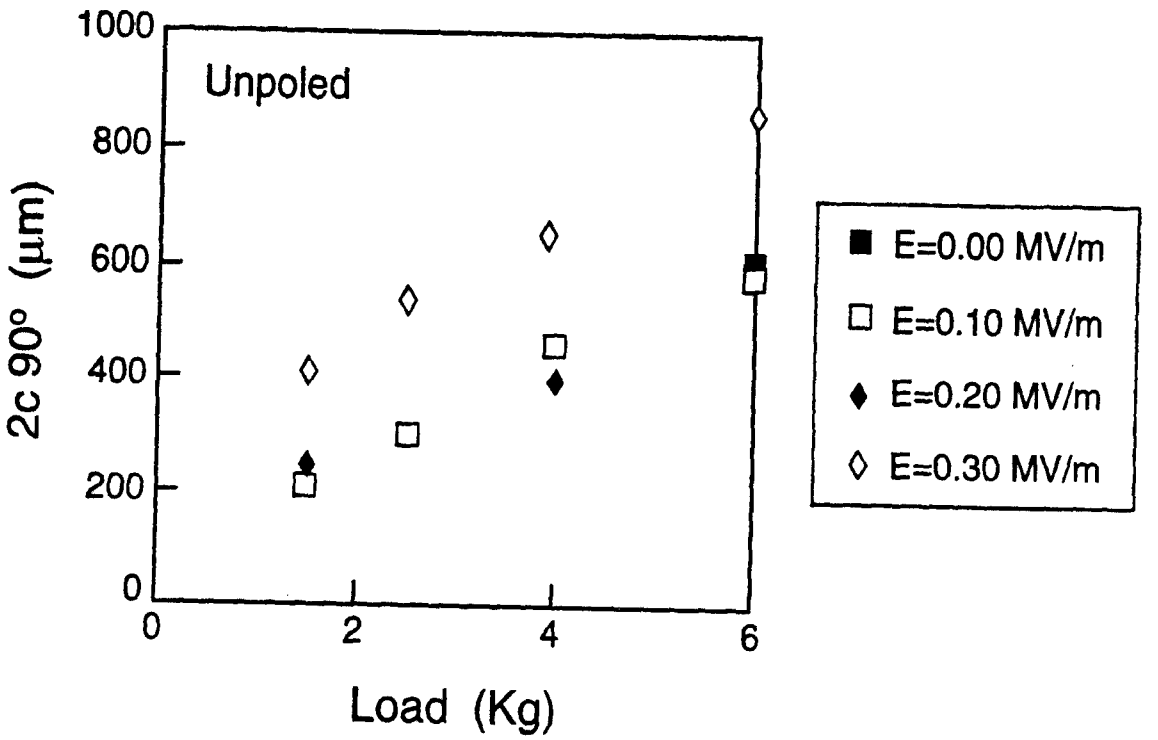

Figure 5. Indentations are performed in the presence of electric field in the 8/65/35 unpoled ferroelectric composition. Crack growth is not affected by electric field until the coercive field is approached.

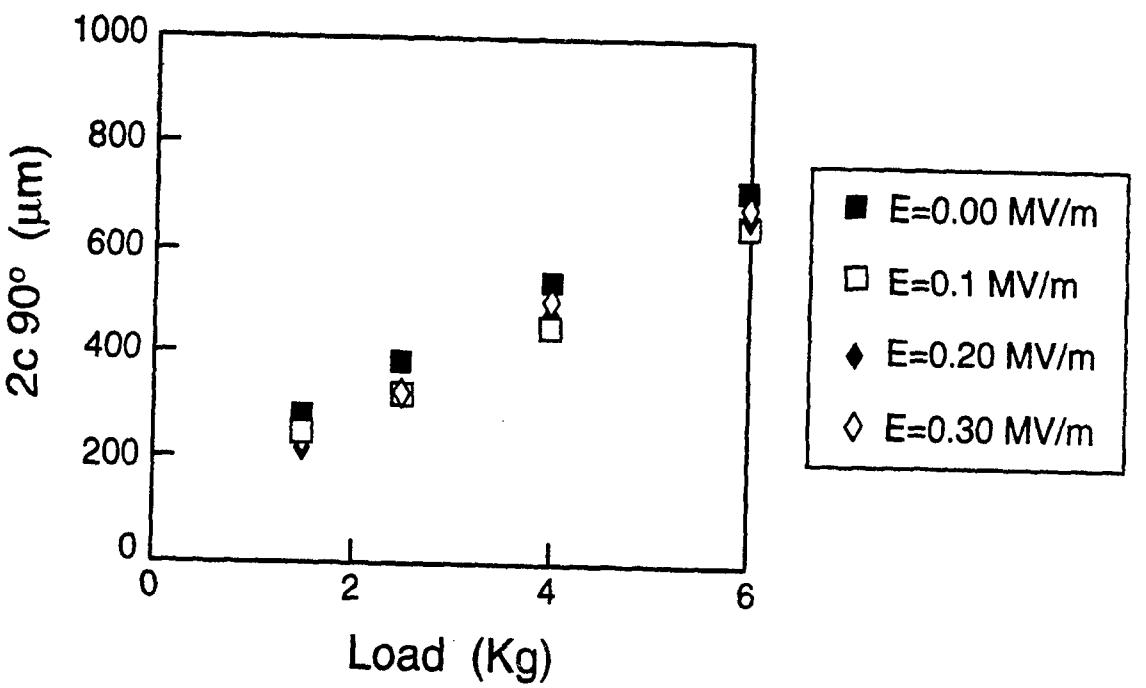

Figure 6. Indentations are performed in the presence of electric field on the 9.4/65/35 quadratic electrostrictive composition. The presence of electric field may slightly hinder crack growth, but the amount is not significant.

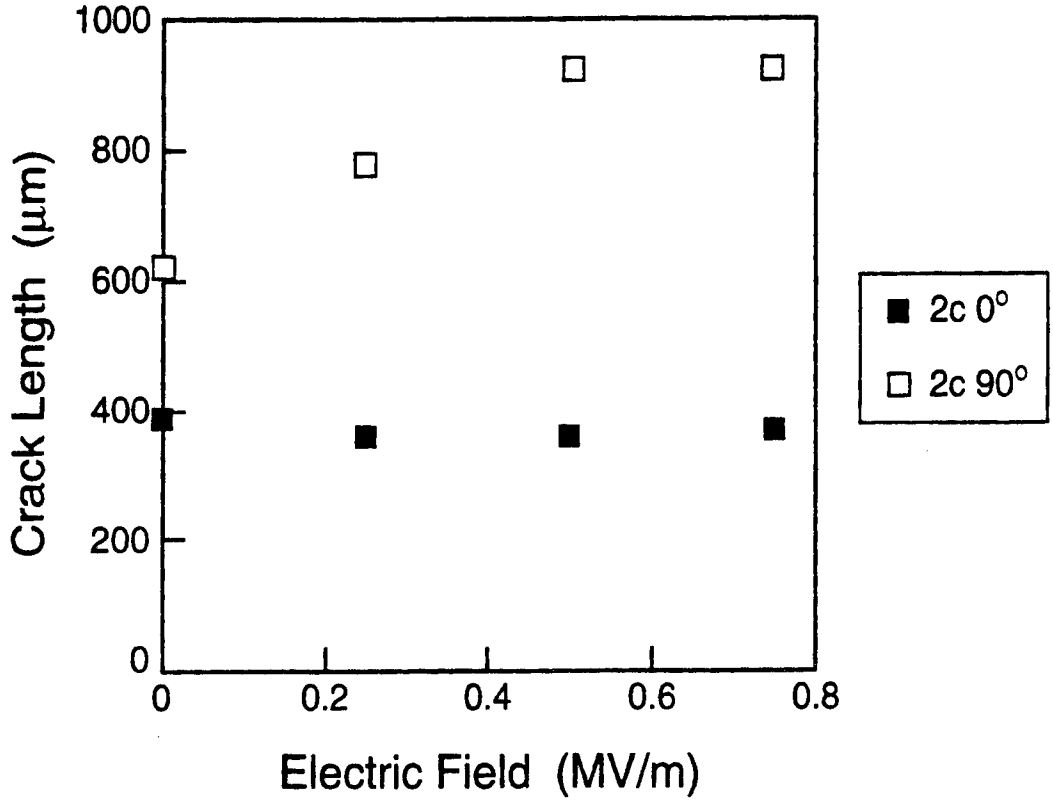

Figure 7. Indentations in the polarized 8/65/35 composition in the presence of electric field. As the electric field is increased, the cracks perpendicular to the polarization direction become longer. This effect saturates just above the coercive field.

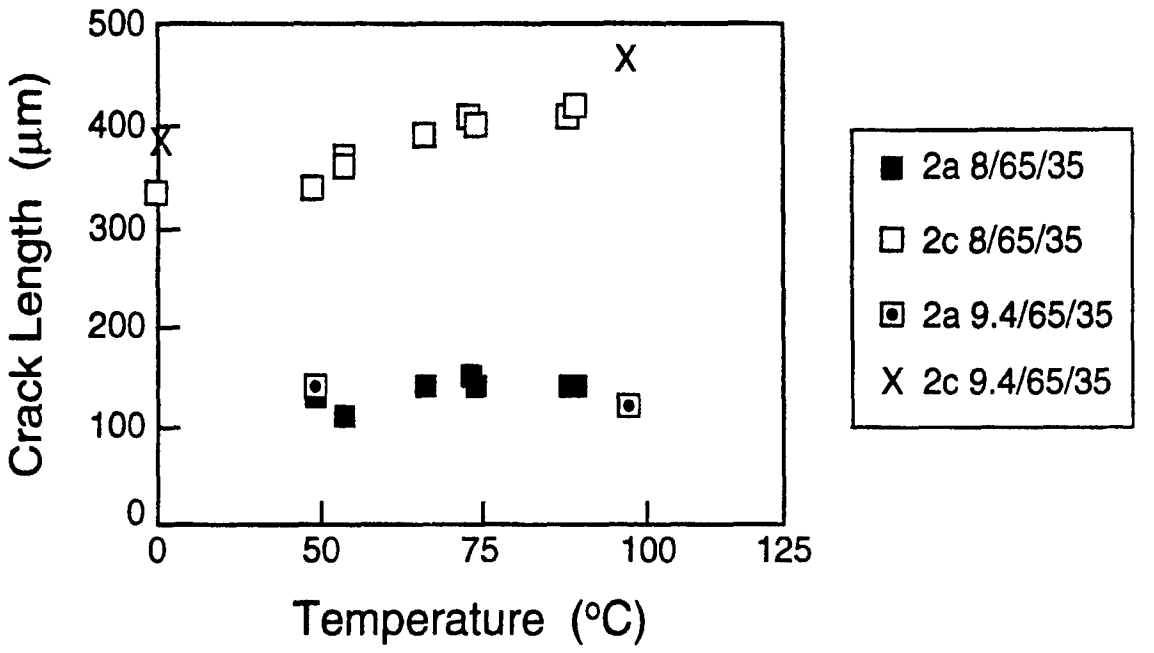

Figure 8. Crack length and indentation size produced by a 3 kg load are measured at various temperatures. The indentation size is independent of temperature. Crack growth increases with temperature. The 8/65/35 composition goes from ferroelectric to quadratic electrostrictive behavior over this temperature range. The 9.4/65/35 composition goes from quadratic electrostrictor to cubic paraelectric behavior over this temperature range. As the availability of twinning decreases, crack growth increases.

J-Integral for Ferroelectric Compact Tension Specimens with Electric Field

Christopher S. Lynch

The G.W. Woodruff School of Mechanical Engineering
(Mechanics of Materials Group)
The Georgia Institute of Technology
Atlanta, Georgia 30332-0405

Submitted to the
SPIE 1997 Symposium on
Smart Structures and Materials
San Diego, Ca. March 1997

J-Integral for Ferroelectric Compact Tension Specimens with Electric Field

Christopher S. Lynch
Georgia Institute of Technology, School of Mechanical Engineering
Atlanta, Georgia 30332-0405

ABSTRACT

Experiments based on the compact tension geometry are applied to a relaxor composition of lead lanthanum zirconate titanate (PLZT). This composition is transparent, and displays electro-optical and piezo-optical coupling. A standard photo-stress arrangement (crossed polarizers and quarter wave plates) gives a direct view of electric field and stress concentrations. Electric field is observed to cause cracks to close. This is consistent with earlier predictions of a negative energy release rate.

keywords: ferroelectric, relaxor, compact tension, electric field, piezoelectric, PLZT

1. INTRODUCTION

Fracture toughness is a measure of a material's ability to resist crack growth. Many observations (most based on Vickers indentations[1,2,3]) indicate that stress and electric field interact with cracks in ferroelectric ceramics. In poled piezoelectrics, additional crack growth is observed perpendicular to the polarization direction. Recently there have been many efforts to extend the mathematical formalisms of fracture mechanics to ferroelectric ceramics. Asymptotic analysis has been done with assumed boundary conditions of an impermeable or conducting crack interior. This work presents direct observations of the effect of finite permittivity and finite dielectric strength within a notch or a crack.

2. EXPERIMENTS

2.1. Material Characteristics

PLZT (lead lanthanum zirconate titanate) is a relaxor ferroelectric. Specimens were produced from two compositions, 8/65/35 and 9.4/65/35 (at%La/PZ/PT) . At room temperature 8/65/35 is ferroelectric and 9.4/65/35 is quadratic electrostrictive. These will be referred to as ferroelectric and relaxor compositions in the following discussion. The properties of both compositions are given in Table 1. They have a rhombohedral crystal structure and an average 5 μm grain size.

TABLE I. PROPERTIES OF PLZT[4]

Composition (%La/Zr/Ti)	8/65/325	9.5/65/35
d_{33} ($\times 10^{-12}$ C/N)	682	0
P^R (C/m^2)	0.30	0
Ec (MV/m)	3.6	0
Tc (°C)	110	25
25°C Phase	Ferro. Rh.	
ε_r	3350	5500
tan δ (%)	2.5	5.5
resistivity (Ω-cm)	10^{13}	10^{13}
k	0.648	0
S_{11} ($\times 10^{-12}$ m^2/N)	12.4	12.4
Q_{11} (m^4/C^2)	0.018	0.021
Q_{12} (m^4/C^2)	-0.008	-0.009

2.2 Test Technique

Specimens were cut to the dimensions shown (Fig. 1). They were then places in a servo-hydraulic test frame between crossed polarizers and quarter wave plates as shown (Fig. 2). A tensile load, a voltage, or both were applied. The voltage was applied to silver epoxy electrodes on the top and bottom of the specimen. The electrodes were insulated with epoxy to prevent arcing. Birefringence was observed at the front of the saw cut notch.

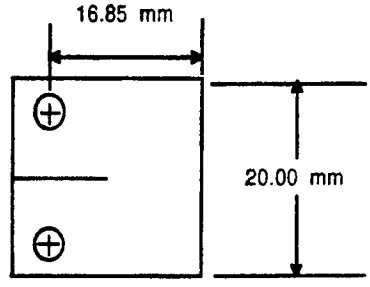

Figure 1. Compact Tension Specimen

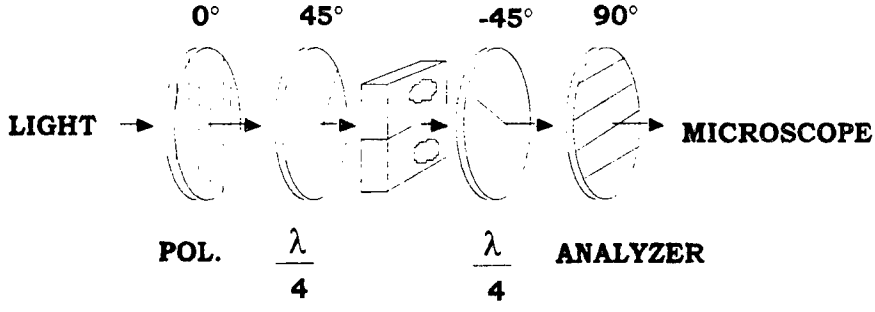

Figure 2. Experimental arrangement for monitoring notch tip birefringence.

2.3 Results

2.3.1 Mechanical Load Only

When mechanical load is applied to the specimen, the pattern of birefringence is similar to that of a mode I stress concentration (Fig. 3). The micro-twinning that is responsible for the birefringence is shear induced. This gives rise to birefringence patterns of the same shape as those predicted for small scale yielding.

2.3.2 Electrical Load Only

When electric field is applied to the specimen, the pattern of birefringence is circular in shape. This is consistent with the asymptotic solution for electric field in a dielectric with an impermeable crack. The solution is the same in form as that of the Mode III stress field. This leads to circular patterns similar to the shape of a plastic zone ahead of a mode III crack.

Figure 3. Birefringence contours produced by tensile stress.

Figure 4. Birefringence contours produced by electric field.

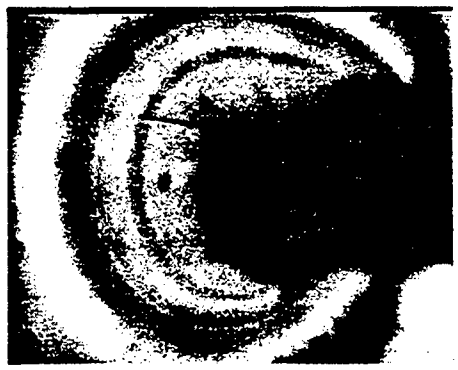

Figure 5. Electric field closes the crack, even when stress is present.

2.3.3 Electric field closes the crack

When the mechanical load was increased to 110 N, some stable crack growth occurred. The crack extended from the corner of the notch. The crack did not extend through the thickness of the specimen. The load was reduced to 60 N. At this point the crack was held open by the load. A 4000 V was then applied to the electrodes. As the voltage increased, the crack opening diminished. The voltage and stress were then reduced to zero and little or no residual birefringence were observed.

2.3.4 Evidence of Internal Arcing and Residual Charge

A voltage of 6000 V was applied next. When this voltage was reduced to zero, residual birefringence was observed (Fig. 6). This residual birefringence could be eliminated by application of 2000 V to the electrodes. The air within the notch or within the crack apparently ionized and distributed charge on the crack surfaces. This charge reduced the electric field concentration at the front of the notch.

Figure 6. Residual birefringence observed upon removal of a strong electric field.

3. DISCUSSION

3.1. Cracks in Permeable Dielectrics

Cracks with a low permittivity interior in a high permittivity material, that lie perpendicular to the electric field, concentrate the field at their tips[5-8]. This is clearly observed in the figures resented above. Polarizing PZT and BT by application of a strong electric field changes the toughness[7-13], with a decrease perpendicular to the polarization. A DC electric-field further changes the toughness[12,13]. Dielectric breakdown within notches or pores decreases electric field concentration by spreading a surface charge over the interior surface. This charge terminates the normal component of electric displacement.

3.1. J-Integral

The compact tension specimen is being developed as a J-integral test specimen. The energy release rate definition of J states that the external work done per unit crack advance is a measure of the toughness of the material. The external work can be directly measured by monitoring the load vs. displacement and the voltage vs. charge curves at several crack lengths.

ACKNOWLEDGEMENTS

This work was supported by ONR through contract E25-L35.

REFERENCES

1. Anstis G.R., Chantikul, P., Lawn, B.R., Marshall, D.B., "A Critical Evaluation of Indentation Techniques for Measuring Fracture Toughness: I, Direct Measurements" *J. Am. Ceram. Soc*, **64** (9), 533-538, 1981
2. Braun L.M., S.J. Bennison, B.R. Lawn, "Objective Evaluation of Short Crack Toughness Curves Using Indentation Flaws: Case Study on Alumina-Based Ceramics", *J. Am. Ceram. Soc.*, 75[11] 3049-57 (1992)
3. Marshall D.B., B.R. Lawn, "An Indentation Technique for Measuring Stresses in Tempered Glass Surfaces", *J. Am. Ceram. Soc.* 60 [1,2] Jan-Feb (1977)
4. Lynch C.S., "The effect of uniaxial stress on the electro-mechanical response of 8/65/35 PLZT", Submitted to Acta. Met. (1995)
5. Suo Z., "Mechanics Concepts for Failure in Ferroelectric Ceramics", in *AD-Vol. 24/AMD-Vol. 123, Smart Structures and Materials, ASME Proceedings*, 1991
6. McMeeking, R.M., "Electrostrictive Stress near Crack-like Flaws," *J. Appl. Math. Phys.* **40**, 615-627 (1989)
7. Yang, W. and Z. Suo, "Cracking in Ceramic Actuators Coused by Electrostriction", *J. Mech. Phys. Solids*, 42[4], 649-63, (1994)
8. Suo, Z., "Models for Breakdown-Resistant Dielectric and Ferroelectric Ceramics," *J. Mech. Phys. Solids.* **41**, 1155-1176, 1993.
9. Pisarenko, G.G., V.M. Chushko, and S.P. Kovalev, "Anisotropy of Fracture Toughness of Piezoelectric Ceramics", *J. Am. Ceram. Soc.*, **68** [5] 259-65, 1985
10. Tobin A.G., Y.E. Pak, "Effect of electric field on fracture behavior of PZT ceramics", Proceedings SPIE Vol. 1916/79, March (1993)
11. Okazaki K., "Mechanical behavior of ferroelectric ceramics", Ceramic Bulletin, 63[9] (1984)
12. Sun C.T., S.B. Pak, "Determination of fracture toughness of piezoelectrics under the influence of electric field using Vicker's indentation", School of Aeronautics and Astronautics, Purdue University, unpublished work
13. Raynes A.S., G.S. White, S.W. Frieman, B.S. Rawal, "Electric field effects in a lead magnesium niobate ceramic", NIST (need reference)
14. Mehta K., A.V. Virkar, "Fracture Mechanisms in Ferroelectric-Ferroelastic Lead Zriconate Titanate (Zr:Ti=0.54:0.46) Ceramics", J. Am. Ceram. Soc. 73[3] 567-74 (1990)
15. Cao H.C., A.G. Evans, "Electric Field Induced Fatigue Crack Growth in Ferroelectric Ceramics", *J. Am. Ceram Soc* (in press 1995)
16. Lynch C.S., W. Yang, L. Collier, Z. Suo, R.M. McMeeking, "Electric Field Induced Cracking in Ferroelectric Ceramics", Accepted for Publication in Ferroelectrics, (1994)

Experimental Measurements of Electro-Mechanical Constitutive Behavior of Four Compositions of PZT

William A. Stoll and Christopher S. Lynch

The G.W.W. School of Mechanical Engineering
The Georgia Institute of Technology
Atlanta, Georgia 30332-0405

Abstract - Four compositions of commercially available PZT are characterized under combined stress and electric field loading. The loading consists of a series of increasing compressive stress increments alternating with a series of bipolar electric field cycles. The softest composition has the lowest Young's modulus and shows hysteresis in the electric field cycle that increases as the compressive stress is increased. A distinct yield stress associated with the onset of deformation twinning (depolarization) is evident at around 25 Mpa. After loading to 180 Mpa and unloading, there is a large residual strain. The hardest composition has a higher Young's modulus, shows little or no hysteresis in the electric field cycle until the compressive stress has been applied, has a distinct yield point at around 75 Mpa associated with the onset of deformation twinning, and after loading to 180 Mpa and unloading the non-linear strain is recovered. There is no residual strain. The two compositions that lie between the extremes display intermediate behavior.

1. INTRODUCTION

The selection of an active material for the design of an actuator system is often based on the d_{33} linear piezoelectric coefficient and the loss tangent. These coefficients are measured at small field and are not adequate for predicting the behavior under large electric field or stress. This work presents the results of an experimental survey of several compositions of PZT under high stress and electric field loading.

The recent interest in developing PZT as an actuator material for large force and displacement applications has pushed the use of the materials beyond the regime where there is design data. Operating the material at high stress and electric field levels results in non-linear and irreversible behavior. This is associated with deformation twinning (depolarization by 90° domain wall motion in the tetragonal case) when critical stress and electric field levels are exceeded. A combination of stress and electric field acting simultaneously can reduce the levels that cause depolarization.

The properties that are most familiar to users are those measured at small stress and electric field, usually using an acoustic resonance technique [1]. The linear properties [2] and the loss tangent are published by most of the suppliers of PZT. Reported stress/strain curves [3] and detailed measurements of the stress/strain/electric-field behavior of 8/65/35 PLZT [4] led to this survey of several compositions of soft and hard commercially available materials. Creep and stress relaxation [5] (associated with aging) are not addressed in this work.

There has been relatively little modeling of constitutive behavior from the mechanics perspective. An elementary micromechanics model [6] was developed for tetragonal materials. This model simulates the electric-displacement/electric-field, strain/electric-field, and stress-strain behavior with some success. An extension of the model is needed to include a back stress and back electric field that induce strain and polarization recovery, the ability to simulate the rhombohedral geometry, and the interaction effects between the grains of the ceramic. Phenomenological models of multiaxial deformation twinning induced by stress and electric field are still needed for finite element calculations of material response. This will facilitate computational studies of non-uniform material loading such as occurs in the fracture process and in complex transducer designs.

These models have not been developed largely due to a lack of data. Experimental techniques for this type of measurement have only recently been developed. This work presents a survey of four commercially available compositions under combined stress and electric field loading. The loading is isothermal (room temperature) and quasi-static. The materials range from soft to hard. These are terms used to describe the effects of dopants [7].

Proceedings of the 1996 IEEE International Symposium on the Application of Ferroelectrics.

2. MATERIALS

The materials were obtained in a prepoled state from a commercial source [8]. The manufacturer's names for the various compositions are listed in each figure. A loading fixture (Fig. 1) was developed to simultaneously apply compressive stress and electric field.

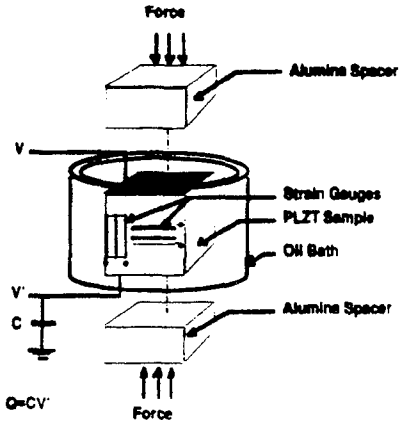

Figure 1. Combined compressive stress and electric field loading fixture.

3. EXPERIMENTAL RESULTS

The data presented below (Figs. 2-5) describe the behavior of PZT ranging from soft to hard under combined stress and electric field loading. Starting at zero stress and strain the electric field is positively cycled to approximately -0.7 MV/m and then back to zero. Next, it is negatively cycled to -.07 MV/m then back to zero. The stress is then increased at zero electric field. Holding the stress constant, the electric field is cycled again. This loading is repeated until the sample is unloaded at zero electric field. Several features are of note. The soft composition has depoled after the stress is removed. This results in a residual strain of about 6000 microstrain. (See [4] for a detailed discussion of depolarization and loss of remanent strain.) The hard material depoles, but the internal field causes it to spontaneously repole when the stress is removed. There is no residual strain. Also, the hysteresis seen in the zero stress electric field cycle of the soft material is associated with the large loss tangent and low Q. This does not occur in the hard material.

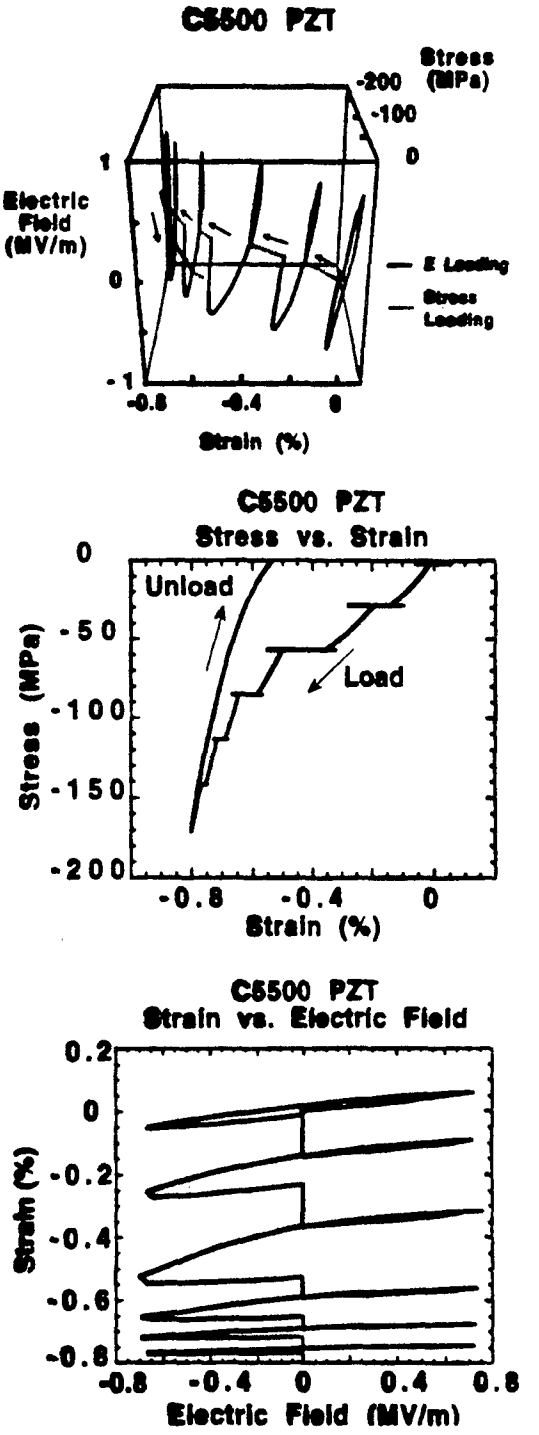

Figure 2. Softest composition of PZT tested. Full stress/strain/electric-field cycle (top). Stress/strain cycle (middle). Strain/electric-field (bottom). Note the low elastic modulus and the large d_{33}. These are associated with domain wall motion and hysteresis. This material is easily depoled.

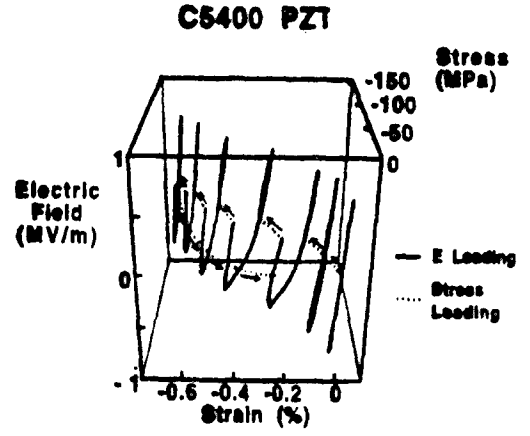

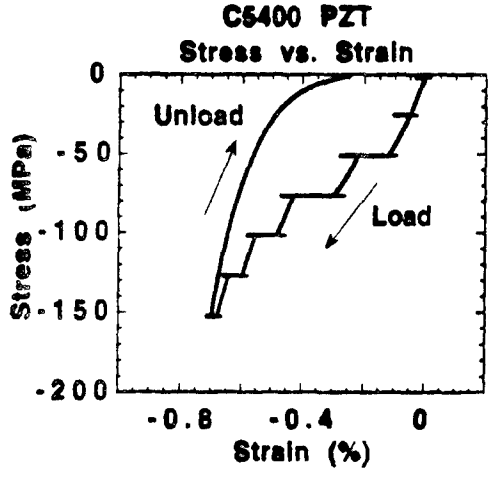

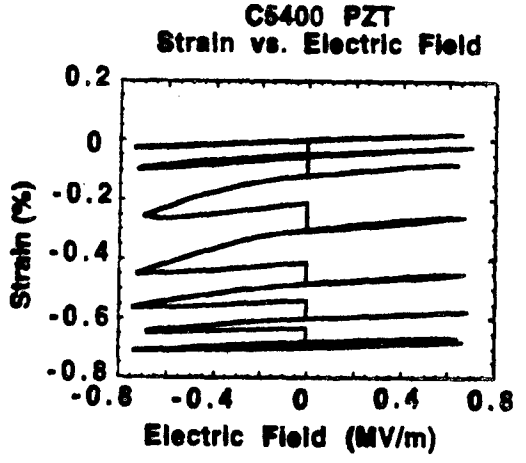

Figure 3. Intermediate/soft composition of PZT. Full stress/strain/electric-field cycle (top). Stress/strain cycle (middle). Strain/electric-field (bottom). Note the increased elastic modulus and some strain recovery after the stress is removed.

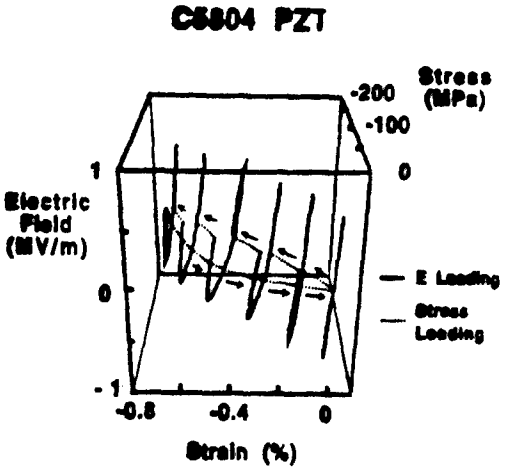

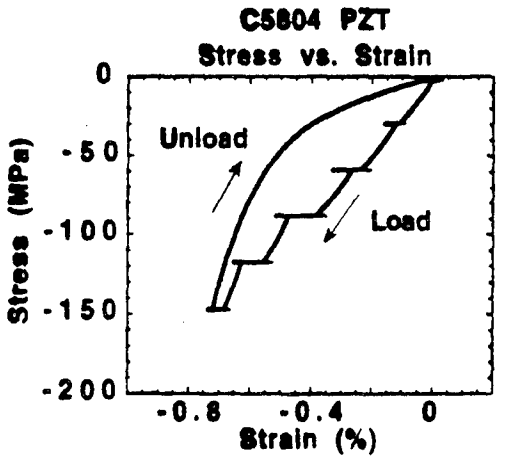

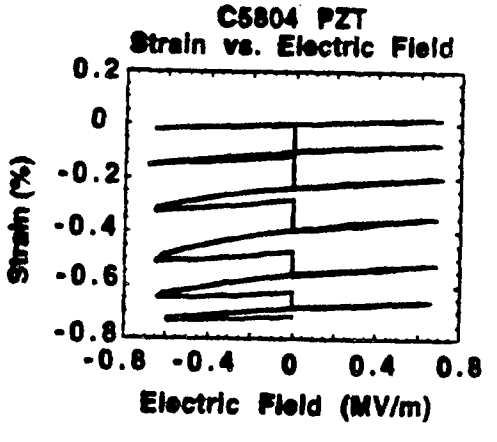

Figure 4. Intermediate/hard composition of PZT. Full stress/strain/electric-field cycle (top). Stress/strain cycle (middle). Strain/electric-field (bottom). Note the further increased elastic modulus and full strain recovery after the stress is removed.

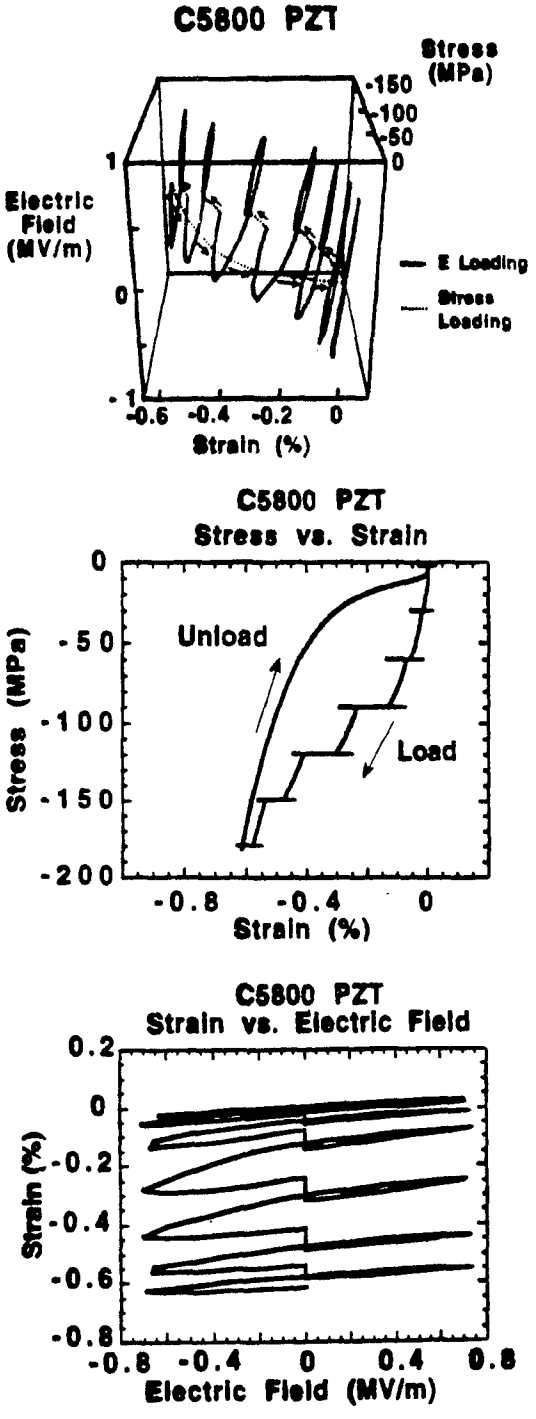

Figure 5. Hardest composition of PZT tested. Full stress/strain/electric-field cycle (top). Stress/strain cycle (middle). Strain/electric-field (bottom). Note the high elastic modulus and full strain recovery even before the stress is fully unloaded.

4. Concluding Remarks

The softest composition has the lowest elastic modulus (slope of the stress/strain curve) and highest d_{33} coefficient (slope of the strain/electric-field curve). In actuator applications, the high d_{33} coefficient does not make up for the lower blocking load. The hard compositions do not begin to depolarize until the stress level has exceeded 50 to 75 MPa or more. The soft compositions depole at much lower stress level. This further limits their application as actuators. The hard compositions have far less hysteresis in the strain/electric-field response. This makes them better candidates for micro-positioning applications. The strain recovery upon unload of the stress in the hard compositions gives a more robust design for actuator applications. An occasional stress overload does not permanently depole the ceramic.

All of these tests were run in about a one hour time frame. The hard materials will quite likely permanently depole if subjected to a compressive stress for a long duration. The tests were also conducted at room temperature. At elevated temperature, permanent depolarization of the hard material is expected to occur under compressive stress loads. Further work is needed in this area before reliable device design can be accomplished.

5. Acknowledgments

This work was supported by the Office of Naval Research through Contract E-25-L35.

6. References

[1] Cady, W.G. Piezoelectricity, Dover, N.Y, 1964

[2] Lines and Glass, *"Principles and Applications of Ferroelectrics and Related Materials"*, Oxford 1977

[3] Cao H.C., A.G. Evans, "Nonlinear Deformation of Ferroelectric Ceramics", J. Am. Ceram. Soc., 76[4] 890-96, (1993)

[4] Lynch C.S., "The effect of uniaxial stress on the electro-mechanical response of 8/65/35 PLZT", Submitted to Acta. Met. (1995)

[5] Esaklul K.A., W.W Gerberich, B.G. Koepke, "Stress relaxation in PZT", J. Am. Ceram. Soc. 63[1,2], 25-30, (1980)

[6] Hwang S.C., C.S. Lynch, and R.M. McMeeking, *"Ferroelectric/Ferroelastic Interactions and a Polarization Switching Model"*, Accepted for publication in Acta Met. June 1994

[7] Jaffe B., W.R. Cook, and H. Jaffe, *"Piezoelectric Ceramics"*, p 162, Academic Press London and New York, 1971.

[8] Channel Industries, Goleta, California

Defense Special Weapons Agency
Alexandria, VA 22310-3398

DNA-TR-96-12

Microelectronic Radiation Hardening Process and Design Development, Test, and Evaluation

Patrick McMarr
Akos Revesz
SFA Inc.
1401 McCormick Drive
Largo, MD 20774-5322

Reek Lawrence
Advanced Research and Applications
425 Lakeside Drive
Sunnyvale, CA 94086

March 1997

Technical Report

CONTRACT No. DNA 001-91-C-0054

DESTRUCTION NOTICE:

Destroy this report when it is no longer needed.
Do not return to sender.

PLEASE NOTIFY THE DEFENSE SPECIAL WEAPONS AGENCY, ATTN: CSTI, 6801TELEGRAPH ROAD, ALEXANDRIA, VA 22310-3398, IF YOUR ADDRESS IS INCORRECT, IF YOU WISH IT DELETED FROM THE DISTRIBUTION LIST, OR IF THE ADDRESSEE IS NO LONGER EMPLOYED BY YOUR ORGANIZATION.

DISTRIBUTION LIST UPDATE

This mailer is provided to enable DSWA to maintain current distribution lists for reports. (We would appreciate your providing the requested information.)

☐ Add the individual listed to your distribution list.

☐ Delete the cited organization/individual.

☐ Change of address.

NOTE:
Please return the mailing label from the document so that any additions, changes, corrections or deletions can be made easily. For distribution cancellation or more information call DSWA/IMAS (703) 325-1036.

NAME: _____

ORGANIZATION: _____

OLD ADDRESS	CURRENT ADDRESS
_____	_____
_____	_____
_____	_____

TELEPHONE NUMBER: ( ) _____

DSWA PUBLICATION NUMBER/TITLE	CHANGES/DELETIONS/ADDITIONS, etc.) *(Attach Sheet if more Space is Required)*
_____	_____
_____	_____
_____	_____

DSWA OR OTHER GOVERNMENT CONTRACT NUMBER: _____

CERTIFICATION OF NEED-TO-KNOW BY GOVERNMENT SPONSOR (if other than DSWA):

SPONSORING ORGANIZATION: _____

CONTRACTING OFFICER OR REPRESENTATIVE: _____

SIGNATURE: _____

CUT HERE AND RETURN

DEFENSE SPECIAL WEAPONS AGENCY
ATTN: IMAS
6801 TELEGRAPH ROAD
ALEXANDRIA, VA 22310-3398

DEFENSE SPECIAL WEAPONS AGENCY
ATTN: IMAS
6801 TELEGRAPH ROAD
ALEXANDRIA, VA 22310-3398

DOCUMENT 2

Microelectronic Radiation Hardening Process and Design

AD-A322246

March 1997

SFA INC

Landover, MD

REPORT DOCUMENTATION PAGE

Form Approved
OMB No. 0704-0188

1. AGENCY USE ONLY (Leave blank)	2. REPORT DATE	3. REPORT TYPE AND DATES COVERED
	970301	Technical 910404 - 960115

4. TITLE AND SUBTITLE
Microelectronic Radiation Hardening Process and Design Development, Test, and Evaluation

5. FUNDING NUMBERS
C - DNA 001-91-C-0054
PE - 62715H
PR - AF
TA - AK
WU - DH308950

6. AUTHOR(S)
Patrick McMarr and Akos Revesz (SFA); and
Reek Lawrence (ARA)

7. PERFORMING ORGANIZATION NAME(S) AND ADDRESS(ES)
SFA Inc.
1401 McCormick Drive
Largo, MD 20774-5322

Advanced Research and Applications
425 Lakeside Drive
Sunnyvale, CA 94086

8. PERFORMING ORGANIZATION REPORT NUMBER

9. SPONSORING/MONITORING AGENCY NAME(S) AND ADDRESS(ES)
Defense Special Weapons Agency
6801 Telegraph Road
Alexandria, VA 22310-3398
ESE/Palkuti

10. SPONSORING/MONITORING AGENCY REPORT NUMBER
DNA-TR-96-12

11. SUPPLEMENTARY NOTES
This work was sponsored by the Defense Special Weapons Agency under RDT&E RMC Code B4662D AF AK 00100 3400A 25904D.

12a. DISTRIBUTION/AVAILABILITY STATEMENT
Approved for public release; distribution is unlimited.

12b. DISTRIBUTION CODE

13. ABSTRACT *(Maximum 200 words)*
Radiation induced charge trapping versus Buried-Oxide (BOX) thickness on various Separation by Implantation (SIMOX) buried oxides has been determined. An inflection point has been observed in the voltage shift vs. buried oxide thickness relationship. As such, the radiation-induced voltage shifts for thin-buried-oxides are greater than what could be expected from a simple square-law relationship. These results can be explained by the location and magnitude of the radiation-induced oxide charge centroid and its relationship to the BOX thickness. The location of the centroid for trapped positive charge is dependent on the radiation-induced hole mobility, which is related to SIMOX processing as well as on geometry and charge saturation.

Photo-injection was used to study the charge trapping properties of high temperature oxidation (HITOX) SIMOX buried oxides, provided by two independent vendors. After electron injection, the electron trapping per area for both HITOX material sources was found to be larger than their respective standard (control) SIMOX structures.

14. SUBJECT TERMS
Photo-Injection
Buried-Oxide (BOX)
Oxide Charge Centroid
Electron Capture Cross Section
High Temperature Oxidation (HITOX)
Separation by Implantation of Oxygen

15. NUMBER OF PAGES
46

16. PRICE CODE

17. SECURITY CLASSIFICATION OF REPORT	18. SECURITY CLASSIFICATION OF THIS PAGE	19. SECURITY CLASSIFICATION OF ABSTRACT	20. LIMITATION OF ABSTRACT
UNCLASSIFIED	UNCLASSIFIED	UNCLASSIFIED	SAR

CLASSIFIED BY:

N/A since Unclassified.

DECLASSIFY ON:

N/A since Unclassified.

PREFACE

The authors would like to thank H.L. Hughes (NRL) for his assistance in research and material selection. The authors would also like to recognize B.J. Mrstik (NRL) for assistance in ellipsometry measurements, and D.E Ioannou (GMU) for semiconductor-device modeling assistance. And finally, the authors would like to thank R.E. Stahlbush (NRL) and D.A. Buchanan (IBM) for helpful insight in the set-up of the photo injection technique.

CONVERSION TABLE

Conversion factors for U.S. customary to metric (SI) units of measurement

To Convert From	To	Multiply
angstrom	meters (m)	1.000 000 X E-10
atmosphere (normal)	kilo pascal (kPa)	1.013 25 X E+2
bara	kilo pascal (kPa)	1.000 000 X E+2
barn	meter^2 (m^2)	1.000 000 X E-28
British Thermal unit (thermochemical)	joule (J)	1.054 350 X E+3
calorie (thermochemical)	joule (J)	4.184 000
cal (thermocemical)/cm^2	mega joule/m^2 (MJ/m^2)	4.184 000 X E-2
curie	giga becquerel (GBq)*	3.700 000 X E+1
degree (angle)	radian (rad)	1.745 329 X E-2
degree Fahrenheit	degree kelvin (K)	$^tK=(t^of + 459.67)/1.8$
electron volt	joule (J)	1.602 19 X E-19
erg	joule (J)	1.000 000 X E-7
erg/second	watt (W)	1.000 000 X E-7
foot	meter (m)	3.048 000 X E-1
foot-pound-force	joule (J)	1.355 818
gallon (U.S. liquid)	meter^3 (m^3)	3.785 412 X E-3
inch	meter (m)	2.540 000 X E-2
jerk	joule (J)	1.000 000 X E+9
joule/kilogram (J/Kg) (radiation dose absorbed)	Gray (Gy)	1.000 000
kilotons	terajoules	4.183
kip (1000 lbf)	newton (N)	4.448 222 X E+3
kip/inch^2 (ksi)	kilo pascal (kPa)	6.894 757 X E+3
ktap	newton-second/m^2 ($N-s/m^2$)	1.000 000 X E+2
micron	meter (m)	1.000 000 X E-6
mil	meter (m)	2.540 000 X E-5
mile (international)	meter (m)	1.609 344 X E+3
ounce	kilogram (kg)	2.834 952 X E-2
pound-force (lbf avoirdupois)	newton (N)	4.448 222
pound-force inch	newton-meter (N•m)	1.129 848 X E-1
pound-force/inch	newton/meter (N/m)	1.751 268 X E+2
pound-force/foot^2	kilo pascal (kPa)	4.788 026 X E-2
pound-force/inch^2 (psi)	kilo pascal (kPa)	6.894 757
pound-mass (lbm avoirdupois)	kilogram (kg)	4.535 924 X E-1
pound-mass-foot^2 (moment of inertia)	kilogram-meter^2 ($kg•m^2$)	4.214 011 X E-2
pound-mass/foot^3	kilogram/meter^3 (kg/m^3)	1.601 846 X E+1
rad (radiation dose absorbed)	Gray (Gy)**	1.000 000 X E-2
roentgen	coulomb/kilogram (C/kg)	2.579 760 X E-4
shake	second (s)	1.000 000 X E-8
slug	kilogram (kg)	1.459 390 X E+1
torr (mm Hg, 0^oC)	kilo pascal (kPa)	1.333 22 X E-1

*The becquerel (Bq) is the SI unit of radioactivity; Bp = 1 event/s.
**The Gray (Gy) is the SI unit of absorbed radiation

TABLE OF CONTENTS

TABLE OF CONTENTS (Continued)

FIGURES

FIGURES (Continued)

SECTION 1
INTRODUCTION

Various Silicon-On-Insulator (SOI), in principle SIMOX, and thermal oxide materials were evaluated for their oxide (SOI: buried-oxide) charge trapping properties over the duration of the contract. The contractual material arrived in wafer form, often only portions of a whole wafer. Quick turn-around test structures, the dual C-V and the point contact transistor (or 2ptIV), described in detail later in this report, were the benchmark vehicles for material characterization throughout this contractual effort. Two major finding are discussed below. The first has to do with the SIMOX buried-oxide charge trapping response versus buried-oxide thickness. The second observation deals with a unique post oxidation treatment to the finished SIMOX wafer, called HITOX.

Throughout this report the two findings will be discussed in parallel. The work performed in both material areas complements each other in a better understanding of the charge trapping response on the SIMOX buried-oxide.

1.1 CHARGE TRAPPING VS. BURIED-OXIDE THICKNESS.

As device geometries are scaled to smaller dimensions to the far submicron regime, the film thickness of silicon-on-insulator structures will need to be reduced. As the superficial silicon is being reduced in thickness from 300nm to 50nm, the buried-oxide thickness is being reduced from 400nm to 70nm. Will the radiation-sensitivity of the thinner SIMOX buried-oxide scale in thickness with the same relationship that holds for thermal oxides?

Thermal oxides have a known square-law thickness dependence [1], but due to large variations in material properties, the thickness dependence for SIMOX structures has remained undetermined. In earlier work, which was limited to the lower interface of standard SIMOX material (300nm<BOX<450nm), a square-law thickness dependence was observed [2]. With the availability of improved material, and new diagnostic techniques (spectroscopic ellipsometry and quick-turn-around test structures), the relationship can now be determined for the top interface and extended to BOX thicknesses below 100nm. The work in this report will cover BOX thicknesses from 68nm to 401nm.

The importance of monitoring the charge trapping response of the BOX top interface is that it is this interface that controls the back-channel transistor threshold. In fully-depleted SOI structures the front-channel transistor is electrically coupled

to the back-channel transistor. The electrical performance of SOI CMOS circuity can be severely limited by the degradation of the back-channel transistor threshold [3].

One of the purposes of this report is to enhance the knowledge of the radiation induced voltage shift of BOX material as a function of BOX thickness. This thickness relationship is needed for design and testing considerations for SOI technology as scaling in thickness occurs. The understanding of radiation induced voltage shifts as BOX thickness scales downward is important for properly designing and interpreting device measurements. Device designers need these results to aid in predicting device response, and assist in selecting approaches for radiation hardening of BOX material.

1.2 POST HIGH-TEMPERATURE OXYGEN TREATMENT OF SIMOX.

As mentioned above, additional work was performed on an unique post high temperature oxidation treatment to the finished SIMOX wafer. Several advances in SIMOX substrate fabrication are now making possible the use of the SIMOX technology for mainstream microelectronics applications [4]. This has generated an increased interest for further quality improvement of the silicon film/buried oxide. An approach taken recently is a high temperature oxidation of the finished SIMOX wafer [5,6], which was found to increase the buried oxide thickness in addition to oxidizing the top silicon film surface. Cross-sectional transmission electron microscopy (XTEM) photomicrographs indicated this high temperature oxidation (HITOX) process reduced the roughness and improved the morphology of the interface between the silicon film and the buried oxide [7].

This HITOX/BOX structure was considered to have improved material characteristics; however, the electrical properties, and in particular the charge trapping characteristics, were not evaluated. In addition to the aforementioned effort dealing with charge trapping versus BOX thickness, this report will also evaluate the electron trapping behavior of HITOX material versus standard SIMOX obtained from two separate sources. The sources will be referred to as vendor A and vendor B. It should be noted, it was not the purpose of this endeavor to compare vendor A to vendor B, but only to have two different sources of material for evaluation of a given research and development technology.

SECTION 2
EXPERIMENTAL

2.1 MATERIAL PREPARATION.

The SIMOX wafers arrived fully processed with respect to the SIMOX buried oxide and it's high temperature anneal. Any additional contractual processing adjustments made to the buried oxide for charge trapping modification would be classified and are not mention in this report. Below are briefly described the two main material categories, the SIMOX material and the HITOX/SIMOX material.

2.1.1 Formation of SIMOX Buried-Oxide.

The SIMOX samples used in this report were obtained from a variety of different vendors. The high-energy (120keV to 200keV) oxygen implantation dose (single and multiple) used to form the BOX ranged from 0.4×10^{18} O^+/cm^2 to 1.8×10^{18} O^+/cm^2. In all cases a post implantation anneal was performed for a standard anneal time [4].

2.1.2 The Post High-Temperature Oxygen Treatment.

In approaching the characterization of the HITOX technology, a SIMOX control was selected for comparison. The samples were processed in a similar fashion as those in previous publications [2,4]. The SIMOX wafers were formed by a standard process [5,7]. The resulting thicknesses of the buried oxides were 97.5nm for vendor A, and 103nm for vendor B. This thickness range is considered thin for SOI material and is currently gaining importance [8]. Following the formation and anneal of the BOX (the finished SIMOX wafer), the HITOX process is performed. From spectroscopic ellipsometry measurements, it was found [9] that the HITOX process increased the BOX thickness by 25nm for vendor A and 5nm for vendor B.

2.2 DEVICE FABRICATION.

The material evaluated throughout this report arrived in whole or portion of wafer form. The SIMOX wafers were finished SIMOX wafers (BOX formed, and high-temperature anneal performed). Using our simple processing procedures, quick turn around test structures were fabricated. Listed below are three of the principle test structures fabricated for material evaluation.

2.2.1 Dual C-V Structure.

The dual capacitance-voltage C-V device was a fundamental structure used throughout this work. The first device fabrication step was to deposit aluminum dots onto the SIMOX top silicon film. These aluminum gates were than used as a mask for

a hydrazine etch which removed the surrounding top silicon film down to the buried oxide. The finished structure was an aluminum gate on top of a silicon island, which resided on top of the buried oxide and silicon substrate. Figure 2-1 a) shows the $Al/Si/SiO_2/Si$ structure, or the dual C-V device.

2.2.2 Point-Contact Transistor.

The point contact transistor (or 2ptIV, for two point current voltage) was also a fundamental structure used throughout this work. The fabrication of the point contact transistor was similar to the above dual C-V structure. First the SIMOX wafer had aluminum dots deposited on the top silicon film. These aluminum gates were than used as a mask for a hydrazine etch which removed the surrounding top silicon film down to the buried oxide. (At this point, the structure is identical to the above capacitance C-V dot.) Next, the aluminum gate was removed. The remaining structure was an isolated silicon island. The height of the silicon island depended on the arriving top silicon film

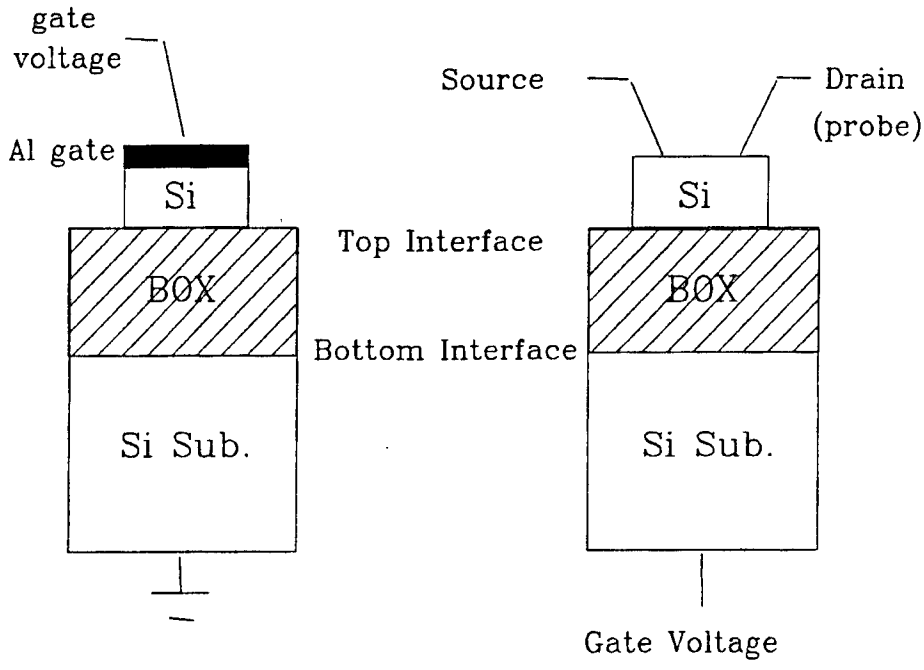

Figure 2-1. Simple diagram of the SIMOX a) dual C-V structure, and b) the point-contact transistor.

thickness. This isolated silicon island was the finished structure. Two probes were placed upon the top silicon (approximately 5mil apart) acting as source and drain, and the wafer substrate acted as the gate. With the buried oxide acting as the gate oxide, the device response was that of a MOSFET transistor from weak-midgap to strong inversion for both carrier types. Figure 2-1 b) shows the finished point contact transistor.

2.2.3 Photo I-V Structure.

Fabrication of the photo I-V structure requires the removal of the top silicon film [10,11]. With the BOX exposed, large but thin aluminum gates were deposited. The aluminum gate allows the structure to perform as a capacitor (the largest of the gate is need for measurable electron injection current levels), and the thin aluminum gate allows the 5ev mercury light to pass through. The finished photo I-V structure is shown in Figure 2-2.

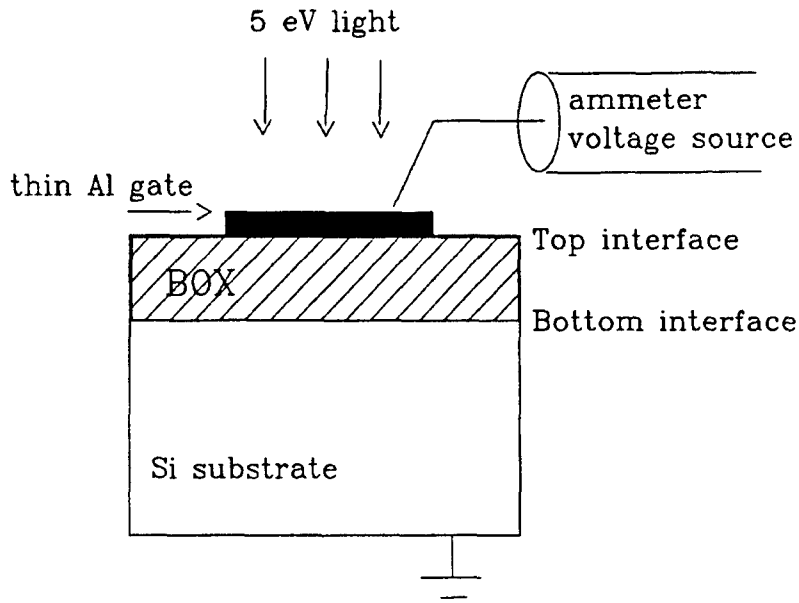

Figure 2-2. The SIMOX photo I-V structure used for photo-injection.

2.3 EQUIPMENT.

The equipment used throughout this effort was all part of an advanced computer controlled semiconductor parameter analysis system. Each measurement capability was automated by computer code for controlled data collection. Listed below are descriptions of select sub-systems that were used to characterize delivered material throughout the reported period.

2.3.1 Capacitance and Current Measurement Equipment.

The computer automated data acquisition of capacitance and current versus voltage data routines were controlled by a Hewlett Packard (HP) model 9000 series 300 computer. The capacitance vs voltage data was collected by any of the following; a HP 4280A 1Mhz C meter, HP 4274A or HP 4275A multi-frequency LCR meter. The current vs voltage data was collected by any of the following; a Keithley 617 ammeter, a HP 4140B pico-ammeter, or a HP 4145A semiconductor parameter analyzer.

2.3.2 X-Ray Source.

To generate electron/hole pairs in the buried oxide, thus creating oxide trapped charge, our samples were exposed to 10 KeV

X-rays from an ARACOR 4100 X-ray source. The dose rate was variable, but the standard dose rate was 1800rad(SiO_2)/sec. The samples were exposed in a total dose fashion to total doses as high as 10Mrad(SiO_2). The standard dose was 1Mrad(SiO_2). All sample biasing, irradiations, and measurements were done by probecards at room temperature.

2.3.3 Photo-Injection Equipment.

The photo-injection system is more complex than the other mentioned data acquisition systems. The light source, which yields the needed energy for electron injection, must be shutter controlled. With the lamp on and shutter open the electron injection current must be monitored, then intermittently the shutter must be closed to allow for capacitance monitoring. The controlling computer is the above mentioned HP system. The capacitance and current meters are also the same as mentioned above. The light source was an Oriel 500 watt mercury lamp powered by a Oriel 68810 arc lamp power supply.

2.4 METHODS OF INVESTIGATION.

A variety of techniques were used to characterize the charge trapping of the buried oxide. Listed below are three principle techniques used. Each section briefly describes a technique, and the expected results obtained by using the technique.

2.4.1 Capacitance-Voltage Method.

The capacitance versus voltage technique is a standard for monitoring trapped charge in the oxide [12]. Since the SIMOX buried oxide is known the exhibit bulk oxide trapping [13], the dual C-V structure is ideal for top and bottom voltage shift parameter extraction. The ratio of the voltage shifts also yields a charge centroid [12].

The SIMOX wafer lends itself naturally for the dual C-V structure. The problems arise in data extraction though. Often the top interface is difficult to identify, due to doping differences between top silicon film and bottom silicon substrate. The bulk of the work presented here is done n-type top silicon and p-type silicon substrates. The bottom C-V curve is clear and data extraction is excellent. The top C-V curve is often a bit more evasive, but with good correlation between the top C-V shift and that of the point-contact transistor confidence in the top C-V shift is obtained. In general, only a ΔV_{mg} is monitored for the top and bottom interface. Additional information is not necessary for material characterization at these stages of investigation.

2.4.2 Current-Voltage Method.

The principle technique used to characterize the material provided was the two-point-current-voltage (2ptIV) technique (sometimes referred to as: point contract or quick-turn-around structure (QTA)). When introduced, this new measurement technique demonstrated a fast turn-around testing capability for the top interface of SIMOX material [14,15]. Later the current-voltage data was shown to be consistent to that of a finished transistor [16]. The 2ptIV technique was used throughout this effort, and the test structure is shown in Figure 2-1 b).

Typical 2ptIV and dual C-V (n-type top Si, and p-type bottom Si) characteristics before and after radiation are shown in Figure 2-3. The BOX structure used in Figure 2-3 is a typical medium BOX thickness structure (T_{BOX}=164nm). Note that both the 2ptIV and the dual C-V structure yield the same top interface voltage shift information. This is a key correlation to support the use of the 2ptIV technique throughout the effort.

Additional validity of the 2ptIV technique can be shown by comparing C-V and 2ptIV charge trapping results for the a variety of samples. Figure 2-4, shows this comparison for ground bias as well as for biased data. The two techniques yield the same voltage shift information. Thus, for charge trapping information on the top interface, the 2ptIV technique has been used in this effort for material evaluation.

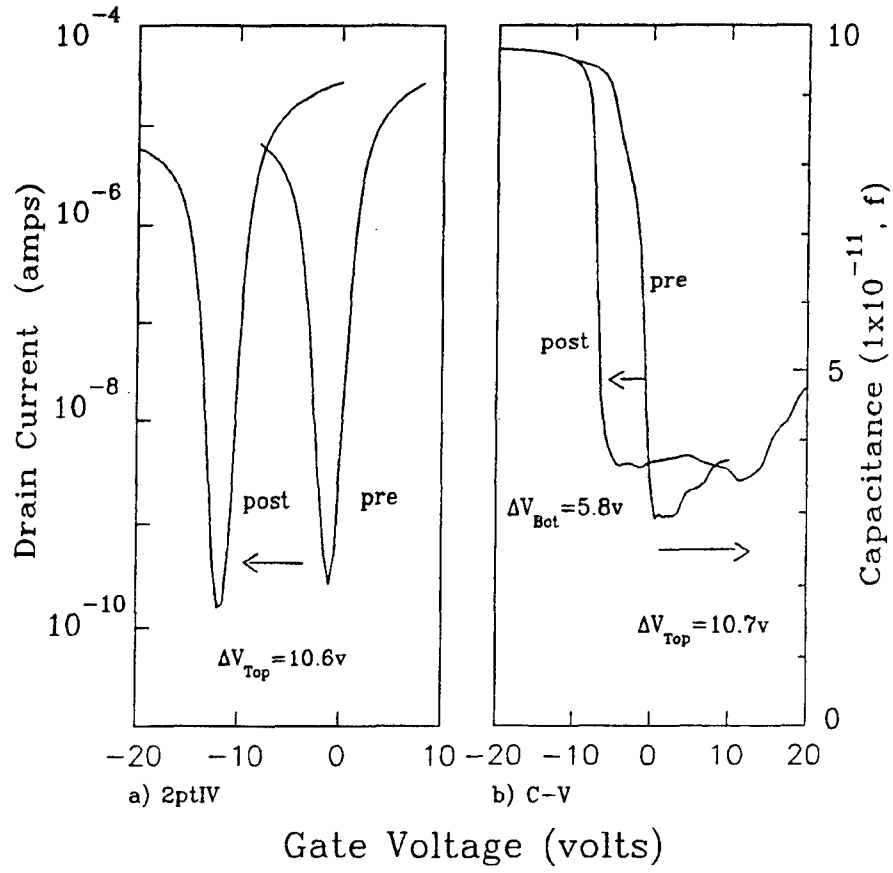

Figure 2-3. Sample results after 1Mrad (SiO2) with V_{BG}:+5x10^4 V/cm, a) 2ptIV results, and b) dual C-V results.

2.4.3 Photo-Injection Method.

Electron trapping in the BOX was investigated with the use of the photo injection technique. The photo-injection structures, as mentioned earlier, were fabricated by removing the top silicon layer, and depositing a thin (20nm) aluminum gate. The structure represents a capacitor with a thin gate, the thinness of the gate allows the mercury light to pass through. A Oriel 500 watt mercury lamp supplies the energy for electron injection into the oxide, and is filtered to prevent hole injection (Oriel filter 59418). For the work presented in this report, a constant electron injection current density of 1x10^{-7} A/cm^2 was maintained for approximately 42 hrs by varying the negative applied gate voltage, causing electron injection from the aluminum gate. The applied field remained under 0.5 MV/cm.

The electron trapping behavior within the BOX was evaluated by capacitance and photo-current measurement techniques. The midgap

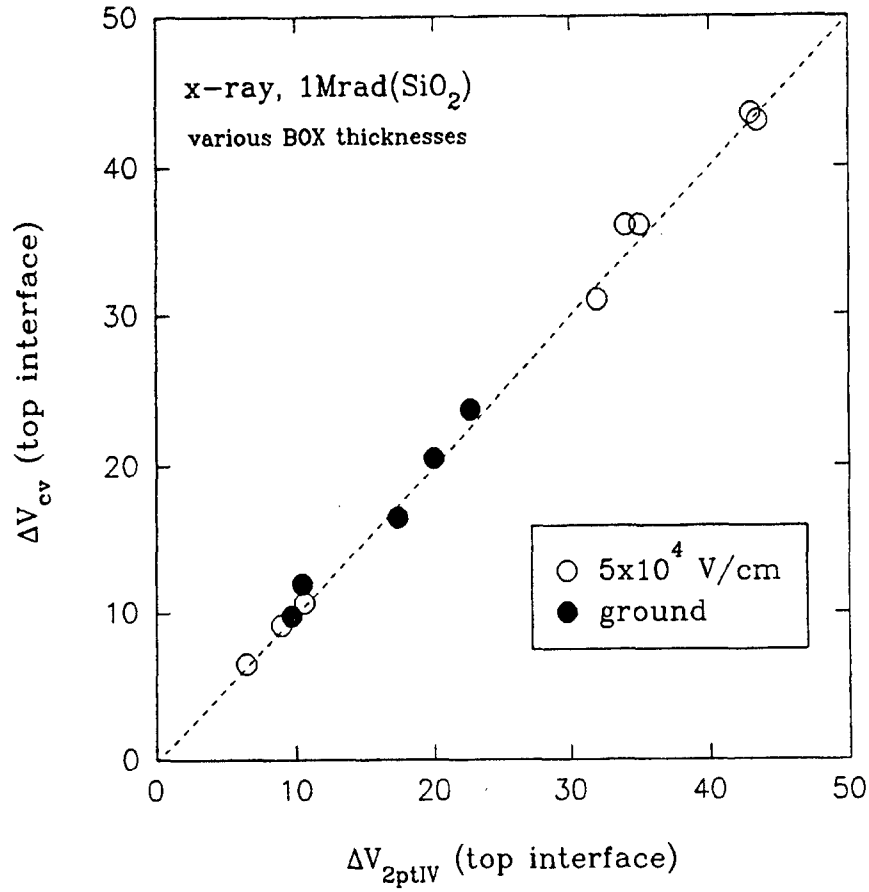

Figure 2-4. A comparison of top interface voltage shifts for the C-V and the 2ptIV techniques.

capacitance of the capacitor is monitored as a function of electron injection (a ΔV_{mg} vs injection-time is recorded). From this data an electron capture cross section can be determined [7]. Finally, from the photo-injection I-V curve, the total number of occupied electron trap and a charge centroid can be determined [12].

SECTION 3
EXPERIMENTAL RESULTS

3.1 CHARGE TRAPPING IN BURIED-OXIDES.

For SOI circuits in space bound systems, fringing fields in the BOX are of extreme importance for BOX charge control. Charge buildup within the BOX effects the threshold voltage of the back-channel transistor. The pass-gate bias condition, where both the source and drain are in the "high" bias condition (V_{dd}=high (+5v)) is considered the worst case bias condition for total dose testing. It is the fringing fields due to this bias condition that wrap-around and are terminated at the back-channel interface that cause the greatest device degradation. These fringing fields cause radiation-induced positive charge to drift to the back-channel interface, where it is then trapped. Here the positive trapped charge lowers the back-channel threshold of N-channel transistors, which in turn affects the front-gate-channel FET operation. Controlling, as well as predicting, the charge trapping behavior of the BOX is of extreme importance to ensure proper operation in a radiation environment.

Modeling work by Smith found that the SOI fringing field in the BOX oxide for V_{dd} "high" was an electric field of 5×10^4 V/cm [6]. Our BOX testing has focused on this fringing field effect within the BOX. The test structures have been evaluated with a substrate bias of 5×10^4 V/cm to simulate the fringing field BOX effect.

3.1.1 Charge Trapping vs. Electric Field.

The polarity and magnitude of the applied electric field across an oxide under the influence of ionizing irradiation will effect the charge trapping results [17,18]. For our dataset of SIMOX wafers the effects are of importance since the buried oxide differs so from that of a thermal oxide [19]. The effect of electric field on BOX charge trapping for a sample in our SIMOX dataset is shown in Figure 3-1. The ΔV_T voltage shifts are from point contact transistor results (the top interface) on a thick BOX structure (T_{BOX}=400.9nm). The influence of the applied electric field during irradiation on BOX charge trapping begins at 1×10^4 V/cm and is very strong by 1×10^5 V/cm. These fields are in reference to the substrate (positive bias to substrate). The work presented throughout this report on voltage shifts versus BOX thickness will cover biases from -5×10^5 V/cm to 5×10^5 V/cm. Again, the emphasis of this effort was V_{BG}:$+5\times10^4$ V/cm, simulating typical device application BOX electric fields.

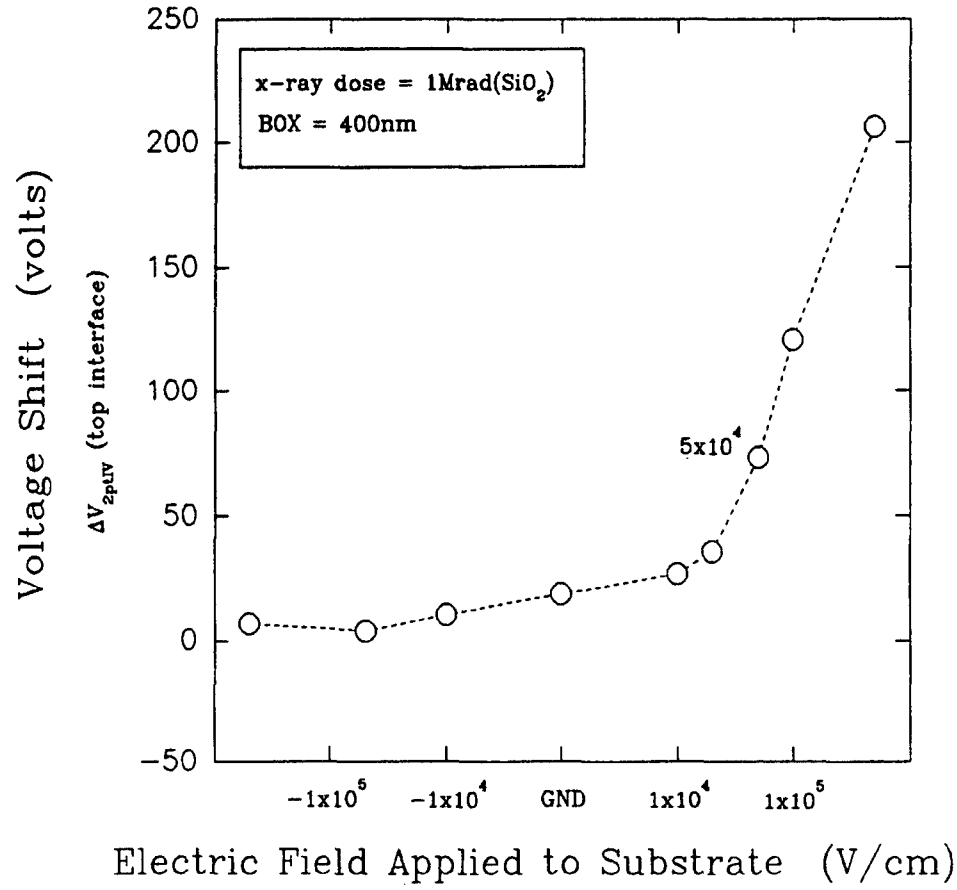

Figure 3-1. Voltage shift versus applied electric field for a dose of 1Mrad (SiO_2).

3.1.2 Charge Trapping vs. Buried-Oxide Thickness.

In efforts to compare a variety of SIMOX buried oxide technologies we have gathered a large database of BOX charge trapping results for V_{BG}: +5x10^4 V/cm at 1Mrad(SiO_2).

Figure 3-2 shows a plot of point-contact (top interface) voltage shifts for various BOX thicknesses. The entire dataset is shown in Figure 3-2.

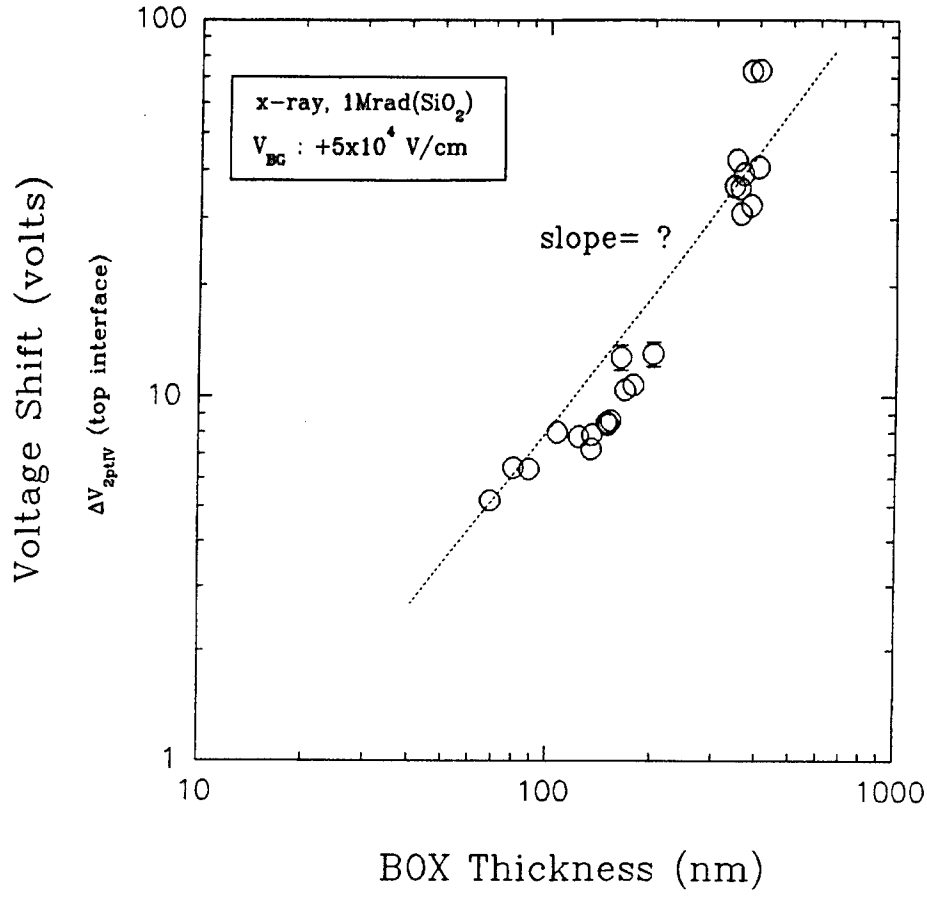

Figure 3-2. Voltage shift versus BOX thickness for VBG:+5x10^4 V/cm at 1Mrad (SiO_2), (all data included).

A primary research goal would be to extract a relationship from Figure 3-2, (graphical at the minimum) that would allow the prediction of the radiation response of SIMOX structures. A

first attempt would be to represented the dataset by a line with unity slope, (as shown in Figure 3-2). Although, scatter in the data causes some uncertainty, and knowing that SIMOX radiation results vary greatly with processing, the graph basically raises more questions than it answers. Later in this report these questions and research approaches will be addressed.

3.1.3 Charge Trapping vs. Density of Buried-Oxide.

For help in interpreting Figure 3-2, we revisited the work published by Mrstik [20]. This work compared radiation charge trapping for SIMOX BOX oxides versus an optically determined BOX density (spectroscopic ellipsometry (SE). The results were found

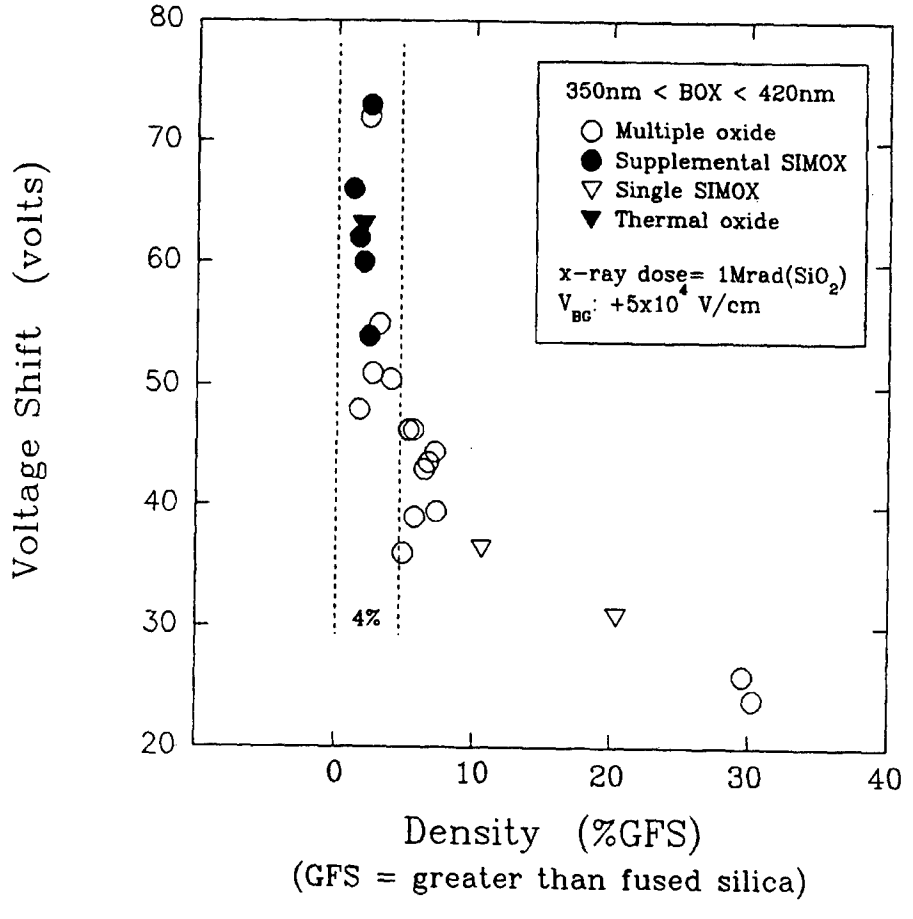

Figure 3-3. Voltage shift versus BOX density for thermal oxide and various SIMOX structures (reprint from: B.J. Mrstik [20]).

useful in analyzing our dataset. For clarity, Figure 3-3 is an annotated graph from the Mrstik publication showing the strong charge trapping variation versus a BOX density parameter.

All the samples evaluated throughout this report were characterized by the spectroscopic ellipsometry technique [9]. The optically determined density did vary among our sample dataset and material suppliers. The SE technique was also considered very accurate in determining the BOX thickness. It should be noted, this contractual effort relied largely on transistor ΔV_T BOX shifts for evaluating the charge trapping response of the buried oxide (which is fine, and necessary), but the value of the SE results should be underscored.

3.2 ELECTRON TRAPPING IN BURIED OXIDES.

The use of ionizing irradiation (X-rays) to generate electron/hole pairs within the SIMOX buried oxide usually results in a net trapped positive charge. To investigate the influence of only electron trapping on the charge trapping behavior of the BOX, the technique of photo-injection was implemented. Here only electrons are injected into and trapped within the oxide. The BOX can now be evaluated as to solely electron trapping behavior. The results below compare the electron trapping results of a standard SIMOX to a recent post-oxygen treatment applied to SIMOX.

As mentioned earlier, during the photo-injection process the midgap capacitance is monitored to evaluate the electron trapping of the BOX. With the 5ev mercury light on, and using a computer to continually adjusting the applied gate voltage to maintain a constant injection current level, the electron injection process proceeds. The computer records a capacitance ΔV_{mg} as a function of injection time (or fluence). Note, this capacitance information is from the lower (bottom) interface, and the motion of this ΔV_{mg} will saturate in time. The magnitude and shape of this ΔV_{mg} vs fluence curve is the key information extracted for the photo-injection technique.

Figure 3-4 shows the photo-injection results for both HITOX material sources with their respective control SIMOX structures. The y-axis, the midgap (ΔV_{mg}) voltage shift, has been converted into a -charge/area (electron trapping) to normalize out any thickness dependencies, and the x-axis, time of electron injection, has been converted into a number of injected electrons per area (N_{inj} cm^{-2}, a fluence). Both vendors' HITOX structures show more electron trapping per area than their respective control SIMOX structure, indicating that the HITOX process increases the electron trapping response for both vendors baseline technology. Figure 3-5 (a,b) shows the pre and post C-V curves, post referring to the end of the entire electron injection sequence. The post C-V curves show no stretch-out, and

therefore interface states, or lateral non-uniformity effects, can not account for the HITOX increase in electron trapping.

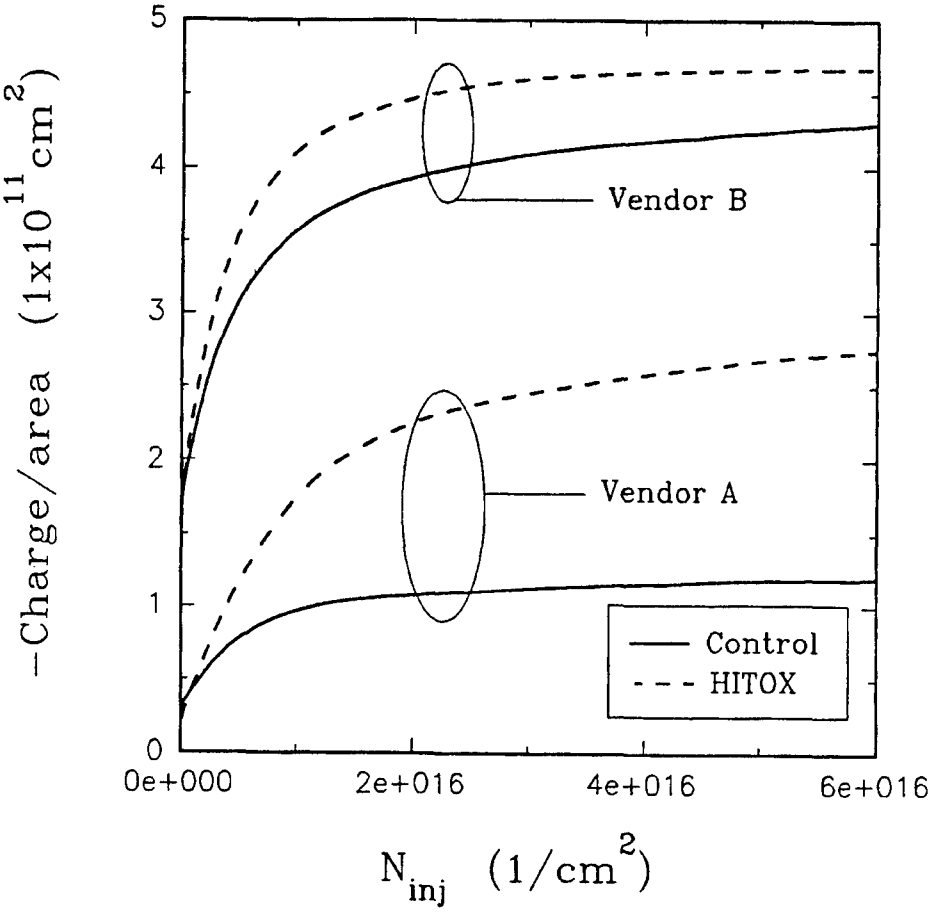

Figure 3-4. The photo-injection results for standard SIMOX and HITOX for two separate vendors. The HITOX indicates more electron trapping than the standard SIMOX material.

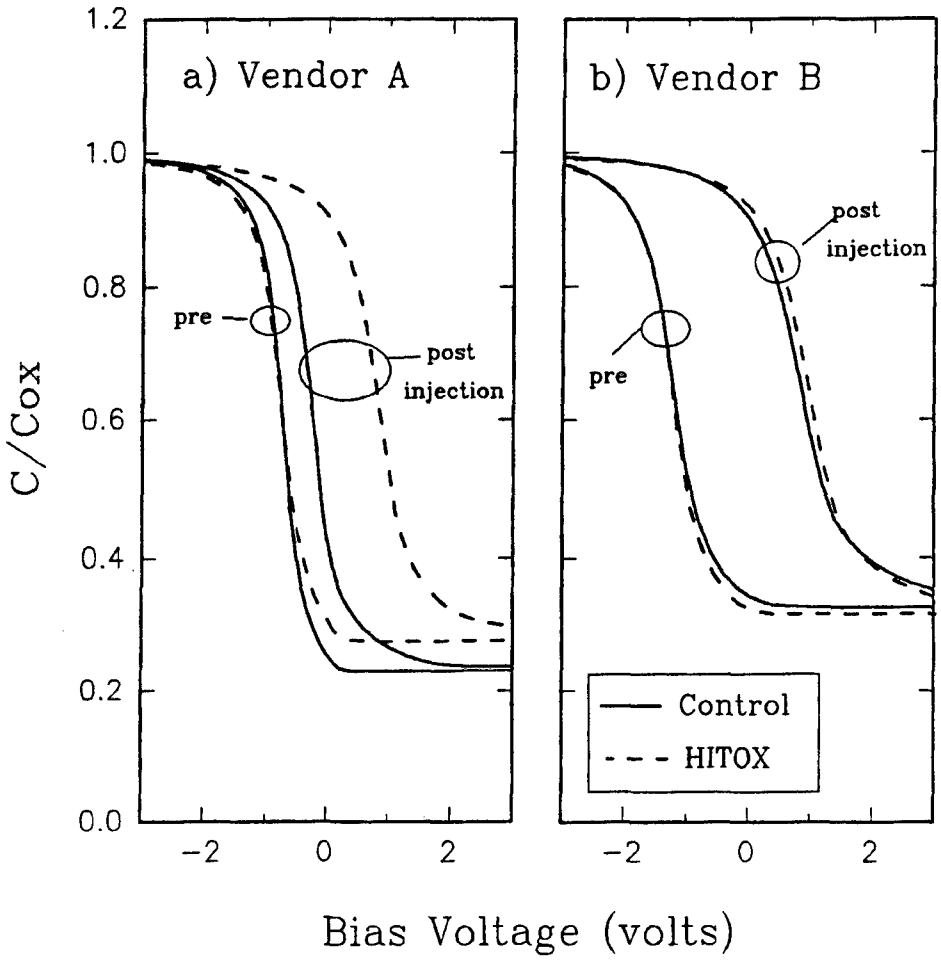

Figure 3-5. The capacitance-voltage curves for pre- and post-electron injection for standard SIMOX and HITOX for a) vendor A, and b) for vendor B.

SECTION 4
DISCUSSION AND ANALYSIS

4.1 LACK OF SQUARE-DEPENDENCE IN THICKNESS RELATIONSHIP.

By considering the results of the Mrstik et al. work on charge trapping vs. density of the BOX on similar SIMOX material, our dataset in Figure 3-2 has been re-evaluated. We selected only those samples from our dataset which had a density close to that of a thermal oxide. The assumption being that BOX with densities close to thermal oxide would behave like thermal oxide. This was supported by the wide variation in radiation induced voltage shifts observed for similar thickness samples but varying in BOX density. For instance, at a given BOX thickness, such as 430nm, the radiation induced shift was observed to vary, depending on BOX density, from 40 to 85 volts. Using the spectroscopic ellipsometry (SE) technique, we selected only those samples which had a low density (near to a thermal oxide, less than 4% Greater than Fused Silica (GFS), (density<4%GFS).

By selecting a narrow range of densities (density<4%GFS) our dataset from Figure 3-2 has been re-evaluated. Figure 4-1 shows the voltage shift versus BOX thickness for these samples with near thermal oxide density. Note the inflection point in Figure 4-1, which begins at about 180nm (the inflection point refers to the region of data with slope=0.7, the non-square-law portion). When an oxide is exposed to ionizing irradiation, there are known processes that take place; namely, the motion of radiation induced electron/hole pairs under the influence of an applied electric field, and secondly recombination within the oxide. The two processes are in competition with each other. It is known that in high density SIMOX the radiation induced holes are not mobile [20,21], in low density SIMOX the holes are mobile [20,13,22]. The value of mobility of the radiation induced holes in low density SIMOX is unknown, and beyond the scope of this work. Nevertheless, the mobility of these holes play an important role in the observed electrical voltage shift at the top interface of the BOX. More will be mentioned later on the role and influence of these radiation induced holes on the observed inflection point.

4.1.1 Location of Charge Centroid.

To better understand the observed inflection point for the V_{BG}:$+5\times10^4$ V/cm data, a few selected dual C-V structures were also irradiated (a thin=80nm, medium=164nm, and thick=350nm). The dual C-V structure yields voltage shift information for both top and bottom BOX interfaces. From these dual C-V structures a charge centroid was extracted, using the following equation [12,23]:

$$\chi = T_{BOX} * (1-\Delta V_{top}/\Delta V_{bot})^{-1} .$$

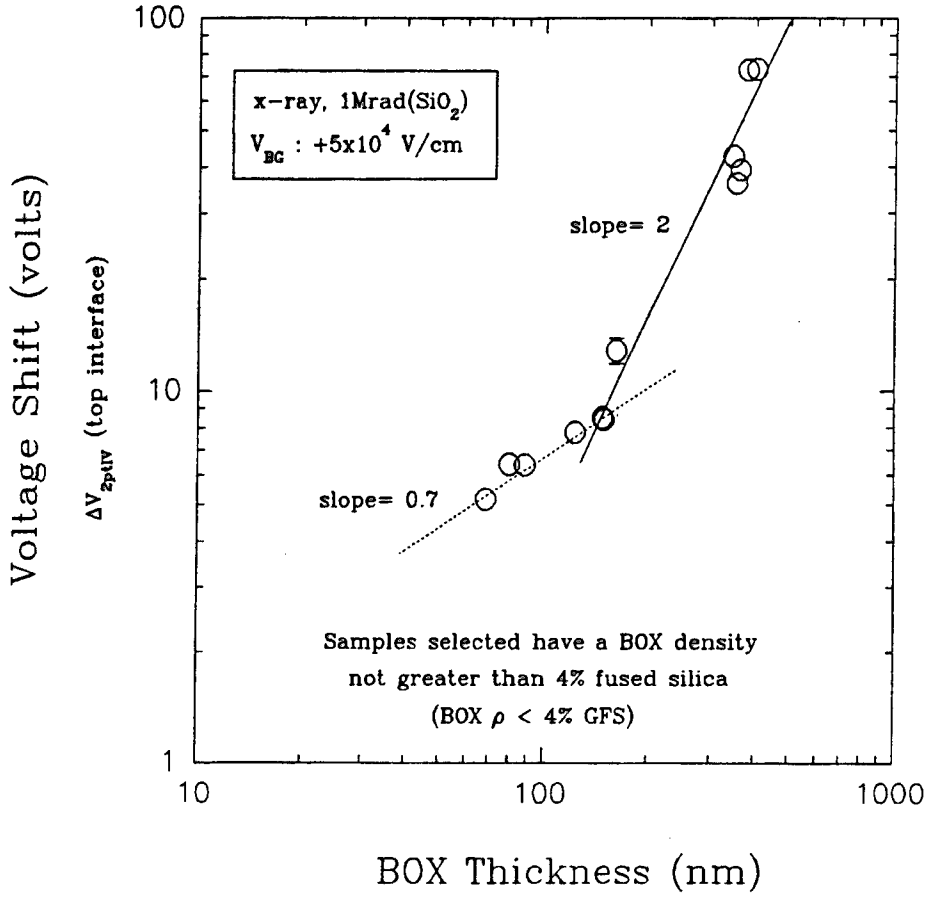

Figure 4-1. Replot of Figure 3-2 with using a density limitation.

Figure 4-2 shows the centroid data in a bar chart format. The key observation from the centroid measurements is that the centroid location has a thickness dependence. All three thicknesses appear to trap the same level of charge, 4×10^{-7} C/cm^2, at 1Mrad(SiO_2). The key difference is the location of the centroid. Namely, the thin BOX sample has its centroid at 34nm; whereas, the thick has its centroid at 76nm. The location of the BOX centroid vs. thickness must be a material property, since we still observe a similar phenomena at saturation (shown later in this report). The observation that all three thicknesses have approximately the same trapped oxide charge is probably related to hole mobility and trap concentration limitations. Since the holes in the thick BOX relative to the thin BOX have to move farther to reach their centroid location (almost a factor of six

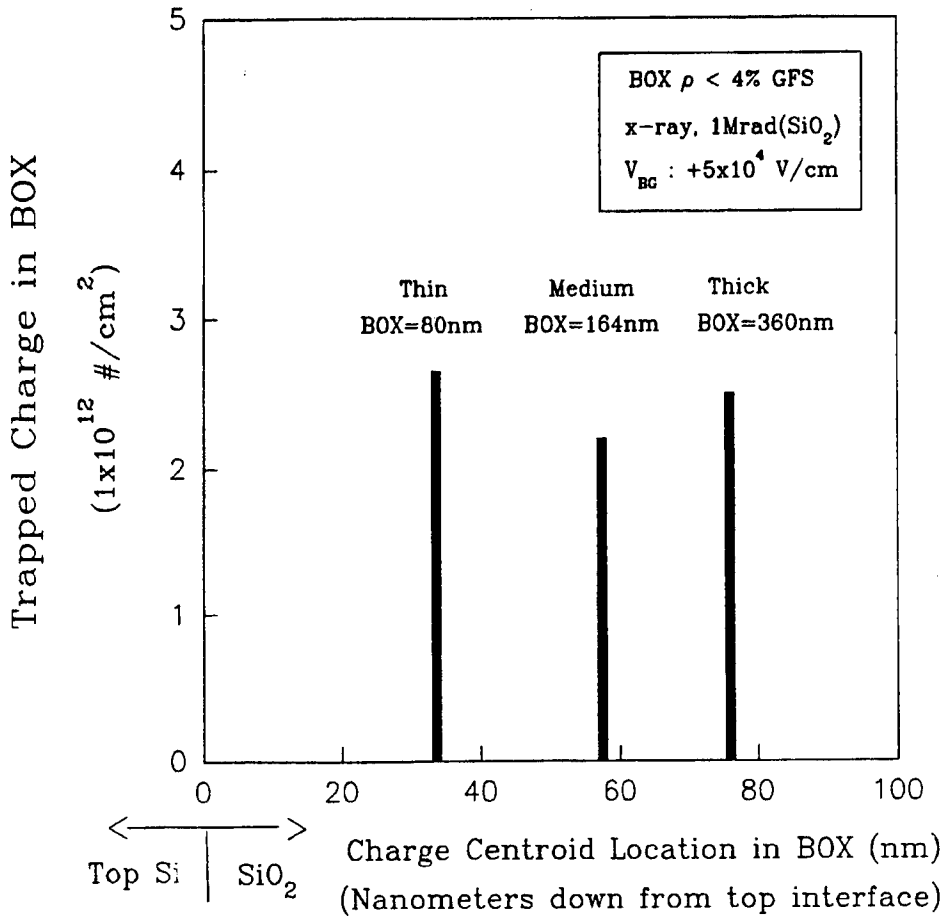

Figure 4-2. The centroid magnitude and location for three difference thicknesses. The radiation was done for V_{BG}:+5x10^4 V/cm at 1Mrad (SiO_2).

in distance).

Now returning to Figure 4-1, what if a simple geometric correction is made to the centroid locations for the medium and thin BOX structures? Basically, if the thin BOX centroid is moved from 34nm to 76nm, where it is for the thickest sample, the interface should sense approximately half the trapped charge. Using this argument, the medium and thin BOX have been adjusted. The result is shown in Figure 4-3.

This geometric correction reestablishes the square-law dependence. Thus, the observed inflection point can be explained by the location of the charge centroid for the medium to thin non-saturated BOX structures.

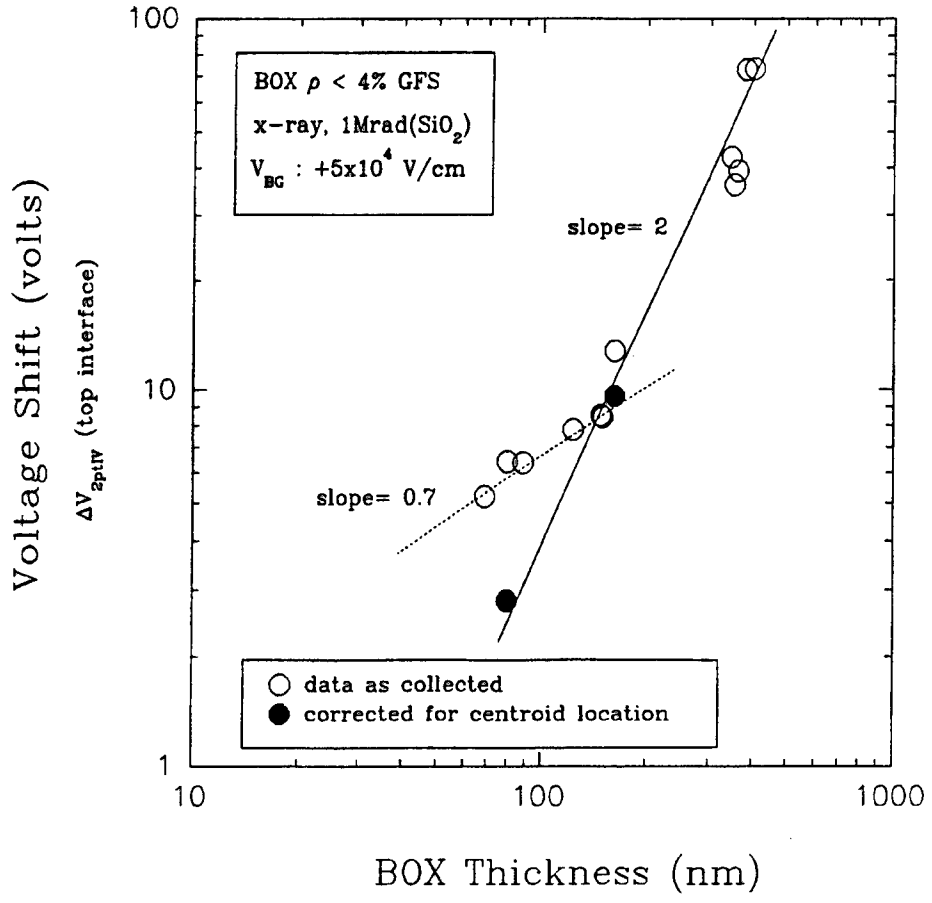

Figure 4-3. A re-plot of the V_{BG}:+5x10^4 V/cm data using a simple geometric correction for the medium and thin BOX centroid.

4.1.2 Motion of Radiation-Induced Holes.

To better understand the above observed BOX charge trapping phenomena, a more detailed knowledge of the total dose charge trapping response was needed. Figure 4-4 shows the total dose response for a BOX=350nm with low density and an applied fringing field of V_{BG}:+5x10^4 V/cm.

Note that the 1Mrad(SiO_2) location appears to be in the middle of the total dose curve. This location indicates a non-saturation condition within the BOX. The term non-saturation implies that the given process has not come to completion. The two processes involved here are; the radiation induced hole drift under the

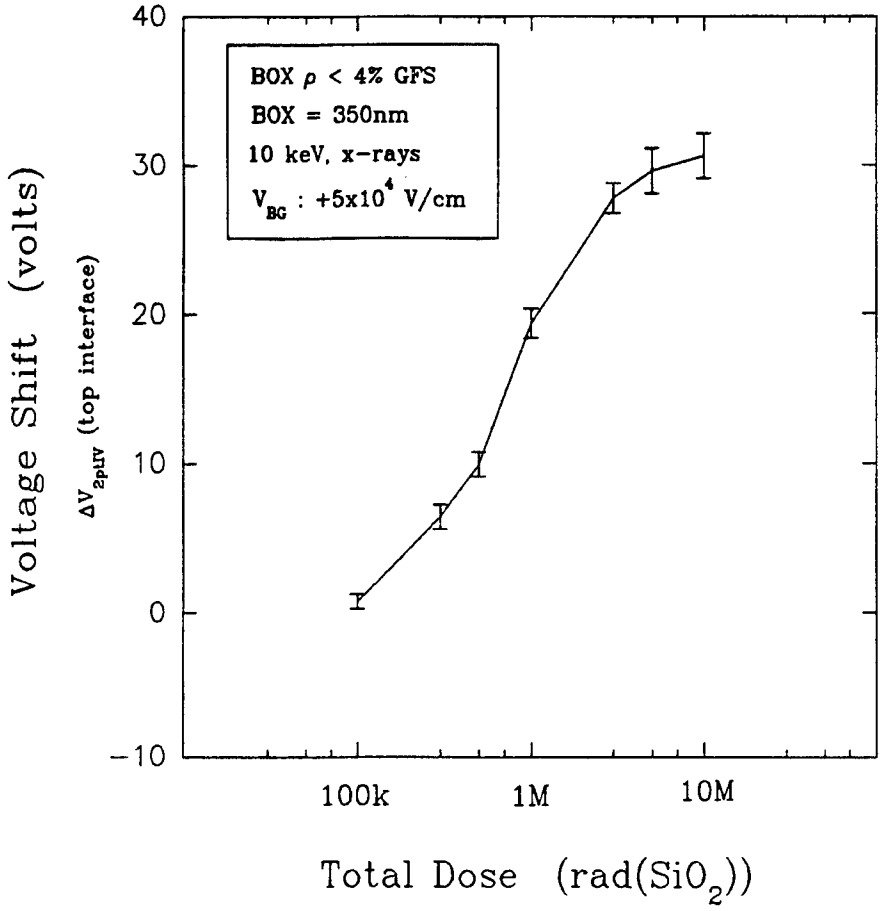

Figure 4-4. A total dose plot for V_{BG}:+5x10^4 V/cm. (The observed reduction in voltage shifts in Figure 4-4, as compared to Figure 4-1, is due to brief isothermal annealing at each dose location.)

influence of an applied electric field, and second, recombination. The more likely incomplete process here is the mobility of the holes.

Normally when comparing charge trapping among various oxides, only charge saturated conditions are considered. For this purpose a field of 5x10^5 V/cm was selected and a total dose evaluation was conducted. Figure 4-5 shows the total dose response for a 350nm BOX, low density, and with V_{BG}:+5x10^5 V/cm. Note that at a dose of 1Mrad(SiO_2) the BOX appears charge saturated.

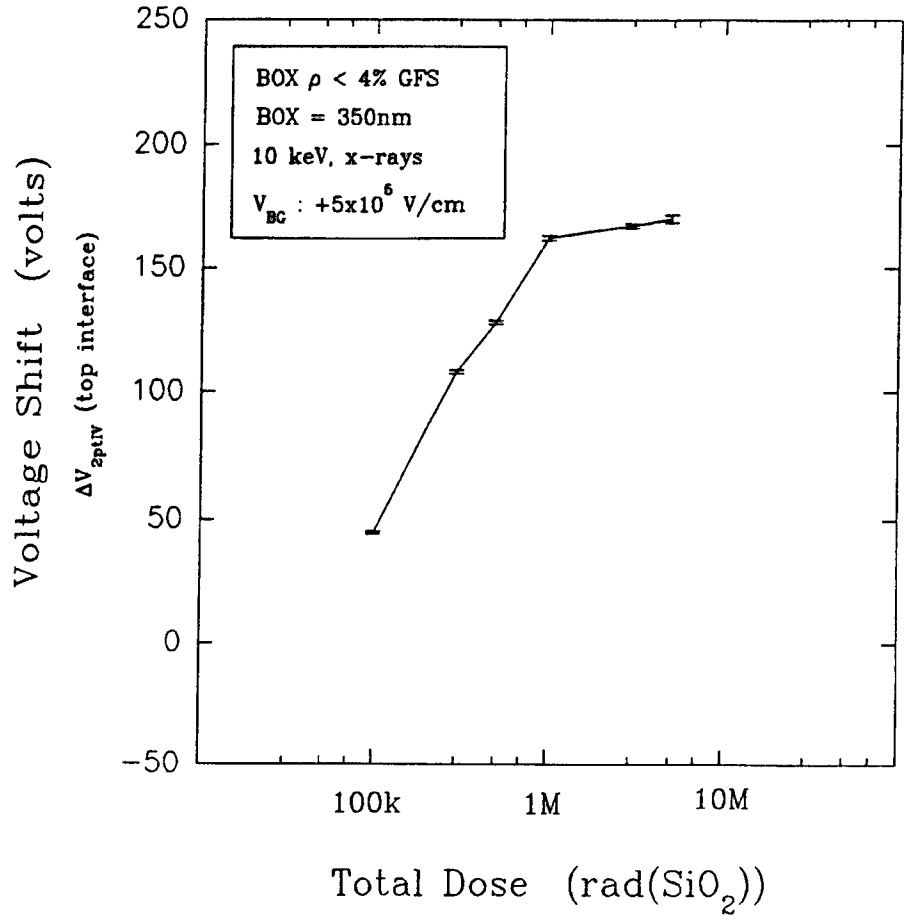

Figure 4-5. Voltage shift plot versus total dose for V_{BG}:+5x10^5 V/cm.

The voltage shift versus BOX thickness data for V_{BG}:+5x10^5 V/cm under a BOX-saturation condition is shown in Figure 4-6. The square-law dependence fits well. However the data in Figure 4-6 is related to an unrealistic device operating condition. The results from Figure 4-6 would be misleading to the applied "real-world" device designers. Namely, SOI components do not normally have such high fringing fields in the BOX region, and more importantly satellite systems are concerned with lower (non-saturation) level doses. The present emphasis is for components that can tolerate low field and low dose conditions. Charge trapping information from a saturation condition would be misleading to device designers.

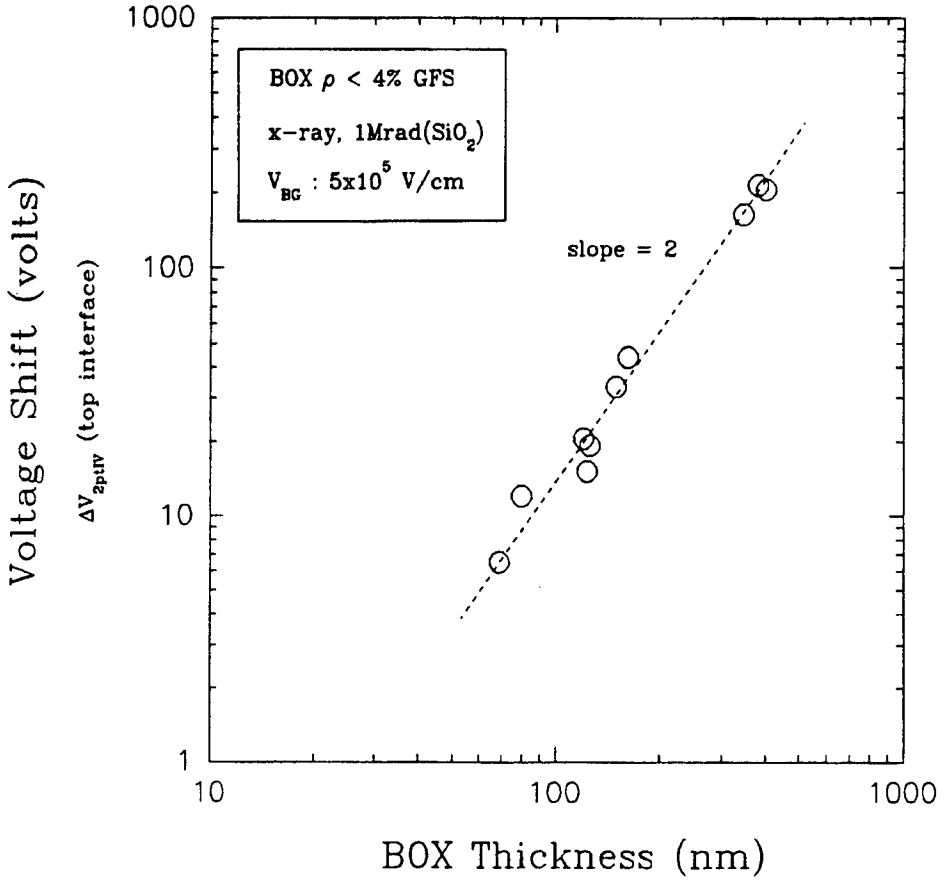

Figure 4-6. Voltage shift versus BOX thickness for V_{BG}:+5x10^5 V/cm at 1Mrad(SiO_2).

Even though the higher bias is a non-typical device electric field across the BOX, we investigated this saturation bias to gain insight into the BOX charge trapping mechanisms. Similar to above, selected dual C-V structures were repeated using V_{BG}:+5x10^5 V/cm 1Mrad(SiO_2). From these results an oxide charge centroid versus thickness relationship was obtained. Figure 4-7 shows the centroid location and magnitude for the three selected thicknesses. Note that in saturation the thicker the oxide the more charge is trapped in the BOX.

The charge to thickness relationship for this saturation condition is shown in Figure 4-8. Note the sub-linear

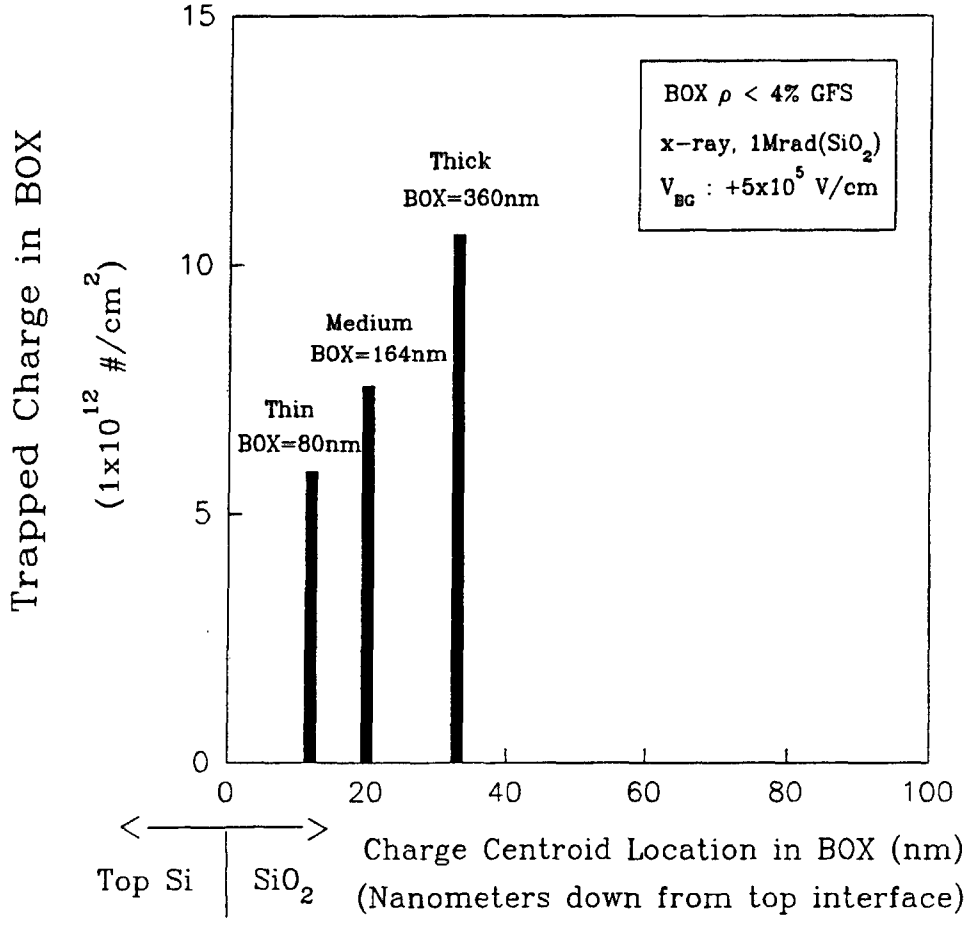

Figure 4-7. The centroid magnitude and location for three different thicknesses. The radiation was performed for V_{BG}:+5x10^5 V/cm at 1Mrad(SiO_2).

relationship, which differs from that expected for a thermal oxide (a power of unity). It is known that SIMOX, due to the oxygen implantation process used to form the buried oxide, has bulk oxide trapping [21]; whereas, thermal oxides only have charge trapped at the Si-SiO_2 interface [1]. It would also be expected that the BOX charge centroid and magnitude might vary with thickness, due to the different levels of implant damage caused by the varying oxygen implant energies needed to form the various BOX thicknesses. An etch-back experiment would be necessary to obtain a detailed charge to thickness relationship needed to explain the above saturation square law behavior. At this point we present the above charge to thickness relationship

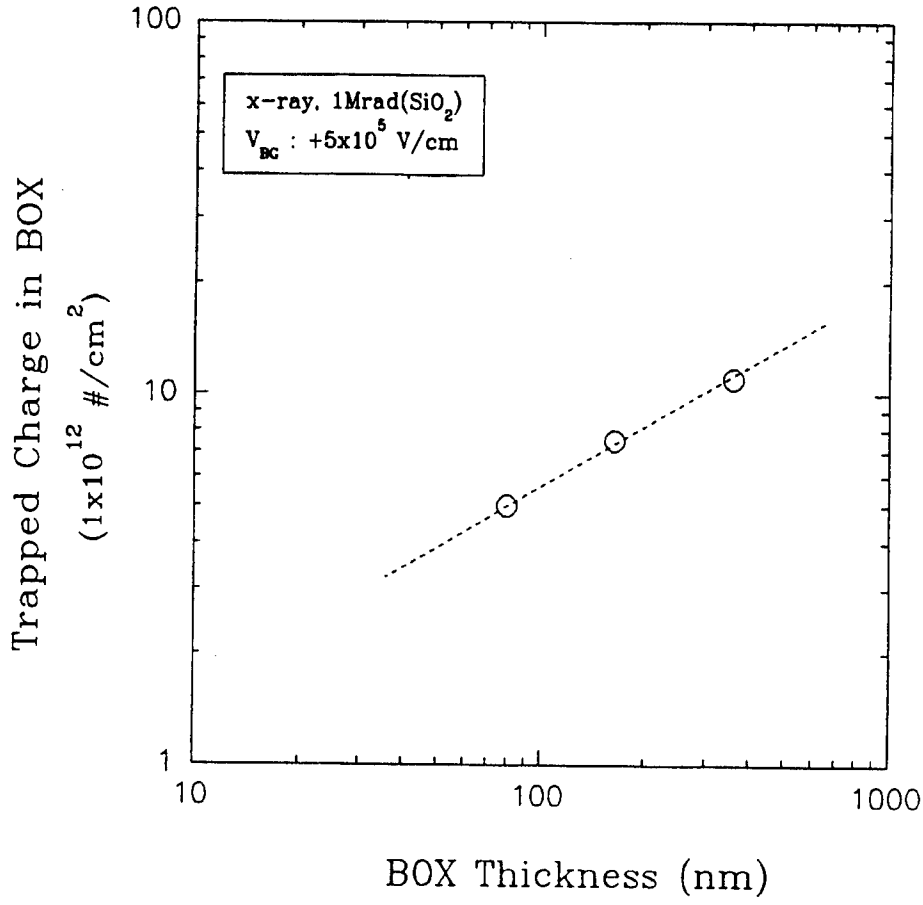

Figure 4-8. BOX trapped charge vs BOX thickness under saturation bias condition (V_{BG}:+5x10^5 V/cm, 1Mrad(SiO_2).

as an observational finding, and note that when the BOX is biased in saturation the square law dependence is observed.

To complete the bias range, other biases were also evaluated. Figure 4-9 shows voltage shift data versus BOX thickness for biases ranging from -5x10^5 V/cm to 5x10^5 V/cm. The negative biases show very little thickness dependence. From ground to 1x10^5 V/cm the inflection point is observed. Note the slope of the inflection point migrates into the square-law dependence as the applied bias during irradiation increases. This behavior is attributed to the centroid magnitude and location, which is now known to be influenced by the applied bias during irradiation and the BOX thickness.

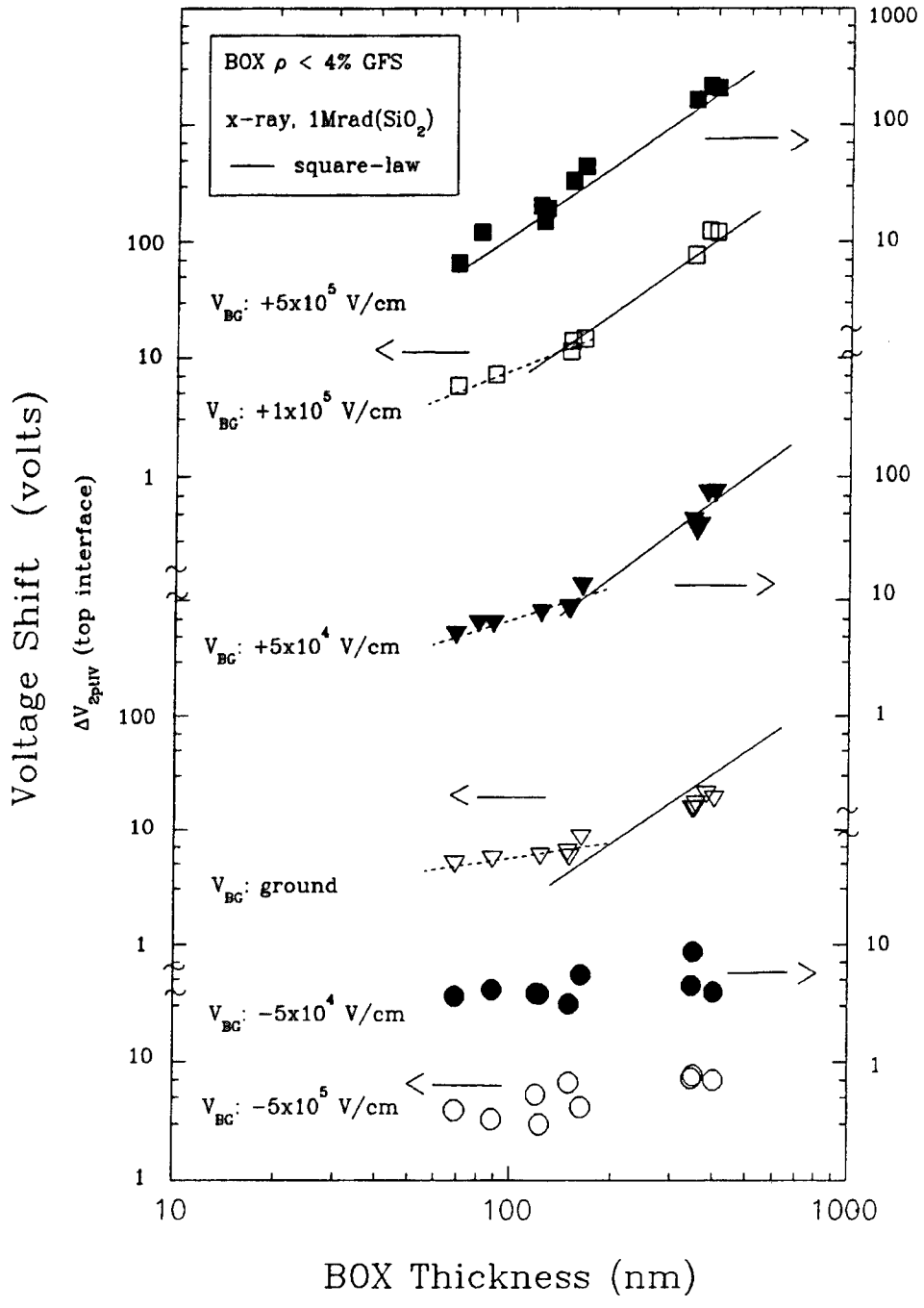

Figure 4-9. A group plot of voltage shift versus BOX thickness for various biases.

The main observation of this work is the appearance of an inflection point in the voltage shift versus BOX thickness relation for bias and radiation conditions typical of real applications. This inflection point is observed to appear at biases of ground and migrate into the square-law dependence at biases greater than V_{BG}:$+5\times10^5$ V/cm. The inflection point can be removed by allowing the BOX to saturate in radiation induced charge buildup.

The results for the non-saturation condition can also be explained by considering the influence of the applied electric field during irradiation on the motion of the radiation induced holes versus the BOX thickness. The applied electric field (V_{BG}:positive) in this experiment causes the radiation induced holes to drift toward the top interface (simulating the pass-gate (source and drain "high") fringing field effect). For thin BOX material (<100nm) all the radiation induced holes are swept to the top interface. In the medium to thick BOX material only a fraction of the radiation induced holes drift to the top interface, due to hole mobility limitations. Increasing the applied field during irradiation increases the fraction of mobile holes that will make it to the top interface for the thicker material, thus removing the inflection point in the thickness relationship.

Thus, the observed inflection point is a phenomena of non-saturation, and results from the radiation induced holes in the BOX not being able to move the greater distances required by the thicker BOX structures. When the BOX is biased into saturation during irradiation, the holes drift as far as they can go under the influence of the applied electric field and avoid recombination.

The importance of this work is in the comparison of SIMOX material as technology moves from the standard thick BOX material (>340nm) to the thinner BOX material (<100nm, possibly fully depleted). Having an understanding of the charge trapping to thickness relationship will help in determining material improvements, and aid device designers to predict circuit response.

4.2 BURIED-OXIDE ELECTRON TRAPPING RESPONSE.

From the photo-injection current vs. voltage curves (not shown here), the total bulk electron trapped charge and an electron charge centroid can be determined [10,12,23]. In contrast to the C-V measurements, the photo I-V obtains information from both interfaces, and thus the total bulk trapped charge Q_T per area is

$$Q_T = (\epsilon_{BOX} / T_{BOX}) * (\Delta V_+ + \Delta V_-),$$

where ϵ_{BOX} is the permittivity of the oxide, T_{ox} the BOX thickness, ΔV_+ is the voltage shift when injection occurs from the BOX/Si interface, and ΔV_- is the voltage shift when injection occurs from the Al/BOX interface. The total number of occupied traps N_T per area is

$$N_T = Q_T/q,$$

where q is the electron charge, and the position χ of the charge centroid from the Al/BOX interface is

$$\chi = T_{BOX} / (1- \Delta V_- / \Delta V_+).$$

In addition, from the data in Figure 3-4, the electron capture cross sections can be determined [24]. The results of the above calculations are summarized in Table 4-1 for the materials provided by vendors A and B.

What can clearly be observed from Table I is that the HITOX process, when compared to the corresponding control, has a larger total number of occupied traps. This is in agreement with the increased electron trapping observed in Figure 3-4. No significant difference is observed in the centroid location. Also, no difference is observed in the electron trap capture cross sections between HITOX and control samples. Thus, the trap capture cross section can not account for the increase in electron trapping levels. Both the control and HITOX structures had the same three electron trap capture cross sections: 2×10^{-14} cm^2, 5×10^{-17} cm^2, and 1×10^{-17} cm^2 (approx. values). The two larger capture cross sections are associated with electron trapping at amorphous silicon clusters (the BOX is considered to be silicon rich), and the smallest cross section is associated with network defects within the BOX [25].

Table 4-1. Listed are the total occupied charge (electron traps), the charge centroid, and the determined electron capture cross sections for the SIMOX standard and HITOX structures.

Vendor	Process	Trap Density	Centroid	Cross Section
		$1/cm^2$	% down	cm^2
A	C	$-3.1x10^{11}$	50%	$1x10^{-14}$, $7x10^{-17}$, $1x10^{-17}$
A	HITOX	$-9.4x10^{11}$	43%	$4x10^{-14}$, $5x10^{-17}$, $1x10^{-17}$
B	C	$-1.2x10^{12}$	39%	$3x10^{-14}$, $7x10^{-17}$, $2x10^{-17}$
B	HITOX	$-1.6x10^{12}$	42%	$3x10^{-14}$, $9x10^{-17}$, $3x10^{-17}$

SECTION 5
CONCLUSIONS

5.1 NOTEWORTHY RESULTS.

This work has compared the radiation induced charge trapping response versus buried oxide thickness on various SIMOX buried oxides. It has been observed that medium to thin BOX material (<180nm) deviates from the square-law dependence for conditions typical in actual applications. Increasing the applied field (>=5×10^5 V/cm), or allowing the BOX to charge saturate during ionizing irradiation, returns the relationship to the square-law dependence. These observations are explained by the influence the applied electric field has during irradiation on the motion of radiation induced holes within the BOX. The observed inflection point was explained by the location and magnitude of the radiation induced BOX charge centroid and its relationship to BOX thickness.

In addition, this work has shown that the HITOX process causes an increase in the electron trapping for a SIMOX buried oxide. The increase can not be accounted for by changes in electron trap capture cross sections, nor by the influence of interface effects. Since these device electrical observables do not explain the HITOX's increase in net electron trapping, then the cause is likely an increase in trap generation resulting from the kinetics of the HITOX/BOX growth. Thus, the observed difference must be associated with the HITOX's process influence on the formation of HITOX/BOX oxide.

5.2 SUGGESTIONS FOR FUTURE INVESTIGATIONS.

The work in the above effort dealt with typical device application electric fields across the buried oxide (low fields). A possible suggestion for future experiments would be to investigate the saturation (high fields) total buried oxide trapped charge (top & bottom interface shifts) for various technologies (thin, thick, post-oxygen treated). The purpose would be to evaluate how the various technologies behave. Do thinner buried oxides (50nm - 200nm) trap more or less overall charge than thick (340nm - 400nm) buried oxides? The concern would be for a thin fully depleted technology where vertical charge control is important. For this thinner technology charge buildup at the lower (bottom, SiO_2/substrate) interface can be detrimental to the charge control of the device building top silicon film above. For the SIMOX technology to be of value in low power application, this charge control concern will be of importance.

SECTION 6
REFERENCES

1. T.P Ma, and P.V. Dressendorfer, *Ionizing Radiation Effects in MOS Devices & Circuits* (U), John Wiley & Sons, 152-153 (1989) (Unclassified).

2. R.K Lawrence, H.L. Hughes, and R.E. Stahlbush, "Radiation Sensitivity of Beam-Synthesized Oxides (U)," *Journal of Electronic Materials* Vol. 19, No. 7, 665-670 (1990) (Unclassified).

3. W.C. Jenkins and S.T. Liu, "Radiation Response Of Fully-Depleted MOS Transistors Fabricated in SIMOX (U)," *IEEE Trans. Nucl. Sci.* NS-41, No. 6, 2317-2321 (1994) (Unclassified).

4. S. Cristoloveanu, and S.S. Li, "*Electrical Characterization of Silicon-On-Insulator Materials and Devices*", Kluwer Academic Publishers, 1995 (Unclassified).

5. S. Nakashima, T. Katayama, Y. Miyamura, A. Matsuzaki, M. Imai, K. Izumi, and N. Ohwada, "Thickness Increment of Buried Oxide in a SIMOX Wafer by High-Temperature Oxidation (U)", *Proceeding 1994 IEEE International SOI Conference*, 71-72, Oct. 1994 (Unclassified).

6. Y. Takahashi, T. Ishiyama, and M. Tabe, "Counter-Oxidation of Superficial Si in Single-Crystalline Si on SiO_2 Structure (U)", *Appl. Phys. Lett.*, Vol. 65, No. 23, 2987-2989, Dec. 1994 (Unclassified).

7. T. Katayama, S. Nakashima, Y. Miyamura, M. Kataoka, M. Danbata, M. Imai, K. Izumi, and N. Ohwada, "Improvement of Surface Morphology of SIMOX Wafers by High-Temperature Oxidation (U)", *Proceeding 1994 IEEE International SOI Conference*, 75-76, Oct. 1994 (Unclassified).

8. A.J. Auberton-Herve', "New SOI-Based Applications (U)," *Proceeding 1993 IEEE International SOI Conference*, 8-9, Oct. 1993 (Unclassified).

9. Spectroscopic ellipsometry measurements (U) made by B.J. Mrstik of the Naval Research Laboratory and P.J. McMarr of SFA Inc. (Unclassified).

10. D.J. DiMaria, "Determination of Insulator Bulk Trapped Charge Densities and Centroids From Photocurrent-Voltage Characteristics of MOS Structures (U)", *J. Appl. Phys.*, Vol. 47, No. 9, 4073-4077, Sept. 1976 (Unclassified).

11. D.A. Buchanan and D.J. DiMaria, "Interface and Bulk Trap Generation in Metal-Oxide-Semiconductor Capacitors (U)", *J. Appl. Phys.*, Vol. 67, No. 12, 7439-7451, June 1990 (Unclassified).

12. E.H. Nicollian and J.R. Brews, *MOS (Metal Oxide Semiconductor) Physics and Technology*, John Wiley & Sons, 531-532, 1982 (Unclassified).

13. H.E. Boesch Jr., T.L. Taylor, and W.A. Krull, "Charge Trapping and Transport Properties of SIMOX Buried Oxide with a Supplemental Oxygen Implant (U)," *IEEE Trans. Nucl. Sci.* NS-40, No. 6, 1748-1754 (1993) (Unclassified).

14. S.T. Liu, P.S. Fechner, and R.L. Roisen, "Fast Turn Characterization of SIMOX Wafers (U)," IEEE SOS/SOI Technology Conference, 61-62 (1990) (Unclassified).

15. S.T. Liu, P.S. Fechner, and J. Schrankler, "Radiation Hardening of SIMOX Buried Oxides (U)," *Journal of Radiation Effects*, Vol. 12, No. 1, 40-44, (1991) (Unclassified).

16. S. Williams, S. Cristoloveanu, and G. Campisi, "Point Contact Pseudo-MOS Transistors in As-Grown Silicon on Insulator Wafers (U)," *Mat. Sci. and Engr.* B12, 191-194 (1992) (Unclassified).

17. J.H. Smith, R.K Lawrence, G.J. Campisi, "Numerical Analyses of Silicon-on-Insulator Short-Channel Effects in a Radiation Environment (U)," *Journal of Electronic Materials* Vol. 21, No. 7, 683-687 (1992) (Unclassified).

18. R.J. Krantz, L.W. Aukerman, and T.C. Zietlow, "Applied Field and Total Dose Dependence of Trapped Charge Buildup (U)," *IEEE Trans. on Nucl. Sci.*, NS-34, No. 6, 1196-1201, (1987) (Unclassified).

19. H.E. Boesch Jr., T.L. Thomas, L.R. Hite, and W.E. Bailey, "Time-Dependent Hole and Electron Trapping Effects in SIMOX Buried Oxides (U)," *IEEE Trans. on Nucl. Sci.*, NS-37, No. 6, 1982-1989, (1990) (Unclassified).

20. B.J. Mrstik, P.J. McMarr, R.K. Lawrence, and H.L. Hughes, "The Use of Spectroscopic Ellipsometry to Predict the Radiation Response of SIMOX (U)," *IEEE Trans. Nucl. Sci.* NS-41, No. 6, 2277-2283 (1994) (Unclassified).

21. C.A. Pennise and H.E. Boesch Jr., "Determination of The Charge-Trapping Characteristics of Buried Oxides Using a 10-KeV X-ray Source (U)," *IEEE Trans. Nucl. Sci.* NS-37, No. 6, 1990-1994 (1990) (Unclassified).

22. R.E Stahlbush, H.L. Hughes, and W.A. Krull, "Reduction of Charge Trapping in Electron Tunneling in SIMOX by Supplemental Implantation of Oxygen (U)," *IEEE Trans. Nucl. Sci.* NS-40, No. 6, 1740-1747 (1993) (Unclassified).

23. R.S. Muller and T.I. Kamins, *Device Electronics for Integrated Circuits*, John Wiley & Sons, 400-401 (1986) (Unclassified).

24. G. Barbottin, and A. Vapaille, "*Instabilities in Silicon Devices*," North-Holland, pp. 56-57, 1989 (Unclassified).

25. V.V. Afanas'ev, A.G. Revesz, G.A. Brown, and H.L. Hughes, "Deep and Shallow Electron Trapping in the Buried Oxide Layer of SIMOX Structures (U)," *J. Electrochem. Soc.*, Vol. 141, No. 10, pp. 2801-2806, Oct. 1994 (Unclassified).

DISTRIBUTION LIST
TR-96-12

DEPARTMENT OF DEFENSE

DEFENSE ELECTRONIC SUPPLY CENTER
ATTN: DESC-E

DEFENSE INTELLIGENCE AGENCY
ATTN: DT-1BT
ATTN: TWJ

DEFENSE SPECIAL WEAPONS AGENCY
ATTN: ESA, W SUMMA
ATTN: ESE/L COHN
ATTN: ESE/L PALKUTI
ATTN: ESE, R C WEBB
2CY ATTN: ISST

DEFENSE TECHNICAL INFORMATION CENTER
2CY ATTN: DTIC/OCP

FC DEFENSE SPECIAL WEAPONS AGENCY
ATTN: FCINI
ATTN: FCTO
ATTN: FCTT, DR BALADI

TECHNICAL RESOURCES CENTER
ATTN: JNGO

DEPARTMENT OF THE ARMY

ADVANCED RESEARCH PROJECT AGENCY
ATTN: ASST DIR (ELECTRONIC SCIENCES DIV)

ARMY RESEARCH LABORATORIES
ATTN: AMSRL-PS-PD
ATTN: AMSRL-WT-NJ
ATTN: DR TIM OLDHAM

MDSTC
ATTN: CSSD-WD

MISSILE DEFENSE & SPACE TECHNOLOGY CTR
ATTN: CSSD-TC-SR

U S ARMY RESEARCH OFFICE
ATTN: R GRIFFITH

USAISC
ATTN: ASOP-DO-TL

DEPARTMENT OF THE NAVY

NAVAL RESEARCH LABORATORY
ATTN: C DALE
ATTN: D BROWN
ATTN: A B CAMPBELL
ATTN: N SAKS
ATTN: H HUGHES

NAVAL WEAPONS SUPPORT CENTER
ATTN: D PLATTETER

OFFICE OF NAVAL INTELLIGENCE
ATTN: LIBRARY

PROGRAM EXECUTIVE OFFICE
ATTN: AIR-536T

DEPARTMENT OF THE AIR FORCE

AIR FORCE CTR FOR STUDIES & ANALYSIS
ATTN: AFSAA/SAI

AIR UNIVERSITY LIBRARY
ATTN: AUL-LSE

PHILLIPS LABORATORY
ATTN: CAPT CHARLES BROTHERS
ATTN: PL/VTE
ATTN: PL/VTEE, S SAMPSON
ATTN: PL/WSC

ROME LABORATORY/CC
ATTN: ESR

SMC/MCX
ATTN: LT SCOTT BECHTLOFF

SMC/MTAX
ATTN: K BASANY

USAF ROME LABORATORY TECHNICAL LIBRARY
ATTN: RBR

WL/ELE BLDG 620
ATTN: WL/ELE

WL/MTE
ATTN: MTE

DEPARTMENT OF ENERGY

ALBUQUERQUE OPERATIONS OFFIC
ATTN: NESD

LAWRENCE LIVERMORE NATIONAL LAB
ATTN: L-84/G POMYKAL
ATTN: W ORVIS

LOS ALAMOS NATIONAL LABORATORY
ATTN: MS B230/E LEONARD

SANDIA NATIONAL LABORATORIES
ATTN: F SEXTON
ATTN: L D POSEY
ATTN: P WINOKUR
ATTN: T A DELLIN

OTHER GOVERNMENT

CENTRAL INTELLIGENCE AGENCY
ATTN: OSWR/NED 5S09 NHB
ATTN: OSWR/STD/MTB 5S09 NHB

GODDARD SPACE FLIGHT CENTER
ATTN: V DANCHENKO
ATTN: E STASSINOPOULOS
ATTN: K LABEL

DEPARTMENT OF DEFENSE CONTRACTORS

ALLIED-SIGNAL, INC.
ATTN: DOCUMENT CONTROL

ANALYTICAL SERVICES, INC. (ANSER)
ATTN: A SHOSTAK

BOEING CO
ATTN: M/S 2T-50 D EGELKROUT

BOOZ ALLEN & HAMILTON INC
ATTN: D VINCENT
ATTN: T J ZWOLINSKI

JET PROPULSION LAB
ATTN: C BARNES

CHARLES STARK DRAPER LAB, INC.
ATTN: J BOYLE

CLEMSON UNIVERSITY
ATTN: P J MCNULTY

DATA SYSTEMS CORP
ATTN: B RICKARD
ATTN: K WRIGHT

DAVID SARNOFF RESEARCH CENTER, INC
ATTN: R SMELTZER

DEFENSE GROUP, INC
ATTN: ROBERT POLL

EATON CORP.
ATTN: R BRYANT

GENERAL ELECTRIC CO (ASD)
ATTN: D SWANT
ATTN: D TASCA
ATTN: H O'DONNELL
ATTN: J ANDREWS
ATTN: J LINNEN
ATTN: J LOMAN

GENERAL ELECTRIC CO.
ATTN: B FLAHERTY
ATTN: L HAUGE

GEORGE WASHINGTON UNIVERSITY
ATTN: A FRIEDMAN

HARRIS CORPORATION
ATTN: E YOST
ATTN: W ABARE

HONEYWELL INC
ATTN: C SANDSTROM

HONEYWELL, INC.
ATTN: MS 725-5

HUGHES AIRCRAFT COMPANY
ATTN: E KUBO

IBM CORP.
ATTN: A SADANA

JAYCOR
ATTN: D WALTERS

TR-96-12 (DL CONTINUED)

JAYCOR
ATTN: CYRUS P KNOWLES
ATTN: R SULLIVAN

JOHN HOPKINS UNIVERSITY
ATTN: R MAURER

KAMAN SCIENCES CORPORATION
ATTN: DASIAC
ATTN: R RUTHERFORD

LOCKHEED MARTIN CORPORATION
ATTN: TECHNICAL INFORMATION CENTER

LOCKHEED MARTIN CORPORATION
ATTN: G LUM
ATTN: J CAYOT

LOCKHEED MARTIN FEDERAL SYSTEMS, INC
ATTN: L ROCKETT
ATTN: N HADDAD

LOGICON R AND D ASSOCIATES
ATTN: D CARLSON

LORAL AERONUTRONIC
ATTN: TECHNICAL LIBRARY

MARTIN MARIETTA
ATTN: J MILLER

MARTIN MARIETTA DENVER AEROSPACE
ATTN: RESEARCH LIBRARY

MARYLAND, UNIVERSITY OF
ATTN: H C LIN

MAXWELL LABORATORIES INC
ATTN: DR JASON WILKENFELD

MISSION RESEARCH CORP.
ATTN: D ALEXANDER

MISSION RESEARCH CORP.
ATTN: J LUBELL

MITRE CORPORATION
ATTN: J R SPURRIER
ATTN: M FITZGERALD

ORBITAL SCIENCE CORP.
ATTN: ROB CHERNEY

PACIFIC-SIERRA RESEARCH CORP.
ATTN: H BRODE

RAYTHEON CO.
ATTN: D D LEE
ATTN: JOSEPH SURRO

RESEARCH TRIANGLE INSTITUTE
ATTN: M SIMONS

ROCKWELL CORP.
ATTN: V DE MARTINO

SCIENCE APPLICATIONS INTL CORP
ATTN: W CHADSEY

SCIENTIFIC RESEARCH ASSOC, INC.
ATTN: H GRUBIN

SFA INC.
2CY ATTN: A G REVESZ
2CY ATTN: P J MCMARR
2CY ATTN: R K LAWRENCE

SUNDSTRAND CORP.
ATTN: C WHITE

SYSTRON-DONNER CORP
ATTN: SECURITY OFFICER

TECHNOLOGY DEVELOPMENT ASSOCIATES
ATTN: R V BENEDICT

TELEDYNE BROWN ENGINEERING
ATTN: G R EZELL
ATTN: LEWIS T SMITH
ATTN: M P FRENCH

THE AEROSPACE CORP
ATTN: D SCHMUNK
ATTN: K G HOLDEN
ATTN: LEE MENDOZA
ATTN: N SRAMEK
ATTN: R KOGA

THE RAND CORPORATION
ATTN: C CRAIN

TRW
ATTN: M J TAYLOR

TRW INC.
ATTN: T.I.C., S/1930

TRW S. I. G.
ATTN: C BLASNEK

TRW SPACE & DEFENSE SECTOR SPACE & TECH GROUP OGDEN ENG OPERATIONS
ATTN: D M LAYTON

UNISYS CORPORATION-DEFENSE SYSTEMS
ATTN: P MARROFFINO

VISIDYNE INC.
ATTN: C H HUMPHREY
ATTN: W P REIDY

DOCUMENT 3

HTS Josephson Technology on Silicon with Application to High Speed Digital Microelectronics. Phase 1.

AD-A313593

August 1996

Advanced Fuel Research Inc.

East Hartford, CT

531001

REPORT DOCUMENTATION PAGE

Form Approved
OMB No. 0704-0188

1. AGENCY USE ONLY (Leave blank)	2. REPORT DATE	3. REPORT TYPE AND DATES COVERED
	8/27/96	Final Report 9/30/94 - 9/29/95

4. TITLE AND SUBTITLE
HTS Josephson Technology on Silicon with Application to High Speed Digital Microelectronics

5. FUNDING NUMBERS
N00014-94-C-0261

6. AUTHOR(S)
Peter A. Rosenthal, David G. Hamblen

7. PERFORMING ORGANIZATION NAME(S) AND ADDRESS(ES)
Advanced Fuel Research, Inc.
87 Church Street
East Hartford, CT 06108

8. PERFORMING ORGANIZATION REPORT NUMBER
531001

9. SPONSORING/MONITORING AGENCY NAME(S) AND ADDRESS(ES)
Office of Naval Research
Electronics Division
800 Quincy Street
Arlington, VA 22217-5660

10. SPONSORING/MONITORING AGENCY REPORT NUMBER
0001AM

11. SUPPLEMENTARY NOTES
The view, opinions and/or findings contained in this report are those of the author(s) and should not be construed as an official Department of the Navy position, policy, or decision, unless so designated by other documentation.

12a. DISTRIBUTION/AVAILABILITY STATEMENT
Approved for Public release:
STTR Report, distribution unlimited

12b. DISTRIBUTION CODE
1

13. ABSTRACT *(Maximum 200 words)*

The goal of this program was to develop ultra-fast superconducting digital technology based on HTS Josephson junctions on silicon substrates. Working Josephson junctions and SQUID's were successfully fabricated on silicon, and an Yttrium-Barium-Copper-Oxide RSFQ rs flip-flop with 14 junctions and I/O test structures was successfully designed, fabricated, and tested. The kinetic inductance and London penetration depth of the films on silicon were determined from measurements of SQUIDs on silicon. Minimizing kinetic inductance through the use of thicker films will be required in future devices. An approach to alleviating film stress in these thicker films due to thermal expansion coefficient mismatch is outlined. This proposed solution involves fabricating a functionally graded buffer layer that can flow plastically to relieve stress while at the same time, allows nucleation and growth of heteroepitaxial films. A wafer bonding facility was constructed and utilized to demonstrate the successful bonding of silicon and BPSG coated wafers, a key step in the compliant substrate fabrication procedure.

14. SUBJECT TERMS	15. NUMBER OF PAGES
High temperature superconductivity, YBCO, RSFQ, compliant substrates, Josephson junctions.	28
	16. PRICE CODE

17. SECURITY CLASSIFICATION OF REPORT	18. SECURITY CLASSIFICATION OF THIS PAGE	19. SECURITY CLASSIFICATION OF ABSTRACT	20. LIMITATION OF ABSTRACT
UC	UC	UC	UL

ADVANCED FUEL RESEARCH
P. O. Box 380379
East Hartford, Connecticut 06138-0379
Telephone (203) 528-9806
Fax (203) 528-0648

PHASE I
FINAL REPORT

Advanced Fuel Research, Inc.
87 Church Street
East Hartford, CT 06108

Navy Contract No: N00014-94-C-0261

"HTS Josephson Technology on Silicon with Application to High Speed Digital Microelectronics"

Report Sent:
Report No.: (0001AM)
Report Period: September 30, 1994 - September 29, 1995
Contract Period: September 30, 1994 - September 29, 1995

Prepared By:
Peter A. Rosenthal, Principal Investigator
David G. Hamblen
and Joseph E. Cosgrove
Advanced Fuel Research, Inc.

and

Professor Michael Gurvitch, Professor Sergey Tolpygo,
Professor K.K. Likharev
Boris Nadgorny & Sergey Shokhor

for

Office of Naval Research, Arlington, VA

AFR Project No.: 531001

UNCLASSIFIED

August 27, 1996

Table of Contents

I.1. Introduction

I.1.1. The Problem

Manufacturable High Temperature Superconducting Digital Electronics - Superconducting electronics have long been regarded as having the potential for superior switching speeds and reduced power consumption compared to semiconducting device families, however, the requirement for refrigeration to temperatures near 4.2 K has been a major stumbling block to the commercialization of low T_c superconducting logic. High temperature superconducting (HTS) materials present new opportunities for superconducting electronics.

At present there are very few Josephson HTS technologies which can be considered for applications requiring a non-trivial number of high quality junctions. Among these are SNS junctions, where N may be a noble metal[1] or a conductor compatible with HTS materials[2], bi-epitaxial junctions[3], and e-beam written junctions.[4] It is fair to say that none of the existing HTS Josephson technologies have fully matured, and much additional work is required to make them useful in applications. Because many targeted applications of superconducting electronics rely on the high switching speeds attainable by Josephson junctions, rf properties have played a significant role in the search for practical substrates.

Silicon, quartz, sapphire and glass substrates are attractive substrates for HTS device technology due to their:

- Large size availability and low cost
- Superior dielectric, thermal conduction, and strength properties compared to MgO or the perovskite related substrate materials.
- Compatibility with both VLSI silicon and HTS materials technologies through various wafer bonding or ion-implantation fabrication procedures.
- Extensive preexisting technology base.
- Transparency from mid-infrared to microwave frequencies (at cryogenic temperatures)[5]

I.1.2. The Opportunity

HTS digital josephson technology for silicon and other rf compatible substrates- A method for growing epitaxial thin films of $Y_1Ba_2Cu_3O_7$ (YBCO) on silicon substrates and the demonstration of YBCO Josephson junctions on silicon during this Phase I program bring the possibilities of practical manufacturable, high performance superconducting electronics closer to reality. The adoption of silicon as a substrate material raises the tantalizing possibility of a monolithically integrated technology, combining the speed and power consumption of superconducting electronics with the tremendous benefits offered by modern VLSI silicon technology. In addition to novel hybrid applications involving integrated semiconducting and superconducting components, a Josephson technology fully compatible with silicon substrates would find broad acceptance for most of the classic applications of the Josephson effects[6] including Superconducting Quantum Interference Devices (SQUIDs), Josephson array oscillators, infrared detectors, Josephson mixers and heterodyne receivers, digital logic, A to D converters, and millimeter/submillimeter-wave spectrum analyzers.

Developments in wafer bonding and etchback raise the additional possibility of developing a YBCO technology for silicon, quartz or glass substrates with greatly reduced stress due to thermal expansion mismatch during growth and cooldown. Applying these techniques could greatly improve the performance of many rf components such as filters, delay lines and receivers as well as high speed active Josephson components.

I.2. Summary of Phase I

Phase I was performed in three tasks with the following objectives:

Task 1. - Josephson Junction Fabrication and Testing: To verify the junction fabrication process on silicon substrates, and to produce a set of junctions for electrical and statistical testing.
Task 2. - RSFQ Logic Modeling and Design: To design and simulate RSFQ circuit elements that can be successfully fabricated and tested.
Task 3. - RSFQ Circuit Fabrication and Testing: To fabricate working HTS RSFQ logic elements on silicon substrates.

The junction technology developed in Phase I was based on the electron beam modification technique. To summarize briefly, thin Ytrria stabilized zirconia (YSZ) buffered HTS films were deposited on silicon substrates, and patterned into narrow ~4 μm wide bridges. These bridges were then written over by a narrow (~5 nm width) electron beam of high energy. The electron beam has the effect of "damaging" the HTS material over a length comparable to the coherence length, forming a Josephson junction. The electron beam writing process is believed to be associated with the formation of displaced-oxygen/vacancy pairs in the crystal structure that locally disrupt the superconductivity.

The highlights of the Phase I accomplishments include:

Working Josephson junctions and SQUIDs have been fabricated on silicon substrates. The electrical properties are similar to those fabricated on more conventional substrates such as $LaAlO_3$.

A YBCO RSFQ rs flip flop with 14 junctions and I/O test structures was successfully designed, fabricated and tested.

The kinetic inductance and London penetration depth of the films on silicon have been determined from measurements of HTS SQUIDs on silicon.

An approach to alleviating film stress due to thermal expansion coefficient mismatch has been outlined. The proposed solution involves fabricating a functionally graded buffer layer that flows plastically to relieve film stress while at the same time, allows nucleation and growth of heteroepitaxial films.

A wafer bonding facility was constructed at AFR and utilized to demonstrate the successful bonding of silicon and BPSG coated wafers, a key step in the compliant substrate fabrication procedure.

I.3. Conclusions

The quality of the junctions in the exploratory Phase I program was sufficient to fabricate complex HTS devices based on these junctions. However, several factors associated with the use of silicon as a substrate emerged as technical barriers. HTS film thickness was identified as a particularly important factor. It is necessary to minimize parasitic inductance in order to achieve high quality HTS RSFQ circuits, and to do this thicker films will be required. The maximum crack-free YBCO film thickness on YSZ-buffered silicon seems to be about 70 nm. The 25 nm films used in Phase I were adequate for forming good junctions, as determined by the measurements of Shapiro steps, and the magnetic modulation, but this is not good enough for complex circuits. To obtain the required thicker films, without cracking, we have devised methods to use a compliant buffer layer on the silicon substrates. This buffer layer, of a plastically deformable glass, would relieve the stress due to differential thermal expansion between the silicon wafer and the YBCO, potentially allowing thick (>500 nm) crack-free YBCO films. We have proposed in Phase II to pursue development of the deformable buffer layer and e-beam junction technology to achieve stable, reproducible fabrication of devices using the ultra-fast RSFQ logic family.

II. Detailed Results and Discussion

For completeness, the background section from the Phase I proposal is repeated here.

II.1. Background From Phase I Proposal

The backround of the proposal is in three areas: i) HTS Josephson junction technology, ii) the RSFQ logic family, and iii) HTS thin film fabrication on silicon substrates.

II.1.1. HTS Josephson Junction Technology

Josephson junctions are the building blocks of any superconducting digital switching circuit. While a low-T_c niobium technology has a choice between hysteretic and nonhysteretic (latching - nonlatching) Josephson elements, the HTS technology is limited to nonhysteretic elements. This in turn dictates a choice of logic implementations, with Rapid Single Flux Quantum (RSFQ) logic at the top of the list in terms of concept maturity, proven low -T_c performance and its potential for ultra-high data throughput.[7] In this context, the nonhysteretic nature of HTS junctions is not a limitation; in fact quite the opposite[7]. With low -T_c junctions, the main challenge faced by this new digital technology is helium refrigeration which is unacceptable for many potential users. Transfer to HTS circuits operating at temperatures above 20 - 30 K would go a long way toward the acceptance of this technology.

Electron beam modified junctions

Electron beam writing method - The method developed at Stony Brook consists of direct writing of Josephson weak links on prepatterned HTS thin-film microbridges by a focused electron beam[4]. In the present Stony Brook junctions, 25 nm and 50 nm $c_{\perp}$-oriented YBCO films, grown by the BaF_2 process[8] on $LaAlO_3$ substrates, are patterned into 2-3 μm wide and 4 μm long bridges using standard photolithography with PMMA resist and Br-methanol etching. A 1.5 nm electron beam of a Philips CM-12 electron microscope with energy ranging from 20 keV to 120 keV and beam current 0.6 nA at 120 keV is scanned once across the microbridge, stopping at 2048 equidistant points, about 2 nm center- to-center, for a preset dwell time between 0.1 s and 2 s. Preliminary studies using a much higher beam current of about 10 nA, a 10 nm spot size and shorter dwell time suggests that the junction quality is as good as with the small spot size and longer dwell time. It is likely that the writing speed of the Philips CM-12 microscope can be increased to about 2 μm/min., i.e. one junction per minute, which will allow the fabrication of multi-junction circuits of reasonably high complexity. Thus produced junctions can be studied and utilized in circuits either as made , after e-beam writing, or, more commonly, after a mild stabilizing annealing at 330 K- 360 K. The purpose of this annealing is to slow down the drift of the junction parameters at room temperature, and to adjust junction T_c and operating temperature to a desired level.

Junction properties

Critical temperature - One of the big advantages of e-beam writing technology is that the most important junction parameters such as T_c, I_c, and, to a lesser degree, R_n can be tuned to the desired values simply by changing the irradiation dose given to the junction or by adjusting the parameters of a subsequent stabilizing anealing. For example, the T_cs from a few degrees K to 88 K can be obtained. The best operating temperature for the e-beam junctions is of the order of (0.9-0.95) T_c (see below). An ability to change T_c implies an ability to choose the operating temperature. This is important if one needs to adjust the operating temperature as may be dictated by design considerations, such as circuit tolerance to the digital error rates.

We further note that the T_c vs. dose dependence shows a pronounced 60 K plateau, which is qualitatively similar to the well known T_c vs. oxygen content dependence in YBCO. This is especially beneficial for reproducible junction fabrication due to a weak dose dependence in the plateau region.

Current - voltage characteristics - At critical current densities J_c up to $2\times10^5 A/cm^2$, or I_c up to 0.2 mA in 2 μm wide and 50 nm thick bridges, the junctions are perfectly described by the RSJ model with thermal noise (see Figure 1). At higher j_c there is a transition to flux flow I-V characteristics which can be attributed to the transition from short ($w<\lambda_J$) to long ($w>\lambda_J$) junction behavior. Temperature dependences of I_c and normal resistance R_n can be inferred from the RSJ fit. Figure 2 shows j_c as a function of reduced temperature T/T_c for junctions with different T_c's. The last point on each curve roughly corresponds to the boundary of the RSJ behavior. At 77 K the I_cR_n product for e-beam junctions is in the range of 0.2 mV - 0.4 mV.

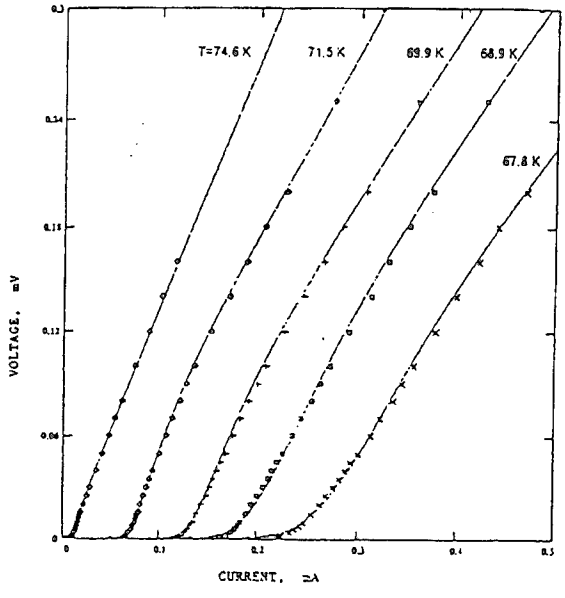

Figure 1 Current-Voltage characteristics of e-beam junctions at different temperatures. Lines indicate fits to RSJ model with fluctuations

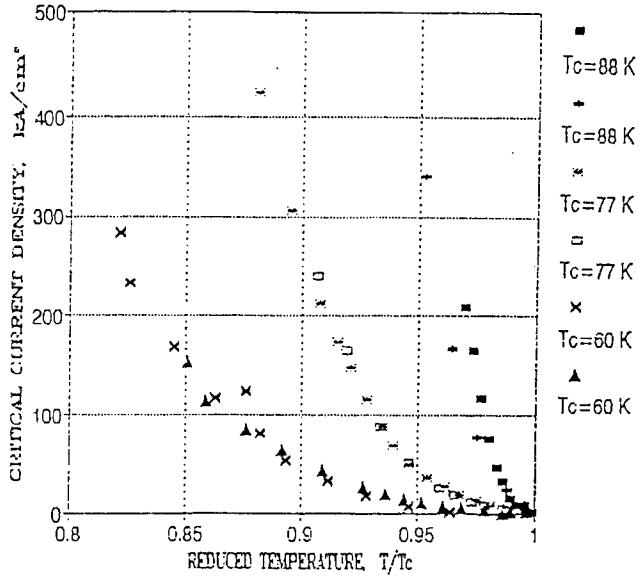

Figure 2 Temperature dependences of the critical current density of e-beam junctions with different critical temperatures..

Electromagnetic properties - It is well known that the magnetic field modulation of the Josephson critical current serves as a fine characteristic of the junction uniformity, which in turn implies good noise characteristics. Perfect magnetic field modulation can seldom be seen in the literature on HTS junctions. The e-beam writing technology has great potential in this respect. For j_c in the RSJ range (see Figure 2 and the discussion in the previous paragraph,) the magnetic field modulation of the critical current for our junctions is almost perfect (see Figure 3). At higher critical current densities, the modulation is not complete since the junctions are in the long junction regime.

Under microwave irradiation, the e-beam junctions show oscillations of the critical current with microwave power according to the RSJ model and Shapiro steps to high order (Figure 4), once again indicating the high quality of the e-beam junctions. The measurements of junction noise we are currently performing show that the high frequency noise is of purely thermal nature. Low frequency (1Hz - 10 Hz) noise of our junctions at 77 K shows the usual 1/f component and is also low compared to most HTS junctions.

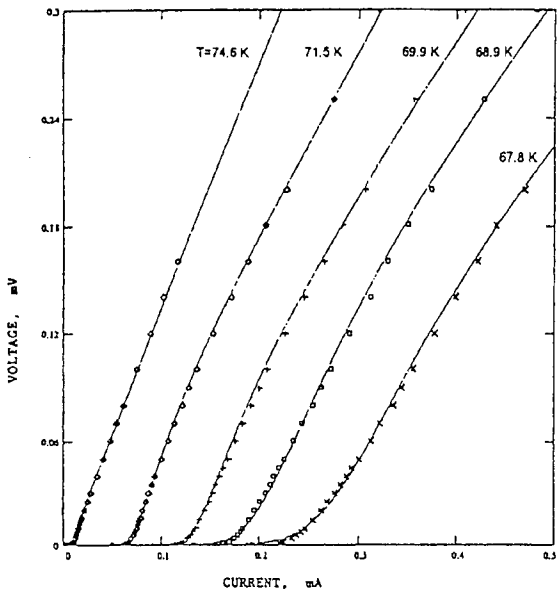

Figure 3 Magnetic field modulation of the critical current.

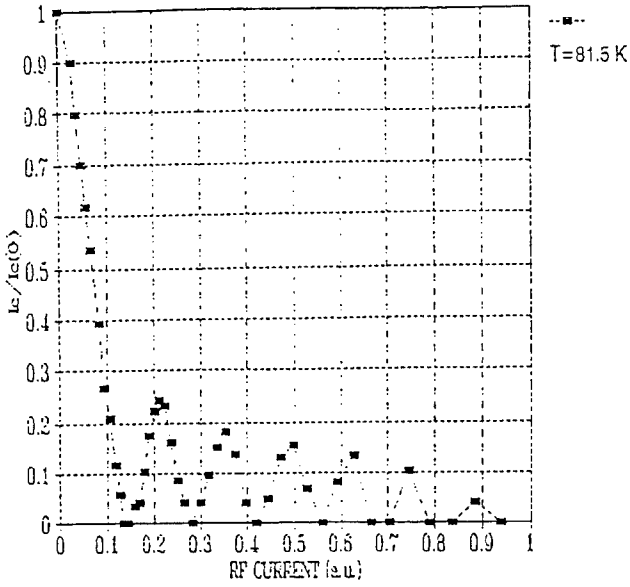

Figure 4 Oscillations of the Josephson critical current in a 10 GHz microwave field.

We conclude that the e-beam writing technology enables fabrication of high quality HTS Josephson junctions suitable for digital applications. The key issue to be addressed in this proposal is the applicability of silicon for HTS digital applications.

Fabrication issues

On - chip uniformity and reproducibility - Based on our present experience with the e-beam junctions, we are reasonably confident that uniformity and reproducibility will not be a problem. Nevertheless, they should be addressed and evaluated in the context of a multi-junction technology on silicon substrates. The main issues of importance are:

- uniformity of the initial HTS film;
- I_c, R_n, and I_cR_n product spreads on a chip
- run-to-run reproducibility for various writing conditions;
- uniformity after the stabilizing annealing

II.1.2. RSFQ Circuits

We will use the e-beam junctions to implement simple digital circuits of the RSFQ family, which use single quanta of magnetic flux to code digital bits.[7] Theoretical estimates and experiments with LTS (Nb trilayer) circuits of this kind indicate that this family can be used for ultra-fast processing of digital information, with very low power consumption, dc power supply, and convenient option of self-timing. These features make the RSFQ technology very promising for several application niches in instrumentation, radars, communications, and high-performance computing.[7] The first attempts to implement the simplest HTS RSFQ circuits were, however, either not conclusive[9] or confined to helium temperatures due to use of a LTS ground plane.[10]

We believe that the major challenge here is a necessity of quantitative circuit design (which was lacking is the previous work[11,12]). In fact, due to operation at higher temperatures the HTS RSFQ circuits should use Josephson junctions with proportionally higher critical currents to avoid thermally activated errors. Higher currents imply lower inductances ($L \propto \Phi_0/I_c \propto T^{-1}$) which may have to decrease

to the values below 1 pH in some cases. Present-day HTS integrated circuit technologies are still confined to 1 - 2 superconducting layers, making reduction of the inductances and their calculation for a given layout a very complex task involving 2D and 3D magnetic field modeling.

II.1.3. HTS Thin Films on Silicon:

The "conventional" HTS compatible metal oxide substrates such as $SrTiO_3$ and $LaAlO_3$ are problematic for high frequency applications. Large epitaxial quality metal-oxide wafers are typically expensive and difficult to acquire. The dielectric constants of these materials tend to be large (e_r between 25 and 1000), lossy, with strong temperature dependence and substantial sample to sample variability. The electronic properties and defects of these substrate materials are quite poorly understood. These factors make it extremely difficult to develop high performance HTS components, and these difficulties will translate at best into higher cost and lower yields in a manufacturing environment. High quality Josephson junctions have so far only been achieved on a handful of expensive, lossy and mechanically fragile oxide materials (the previously mentioned $LaAlO_3$, $SrTiO_3$ and related perovskites being the most notably

The absence of an inexpensive substrate material good high frequency properties and a compatible HTS Josephson junction technology is a serious obstacle for high speed digital applications of Josephson junctions.

The most promising substrate material for integrating HTS and semiconducting devices is silicon. A process for growing high quality epitaxial HTS films on buffer layers on silicon has been developed[13,14] and is utilized routinely at Advanced Fuel Research for its work in bolometric infrared detectors. A facility for growth of the HTS films on Si wafers, originally developed at *Xerox* PARC[13], was established at *AFR, Inc.* in early 1991. The method used is the technique called pulsed-laser deposition (PLD). Our work centers on the most common electronic thin-film HTS-application material: $YBa_2Cu_3O_{(7-d)}$ or YBCO. Silicon wafers and Si compounds react chemically with YBCO at film growth temperatures[15], so a buffer layer of yttria-stabilized zirconia (YSZ) is first grown epitaxially on the Si wafer surface. Preparation of the fresh Si surface must also be included in the process, since all Si surfaces are coated with a native oxide that typically degrades epitaxy unless it is removed by chemical or thermal treatment.[13,16] The facility depicted in Figure 7, epitaxial YBCO films on the YSZ-buffered Si (i.e., $J_c \sim 3 \times 10^6$ A/cm^2).

II.2 Task 1 - Josephson Junction Fabrication and Testing

There were three areas of activity in this Task: 1) improvements to the Pulsed Laser Deposition (PLD) facility to achieve HTS films suitable for junctions, 2) patterning and testing the films and junctions, and 3) developing methods for overcoming films stresses so that thick films can be formed.

II.2.1 Improvements to the PLD Facility

During the course of fabricating working junctions and SQUIDs from thin YBCO films fabricated on silicon substrates, it was observed that the junctions were not well matched in critical temperatures. This non-uniformity was primarily attributed to non-uniformities within the films. To improve the film uniformity, and to accomodate the demands of other projects, we built a new substrate heater for the deposition system to provide more uniform temperatures over larger substrate areas. The new heater was built to allow deposition onto 12 mm square chips, which can subsequently be diced into four 5-mm square chips. With this arrangement, it is possible to fabricate and test many more junctions from a single deposition and gather more and better statistics on junction properties.

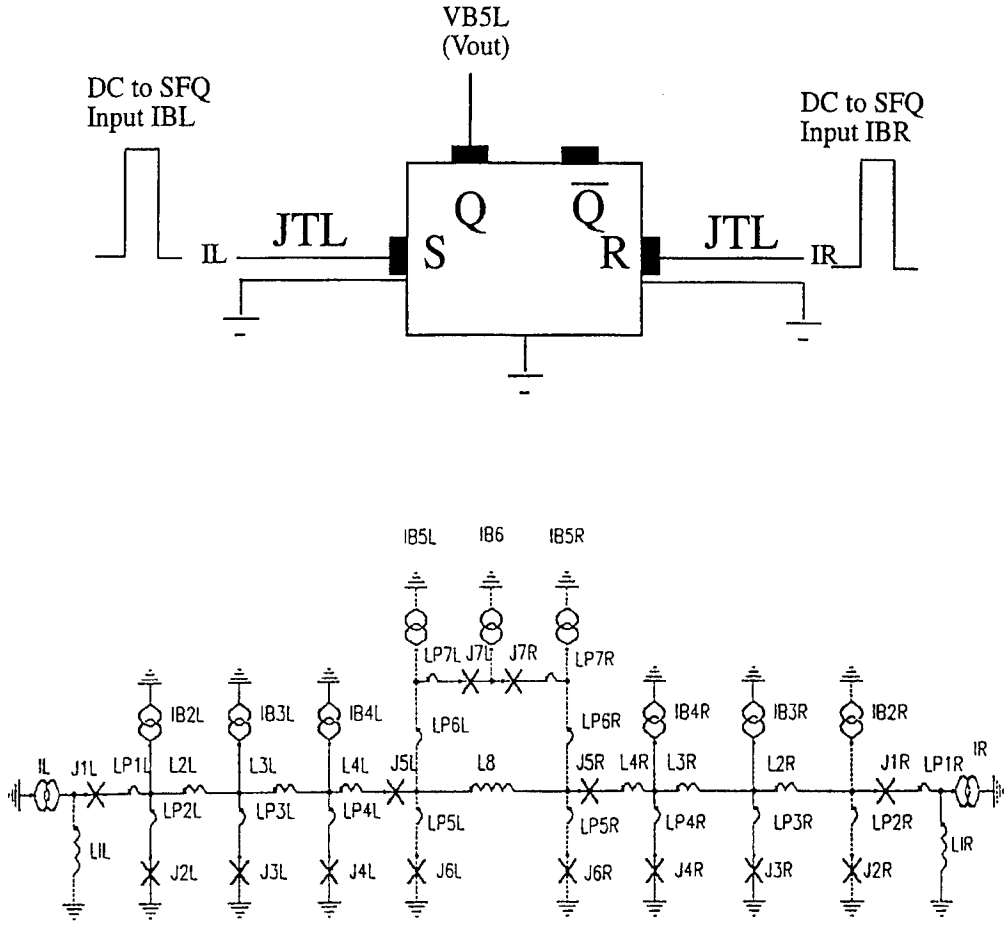

Figure 5 Equivalent circuit of an RSFQ structure comprising two input DC/SFQ converters, two JTLs, RS flip-flop and output SFQ/DC converter.

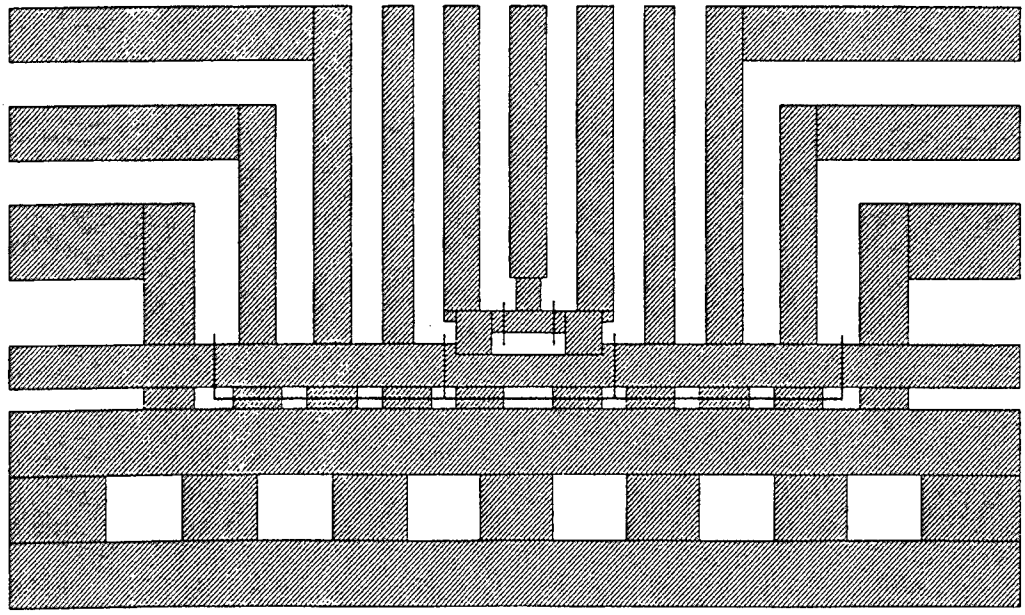

Figure 6 Single-layer layout of the RSFQ circuit shown in Figure 5. Minimum line width is 2 μm. Solid lines across the bridge denote e-beam junctions successful)

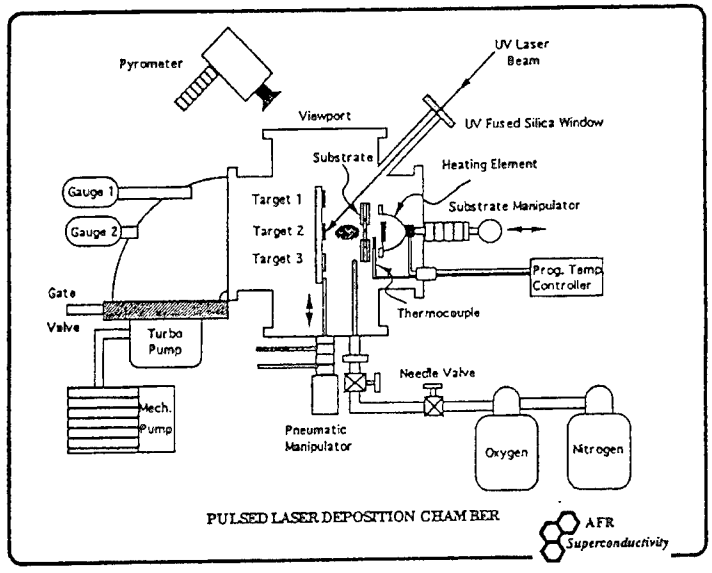

Figure 7 Schematic view of the AFR pulsed laser deposition system.

Two films of YSZ buffered YBCO films were grown on silicon substrates and sent to Professor Gurvitch's laboratory at SUNY at Stony Brook. The films were tested for resistance vs temperature (see Figure 8) and displayed excellent (< 2 K) transition widths. Work there is currently underway at Stony Brook to fabricate Josephson junctions.

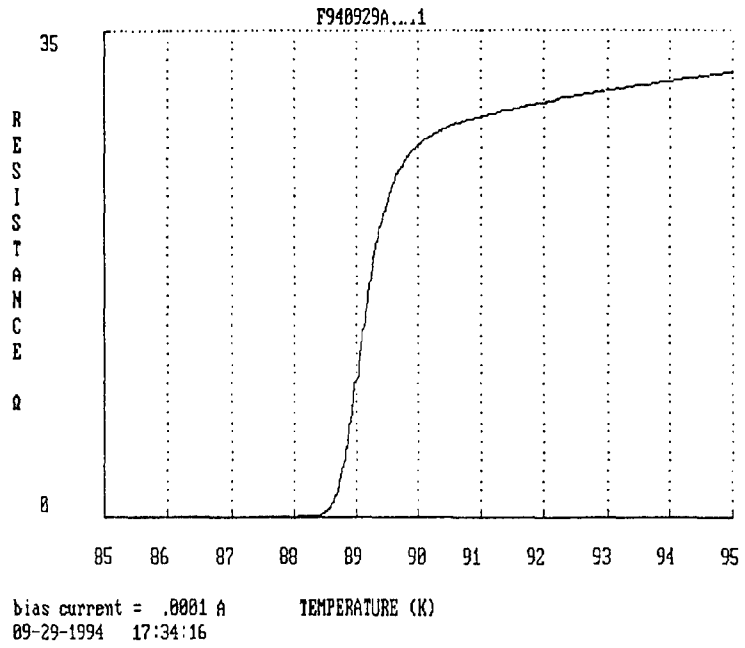

Figure 8 R vs T of YBCO Film to be processed into junctions.

The film had good superconducting qualities as determined by resistance Vs. temperature measurements at AFR and was shipped to Stony Brook for junction fabrication. The film was etched into three bridges approximately four microns across and measured again for resistance vs temperature Unfortunately, the no supercurrents were detected. Two of the junctions were highly resistive at all temperatures, and the third showed a partial transition at 90 K, but retained a residual resistance of 400 Ω below the superconducting transition temperature of the film. The R vs T for the bridge is shown in Figure 9.

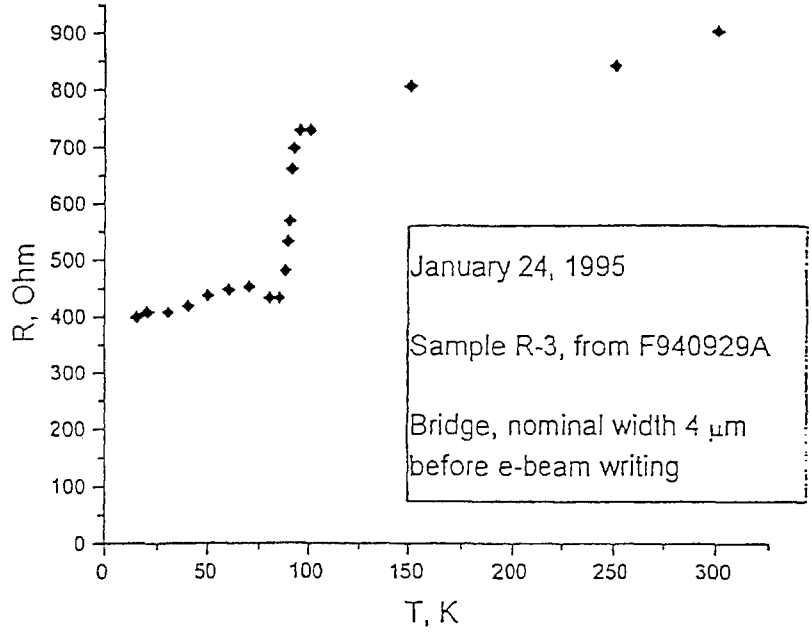

Figure 9 R Vs curve for a microbridge patterned from a YBCO film on YSZ buffered silicon

The rest of the unpatterned film was remeasured using silver paste dots as contacts to determine if the entire film was bad. We found that the film was still superconducting with a T_c of 89 °C. From this we conclude that either the patterning process damaged the bridges, or that the film was sufficiently non-uniform that the bridge was traversed by some completely non-superconducting regions or grain-boundaries.

In order to demonstrate that the process was viable, we processed and earlier film of YBCO on YSZ-buffered silicon into working Josephson junctions in April of 1994. The Josephson behavior of this device was established by measuring microwave induced Shapiro steps, magnetic modulation of the critical current. These results are shown in Figures 10 and 11.

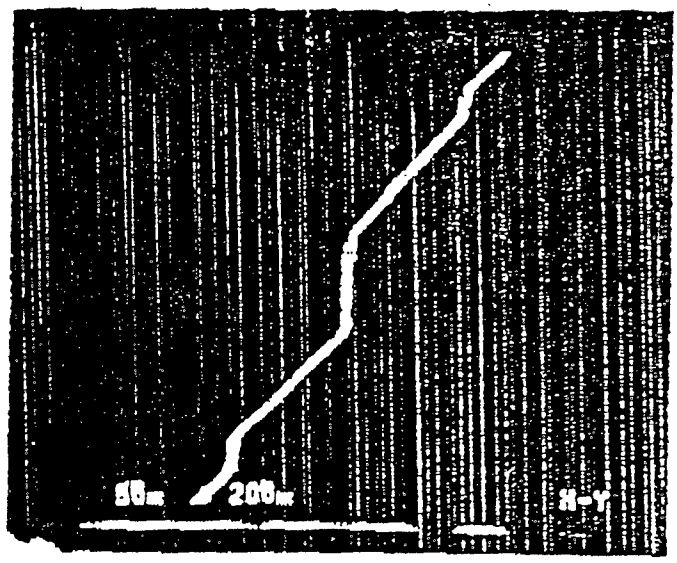

Figure 10 Microwave induced Shapiro steps in the current voltage characteristic of an E-beam modified Josephson junction fabricated from YBCO on YSZ buffered silicon. The data were measured at 52 K.

A new film of YBCO on YSZ-buffered silicon prepared with the improved PLD system was fabricated into working Josephson junctions and a SQUID.

Two SQUID's were fabricated. SQUID R1 did not exhibit any magnetic field modulation, although the shape of the current-voltage (IV) characteristic was RSJ-like. This SQUID exhibited clear microwave induced Shapiro steps in the IV curve. Figure 12 shows the dc IV curve of this SQUID. Figure 13 shows Shapiro steps in the IV curve of SQUID R1 (at 54 K) as induced by a 10.2 GHz microwave source. This SQUID had a resistance of approximately 0.4 s.

SQUID R1 was fabricated by e-beam modification using a beam dwell time of 600 ms, and 2048 dwell points. These conditions usually give T_c of ~50 K, but in this case, T_c for the SQUID was ~61 K. This is probably due to inhomogeneity in the film, which could result in significantly different critical temperatures between the two junctions of the SQUID. If one of the junctions was completely non-superconducting, then we would expect the structure to display the observed behavior.

SQUID R2 showed both SQUID-like magnetic interference and microwave induced steps in the IV curve. Figure 14 shows an SEM image of this SQUID. Figure 15 shows the dc IV curve for this device at a temperature of 40 K. Figure 16 shows the IV curve under the influence of 10.2 GHz microwaves. Note the existence of pronounced Shapiro steps. Figure 17 shows the magnetic interference pattern of SQUID R2.

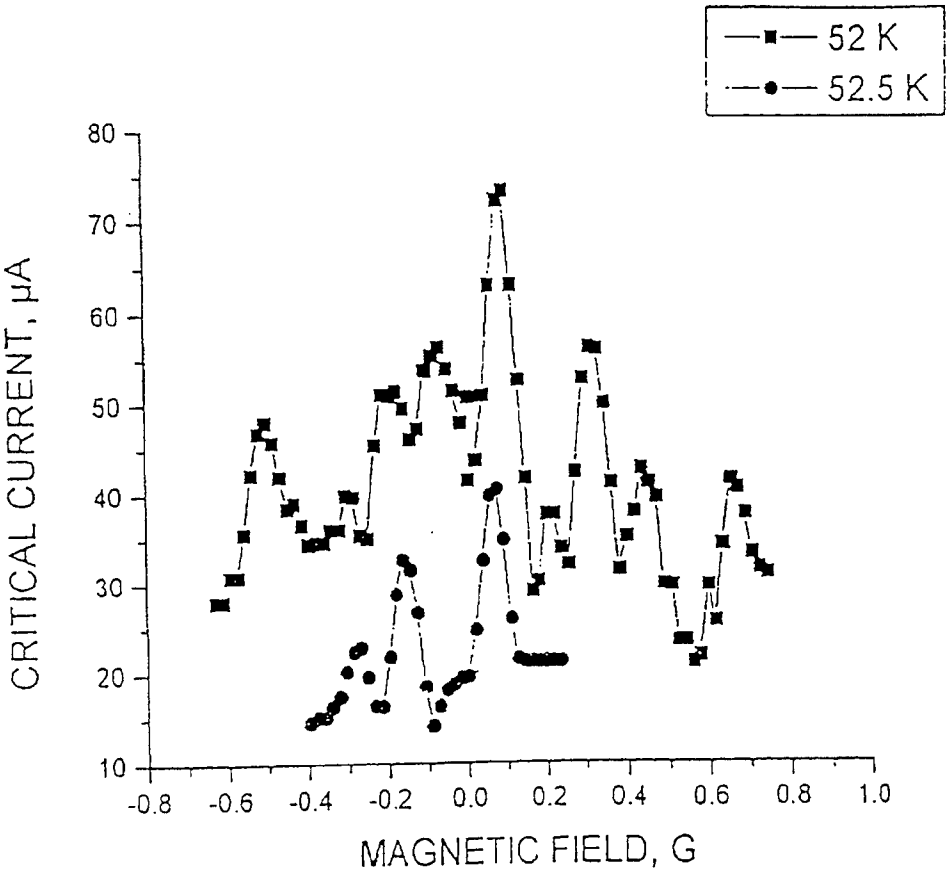

Figure 11 Magnetic field dependence of the critical current fo an E-beam modified Josephson junction fabricated from YBCO on YSZ buffered silicon.

II.2.2. Compliant Buffer Layers

During the course of studying the various parameters which impact the performance of RSFQ devices in Task II, we identified excess parasitic inductance as a significant hurdle for RSFQ fabrication. The dominant contribution to parasitic inductance is the kinetic inductance. This scales inversely with thickness, so it is advantageous to be able to grow thicker films. This is, however, a problem for YBCO films on silicon. The different thermal expansion coefficients of the HTS thin film and the silicon substrate results in the accumulation of tensile strain in the film during cooldown. This causes cracking for films thicker than about 70 nm. A method to deposit thicker films on silicon would be highly desireable, particularly if it did not require the use of buffer layers with inordinately high dielectric constants. We are developing a new type of buffer layer that can relieve strain between film and substrate by plastic deformation. This development, if successful will be a significant breakthrough for HTS on Silicon technology by essentially eliminating both stress induced cracking and parasitic kinetic inductance. The buffer layer consists of a thin film of a soft glass situated between the silicon substrate and the YSZ/YBCO bilayer. The soft glass film will be chosen to have a strain annealing temperature well below the growth temperature. The structure is shown in Figure 18. The fabrication of the buffer layer will involve the processes of film deposition and wafer bonding. During cooldown, as the film cools down, the HTS and YSZ layers can contract faster than the substrate, and the glass film will accomodate the strain by deforming viscously, until the substrates cool below the glass strain point.

Near the end of this Phase I research, we began preliminary work to fabricate this compliant buffer layer on a silicon substrate. We obtained silicon wafers coated with boron-phosphorus-

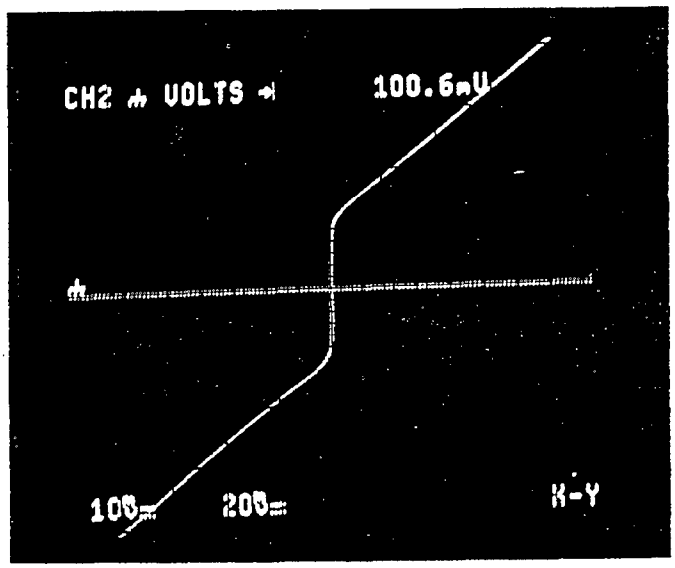

Figure 12 Current-Voltage characteristic of SQUID R1 at a temperature of 61 K.

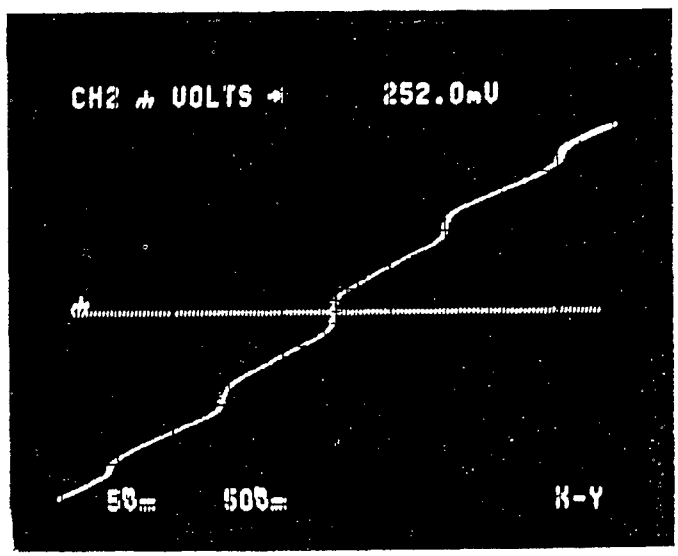

Figure 13 Microwave induced steps in the current voltage characteristic of SQUID R1 at a temperature of 54 K.

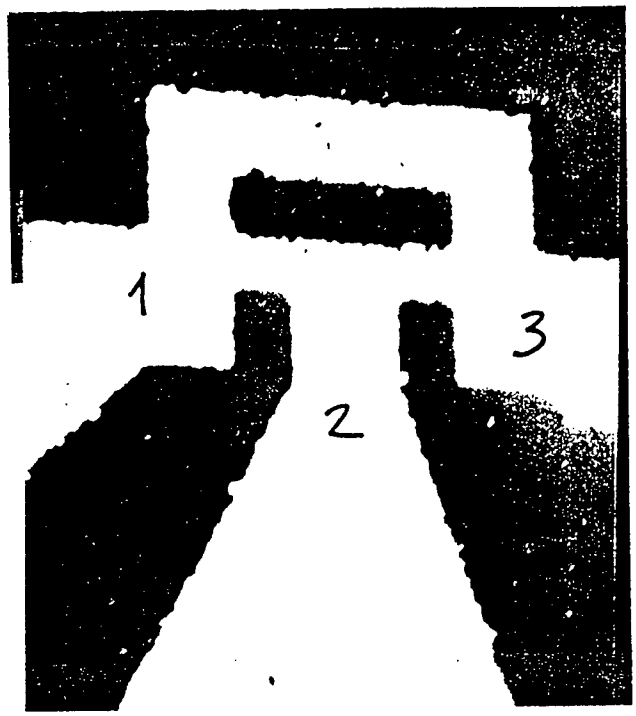

Figure 14 SEM micrograph of SQUID R2.

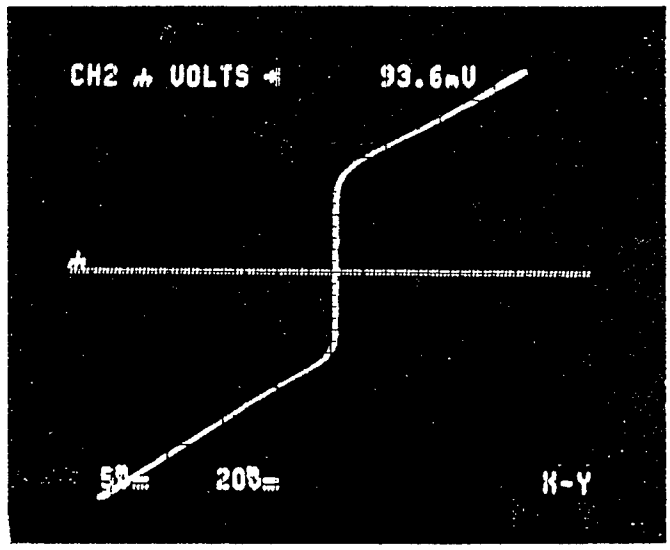

Figure 15 DC IV curve of SQUID R2 at a temperature of 40 K.

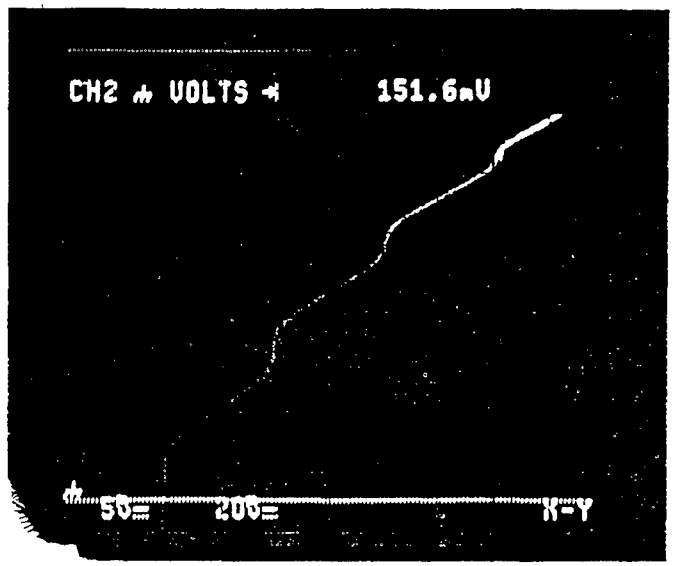

Figure 16 IV curve of SQUID R2 at T = 39 K, under the influence of 10.2 GHz microwaves.

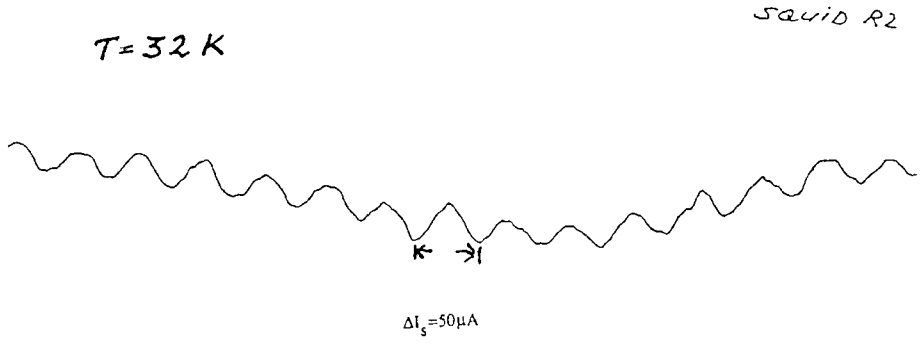

Figure 17 Magnetic interference pattern of SQUID R2 at 32 K.

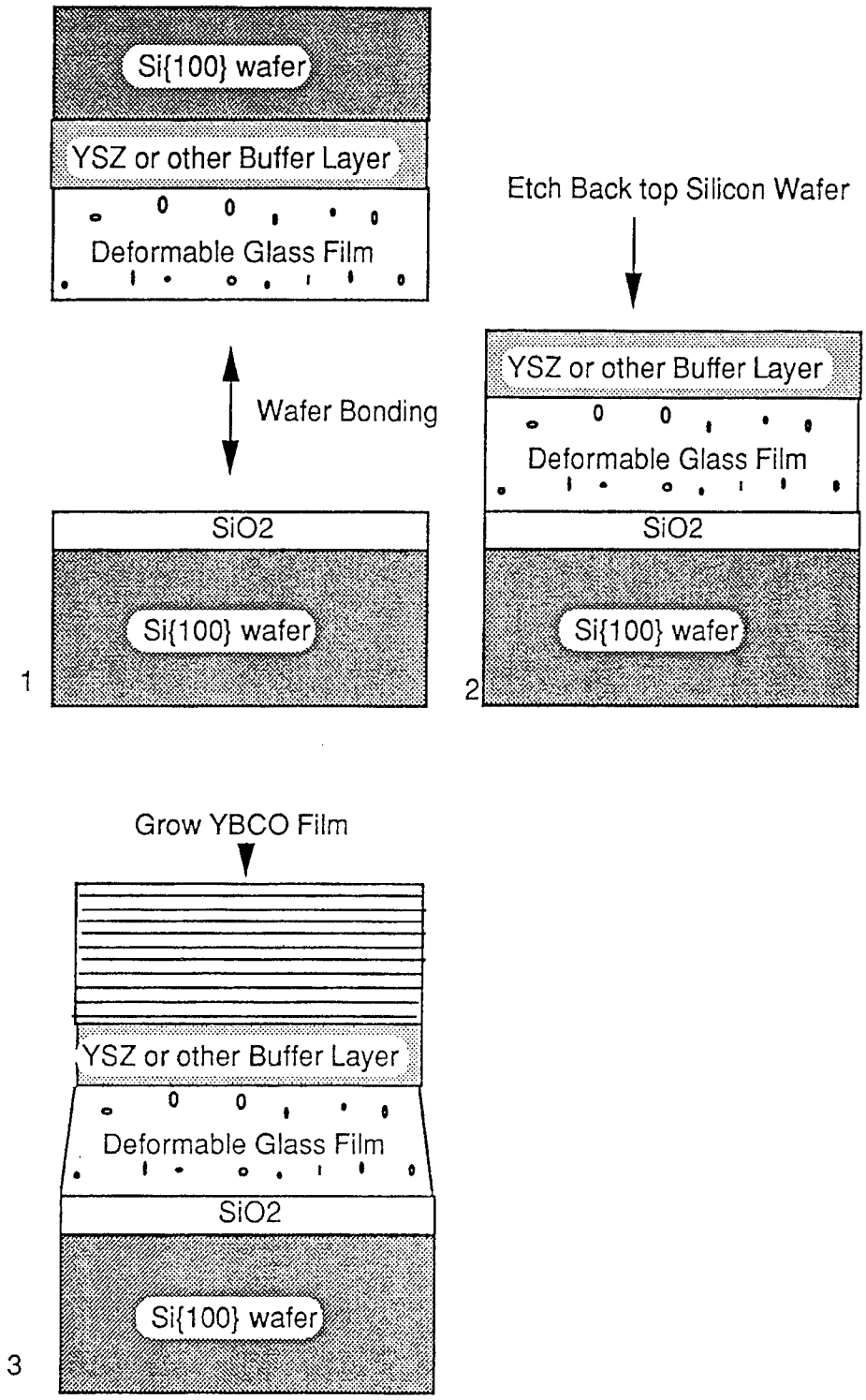

Figure 18 Schematic of plastic buffer layer fabrication process. After growth, deformable glass buffer film layer relieves strain of thermal expansion mismatch by plastic deformation.

silica glass with a strain annealing temperature around 500°C, and constructed a low cost wafer-bonding facility. This facility consists of two small vented acrylic cabinets for manipulating and cleaning samples. The work area is curtained off with polyethylene plastic, and maintained at positive pressure with a filtered blower. Initial efforts to bond two Si wafers together were successful. The process followed was to clean the wafers with conventional techniques to strip the native oxide, followed by formation of a new oxide layer, which provides a hydrophilic surface. These wafers are put together wet, and then dried for 24 hours, followed by a 1-2 hour anneal at 700°C. This bonded structure seems to be well bonded, and indicates that our facilities are sufficiently clean and dust-free.

We next applied this technique to bonding a BPSG (boro-phosphate-silicate glass) coated Si wafer to a SIMOX wafer (Si wafer with a buried oxide layer). The BPSG coating is the desired compliant material, and the buried oxide will serve as an etch stop for removing the Si. This resulted in an Si substrate wafer with a BPSG-Si-SiO_2 layer on top. We were able to achieve a good mechanical bond between the two wafers, but the etching process to remove the Si were unsuccessful due to lack of a sufficiently good way to protect the BPSG wafer.

A third experiment used a BPSG-coated Si wafer bonded to a YSZ coated Si wafer. Again, a good mechanical bond was obtained, and again the attempt to etch the Si on the YSZ failed. The goal was to provide a Si substrate with the compliant BPSG layer overcoated with the YSZ. This, then, would be the desired substrate on which to grow the thick films of YBCO. We feel confident that refinements in the etching procedures will allow this technique to be successful in Phase II.

II.3 Task 2- RSFQ Modeling and Design

Early in the program, we identified parasitic inductance as a critical parameter governing the margins and performance of HTS RSFQ devices. Thermal expansion mismatch induced stress limits the overall thickness of HTS films on silicon substrates to under 70 nm. Because this thickness is less than the london penetration depth, typically 150 nm - 400 nm, we expected a substantial kinetic inductance to be associated with wiring and transmission lines. The kinetic inductance associated with the Josephson junctions themselves is still poorly understood.

Because of the importance of inductance to overall circuit performance, we fabricated and measured (Task 3) some dc SQUIDs and RSFQ flip flops incorporating SQUIDs.

The estimated sheet parasitic kinetic inductance is given by the formula $L_{sq}=\lambda_L^2/d$, where λ_L is the London penetration depth, d is the film thickness ($d<<\lambda_L$) and the current distribution is assumed to be uniform. The total loop inductance in a dc squid can be extracted from the magnitude of the magnetic field induced critical current modulation. We performed measurements on a SQUID fabricated from a 25 nm thick film grown on an $LaAlO_3$ substrate by the barium fluoride process. The inductance calculated over a wide temperature range are plotted in Figure 19. Similar results for a much smaller SQUID imbedded in an RSFQ flip flop are also shown in the figure.

The temperature dependence to the sheet inductance is a signature of substantial kinetic inductance. Since kinetic inductance negatively impacts circuit performance, it is essential that careful quantitative account of all sources of inductance be included in circuit design efforts.

The results indicated that kinetic inductance would be a significant hurdle to the success of HTS RSFQ devices, but that, at least for the purposes of Phase I, the inductance was low enough to proceed, and as discussed in Task I, we developed methods to allow the fabrication of thicker films in Phase II.

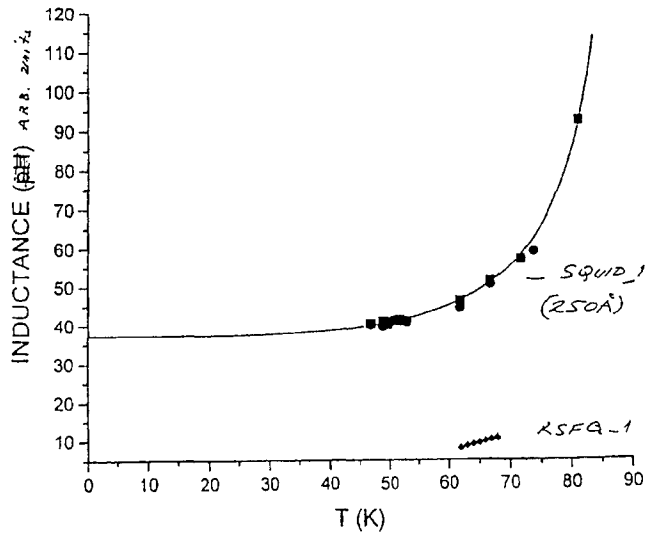

Figure 19. Temperature dependent SQUID inductance for two devices.(AB)

Based on these preliminary measurements and analysis, a more detailed analysis of kinetic inductance was pursued. All RSFQ logic elements depend on maintaining a balance between the Josephson inductance and the SQUID loop inductance such that $2\pi I_c L \approx \phi_0$, where $\phi_0 = h/2e$ is the elementary flux quantum. ϕ_0 is equal to 2.07 mA-pH in practical electrical units. The exact relation between I_C and L is determined by design simulations of a particular logic gate. To ensure that thermal fluctuations do not cause bit errors, the thermal energy unit K_BT must be small compared to the energy scale of the Josephson junction, which is given by $E_J = \phi_0 I_C/2\pi$. Setting $K_BT = 10\ E_J$, we get the result that thermal fluctuations limit the minimum critical current I_c to be at least 38 μA at 90 K. In order that the inductance's can effectively store and process single flux quanta properly, the SQUID inductance is therefore required to be at most $L = \phi_0/(2\pi\ I_C) = 8.6$ pH. Typical inductance numbers for coplanar transmission lines are of the order of 0.5 pH per micron. This implies that careful device design simulations and circuit layout will be required for success. Achieving control over the inductance requires that proper account be taken of all sources of inductance in the SQUID. For this reason, the analysis of the above SQUID results was continued. Assuming that the SQUID modulation depth is entirely due to inductance and not critical current nonuniformity, we found that the low temperature London penetration depth $\lambda_L(0)$ was 370 nm. This is approximately two times higher than what is expected for high quality films. The results under discussion were obtained from films grown by the post-annealed barium fluoride process. It is not surprising that these post-annealed films were of lower quality than films grown in-situ by pulsed laser. If our films on silicon are comparable to PLD grown films on oxide substrates, then we should see approximately a two-fold decrease in penetration depth and a concommittant four-fold decrease in parasitic inductance. If this is born out, then we expect that functional RSFQ logic elements will be possible even with films as thin as 60 nm.

Parasitic inductance - Very thin film transmission lines have two components to the inductance. First, is the more familiar geometric inductance, which arises from the energy stored in the magnetic fields surrounding and penetrating the conductors. Second, is the kinetic inductance, which is often considered a parasitic quantity. The kinetic inductance arises from the kinetic energy of the current carrying cooper pairs. For very thin films, the sheet kinetic inductance is given by $\mu\lambda_L^2/t$ where λ_L is the London penetration depth and t is the film thickness. Using 370 nm for λ_L at low temperatures and t = 5.70 nm we have a parasitic kinetic inductance of 3pH/□ at low temperatures. As T approaches T_C, the London penetration depth diverges, and the parasitic inductance increases as well.

All this implies that thicker films are more desirable from an inductance point of view, and that methods to allow thicker films on silicon would be extremely helpful. At present, film stress provides the main limitation to film thickness. This is one of the reasons why we are examining the roles of new buffer layers in reducing film stress.

SQUID R2, discussed under Task 2 (Figure 17), exhibited magnetic modulation of the critical current only at temperatures at least 7 K below the critical temperature of the SQUID. This suggests that one of the junction had a higher T_c of 45 K, and the other had a T_c around 37 K. The magnetic modulation was measured by injecting current across the SQUID loop, between terminals one and three as shown in Figure 14. For this geometry, the inductance is given by $L=\phi_0/\Delta I_s$, where ΔI_s is current amplitude associated with one oscillation of the SQUID. From the measurement shown in Figure 17, we infer that the inductance is approximately 40 pH. This value is approximately a factor of two higher than is typically seen with SQUID's fabricated on conventional i.e. $LaA1O_3$ substrates. This difference in inductance is likely due to parasitic kinetic inductance associated either an increased magnetic penetration depth, or possible to microstructural defects in the film used for the SQUID.

II.4. Task 3 - RSFQ Circuit Fabrication and Testing

In order to proceed with this Task in parallel with Tasks I and II, we fabricated dc SQUIDs and an RSFQ flip flop incorporating several SQUID's made using the AT&T barium fluoride process on $LaAlO_3$ substrates. The YBCO films were 25 nm thick. The magnetic field dependence of the critical currents and the modulation depth as a function of bias and temperature were measured. Figure 20 shows the current modulation depth as a function of bias voltage for a SQUID imbedded in an RSFQ flip flop at 66 K. The measurements show nearly a 50% modulation in current at low bias voltages, an encouraging result.

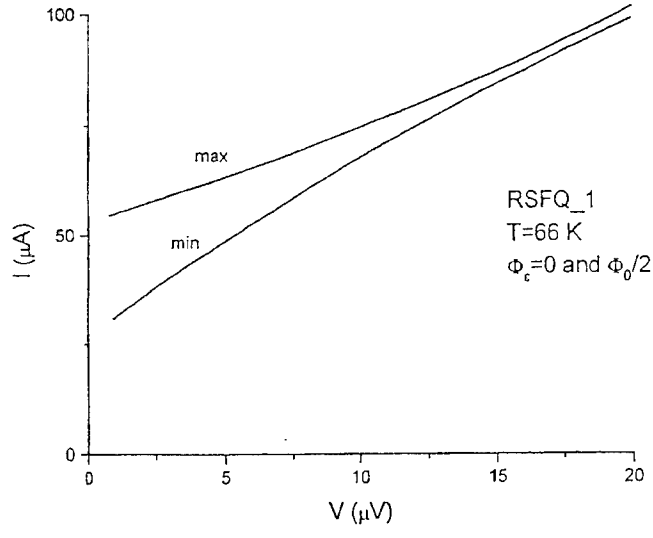

Figure 20 Measured modulation depth of a thin film HTS SQUID in an RSFQ logic element. (AB-2)

Based on the results obtained from this film, a working RSFQ circuit with 14 junctions was successfully fabricated and tested, using a YBCO film grown on a lanthanum aluminate ($LaAlO_3$) substrate. This result is significant because it demonstrates that:

1) the junction technology is sufficiently controllable to manufacture circuits with a significant number of junctions (14 junctions),

2) The circuit design was correct and the film and junction properties e.g. kinetic inductance and critical currents, were within the specified operating margins for successful circuit operation.

3) Correct pulse driven RSFQ logic operation can be successfully verified through dc testing.

The details of this circuit, its preparation and its operation follow:

Direct e-beam writing technique (DEW) was used for preparation of an RSFQ RS Flip-Flop on YBCO thin film operating at 26K.

The most important unique features of the DEW technique instrumental for successful operation of RSFQ circuits are:

1) tunability of the critical temperature T_c (and hence the critical current I_c at an operating temperature).

2) simplicity of the in-plane two-dimensional design combined with the freedom in the arrangement of the junctions.

Technology

Layout of the circuit under investigation was shown in Figure 6. It was made of 500 Å YBCO film deposited on $LaA1O_3$ at AT@T Bell Labs by Shang Hou. After the deposition the wafer was diced into 5x5 mm chips, which were then used for patterning. The patterning was done by standard optical lithography with PMMA resist. YBCO film was wet-etched in diluted HNO_3. Figure 21 shows the final pattern with the minimal feature of 2 μm. Then the junctions were made by DEW in the places shown in Figure 6 as straight lines across the bridges. Electron beam of CM-12 Philips Electron Microscope was scanned once across a bridge to form a weak link. The parameters of the beam were as follows: energy E=120 keV, probe size 35 Å, beam current 5 nA. T_c of the junctions after writing was approximately 35 K.

Operation of the RSFQ RS Flip-Flop

Figure 5 shows the equivalent circuit of the RS Flip-Flop used in the experiment. Below we give a brief description of how it works and then demonstrate its operation at 26 K.

The circuit has a left-right symmetry and consists of four main parts (see Figures 5 and 6).

1. DC/SFQ converter (J1, J2). Current IL opens J2. As a result the fluxoid starts moving to the right by the driving current I2 and antifluxoid to the left. The latter is trapped in the first hole and then comes out of the circuit through J1 when IL is decreased.

2. Transmission line. The fluxoid keeps moving along the transmission line through the junctions J3 and J4 by the driving currents I3 and I4.

3. RS Flip-Flop. (The main cell of the device). Finally the fluxoid gets into the loop J6L, J6R and stays there in the absence of a driving force.

4. SFQ/DC converter (J7L and J7R). It serves as an output of the Flip-Flop. It detects the flux in the lower loop cell. State "1" corresponds to the state when one fluxoid is trapped in the

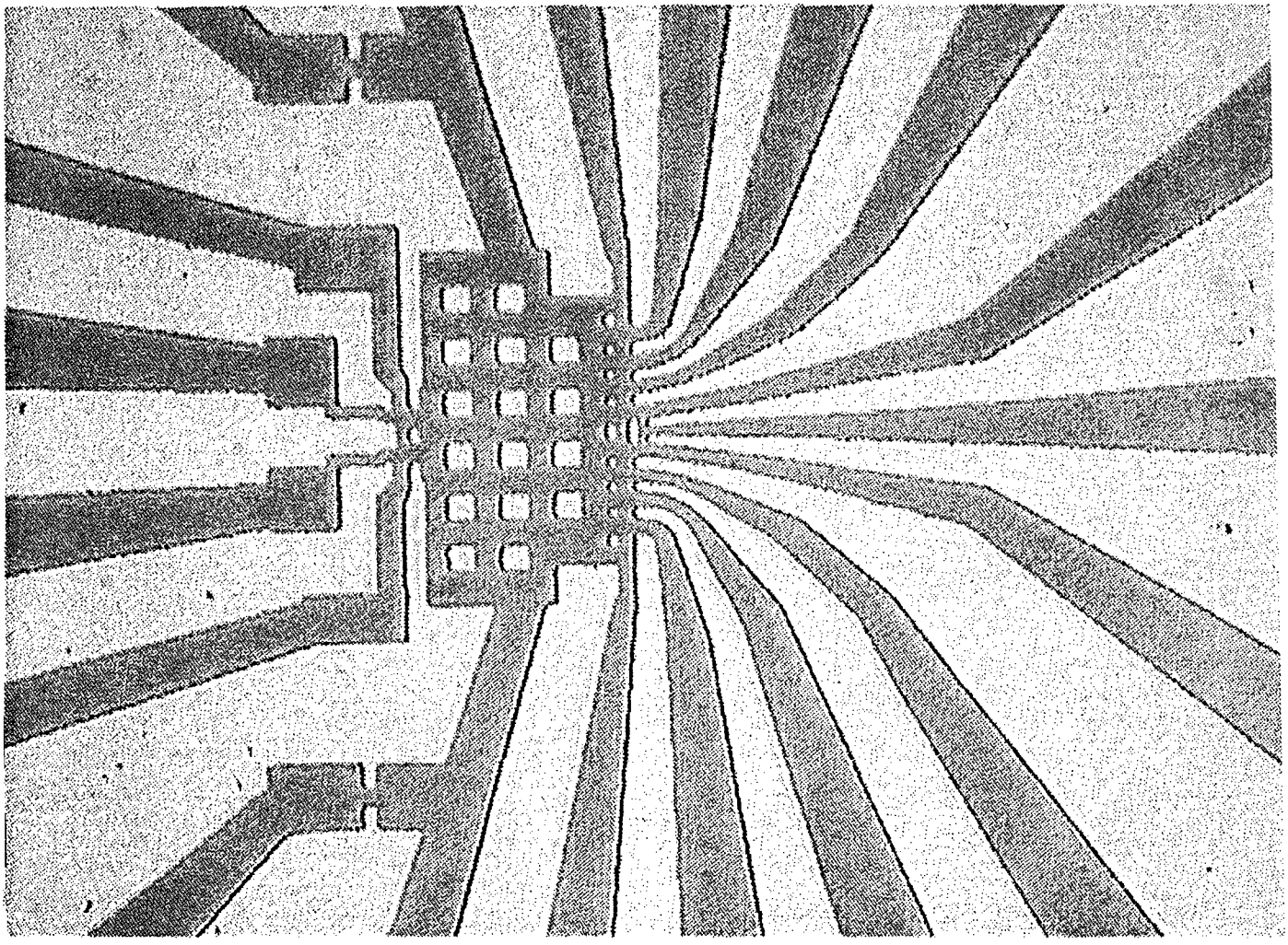

Figure 21. Optical Photograph of the RSFQ Flip-Flop.

lower loop which results in the corresponding voltage in the upper SQUID when it is biased by some current higher than its critical current. State "0" corresponds to the absence of a fluxoid in the lower cell. This is achieved by applying current IR to the right part of the device. It generates an antifluxoid which moves to the left and annihilates with the previously trapped fluxoid in the main cell. If IL generates the fluxoid and the Flip-Flop is currently in the state "1", junction J5 opens and the fluxoid leaves the circuit without disturbing the state of the Flip-Flop. The same is true for the antifluxoid.

Experimental Setup

The chip was installed on a 24 contact probe and placed in a transport helium dewar. Temperature was stabilized by a Temperature Controller (Lake Shore). Measurements were carried out using an automated testing setup which had been developed at Stony Brook. Its hardware part is an advanced version of the system developed earlier at NIST. The setup consists of three main parts: a cryoprobe with passive LF filters located in a transport dewar, a set of 48 ADCs and 48 DACs, and IMB PC running *Octopus* software. *Octopus* was used for all low-frequency analog and digital experiments with High-T_c RSFQ RS Flip-Flop. *Octopus* is a TCL interpreter extended to have low-level access to the buses and system timer. It can display real-time analog data, acquire I-V curves and perform various kinds of digital testing. One of the elementary operation used for testing the high-Tc RSFQ RS Flip-Flop is sending a test pattern to the tested circuit and verifying its response.

Experimental Data

The experimental procedure for testing the RSFQ RS Flip-Flop was the following.

1. The operating temperature 26 K was chosen so that the critical current of the SQUID was 50 μA. At this critical current the maximum voltage modulation depth was 12 μV.

2. Transmission line was biased by currents I2L(R), I3L(R), I4L(R) equal to 0.1 mA each. This value corresponds to approximately half the value of critical current of each junction in the transmission line.

3. The SFQ/DC converter was biased at 65 μA and magnetic currents IB5L-IB5L were chosen to have maximum voltage difference between state "0" and "1".

4. The current IL was applied and voltage V_{sq} on the SFQ/DC converter was measured while increasing IL. At some value of IL there appeared a jump in V_{sq} (Figure 22a) which corresponds to fluxoid entering the main loop ("record" or "flip"). Stability of state "1" can be checked by once more increasing IL to make sure that there are no other states (Figure 22b).

5. To switch the device from "1" to "0" current IR was applied and at some value there is a jump in V_{sq} from "1" back to "0" state ("erase" or "flop", Figure 22c). Figure 22d shows a proof that the device is still in state "0".

To eliminate direct influence of the currents IL and IR on the SFQ/DC converter and Flip-Flop we applied an additional small differential current between IB5L and IB5R proportional to the currents IL or IR to compensate leakage current from the input. The coefficient of proportionality give us an exact value of the leakage current which was approximately 5% of the input currents IL and IR. This procedure fixes a set point of SFQ/DC converter during all measurements. This fact completely rules out the possibility of switching SQUIDS due to the leakage current.

Operation of the flip-flop is demonstrated in Figure 23. A sequence of digital double current pulses is applied to IL and IR and switches the flip-flop to states "0" and "1" respectively. It can be seen that the first pulse from Il sets the flip-flop ("1") and the second IL pulse does not

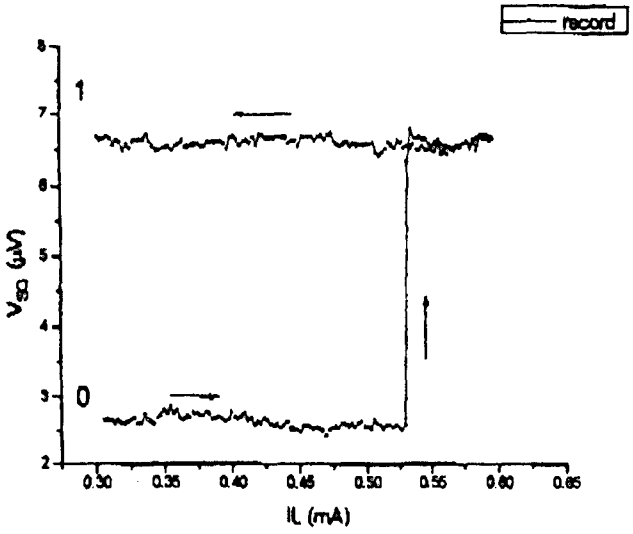

Figure 22a

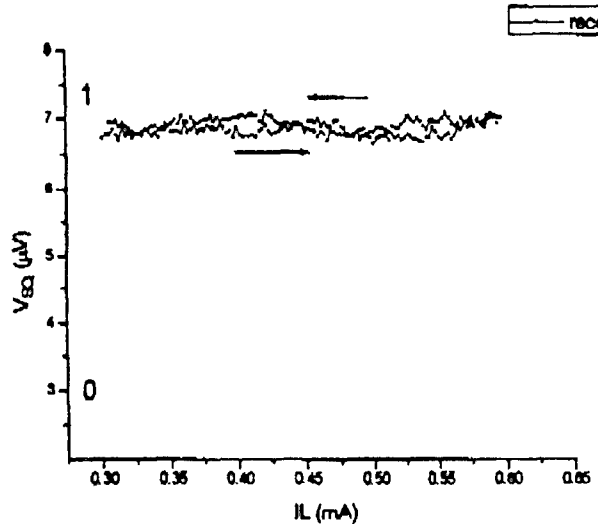

Figure 22b

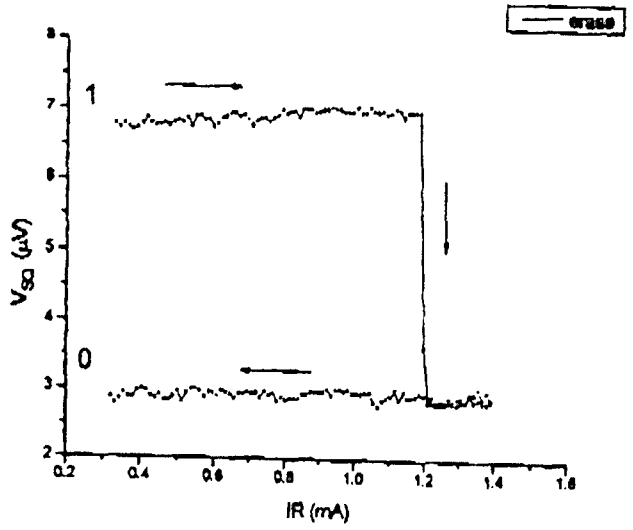

Figure 22c

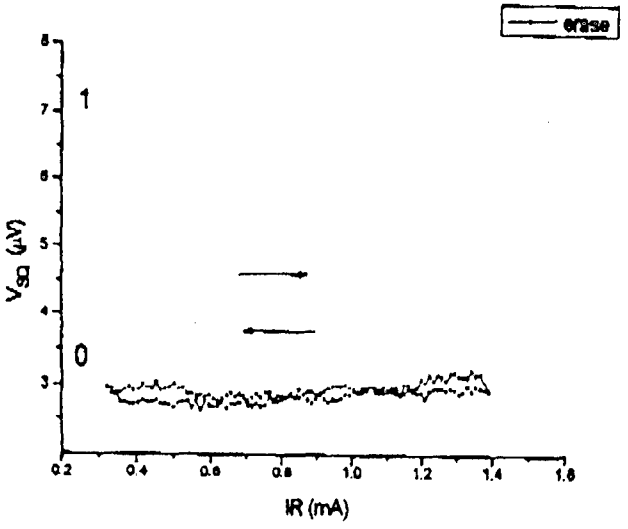

Figure 22d

Figure 22 Measurement of Logic States for RSFQ RS Flip-Flop

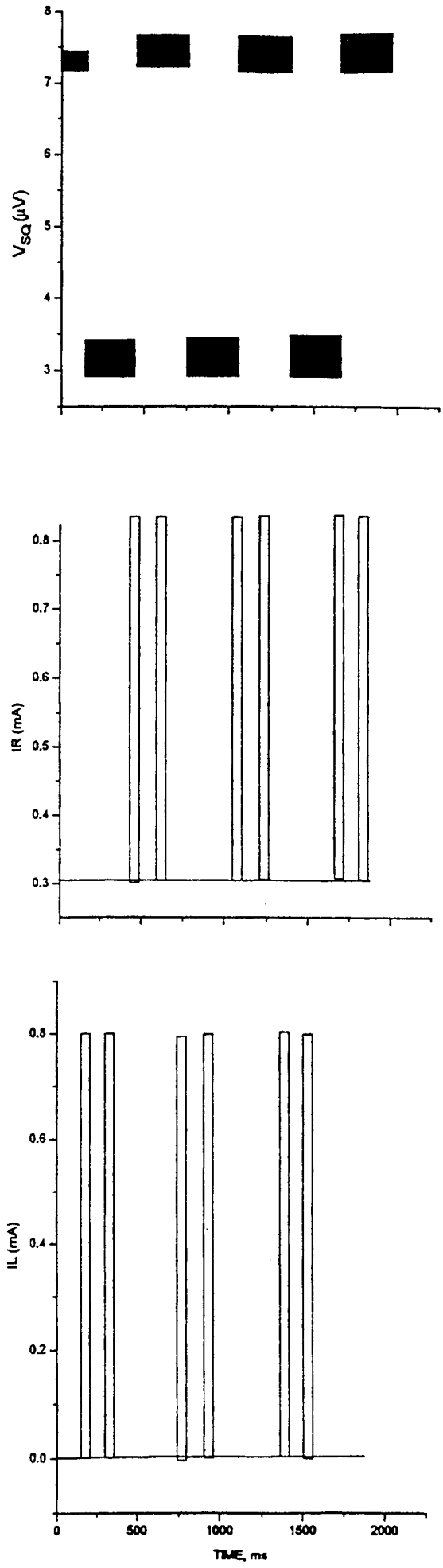

Figure 23 Operation of RSFQ RS Flip-Flop

change the state of the flip-flop. The pulse IR resets the flip-flop ("0"), etc. The noise is characterized by the width of the corresponding voltages V_{sq}.

Additional experiments proved that the device was indeed operating as an RSFQ flip-flop, that the Josephson transmission line inputs circuitry was operating as expected, and that the switching thresholds and statistics were reasonable.

1. Analog data pattern:

The operation of the flip-flop is demonstrated in Figure 24 by applying digital current pulses to IL and IR (IBL and IBR) to switch the flip-flop to state "1" and "0" respectively; analogue voltage signals V_{out} are measured in the main SQUID loop.

Signal/noise ratio corresponding to the readout pulse is approximately 20. The test sequence is as follows. First, a double pulse is applied to IL the s (set) input to the rs flip-flop. The first pulse switches the flip-flop to state "1" (high V_{out}). The second pulse is applied to make sure that this is stable. Next, another pair of pulses is applied to IR (the r or "reset" input). The first pulse resets the flip-flop to the zero state (V_{out} low)as shown in the top trace. The second pulse demonstrates that this state is also stable.

2. Derivatives of the bias currents:

To prove beyond any doubt that the RSFQ works the way it should we conducted another series of experiments. We need to show that DC/SFQ converter operates properly; junction J2 opens and the flux starts moving along the transmission line (through junctions J3 and J4) until it is trapped in the main loop of the device.

In order to do that we measured the change in the values of IBL (IL) and IBR (IR), corresponding to the change in the respecting bias currents IB2L, IB3L, IB4L etc. (partial derivatives). The results are shown in Figure 25. We found that the bias influence is the strongest on the current IB2L, which means that indeed it is this junction that reaches threshold and switches when you apply the current to IL. We obtain the same result for IR as well (for junction J2R). The experimental values of these derivatives do not differ much from the results of the computer simulation (using PSCAN software).

3. Thermal noise distribution of the value of the current IL (IR) (position of the jump).

In order to check the reliability of the device and the influence of the thermal noise we studied a few hundred cycles ("0" - "1"; "1" - "0") and measured the distribution function of the values of IBL (IBR) at which the flip-flop operates. Figure 26 shows the resulsts of 100 cycles. The first conclusion we can come to is that it worked 100 times out of 100.

More importantly the distribution function has the right shape - it is not quite symmetric - and can be very well fitted by a theoretical formula for thermal fluctuations with the mean deviation of IBL approximately 0.010 mA (for this device configuration). The experimental value is approximately 0.015 mA.

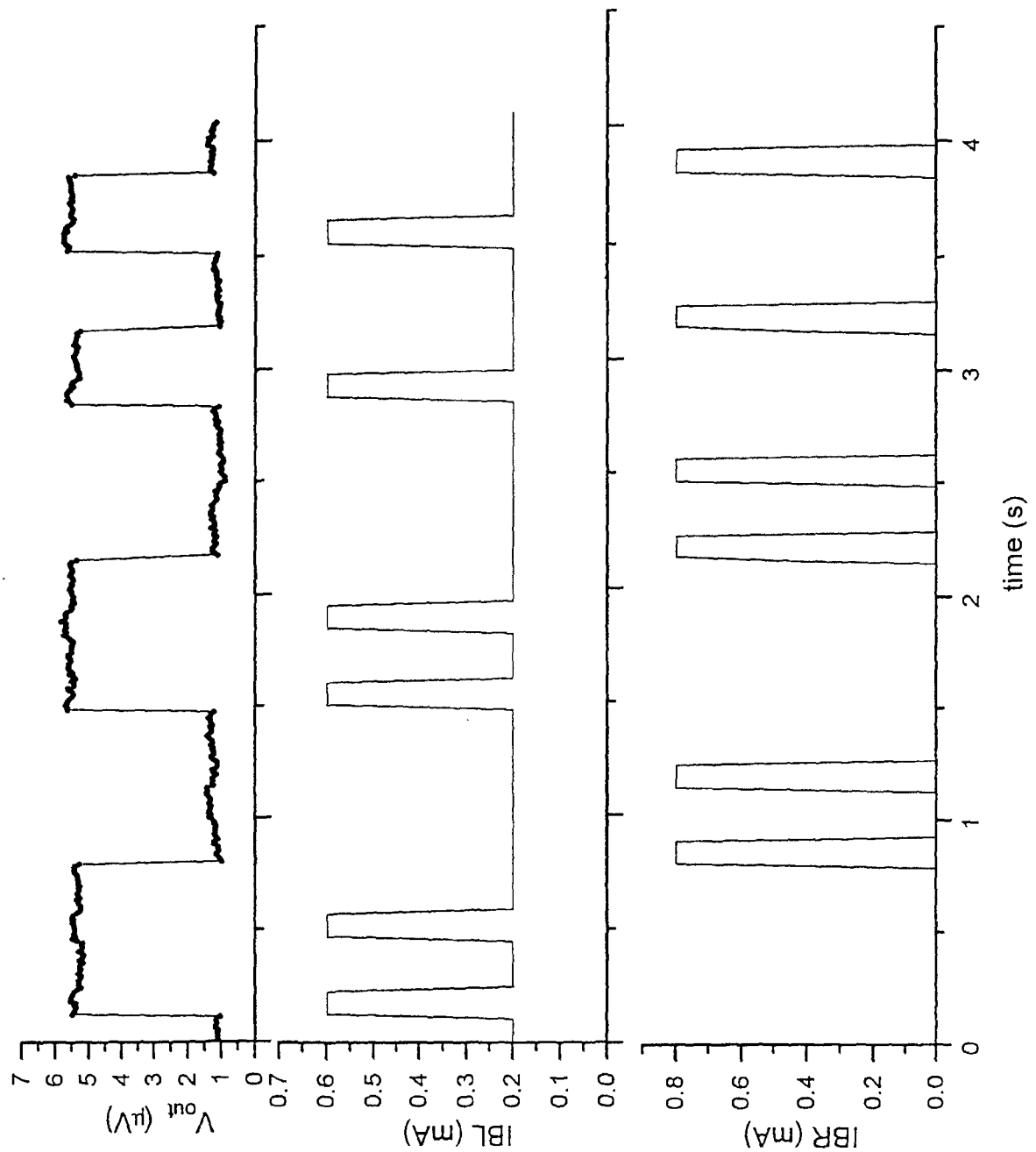

Figure 24 Demonstration of the flip-flop operation. The top trace shows the analogue measurements of the readout SQUID interrogating the flip-flop state. The middle and lower traces show the currents applied to the JTO coupled set and reset inputs.

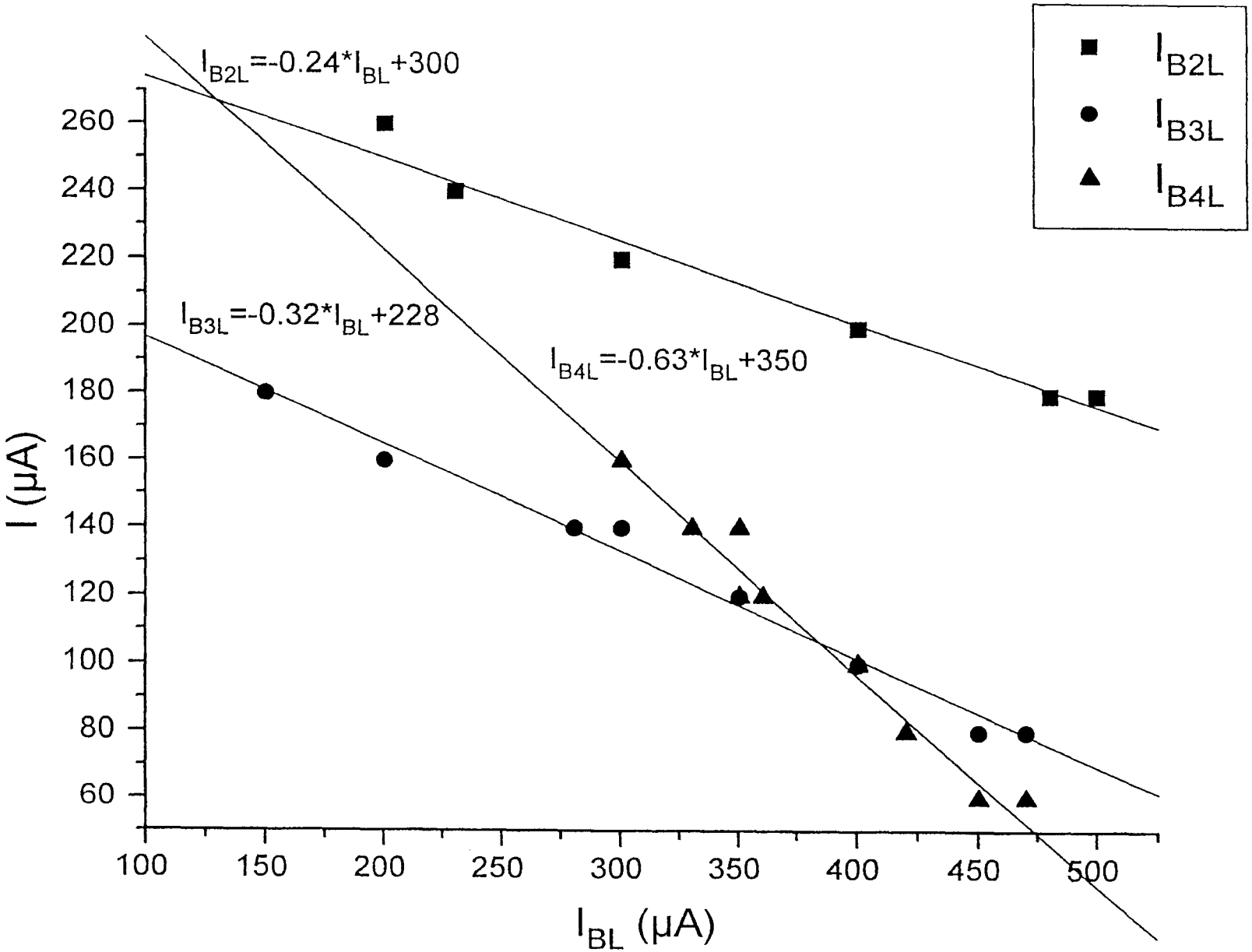

Figure 25 Dependence of the JTL junction bias currents with respect to the input current I_L, showing that the first junction in the JTL will switch first.

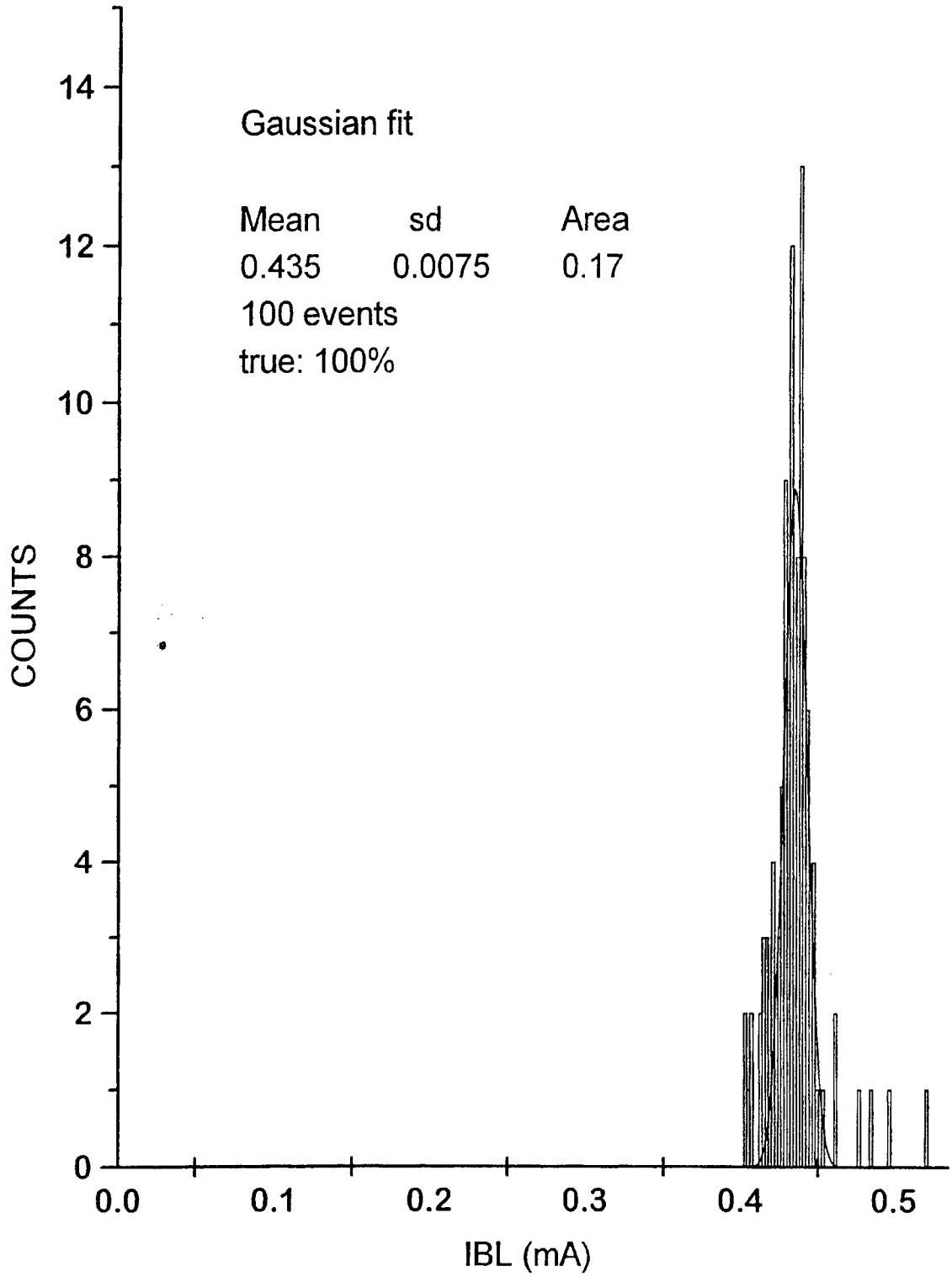

Figure 26 Histogram of switching events vs input current IB_L. Gaussian fit is shown as the solid curve.

[1] P.A. Rosenthal, E.N. Grossman, R.H. Ono, et. al., *Appl. Phys. Lett.* **63**, and references therein.

[2] M.I. Faley, U. Poppe, H. Soltner, et. al., *Appl. Phys. Lett.*, **63,** 2138 (1993).

[3] K.Char, M.S. Colclough, S.M.Harrison et. al., *Appl. Phys.Lett.* **59,** 733 (1991).

[4] S.K. Tolpygo, S. Shokhor, B. Nadgorny, M. Gurvitch., *Appl. Phys. Lett.* **63**, 1696 (1993).

[5] D.B. Fenner, Li Q, Hamblen W.D., Johansson M.E., Hamblen D.G., Lynds L., and Budnick J.I., "Optical and Performance Advantages for Silicon Substrates in YBCO Bolometer Devices," I.E.E.E. Trans. Appl. Supercon., **3**, 2104 (1994).

[6] K.K. Likharev, "Dynamics of Josephson Junctions and Circuits," New York, N.Y., Gordon and Breach (1986).

[7] K.K. Likharev and Semenov V.K., IEEE Trans. on Appl. Supercond, **1**, 3 (1991); K.K. Likharev, in: The New Superconducting Electronics (*Kluwer, Dordrecht, 1993*), p.423.

[8] P.M. Mankiewich, Scofield J.H., Sckocpol W.J., et. al. *Appl. Phys. Lett.* **51**, 1753 (1987); M.P. Siegal, S.Y. Hou, J.M. Phillips et. al. *J. Mater. Res.* 7, 2658 (1992).

[9] Martens et al.,*4-th Superconductive Electronic Conference (Boulder, Colorado, 1993*), p.17-18.

[10] Z.G. Ivanov et al.,*4-th Superconductive Electronic Conference (Boulder, Colorado, 1993*, p.78-79.

[11] Martens et al.,*4-th Superconductive Electronic Conference (Boulder, Colorado, 1993*), p.17-18.

[12] Z.G. Ivanov et al.,*4-th Superconductive Electronic Conference (Boulder, Colorado, 1993*), p.78-79.

[13] D.K. Fork, D.B. **Fenner**, G.A.N. Connell, J.M. Philips, and T.H. Geballe, "Epitaxial Yttria-Stabilized Zirconia on Hydrogen-Terminated Si by Pulsed Laser Deposition", *Appl. Phys. Lett.*, **57**, 1137 (1990).

[14] D.K. Fork, **Fenner** D.B., Barton R., Philips J.M., Connell G.A.N., Boyce J.B., and Geballe T.H, "High Critical Currents in Strained Epitaxial YBaCuO on Si", *Appl. Phys. Lett.*, **57**, 1161 (1990).

[15] D.B.Fenner et al, "Reactions at the Interfaces of Thin Films of Y-Ba-Cu- and Zr-Oxides with Si Substrates," J. Appl. Phys. **69**, 2176 (1991).

[16] A.Lubig,Buchal Ch., .Schubert J., Copetti C., Guggi D., Jia C.L., and Stritzker B., "Epitaxial growth of $YBa_2Cu_3O_{7-x}$ thin films on Si(100) with zirconia buffers of varying crystalline quality and structure," *J. Appl. Phys.* **71** (11), 1 June 1992, p 5560.

DOCUMENT 4

JSEP Annual Report

AD-A313700

February 1996

Stanford University

Stanford, CA

MASTER COPY KEEP THIS COPY FOR REPRODUCTION PURPOSES

REPORT DOCUMENTATION PAGE

Form Approved
OMB No 0704-0188

1. AGENCY USE ONLY (Leave blank)	2. REPORT DATE	3. REPORT TYPE AND DATES COVERED
	March 1, 1996	Annual 1 March 1995 through 29 February 1996

4. TITLE AND SUBTITLE
JSEP Annual Progress Report No. 2

5. FUNDING NUMBERS
DAAH04-94-G-0058

6. AUTHOR(S)
J. S. Harris, Program Director

7. PERFORMING ORGANIZATION NAME(S) AND ADDRESS(ES)
Stanford University
Solid State Electronics Laboratory
CIS-X 329
Stanford, CA 94305-4075

8. PERFORMING ORGANIZATION REPORT NUMBER

9. SPONSORING/MONITORING AGENCY NAME(S) AND ADDRESS(ES)
U. S. Army Research Office
P. O. Box 12211
Research Triangle Park, NC 27709-2211

10. SPONSORING/MONITORING AGENCY REPORT NUMBER
ARO 32283.2-EL-JSEP

11. SUPPLEMENTARY NOTES
The view, opinions and/or findings contained in this report are those of the author(s) and should not be construed as an official Department of the Army position, policy, or decision, unless so designated by other documentation.

12a. DISTRIBUTION/AVAILABILITY STATEMENT
Approved for public release; distribution unlimited.

12b. DISTRIBUTION CODE

13. ABSTRACT (Maximum 200 words)

14. SUBJECT TERMS

15. NUMBER OF PAGES
69

16. PRICE CODE

17. SECURITY CLASSIFICATION OF REPORT	18. SECURITY CLASSIFICATION	19. SECURITY CLASSIFICATION OF ABSTRACT	20. LIMITATION OF ABSTRACT
UNCLASSIFIED	UNCLASSIFIED	UNCLASSIFIED	UL

SOLID STATE
ELECTRONICS
LABORATORY

JSEP ANNUAL REPORT

1 March, 1995 through 29 February, 1996

James S. Harris, Jr.
JSEP Principal Investigator
and Program Director

(415)723-9775

This work was supported by the
Joint Services Electronics program
(U.S. Army, U.S. Navy and U.S. Air Force)
Contract DAAH04-94-G-0058
and was monitored by the
U.S. Army Research Office

STANFORD ELECTRONICS LABORATORIES • DEPARTMENT OF ELECTRICAL ENGINEERING
STANFORD UNIVERSITY • STANFORD, CA 94305-4055

JSEP ANNUAL REPORT

1 March, 1995 through 29 February, 1996

James S. Harris, Jr.
JSEP Principal Investigator
and Program Director

(415)723-9775

This work was supported by the
Joint Services Electronics program
(U.S. Army, U.S. Navy and U.S. Air Force)
Contract DAAH04-94-G-0058
and was monitored by the
U.S. Army Research Office

Abstract

This is the annual report of the research conducted at the Stanford Electronics Laboratories under the sponsorship of the Joint Services Electronics Program from March 1, 1995 through February 29, 1996. This report summarizes the areas of research, identifies the most significant results and lists the dissertations and publications sponsored by contract DAAH04-94-G-0058.

Table of Contents

This work was supported by the Joint Services Electronics Program, contract DAAH04-94-G-0058. The views and conclusions contained in this document are those of the authors and should not be interpreted as representing the official policies either expressed or implied of the U.S. Government.

JSEP ANNUAL REPORT
March 1, 1995 - February 29, 1996

Introduction and Overview of Principal Accomplishments

This annual report covers research accomplishments for the period 1 March, 1995 through 29 February, 1996 for basic electronics research conducted in the JSEP program in the Electrical Engineering Department of Stanford University. The Stanford Electronics Lab JSEP Director and Principal Investigator is Professor James Harris. The program work units are as follows:

Unit 1: Investigation of Transport in Quantum Dots
(James S. Harris)

Unit 2: Patterned Thin Film Media for High Density Magnetic Recording
(R. Fabian W. Pease)

Unit 3: Investigation of a Metal Source and Drain Field Emission Transistor
(C. Robert Helms)

Unit 4: On-chip Thin Film Solid State Micro-battery
(S. Simon Wong)

Unit 5: CVD Epitaxial Germanium *n*-channel FETs Formed on Si using Strain-relief Layers
(Krishna Saraswat)

Unit 6: Portable Video on Demand in Wireless Communication
(Teresa H. Y. Meng)

Unit 7: Adaptive DFE for GMSK in Indoor Radio Channels
(John M. Cioffi)

Unit 8: Robust Estimation Methods for Adaptive Filtering
(Thomas Kailath)

Unit 9: Efficient Data Compression
(Thomas M. Cover)

Highlights

In work unit 1, Professor Harris and students have developed the nanofabrication techniques for large (200X200) arrays of 100nm quantum dots and demonstrated the first Coulomb blockade and hysteretic switching behavior in such large arrays. This work represents a significant advance in nanofabrication and demonstrates the robustness of Coulomb blockade compared to quantum interference effects.

In work unit 2, Professor Pease and students have demonstrated and characterized (with Magnetic AFM, alternating gradient magnetometer) magnetic thin film recording media patterned into deep submicron islands for improved density (>12 Gbytes/sq. in.) and lower transition noise. One medium was Polycrystalline Co 20nm thick on Cr which exhibited 1 bit/1 domain/1 island for dimensions less than 150nm. Another medium was single crystal iron film which, when patterned, demonstrated single domain/island behavior for large (1-micron) islands. Magnetic anisotropy in the iron films was dominated by crystalline orientation which allows us to decouple the magnetic direction from the shape of the island; this is valuable for applications involving horizontal recording.

In work unit 5, Professor Saraswat and his students are developing a technology to fabricate high-performance n-channel heterostructure field-effect devices using germanium-rich GeSi grown via graded-alloy strain reduction on (001) silicon substrates. The goal is to combine the high intrinsic electron mobility of germanium and the carrier confinement available with band-structure engineering in the Ge-Si system. Success with the use of graded-alloy epitaxy to isolate the defects associated with the transition between silicon and germanium lattice constants has been achieved.

In work unit 6, Professor Meng's group focuses on low power communications problems. They have developed an energy-on-demand computation system which dynamically adjusts the supply voltage to meet the throughput requirements. A DC-DC switching regulator has been designed that delivers a power-conversion efficiency in excess of 90-percent with tracking speed of under 1 ms. The regulator supplies power ranging from a few mW to several hundreds of mW for all supply voltages of interest. A second effort has produced a real-time, low-power video encoder for pyramid vector quantization (PVQ). This system dissipates only 2.1 mW for real-time video compression of images of 256x256 pixels at 30 frames per second. Applying this quantizer to subband decomposed images, the PVQ encoding delivers better compression performance than the standard JPEG algorithm.

In work unit 9, Professor Cover and students have been investigating the degree to which one can compress images without recognizable distortion. The experiment involves comparison of human vs computer image compression to estimate the minimal rate at which images can be compressed without perceptual distortion. This work is providing a new method for benchmarking data compression algorithms and may lead to a framework to develop entirely new algorithms.

Transfer of Technology

The research results emanating from the JSEP program are usually of either a more fundamental nature or so early that it is not in the vision of more applied programs. Not too surprisingly, such work does not typically lead to instant transfers to industry. However, one

hopes that more fundamental work ultimately has a greater impact because it leads to things that simply would not have been done if left to only research programs with nearer term, clearly identified needs. The transfers of technology described below are thus the result of JSEP supported programs of 5-10 years ago.

Research into the engineering of silicon nanopillars in Professor Pease's JSEP program has led to new insights into the oxidation of silicon under high stress, confined geometry conditions. As Si ULSI continues to shrink, such high stresses are quite important. The results of this research are now being incorporated into SUPREM process models being developed to simulate the processing of next-generation, ultra-small geometry ULSI circuitry.

An essential element in manufacturing high performance AMLCDs is the ability to fabricate TFT driver circuits and integrate them with the liquid crystals on glass substrates. However, the high temperatures and long thermal cycles generally needed to obtain high performance TFTs cause warpage and shrinkage to glass. As a result, fabrication processes are limited to low temperatures and short times. Early work of Professor Krishna Saraswat funded by JSEP and subsequently by DARPA demonstrated high performance TFTs in poly-GeSi with low thermal budget processing, compatible with glass substrates. He demonstrated significantly lower processing temperatures for deposition, doping, recrystallization, and grain boundary passivation. Several novel device structures have been developed to improve TFT performance, such as, increased drive current in the ``on" state and reduced leakage in the ``off" state. He is actively working with XEROX and Intevac to transfer this technology and several major organizations around the world are now developing the poly-GeSi TFT technology which originated under JSEP support in his laboratory.

The early JSEP work demonstrating the first MBE growth and growth induced layering of the high temperature superconductors by MBE in Professor Harris's program is the basis for the continuing high T_c program at Varian Associates. The focus of their effort is MBE growth induced layering of alternate superconducting and insulating phases to produce well controlled Josephson junctions.

One of the key problems facing modern ultra-high bandwidth communications systems is how to handle the final 100 meters where information delivery is to only a single receiver and the costs of high bandwidth solutions can no longer be divided by a large number of receivers. The early JSEP supported research under Prof. John Cioffi led to the development of the "Discrete MultiTone" (DMT) technology that is now an international standard (ANSI T1.413) for both video transmission and high-speed internet access on twisted pairs, in what is known as Asymmetric Digital Subscriber Lines (ADSL). Stanford holds 4 patents in the area that are exclusively licensed and sublicensed by Stanford to a DMT-spinout, Amati Communications Corporation. Amati has sublicensed the DMT patents to a number of semiconductor and telecom manufacturers around the

world, including Motorola, Northern Telecom, and AT&T (now Lucent Technology). Amati builds products based on the DMT technology and has been extremely successful.

The early JSEP supported work of Professor Tom Cover is now being utilized in many of the WWW browsers. One of the issues is do you wait for all of the information to be supplied serially or do you send information at various levels of refinement so that the description efficiency is optimal at each level ? The idea is to utilize methods of successive refinement to quickly produce a rough picture, then successively more refined pictures until the final version is produced. This work was first described in the paper, "On the successive refinement of information", W. Equitz and T. Cover, IEEE Transactions on Information Theory and is now used by Netscape and many others. Will Equitz was asked by IBM to help write the JPEG data compression standard for progressive transmission based on this work.

UNIT: 1

TITLE: Investigation of Transport in Quantum Dots

PRINCIPAL INVESTIGATOR: J. S. Harris, Jr.

GRADUATE STUDENTS: D. R. Stewart and C. I. Duruöz

1. Scientific Objectives

The continuing drive for increased device density in both IC and memory technologies demands smaller and closer packed future devices. We are pursuing an investigation into the electronic transport in both single quantum devices and large arrays of densely packed quantum dots. A full understanding in both regimes will be required in any successful implementation of single electron electronics. In particular, most studies of quantum devices have concentrated on the very low bias equilibrium behavior [Beenakker][Kouwenhoven]; we concentrate instead on the technologically relevant non-linear high bias operating regime.

We have two main objectives: first, to understand the mechanisms controlling electron transport through single quantum point contacts and quantum dots and second, to study the fundamental characteristics of coulomb blockade and charge coupling in transport through quantum dot arrays.

2. Summary of Research

2.1 Introduction

We previously reported our initial investigations of the electronic transport through 200 x 200 two dimensional quantum dot arrays patterned on a molecular beam epitaxy (MBE) grown GaAs/AlGaAs heterostructure [Harris][Duruöz]. The current-voltage (I-V) relation of the arrays showed two striking features: a threshold for conduction, and multiple switching events accompanied by a hierarchy of hysteresis loops. By changing the voltage applied to a single Schottky gate deposited over the entire array, it was possible to move between the hysteretic and non-hysteretic regimes. A single hysteresis loop was measured in the single control dots fabricated adjacent to the large arrays. No switching or hysteresis was observed above a temperature of 700mK.

We have continued this investigation by focusing on the mechanisms responsible for the switching and hysteresis. It is this behavior, and control of it, that will be most relevant in any technological application.

We have thus characterized in detail the behavior of the single control quantum dots and point contacts in our first generation devices. We have also fabricated a second generation of similar etch defined single devices using a GaAs/AlGaAs heterostructure grown by chemical vapor deposition. All of our single device results have been duplicated in both of these materials to prove the repeatability and robustness of the switching phenomena. Our results show the single hysteresis observed to be the experimental realization of a basic conduction bistability in the I-V relation. When measured on sufficiently fast time scales, the switching bistability manifests as a random telegraph signal in the current under constant voltage bias. Most significantly, we are able to control the bistable switching rate and range with voltages applied to a new back gate and the original front Schottky gate. We are also able to observe the switching in the new devices at a temperature of 4.2K. These results have yielded new insight into the cause of the I-V switching.

2.2 Device Fabrication and Measurement Configuration

All devices measured were fabricated by lithographically patterning a GaAs/AlGaAs epitaxially grown heterostructure. We have utilized a standard modulation doped architecture to create a two dimensional electron gas (2DEG) approximately 800 Å below the wafer surface. First generation and second generation split gate devices were fabricated from MBE material grown in our laboratory with a mobility and sheet density of ≈200 000 cm^2/Vs and $3.5x10^{11}$ cm^{-2}; second generation etched devices were patterned on CVD material grown at Sandia National Labs by our collaborator H.Chui with a mobility and density of ≈300 000 cm^2/Vs and $2.0x10^{11}$ cm^{-2}.

The devices were formed using electron-beam lithography to define the point contact, dot and array features. Minimum feature size as shown in Fig. 1 is 100 nm, point contact barrier openings are 200-400 nm, and the array periodicity is 800 nm. This lithographic pattern was used as a mask for wet chemical etching 800 Å deep through the 2DEG in the case of etched structures, or NiCrAu metal gate evaporation for the split gate devices. A single 1000 Å Au front gate was deposited over the etched devices. A ground plane below the mounted chips was used as a back gate.

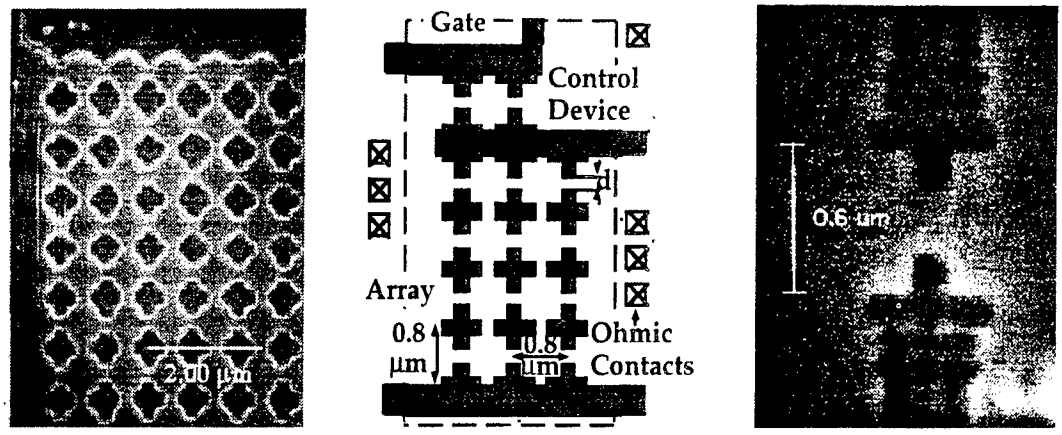

Figure 1: (a) Electron micrograph of part of a 200x200 array. The 2DEG is removed beneath darker regions. (b) Schematic diagram of the array layout (c) Micrograph of a CVD etched point contact of barrier width 260 nm. The 2DEG is removed below the two vertical fingers.

Measurements were conducted at temperatures of 4.2K to 300mK in a pumped He^3 cryostat with a slowly swept dc voltage bias applied to source and drain ohmic contacts across each device. DC voltage biases were also applied to the front and back gates. The dc current was recorded with a slow averaging multimeter and a fast oscilloscope.

2.3 Experimental Results

In Fig. 2 we review the hysteretic behavior observed in the large arrays. All hysteresis loops observed are traversed in a counter clockwise direction in I versus V. This figure shows multiple hysteresis loops shrinking and dissociating into smaller loops as the temperature is raised. All hysteresis has disappeared at 680mK.

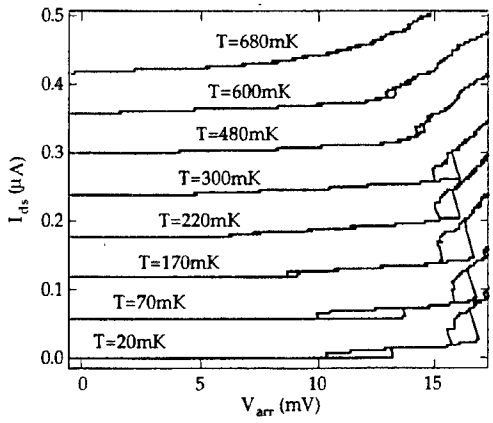

Figure 2: I-V curves (offset for clarity) of an array device at $V_{front\ gate}$=-115 mV and various temperatures.

The single point contact and quantum dot devices we have concentrated on all show one bistable switching region as the dc conductance jumps from zero to a finite value, typically (60 kΩ)$^{-1}$. Figure 3 displays how the conductance switches between two bistable states over a small voltage range as the devices turns on. Applying a constant source drain voltage to bias the device at some midpoint of the switching region yields a random telegraph signal in the current as a function of time. (Fig. 3 inset). Recording the times spent in the high and low conductance state yields an average lifetime t_{high}, t_{low} for each state.

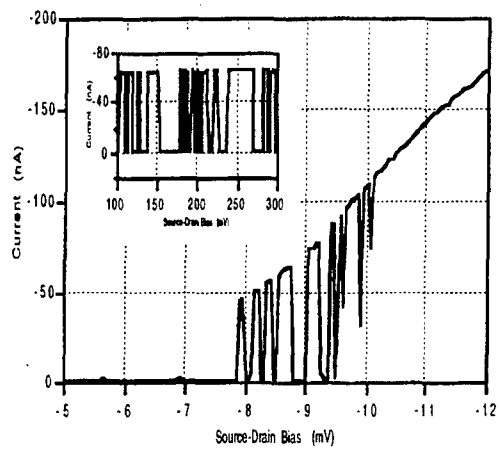

Figure 3: I-V curve of quantum dot displaying bistable conduction switching as the bias is swept up over 8-10 mV. Inset shows random telegraph signal in time at a fixed bias of -9 mV. Temperature is 400 mK.

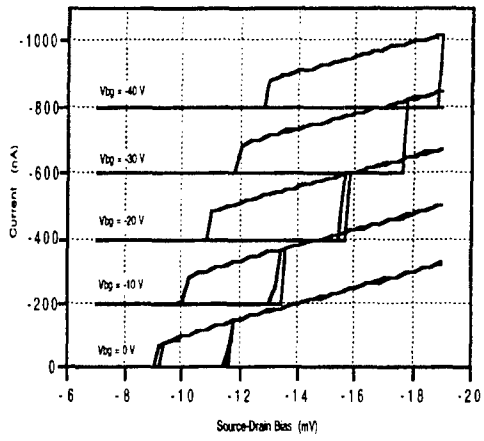

Figure 4: In the hysteretic regime, control over the size and position of the hysteresis loop is effected with a backgate voltage as labeled (curves offset for clarity). Results for an etch defined quantum dot at 400 mK.

As the source-drain bias is swept over the switching range these lifetimes appear to change exponentially; t_{high} increases with bias and t_{low} decreases. The clean hysteresis loops initially observed in the arrays can thus be described as bistable conductance regions with average (t_{high}, t_{low}) » measurement sweep rate. As the device remains cold, the time constants of this switching increase over several hours until even a slow voltage sweep appears hysteretic.

In this long switching time or 'hysteretic' regime when t_{switch} is much greater than our measurement speed of O(10s), we can use the front and back gates to control the size and position of the hysteresis. As an increasingly negative backgate voltage is applied, the hysteresis loop expands in size and the initial turn on threshold shifts to higher source-drain bias, as illustrated in Fig. 4.

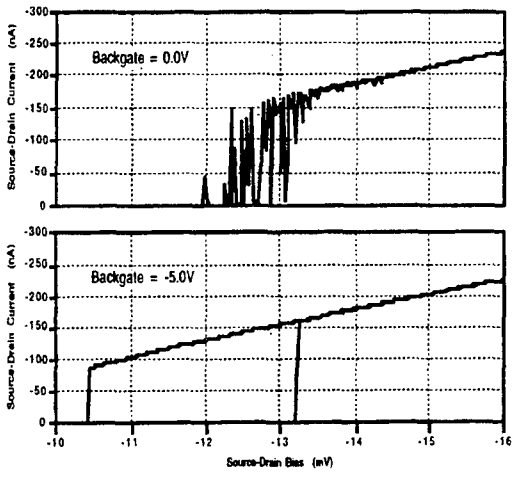

Figure 5: In the fast telegraph switching regime, the backgate is able to reversibly control the bistable state lifetimes. Results from etch defined quantum dot at 400 mK.

In the short switching time or telegraph noise regime we achieve our most significant result; application of a small backgate voltage changes the average state lifetimes dramatically. We are able to continuously control the lifetimes over our full measurement range of 100μs to 1000s, seven orders of magnitude. Fig. 5 demonstrates this control.

The CVD etched devices extended the temperature range of this behavior to above 4.2K. In addition, some of these devices displayed multi-stable switching instead of a simple bistability. The multi-stable devices also showed switching between finite conduction states, and a smoother current turn on. This comparison is made in Fig. 6.

We have also conducted initial tests on the split gate second generation single devices, in

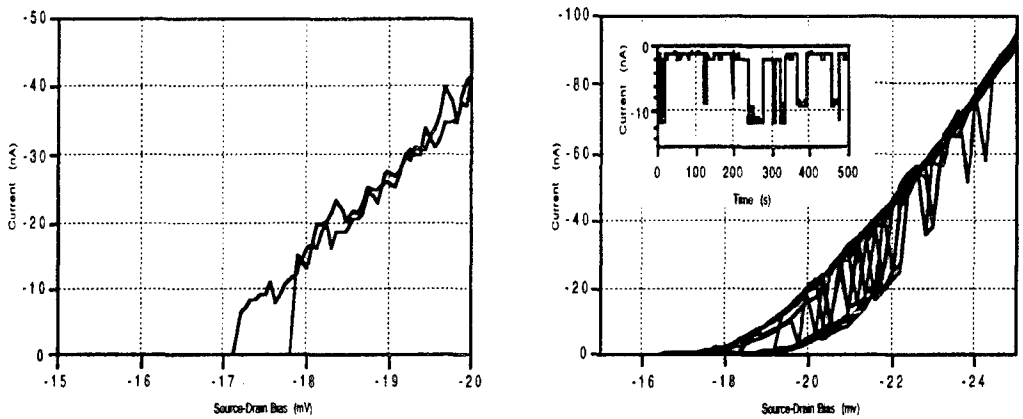

Figure 6: (a) Bistable hysteresis in a CVD point contact at 4.2 K (b) Multi-stable switching and associated multi-level random telegraph signal (inset) in another CVD point contact at 4.2 K.

which the quantum barriers are defined with electrostatic depletion gates instead of wet chemical etching. Well resolved coulomb blockade measurements (Fig. 7) demonstrate that these devices are performing correctly. Future measurements will characterize and compare the switching behavior in this very different architecture to the etched device results.

2.4 Discussion of the Results

The most significant result in the single device investigation has been the characterization of the hysteresis as a basic conduction bistability with a random telegraph signal (RTS). This result has been confirmed in the high bias regime by other groups in an offset split gate [Smith] and a deeply etched lateral barrier [Pilling]. Random telegraph signals have been observed in quantum devices near equilibrium [Dekker][Timp][Sakamoto] and have been attributed to the fluctuations of a single or small number of nearby impurities. Many of our results are consistent with this interpretation, however the exponential dependence of the bistable state lifetimes t_{high}, t_{low} as a function of source drain bias has not been measured before, and remains difficult to interpret

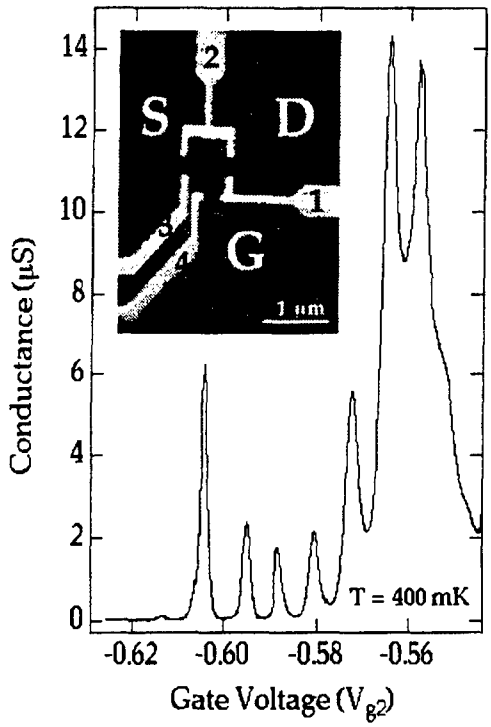

Figure 7: Coulomb blockade oscillations in a three lead dot. The inset shows the SEM picture of the device. Top gates are numbered from "1" to "4". "G", "D" and "S" denote the semi-infinite leads can be used interchangeably as "Source", "Drain" and "Leakage Channel". The result shown here is obtained by varying the voltage on gate "2", and keeping the others constant.

within the impurity model. The very strong control effected by the back gate voltage on switching times is likewise unexplained.

The multi-stability displayed in some of the CVD etched devices (Figure 6) is more typical of fluctuations due to impurities. Yet in this case as before there is an exponential bias dependence of lifetimes, and indeed under controlled circumstances an evolution from bistable on-off switching to multi-stable on-on transitions.

Voltage dependent random telegraph signals have been observed in submicron MOSFET inversion layers and 4μm diameter resonant tunnel diodes [Ralls][Ng]. In each case the dependence of the RTS is attributed to the physical position of a switching impurity and it's bias defined energy with respect to a local Fermi level. In our devices the voltage dependence scale is much smaller - the state lifetimes can vary by two orders over only 500 μV of applied bias, inconsistent with the above explanation.

3. Conclusions and Future Work

The cause of the conduction instability remains unclear. Strong qualitative similarities to impurity switching results are contradicted by the exponential voltage dependencies of the state lifetimes. However, we have already been able to demonstrate remarkable control over the character of the instability as it manifests in the I-V relation using both front and back gate potentials. Further probing of this control should lead to a physical explanation of the switching and hysteresis.

We will continue with a series of measurements characterizing the transition from the well understood equilibrium regime to our high bias non-equilibrium situation. Quantitative dependencies of the state lifetimes as a function of gate voltages, applied bias and temperature across this transition are required. Similar measurements on our split gate devices will quantify the relevance of the surfaces and associated imperfections in the etched devices, and direct future fabrication towards the most robust architecture.

With these results in hand, we will return to the performance of the single device arrays, densely packing the point contacts and quantum dots into 1D and 2D arrays. Single and coupled device behavior can then be separated and accurately characterized. This knowledge will form the design framework of future single electron architectures in this regime.

4. References

[Beenakker] C. W. J.Beenakker *et al., Phys. Rev. B* 44, 1646 (1991)

[Dekker] C. Dekker *et al., Phys. Rev. Lett.* 66, 2148 (1991)

[Duruöz] C. I. Duruöz *et al., Phys. Rev. Lett.* 74, 3237 (1995)

[Harris] J. S. Harris Jr. *et al., JSEP Annual Report* (1994-1995)

[Kouwenhoven] L. P. Kouwenhoven *et al., J. Phys. B - Cond. Matt.* 85, 367 (1991)

[Ng] S.-H. Ng *et al., Appl. Phys. Lett.* 62, 2262 (1993)

[Pilling] G. Pilling *et al., Proceedings EP2DS XI* 347 (1995)

[Ralls] K. S. Ralls *et al., Phys. Rev. Lett.* 52, 228 (1984)

[Sakamoto] T. Sakamoto *et al., Appl. Phys. Lett.* 67, 2220 (1995)

[Smith] J. C. Smith *et al., Proceedings EP2DS XI* 351 (1995)

[Timp] G. Timp *et al., Phys. Rev. B* 42, 9259 (1990)

5. JSEP Supported Publications

1. C. I. Duruöz, R. M. Clarke, C. M. Marcus and J. S. Harris Jr., "Conductance Threshold, Switching and Hysteresis in Quantum Dot Arrays," *Phys. Rev. Lett.* 74, 3237 (1995).

2. C. I. Duruöz, D. R. Stewart, C. M. Marcus and J. S. Harris Jr., "Switching and Hysteresis in Quantum Dot Arrays," *Proceedings EP2DS XI* 349 (1995).
3. G. Pilling, D. H. Cobden, P. L. McEuen, C. I. Duruöz and J. S. Harris Jr., "Intrinsic Bistability in Nonlinear Transport Through a Submicron Lateral Barrier," *Proceedings EP2DS XI* 347 (1995).
4. G. S. Solomon, C. I. Duröz, C.M. Marcus and J. S. Harris, Jr., "Growth Induced and Patterned 0-Dimensional Quantum Dot Structures" in Low Dimensional Structures Prepared by Epitaxial Growth or Regrowth on Patterned Substrates, ed. by K. Eberl et al., NATO ASI Series E, Applied Sciences 298.

6. JSEP Supported Ph. D. Thesis

C. I. Duröz, "Low Temperature Transport in Quantum Dot Arrays", Ph. D. Thesis, Stanford University, March, 1996.

UNIT: 2

TITLE: Patterned Thin Film Media for High Density Magnetic Recording

SENIOR INVESTIGATOR: R. F. W. Pease

RESEARCH STUDENT: R. M. H. New

Background

In conventional hard-disk magnetic recording systems, the signal to noise ratio is often limited by "transition" noise which occurs due to the irregular zig-zag domain walls between adjacent recorded bits [Tong]. In order to address this problem, we are studying recording media composed of large arrays of submicron lithographically defined single-domain magnetic islands. It is known both from theoretical arguments and from experiments that sufficiently small magnetic particles are uniformly magnetized and contain no domain walls. If a single-domain particle of this type has a single uniaxial easy axis of magnetization then it will have only two possible magnetization states and will be ideal for storage of a single bit of information. A magnetic recording medium consisting of an array of equally spaced and uniformly shaped single-domain islands with predictably oriented easy axes could serve as a virtually noise-free alternative to the unpatterned magnetic thin films used in conventional hard disk systems. The ultimate theoretical storage density for such a system would be limited only by the spontaneous thermal switching of bits, a problem that would occur only for particles one hundred angstroms in diameter or less.

In a previous contract period we developed a procedure for patterning polycrystalline magnetic thin films using direct-write electron beam lithography and a multi-step masking and milling process [New (a)]. We used this procedure to define large arrays of 0.15μm by 0.2 μm cobalt islands and studied the physical properties of these islands using atomic force, scanning electron and transmission electron microscopy. The magnetic properties were examined with both magnetic force microscopy and bulk hysteresis loop measurement techniques [New (b)].

For those initial experiments we patterned magnetic islands out of a 200-Å-thick polycrystalline cobalt film. Our results indicated that the transition from the multidomain to single domain state occurs at an island diameter of roughly 0.2mm. The magnetic force microscopy images of these islands showedthat these islands were not single domain. However, smaller islands, roughly 0.15mm by 0.2mm in size, were almost all single domain. Transmission

electron microscopy images of the patterned polycrystalline islands indicated that there were roughly 200 cobalt grains per island, each of which has an easy axis of magnetization randomly oriented in the plane of the film. For islands with only a few hundred grains or less, the magnetocrystalline anisotropies of the individual grains may not completely average out and the net magnetocrystalline anisotropy may be larger than the shape anisotropy for some island geometries. Our calculations indicated that for the island geometries we are using, there is a significant probability that the net easy axis may be misaligned with the long axis of the island [New (c)], and our initial experiments confirmed this. Such unpredictably oriented easy axes would cause problems in a single-bit-per-island recording scheme.

One problem with polycrystalline magnetic recording films, either patterned or unpatterned, is that the fundamental unit of magnetization (typically a single grain or grain cluster of 100 to 500 Å in diameter) is not much smaller than the size of a single recorded bit. For a state of the art 1Gbit/in^2 recording system, there may be only a hundred grain clusters or less per bit. Because the medium is so coarsely discretized, conventional magnetic recording systems suffer from increasing signal to noise problems as recording densities are increased. Medium noise is already the most important component of noise in recording systems that use magnetoresistive readback heads.

One solution to this problem is to switch to a recording medium which is homogeneous over the size range of a single recorded bit. Sputtered single crystal films would provide a more controllable and predictable magnetic behavior when examined at this size range, and patterned islands of single crystal material would not suffer from the problem of randomly oriented easy axes discussed above. One of the major advantages of the patterning technique that we have developed is that, unlike a lift-off process, it can be used to pattern single crystal thin films. In preparation for future experiments we have sputter-deposited single crystal iron films on sapphire substrates and measured their magnetic and structural properties. These films show good epitaxial quality and have a predictably oriented uniaxial anisotropy as required.

Progress during the current Year

During the last year we successfully patterned such films into islands with lateral dimensions ranging from 100nm to several microns, using techniques not dissimilar to those used for patterning the cobalt. The resulting islands were examined using a variety of techniques including SEM, AFM, alternating gradient magnetometer (Princeton Measurements Corp.) and vibrating sample magnetometer (Kobe Steel). In all cases the islands were single crystal. This included islands up to several microns long and with high aspect ratios with the long axis at a

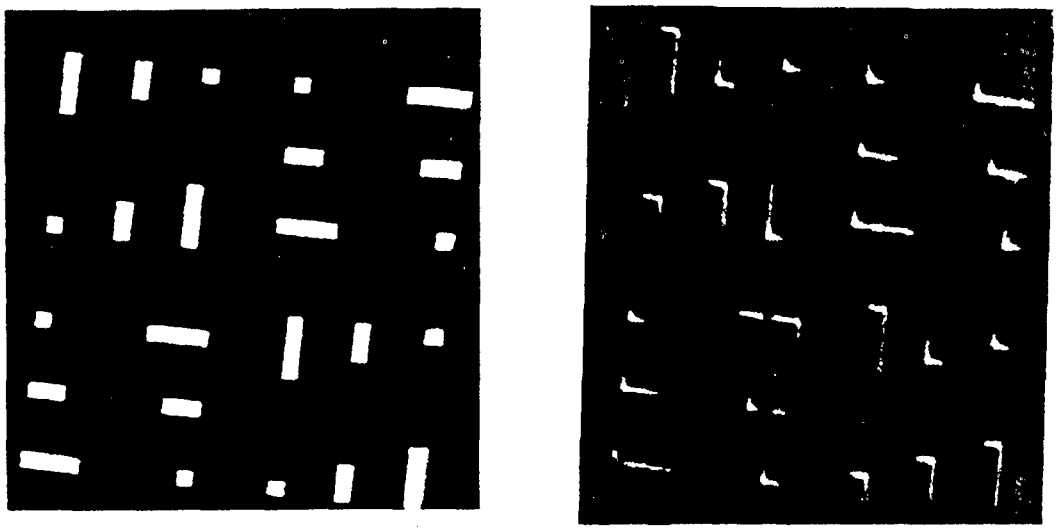

(a) (b)

Figure 1: Topographical (a) and magnetic (b) images of single-crystal iron islands with a smallest feature size of 1.0 microns. Even the largest islands (up to 1.0 by 3.0 microns) are single domain.

variety of orientations (Fig. 1). All of the islands had their easy axis aligned with the surface anisotropy of the film thus we were able to control simultaneously the crystallographic orientation and the shapes of the islands and hence compare the relative strengths of magnetocrystalline and shape anisotropy of these islands. In addition to this scientific advantage it is important technically to have the easy axis across the long direction of the islands because it allows for more efficient coupling of the medium to the read/write head. This can be accomplished when crystal orientation is the dominant factor governing easy axis direction; if shape anisotropy dominated then the easy axis would be along the long direction.

We have also, in collaboration with University of Maryland, been able to examine these islands in a magnetic contrast AFM while applying an external field and observe the external field necessary to switch each island (Fig. 2). By examining a large population of islands under these conditions we were able to predict quantitatively the shape of the magnetization loop of the complete sample. This prediction turned out to be accurate thus confirming the our model of the contrast mechanism for the magnetic contrast AFM.

We have developed a preliminary model for the reduction in transition jitter that might be expected if we employed a patterned recording medium. Current recording systems suffer from a transition jitter described as a standard deviation σ_τ of the transition point of about 5nm for a track width of 3μm. Narrower track widths will show worse jitter because of the lower number of grains being averaged over. With a patterned medium we might expect the jitter to be consistent with the edge roughness when averaged over the length of the island and this could well be a factor of 4 lower. More comprehensive models would have to consider the particular form of read head used and the signal extraction algorithms used.

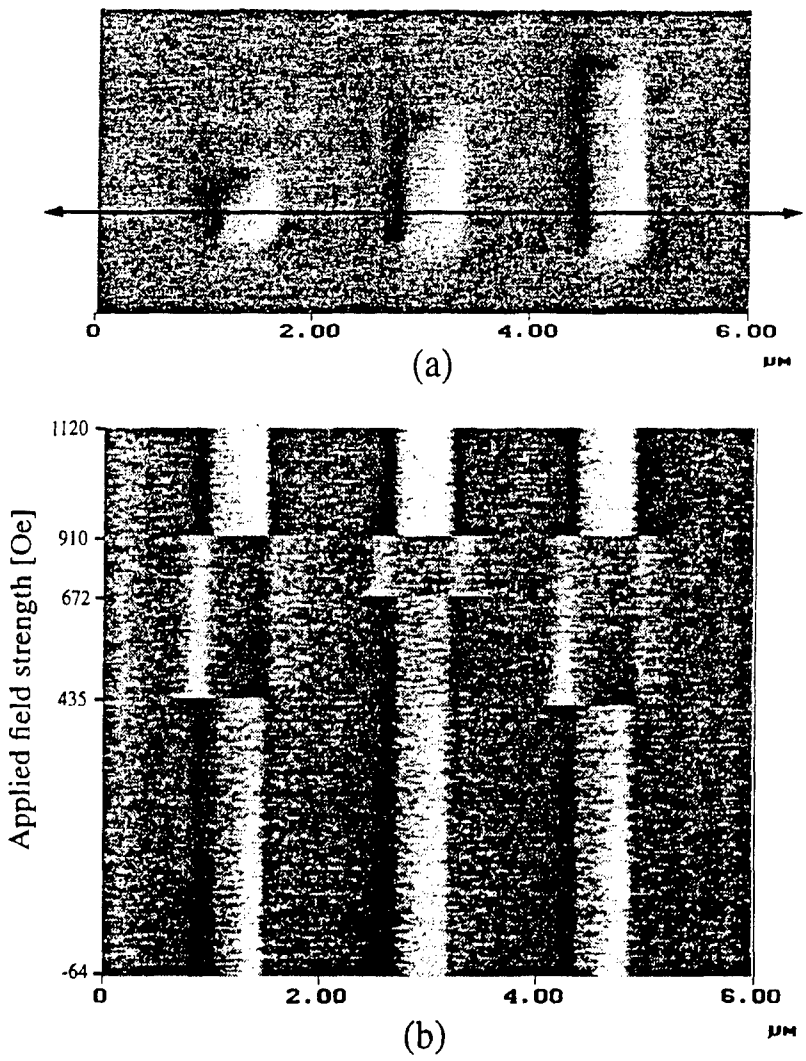

Figure 2: Figure (a) shows a magnetic force image of three islands, each with a width of 0.5μm, but with different lengths. In Figure (b), the vertical scan direction has been turned off, and the magnetic tip moves back and forth along a horizontal line (<------>) as the externally applied field from the electromagnet is ramped up. The filed is applied within five degrees of the easy axis of magnetization. Both the electromagnet and the islands are initially in a saturation remanent state (at the bottom of (b)). As the field is increased, the left and right islands are the first to reverse their magnetizations (at 435 Oe) followed by the center island (at 672 Oe). At 910 Oe, the magnetization of the tip reverses so as to align itself with the applied field.

During the reporting period the student, Richard M. H. New, completed his PhD. requirements and graduated and is now at the IBM Almaden Research Center San Jose CA. His dissertation, "Patterned Media for High Density Recording", was approved in September 1995 and copies are available.

References

[New (a)] R. M. H. New, R. F. W. Pease, R. L. White, *J. Vac. Sci. Technol. B*, **6**, 3196, Nov/Dec 1994.

[New (b)] R. M. H. New, R. F. W. Pease, R. L. White, *J. Vac. Sci. Technol. A*, May/June 1995.

[New (c)] R. M. H. New, R. F. W. Pease, R. L. White, submitted to IEEE International Magnetics Conference, April 1995.

[Tong] H. C. Tong, R. Ferrier, P. Chang, J. Tzeng and K. L. Parker, *IEEE Trans. Mag.*, **20**, 5, 1831 (1984).

JSEP Supported Publications

1. "Magnetic force microscopy of single-domain single-crystal iron particles with uniaxial surface anisotropy," R. M. H. New, R. F. W. Pease, R. L. White, R. M. Osgood, K. Babcock, to be published in the *Proceedings of the 40th Annual Conference on Megnetism and Magnetic Materials (J. Appl. Phys.)* held in Philadelphia, Nov. 1995.
2. "Lithographically patterned single domain cobalt islands for high density magnetic recording," R. M. H. New, R. F. W. Pease, R. L. White, to be published in the *Proceedings of the 6th International Conference on Magnetic Recording Media (J. Magn. Mag. Mater.),* held in Oxford, England, July 1995.
3. "Effect of magnetocrystalline anisotropy in single-domain polycrystalline cobalt islands," *IEEE Trans. Mag.*, MAG-31, p. 3805, Nov. 1995.

JSEP Support Thesis

"Patterned Media for High Density Magnetic Recording," R. M. H. New, Ph.D. Thesis, Stanford University, September, 1995.

UNIT: 3

TITLE: Investigation of a Metal Source and Drain Field Emission Transistor

PRINCIPAL INVESTIGATOR: C. R. Helms

GRADUATE STUDENT: J. P. Snyder

Background

Metal source and drain Metal-Oxide-Semiconductor-Field-Effect-Transistors (MOSFETs) have been shown to have several key advantages over their conventional (doped source and drain) counterparts including ease of fabrication and unconditional immunity to parasitic bipolar and latch-up effects. They were first investigated in the late 1960s [Lepselter], and were thought to have certain advantages over their conventional (diffused source and drain) counterparts including a simplified process, the ability to make very shallow source and drain regions, low source and drain sheet resistance, and complete immunity to latch-up and parasitic bipolar effects. They proved to be poor performers however when compared to a similarly sized conventional MOSFET. The lower drive current in the 'on' state was attributed to the presence of a finite 'gap' between the edge of the poly gate and the edge of the platinum silicide (PtSi) source metal. The much higher leakage currents in the 'off' state originate at the drain end of the device, where electric fields cause the thermally assisted field emission of electrons from the drain into the silicon [Lepselter] [Oh] [Koeneke] [Sugino] [Tsui].

Until recently, the low temperature characteristics of these devices have not been investigated. The only exception to this is a 1968 paper [Lepselter] in which 77 K I-V curves are shown and briefly discussed. Their device was fabricated with a non-self aligned, chemical vapor deposition (CVD) gate oxide process. The data shows a significant *decrease* in current drive at 77 K compared to room temperature.

Since 1993, several papers [Tucker] [Hareland] have reported on simulations on these and similar devices, and have shown acceptable drive current and short channel effects in devices with channel lengths down to 0.025 mm. The scalability of these metal source and drain devices is particularly impressive at low temperatures (77 K), as described by [Tucker]. It seems possible in

light of these recent studies to build a metal source and drain device that has all the advantages previously mentioned, as well as superior scalability to well below 0.1 μm and free of the low drive and high leakage current problems. The only requirement is low temperature operation.

Progress during the current Year

We report the first detailed experimental investigation of the low temperature, field emission characteristics of PtSi source and drain MOSFETs. I-V curves have been measured at

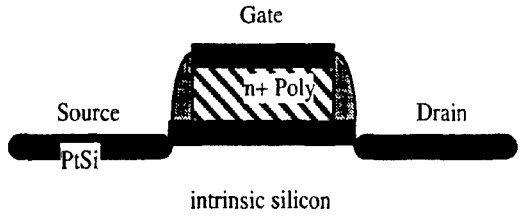

Figure 1: Schematic Diagram of the Device.

various temperatures down to 4.2 K and for channel lengths down to 1 μm. Device fabrication has been optimized so that it is free from the 'gap' at the poly edge described earlier. As will be discussed, we observe a definite transition in the current flow mechanism of the device, from thermal to field emission, as the temperature is reduced below 100 K. In this low temperature 'field emission mode', the drive current when the device is 'on' is comparable to that of a conventional MOSFET, and short channel effects are not observable down to 1 μm, despite the fact that the substrate is nominally undoped. The schematic diagram of the device is shown in Fig. 1.

The band diagrams of Fig. 2 demonstrate the operating principle of the device described in figure 1 at an intermediate temperature (~150 K) such that the various current flow mechanisms are observable. The band diagrams are drawn along a line from source to drain, just underneath the gate oxide, and show the Fermi levels of the source and drain PtSi, as well as the conduction and valence bands of the silicon substrate.

In Fig. 2(a), when the device is in its 'off' state with bias applied only to the drain, hole leakage current enters the channel by thermal emission over the sum of the 0.2 eV Schottky barrier and an electrostatic barrier present because of the difference in workfunction between the n+ polygate and the PtSi source. In this domain of gate voltage (V_g), the thermal emission regime, holes flow by diffusion from source to drain and the silicon bands in the channel are flat. Changing the gate voltage simply changes the amount of hole thermal emission current entering the

channel, as is seen in the 'thermal emission characteristic' drawn in the plot of source current (I_S)

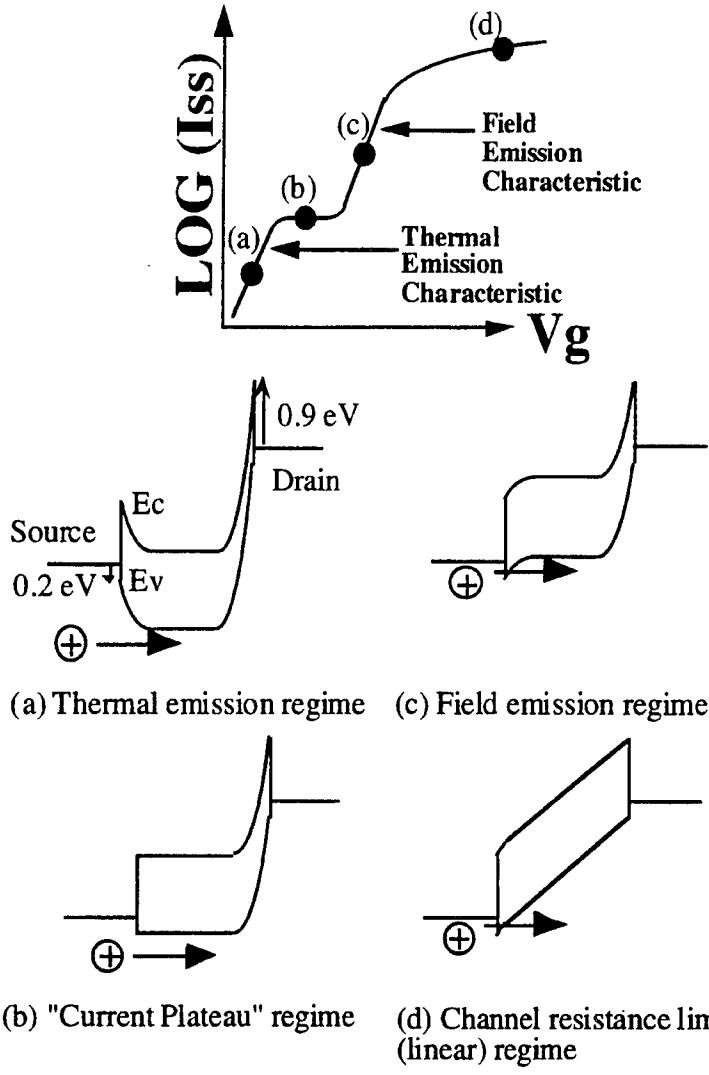

Figure 2. A band diagram description of the different current flow regimes seen in a typical source current vs. gate voltage plot. (a) Thermal emission regime (b) "current plateau" regime (c) field emission regime and (d) channel resistance limited regime.

vs. V_g. There is also the possibility of electrons being field emitted from the drain because of the high electric fields there, but this component of current does not show up in our measurements of source current and will not be discussed in this report.

Eventually, with increasingly negative gate bias, only the fixed Schottky part of the barrier to holes remains and the current is limited by thermal emission over this barrier [Fig. 2(b)]. In this

'current plateau' regime further increases in the magnitude of the gate voltage cease to have an exponential effect on Is. The hole current is, for the most part, dependent only on the temperature and the barrier height (~ 0.2 eV), as is drawn in the topmost plot.

With high enough gate bias, holes eventually can be made to tunnel through the Schottky barrier and Is once again begins to increase in an exponential fashion, this time along a 'field emission characteristic' [Fig. 2(c)]. The current is not yet large enough to give the silicon bands in the channel appreciable slope, which is to say that the current is still field emission limited and still travels by diffusion from source to drain, and is not yet channel resistance limited.

Finally I_s becomes large enough that the channel resistance begins to dominate and the holes travel by drift [Fig. 2(d)]. In this regime of V_g the current drive of the device is similar to that of a conventional MOSFET as the Schottky barrier has been rendered all but transparent to the flow of holes.

Drain curves (I_s vs. drain voltage (Vd)) and gate curves (I_s vs. V_g) were measured with a computer controlled HP 4140B DC voltage source/pA meter. A Lakeshore cryogenic probe station was used to perform measurements down to 4.2 K.

Figure 3(b) shows the experimental gate curves of the device described in Figs. 1 and 2 with width=length=2 μm. Here the thermal emission, plateau, field emission and channel resistance limited regimes are clearly seen, especially for the 200 K curve. As was mentioned previously, the plateau current is solely a function of temperature and barrier height and this dependence is observable. The plateau current drops exponentially with temperature, so that for temperatures less than about 100 K, all significant current flow (> 0.1 pA) occurs by the process of field emission and the device is being operated in the 'field emission mode'. It can be seen that this field emission characteristic is largely independent of temperature. Because n+ poly is used for the gate material, V_g must be brought to about -2 Volts before significant current begins to flow. Referring back to Fig. 2, this implies that even the band diagram in Fig. 2(c) could be used as an effective 'off' state. This could be realized for example, if p+ poly were used for the gate. The Schottky barrier alone is responsible for preventing the flow of current into the channel and thus it is clear why substrate doping is not required.

It is also possible to back out the effective PtSi - Si barrier height to holes from the thermal emission formula $I = AA^*T^2Exp(q\varphi_b/kT/(kT/q))$ using the plateau currents and corresponding

temperatures. This formula gives a barrier of ~0.195 eV, in very good agreement with published

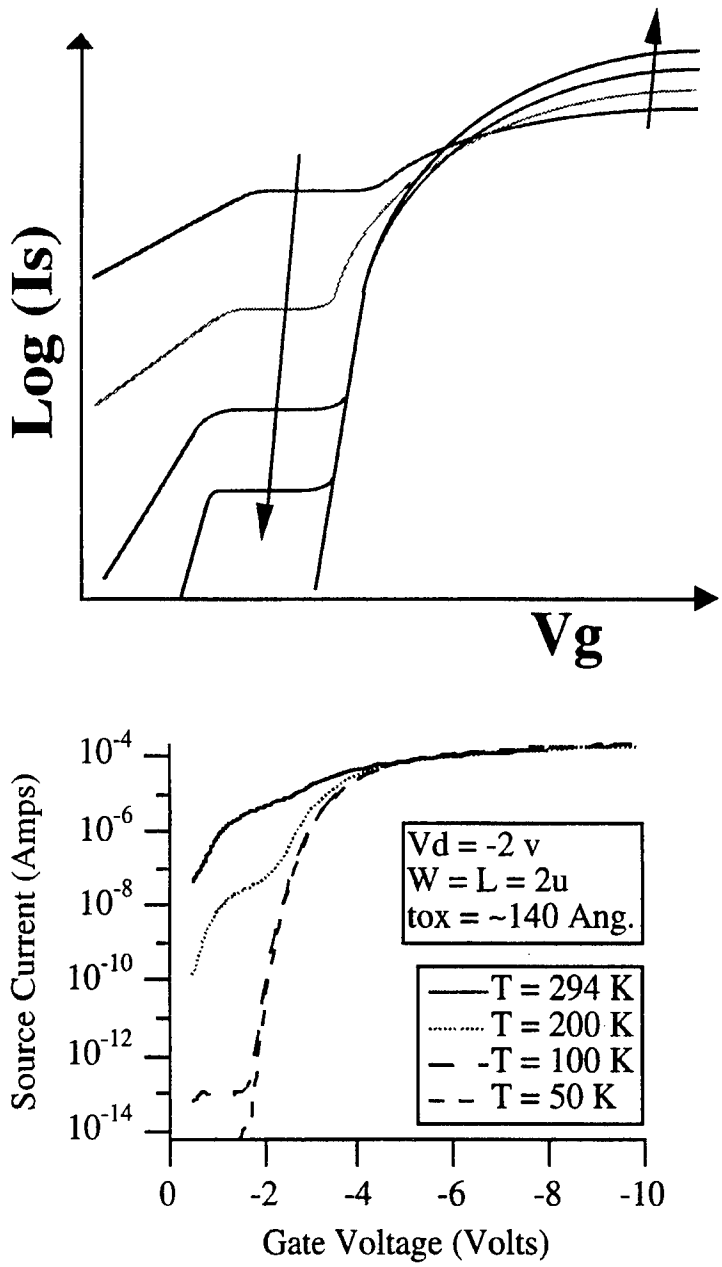

Figure 3. Variation with temperature (a) qualitative example showing the major effects of temperature variation on the gate curves of a PtSi source and drain MOSFET. The arrows point in the direction of decreasing temperature. (b) Actual measured data of a device described in (a).

barrier heights of the PtSi - Si system [Mooney] [Weeks].

During the last year also developed a full 2-D Poisson solver which is integrated with first principles tunneling calculations in order to theoretically examine the effects of device geometry (tip sharpness, channel length, and gate oxide thickness) and materials and system parameters (Schottky barrier height and temperature) on the hole and electron field emission characteristics. The subthreshold slopes of these characteristics were found to decrease monotonically with gate oxide thickness with no theoretical limit. This is in contrast to the theoretical limit, defined by temperature, that exists for the subthreshold region of a conventional device. Subthreshold current levels were also found to be generally smaller than those of conventional devices by several orders of magnitude. Shallow source/drain junctions with sharp tips were found to be optimal in terms of promoting hole field emission drive currents and controlling Drain-Induced-Barrier-Thinning (DIBT) hole leakage currents. Low barrier heights (for good drive currents) and low temperatures (for low leakage over the low barrier) were also found to be optimal.

Possible Future Directions

These devices will be investigated further. Shallower junction, p+ poly, no gap devices (unlike the ones studied in this dissertation) will be investigated especially with regard to drive current and electron leakage current. NMOS devices can be built as long as metal-silicon Schottky diodes with low barriers to electrons can be found. Rare-earth silicides are potential candidates for this application. Finally, full 2-D modeling of these field emission devices with integrated tunneling and hot-carrier models will be used to further explore the 'virtual source voltage' phenomena described in Chapter 8 of J. P. Snyder's Ph.D. thesis, and to determine the effects of this phenomena on device long term reliability.

References

[Hareland] S. A. Hareland, A. F. Tasch, C. M. Maziar, *Electronics Letters*, **29**, 1894 (1993).

[Hareland] S. A. Hareland, A. F. Tasch, C. M. Maziar, *Proceedings of the 21st International Symposium on Compound Semiconductors*, September 18-22, San Diego, CA (1994).

[Koeneke] C. J. Koeneke, S. M. Sze, R. M. Levin, E. Kinsbron, 1981 IEDM, 367.

[Lepselter] M. P. Lepselter, S. M. Sze, *Proceedings of the IEEE*, 1400 (1968).

[Mooney] J. M. Mooney, J. Silverman, M. M. Weeks, *SPIE, Infrared Sensors and Sensor Fusion*, **782**, 99 (1987).

[Oh] C. S. Oh, Y. H. Koh, C. K. Kim, 1984 IEDM, 609.

[Sugino] M. Sugino, L.A. Akers, M.E. Rebeschini, 1982 IEDM, 462.

[Tsui] B. Tsui, M. Chen, *J. Electrochem. Soc.*, **136**, 1456 (1989).

[Tucker] J. R. Tucker, C. Wang, J. W. Lyding, T. C. Shen, G. C. Abeln, *1994 SSDM*, 322.

[Tucker] J.R. Tucker, C. Wang, P.S. Carney, *Appl. Phys. Lett.*, **65**, 618 (1994).

[Weeks] M. M. Weeks, P. W. Pellegrini, SPIE, Test and Evaluation of Infrared Detectors and Arrays, **1108**, 31 (1989).

JSEP Supported Publications

J. P. Snyder and C. R. Helms, Y. Nishi, "Experimental investigation of a PtSi source and drain field emission transistor," *App.Phys.Lett.* **67**(10), 4 September 1995.

UNIT: 4

TITLE: On-Chip Thin Film Solid State Micro-Battery

PRINCIPAL INVESTIGATOR: S. S. Wong

GRADUATE STUDENT: J. Leung

Scientific Objectives

The objectives of this work are to develop the fabrication technology and characterize the performance of thin film solid state micro-batteries that are suitable for monolithic integration with semiconductor devices.

Summary of Research

In the last phase of this research, we successfully fabricated and tested solid-state micro-batteries on a silicon substrate. Charging and discharging up to 1000 cycles were demonstrated. In addition, we identified a suitable diffusion barrier, PECVD oxynitride, that can prevent the lithium ions from penetrating down to the devices in the substrate.

Encouraged by the experimental results, we have designed various circuits to be integrated with the micro-batteries. These circuits include charging and discharging control units, various temperature sensors, and voltage controlled oscillators. Figure 1 shows a basic charging circuit. Both constant and pulse current charging are amongst the various charging modes to be studied. We have also taken into account the possibility of circuit leakage. Simulation indicates that the leakage current should be less than 3 pA when the micro-battery is fully charged to above 2V. Both internal resistance and capacitance of the battery are included in the modeling. The basic op amp is capable of operating in the high MHz range while delivering 200 uA. In addition, various temperature sensors will be placed on chip. The close proximity of these sensors to the battery will yield accurate thermal profile which will be important in the design of large integrated circuits.

We will also incorporate a voltage controlled oscillator (VCO). The VCO operates off the on-chip battery and can be programmed with an external signal. Simulation has indicated that the VCO can run up to 1 MHz. The excellent voltage stability of the micro-battery will be ideal for applications such as frequency synthesizer which requires VCO with an excellent power supply rejection ratio. Noise at VCO is often difficult to be filtered out in a frequency synthesizer, and is the factor that determines channel spacing criteria [Mannasiwitsch].

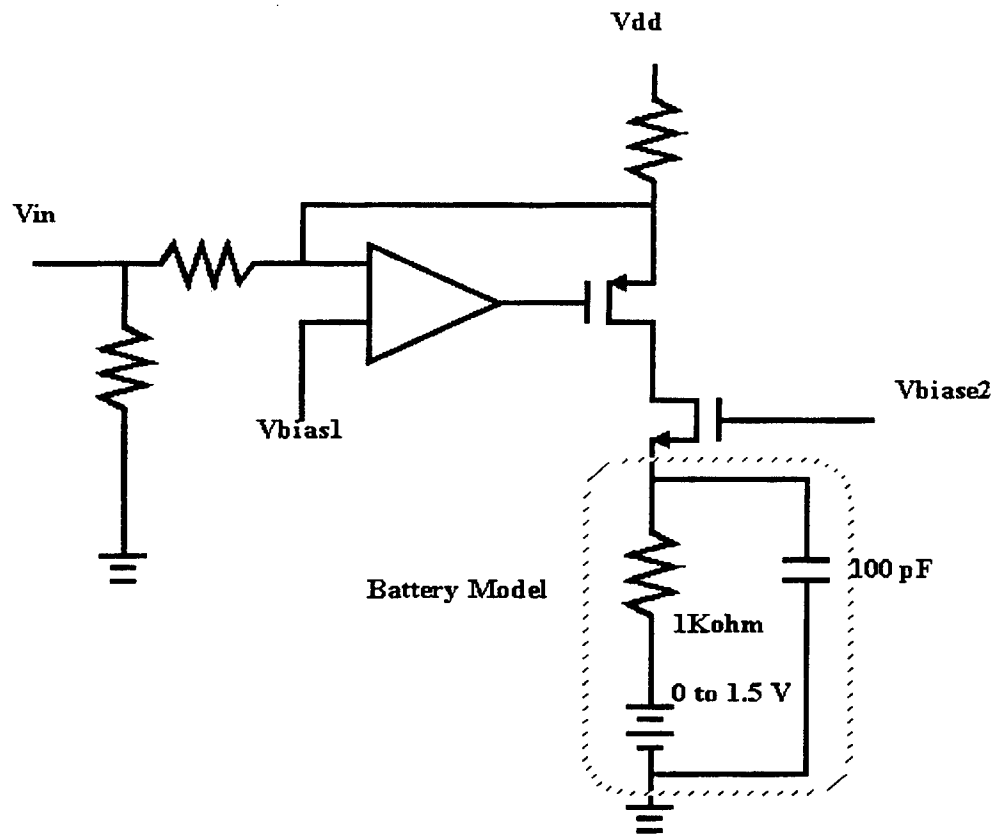

Figure 1. Basic charging circuit.

Figure 2 illustrates the sequence for monolithic integration. The circuits will be first fabricated with a conventional CMOS technology. Afterwards, a layer of silicon oxynitride passivation layer will be deposited using plasma enhanced chemical vapor deposition (PECVD). Lastly, the various layers for the lithium battery will be sputtered on.

The circuits will be fabricate on 4-inch wafers in a 2 μm CMOS technology. Individual die size is limited to about 8 μm by 8 μm. Ten micro-batteries will be sputtered on each wafer. Each battery will be about 1 cm by 1 cm and with a charge capacity of about 1 Coulomb. An overview of the wafer is shown in Fig. 3.

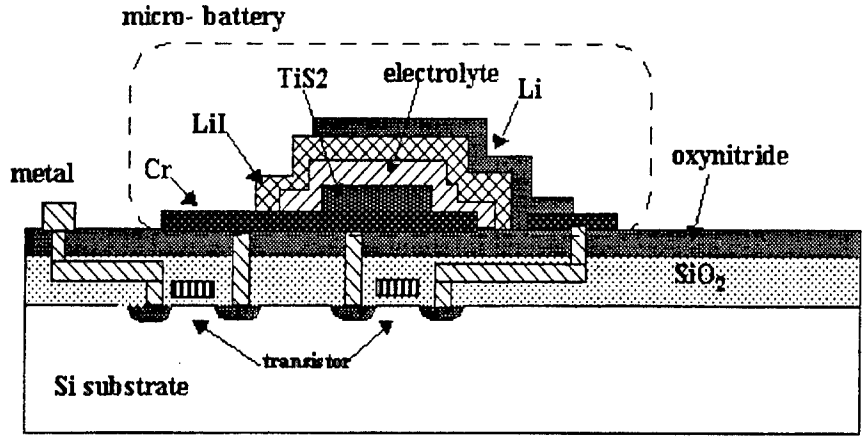

Figure 2. A cross section of the integrated micro-battery.

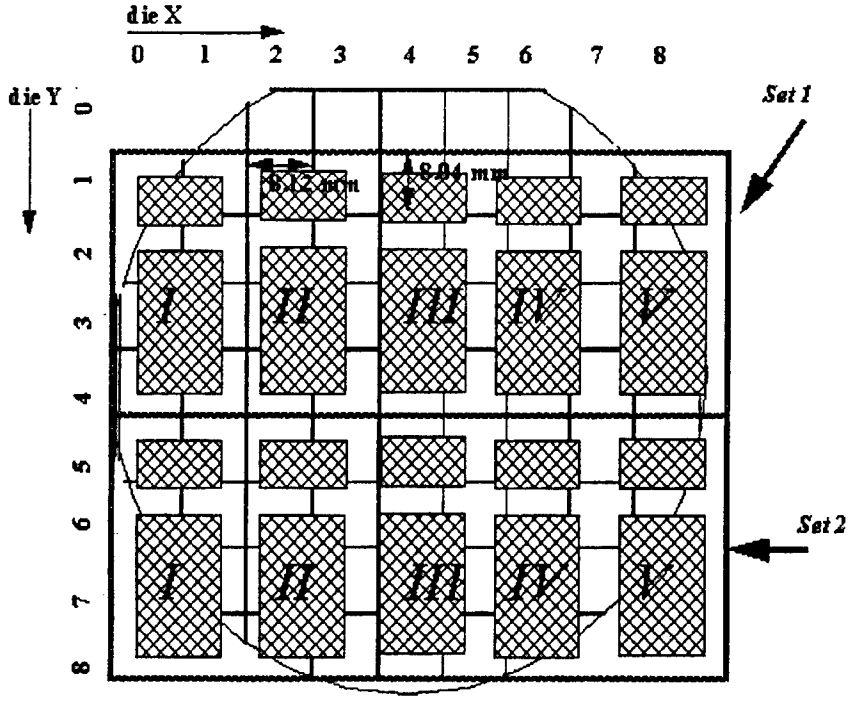

Figure 3. Placement of micro-batteries on a four-inch wafer.

The fabrication will commence shortly. We aim at not only demonstrating the feasibility of such a full integration, but also performing on-chip characterization.

References

[Mannasiwitsch] V. Manassewitsch, Frequency Synthesizer, Wiley, 3rd Edition.

UNIT: 5

TITLE: CVD Epitaxial Germanium *n*-Channel FETs Formed on Si Substrates using Strain-relief Layers

PRINCIPAL INVESTIGATOR: K. Saraswat

GRADUATE STUDENT: D. Connelly

Abstract

N-channel field effect transistors are fabricated in strained and unstrained Ge grown via graded-alloy strain reduction on (001) silicon substrates. Applications of Ge device integration with silicon substrates are discussed. Blanket graded-alloy epitaxy is compared with other strain reduction techniques. The effect of strain on the Ge conduction band structure and hence on electron transport in the *x-y* plane is examined.

Objectives

The following are the primary objectives of this project::

- To fabricate *n*-type Ge-channel MOSFETs on a Si substrate.
- To investigate the effect of different degrees of compressive strain on the electron transport properties in germanium inversion layers.
- To compare different schemes for the formation of strain-relief structure formation including blanket graded epitaxy, selective graded epitaxy, and graded epitaxy on ultra-thin silicon-on-insulator.
- To assess the utility of high-germanium content *n*-channel MODFETs in high-speed transistor applications.

Prior Art

The development of strained layer epitaxy of GeSi alloys on silicon substrates sparked interest in the development of heterostructure devices using silicon-based technology. Much of the work can be placed in one of two categories, vertical heterostructure bipolar transistors (see for example [King]), in which the primary interest is the band-gap difference between the base alloy and the emitter alloy, and confined-carrier field-effect devices (see for example [Pearsall86] and [Daembkes]) in which the parameter of interest is the conduction band offset (for *n*-channel devices) or the valence band offset (for *p*-channel devices).

The biaxial compressive strain formed when GeSi with non-zero x is deposited on silicon enhances the natural positive valence band offset of the GeSi relative to silicon [Pearsall89]. Representative is the work by the group from UCLA [Nayak] in which a 10 nm "undoped" unstrained silicon layer is deposited on an n-type Si substrate. An undoped 15 nm strained $Ge_{0.20}Si_{0.80}$ layer is then deposited to form the channel region. It is capped with a 10 nm silicon layer. A 5 nm SiO_2 layer is then thermally grown to form the insulator, consuming some of the underlying silicon. The structure is capped with a polycrystalline silicon gate electrode. The estimated 0.15 eV valence band discontinuity confines most of the holes to the $Ge_{0.20}Si_{0.80}$ layer for the initial portion of the superthreshold gate bias regime. The Princeton group [Garone] fabricated a similar structure with a 10 nm $Ge_{0.40}Si_{0.60}$ well capped by a 7.5 nm silicon spacer and a 10 nm gate oxide with an aluminum gate electrode.

For electron-confinement structures things are more complicated. For unstrained material of low-to-moderate germanium concentrations the conduction band consists of six degenerate ellipsoids aligned along the x, y, and z axes in momentum space. For material under [001]-directed strain the degeneracy is broken --- the z-directed ellipsoid is either raised or lowered in energy relative to the x and y valleys. Since the z valley exposes its carriers during conduction in the x-y plane to only the light transverse effective mass it is preferable to raise the energy and thereby reduce the carrier population of the x and y ellipsoids. This is done by depositing the channel material in biaxial tension.

Reported work to date has been on structures utilizing strained silicon as the channel material. Representative is the work from Stanford [Welser]. They had two forms of their device. One started with a relaxed (001) $Ge_{0.30}Si_{0.70}$ surface on which was grown a strained silicon layer. Subsequent oxidation of the silicon resulted in a 12.8 nm gate oxide over a 4.6 nm strained silicon channel well. The other used a $Ge_{0.29}Si_{0.71}$ surface on which was grown an 8.0 nm strained silicon layer covered with a 7.2 nm $Ge_{0.29}Si_{0.71}$ spacer and a "sacrificial" strained silicon cap. Thermal oxidation to form the 12.8 nm gate oxide fully consumed the cap. Thus the former devices had surface channels while the latter had buried channels for moderate superthreshold biases.

IBM has published results of Schottky-gated n-channel structures using both Molecular Beam Epitaxy and Ultra High Vacuum Chemical Vapor Deposition (UHVCVD) [Ismail] [Wang]. They used a starting relaxed surface with a 30% germanium content. Their channel was formed in a 10.6 nm strained silicon layer.

The key difficulty in the formation of these structures is the preparation of the initial surface. Ideally if a surface of a given alloy composition is needed a wafer of that composition should be used. Unfortunately wafers of arbitrary germanium content are not available --- silicon wafers are widely available and germanium wafers are available at considerably higher cost. A solution is to deposit a relaxed "buffer layer" in which threading dislocations are isolated below the surface to translate the surface composition to the desired value from what is on hand. Leaders in this technique include AT&T with Molecular Beam Epitaxy and IBM with CVD and MBE. All reference cases described here begin with (001) silicon wafers.

In reference [Fitzgerald] AT&T reports the results of linearly grading the germanium content from zero up to 53% using MBE at 900 C. The alloyed germanium content is ramped at 0.1 per micrometer. The high temperature is used to prevent the accumulation of stress in their films before relaxation events, increasing the number of threading dislocations and canceling the benefits of compositional grading. They fabricate ungated electron confinement structures [Xie] with good results. Other workers [Schaffler] showed that increasing the gradient to 0.45 per micrometer and decreasing the deposition temperature to 750 C can still yield significant advantage over abruptly stepped buffer layers.

IBM has generated strain-relief layers using both continuous grading as per AT&T (see [Legoues91] and grading in discretized steps [Meyerson] using both MBE and CVD. In reference [Tsang] step-grading from pure silicon to pure germanium with fewer than 0.01 threading dislocations per square micrometer in the top germanium film is reported. The deposition is done using UHVCVD with composition graded in 40 steps at approximately 0.20 per micrometer. The quality of the film is sensitive to the deposition temperature, with 450 C optimal for the pure-germanium portion. This is described in reference [Legoues92].

The Stanford group [Welser] used, for example, a graded layer of germanium composition from 6% to 30% continuously graded over 1.6 μm deposited via CVD using "Limited Reaction Processing" at 750 C. They had difficulty grading beyond 50% germanium starting from pure silicon using their technique, although IBM's positive results show it can be done.

Background

Single-crystal GeSi alloy exhibits a peak valence band energy that increases steadily with increasing Ge content. The energy of the sixfold-degenerate *X* (used here to signify all six <100> directions) conduction band valleys is relatively insensitive to the Ge content in unstrained material. Up to approximately 80 atomic-percent Ge these *X*-valleys have the lowest energy of the

conduction states in the material. At higher Ge concentrations, however, the strong alloy-dependence of the eight-fold degenerate <111> *L*-valleys brings them to a lower energy.

Due to the dependence of the valence band energy on alloy content across the material spectrum most unipolar heterostructure devices built in the low-Ge regime have used holes as their carrier. *n*-type devices have been built, however, exploiting the strain-dependence of the conduction band minimum.

When (001) silicon is deposited pseudomorphically on a thick unstrained crystalline GeSi alloy the silicon is in biaxial tension, with decreased lattice spacing in the growth direction (z) and increased lattice spacing in the two orthogonal directions (x and y). The result is that electrons in the z-valleys ([001] and [00-1]) exhibit a reduced energy relative to those in unstrained silicon while the x and y valleys see an increase in the energy of their states. (See [Pearsall89] for a good overview of the strain effects on GeSi bands.) The advantages are two-fold. First, since the unstrained GeSi substrate has similar conduction band energies to unstrained silicon, the Si now has a reduced conduction band energy relative to the surrounding material and electron confinement can be achieved. The second advantage is that these valleys exhibit a transverse effective mass lower than their longitudinal effective mass. Since conduction in the channel by z-valley electrons will be characterized by the lower transverse effective mass while electrons in the other four valleys will be subject to a mixture of the longitudinal and transverse effective masses, preferential occupation of the z valleys results in a decrease in net effective mass and a corresponding increase in mobility for appropriate carrier densities. The stress-induced electron confinement for devices in principle works for alloys from zero Ge up to approximately 80 atomic percent Ge. However, work to date has focused on using strained silicon as the channel material.

In Ge-rich material there is therefore available two mechanisms to yield band offsets. If the unstrained starting material is (001) $Ge_{0.75}Si_{0.25}$ then application of a strained layer of pure Ge will result in a reduced conduction band energy due to the lower energy of the *L*-valleys (due to symmetry the effect of the [001] compression on the <111> *L*-valleys is small). Growth of a strained $Ge_{0.50}Si_{0.50}$ film on the same substrate will result in reduction of the z-valley energies relative to the unstrained material. These offsets could be used in the formation of confined-electron structures.

Of further interest in Ge channel devices is in which valleys the conduction band minimum occurs. As the degree of [001] compression is increased via a lowering of the effective substrate germanium content, the energy reduction of the x and y valleys increases the population of

electrons occupying them until they become the principle repository for channel electrons. The effect of this transition on electron mass and electron scattering is of significant importance.

Of practical interest is the formation of the relaxed buffer layer. Linear grades can be done via different temperature schedules to confine stress-relieving defects below the surface. These grades can be executed either on a blanket wafer or in regions defined in a surface oxide layer. Another option is the formation of a graded buffer layer on ultra-thin silicon-on-insulator, decreasing the energy needed to relax the surface.

Current Work

While there are many interesting possibilities with Ge-on-Si devices, due to the considerable challenges encountered in the optimization of the graded epitaxial process and in the reliable formation of dielectrics on a germanium surface, this project is focusing on two, both currently under fabrication. One is simple Ge-on-Si *n*-channel field effect transistors. These are expected to exhibit conduction-band minima in the *L*-valleys such as those exhibited by bulk germanium, as was discussed in the last section. The second type of device is the strained Ge-channel on strain-reduced GeSi using a germanium atomic fraction of 75%. It is expected that the strain will reduce the energy of *x* and *y*-directed delta-points below the *L*-valleys, yielding a significant and observable difference in in-plane carrier transport.

Strain-relief via graded epitaxy is achieved by grading the composition, pressure, and temperature in the epitaxial reactor. Depositions are done in the Stanford Center for Integrated Systems Applied Semiconductor Materials Epsilon Chemical Vapor Deposition Epitaxial Reactor. The reactor is a multi-lamp-heated single-wafer unit with a graphite susceptor.

Starting wafers are 4-inch 10 ohm-cm boron-doped (001) silicon. These are cleaned via the lab's standard "HF-last" prediffusion clean and immediately placed in the reactor load lock. After at least an hour's nitrogen purge, the wafers are "prepared" by lowering the load-lock elevators into the exchange chamber. The processing of each wafer starts with an atmospheric-pressure hydrogen bake at 1150 C, an *in-situ* H_2+HCl etch at 1150 C, and another 1150 C hydrogen bake.

Germanium grading is achieved by ramping up the germane flow, ramping down the silane flow, and ramping down the temperature continuously during the deposition period. At the end of the grade, a germanium cap of approximately 2 μm is deposited for device formation. Mass flow controller limitations bound the contiguously-available range of germanium fractions at 3% and

98%, however the "discontinuous" jumps from 0 to 3% and 98% to 100% are accommodated without noticeable quality degradation in the film quality.

The key to successful strain relaxation is to maximize the strain reduction achieved via the formation of buried misfit dislocations. These nucleate either homogeneously (thermally) or heterogeneously (due to external factors, such as particles, the wafer edge, etc.). These misfits generally form and propagate in either the [110] or [1-10] direction until either the temperature drops below a kinetic threshold, the edge of the epitaxial region (the wafer edge in the case of blanket epitaxy) is reached, or they scatter towards a wafer surface in the form of threading arms. Since threading arms at the surface can degrade device performance, the distance the misfits are able to travel before scattering should be maximized. A combination of high deposition temperature to drive the propagation kinetics, low deposition rate to give the misfit time to propagate, and low growth rate to maintain an acceptable level of residual strain is thus desirable.

Low deposition rate is accomplished by keeping the partial pressures of silane and germane low. However, the combination of a low deposition rate and a gentle alloy gradient yields long deposition times, a potential practical impediment. High deposition temperature causes other problems. Gas phase nucleation, which causes particulate contamination of the surface and formation of a non-epitaxial film, is activated with temperature. Another practical problem with high deposition temperatures is coating of the chamber wall can occur. Since stopping the deposition in-progress is undesirable, it is important that chamber deposition be kept sufficiently low that quartz transparency is maintained.

The primary tools used for material quality determination, other than device fabrication, have been AFM, TEM, RAMAN spectroscopy, EMP, RBS, and anisotropic etches. AFM is of particular interest, as it can be done nondestructively with rapid turnaround on the full-wafer Park Scientific atomic force microscope in the Stanford Center for Integrated Systems. The strain reduction process results in surface undulations in the material. When grading is done from silicon to pure germanium, the peak slope of these undulations is approximately one degree with a mean spacing between local peaks of order 5 to 10 micrometers. These are the result of the system's attempt to minimize energy -- when the equilibrium mean lattice spacing of an alloy being deposited is greater than the available mean lattice spacing of the exposed alloy surface, the system uses its degree of freedom in the z-direction to increase the mean spacing between deposited atoms. This yields coherent surface undulations in the [110] and [1-10] directions on the surface. For films deposited at sufficiently high temperature, sufficiently shallow alloy gradient, and at sufficiently low deposition rate, these undulations extend for thousands of micrometers. On films deposited under less optimal conditions, these undulations can be quite short, even 10 micrometers or less, at

which point their orientation becomes difficult to determine. Another indicator of poor quality is observed in films deposited with an excessive temperature schedule -- round pits appear in the surface. These are suspected to be due to gas-phase nucleation yielding particulate contamination of the surface and a resulting disruption of "uniform" epitaxial deposition.

Since the source and drain of the FETs are *n*-type, *p*-type doping for the body is needed. The substrate is thus boron doped, and diborane is flowed with the germane during formation of the germanium cap to yield a boron concentration of approximately $10^{17}/cm^3$ there. To effect good contact between the substrate and the FET bodies, it is also desirable to dope the graded-alloy region. Extensive work was done to achieve this. However, it was found that the use of diborane during the graded-layer formation reduced the deposition temperature at which surface pits, considered to be due to gas-phase nuclei, were formed. Additionally, chamber-wall deposition was seen to increase with the addition of diborane. Whether the reduction in film quality with the addition of diborane is an intrinsic effect or is due to nonidealities with the Stanford system is unclear. Nevertheless, it was decided to limit the boron doping to the surface region and use an "intrinsic" graded layer.

Chamber deposition was a considerable problem before it was recognized that the "standard" chamber cleaning procedure used with the reactor, which concluded with a 1050 C deposition of silicon on the susceptor with an atmospheric-pressure mixture of dichlorosilane and hydrogen, was "seeding" the chamber walls and facilitating the subsequent deposition of material there during the long epitaxial process. Replacement of this susceptor coat with a 750 C silane-and-hydrogen process substantially reduced the chamber-coating problem.

After device-grade epitaxy is achieved, the next challenge is the development of an insulator. The most promising candidate is probably an NO thermally grown germanium-oxinitride gate. However, NO, N_2O, and NH_4 atmospheric furnaces are not readily available in the Stanford lab, and therefore deposited SiO_2 was used, using silane and oxygen at 200 mtorr and 400 C. The problem with this method is that during the deposition thermal oxidation of the germanium at the surface can occur. An improvement in interface quality was observed when a thin silicon layer was deposited on top of the germanium immediately prior to oxide deposition. Immediately after etching away the field oxide over the device active area in dilute hydrofluoric acid, wafers are loaded into the reactor load-lock, purged in nitrogen for an hour, and loaded into the reaction chamber at an ambient temperature of 100 C or lower. After a further hydrogen purge, the temperature is ramped up to 400 C, where silane is flowed for 3 minutes, with hydrogen flow maintained throughout. Since the desorption of hydrogen from a silicon surface is generally the

rate-limiting step in silane CVD, and since hydrogen bonds much more readily with silicon than with germanium, this process is effectively self-limiting -- silicon deposits on the exposed germanium surface but, once the surface is all silicon, hydrogen bonds with the surface and the growth is virtually blocked. Oxide deposition immediately follows this process.

The gate electrode is also formed in the epitaxial reactor. *In-situ* boron-doped $Ge_{0.30}Si_{0.70}$ is readily deposited at 500 C with a resulting resistivity of 1 mohm-cm. No further activation anneal is required. Deposition is initiated with a silicon seed layer. This is made thick enough (at least several extrinsic Debye lengths) to establish a well-defined workfunction at the electrode-insulator interface. Then, to avoid problems associated with band discontinuities, the germanium fraction is gradually graded up to 30%. After the bulk of the gate is thus deposited, the germanium fraction is continuously reduced back to zero and the growth is completed with a silicon capping layer, used to present a well-understood surface for later processing.

The remaining fabrication is standard silicon MOS -- implant $10^{15}/cm^2$ arsenic at 25 keV, activate the dopant at 500 C, deposit an LTO sub-metal dielectric, etch contact holes, and deposit and pattern titanium and aluminum sputtered metal. Finally, a 275 C forming gas anneal is done to improve the oxide-semiconductor interface and the conductivity of the metal-semiconductor contacts.

Initial testing of completed devices is expected to begin by the end of March 1996. Testing of strained-Ge devices is expected in April.

Bibliography

[Daembkes] Daembkes et al; *IEEE TED*, **33**:663 1986.

[Fitzgerald] Fitzgerald et al; *APL* **59**:811-813 1991.

[Garone] Garone et al; *IEEE EDL* **12**(5):230-232 1991.

[Hymes] Hymes et al; *Journal of the Electrochemical Society*, **135**(4):961-965 1988.

[Ismail] Ismail et al; *IEEE EDL* **13**(5):229-231 1992.

[King] King et al; *IEEE EDL* **10**:52 1989.

[LeGoues91] LeGoues et al; *Phys Rev Letters*, **66**(22):2903-2906 1991.

[LeGoues92] LeGoues et al; *Journal of Applied Physics*, **71**:4230-4243 1992.

[Meyerson] Meyerson et al; *Applied Phys Letters*, **53**(25):2555-2557 1988.

[Nayak] Nayak et al; *IEEE EDL* **12**(4):154-156 1991.

[Pearsall86] Pearsall and Bean; *IEEE EDL* **7**:308 1986.

[Pearsall89] Pearsall; CRC Critical Reviews of in Solid State and Materials Sciences, **15**(6):551-600 1989.

[Schaffler] Schåffler et al; *Semiconductor Device Tech*, **7**:260-266 1992.

[Tsang] Tsang et al; *Appl Phys Let*, **62**(10):1146-1148 1993.

[Welser] Welser et al; *IEDM Tech Digest* 1000-1002 1992.

[Wang] Wang et al; *Materials Research Society Symp Proc*, **220**:403-408 1991.

[Xie] Xie et al; *Materials Research Society Symp Proc*, **220**:413-417 1991.

UNIT: 6

TITLE: Portable Video on Demand in Wireless Communication

PRINCIPAL INVESTIGATOR: T. H. Meng

GRADUATE STUDENT: K. Precoda

I. Introduction

This research aims at providing low-power video compression for portable wireless video applications. We developed a power efficient video encoder architecture that uses pyramid vector quantization (PVQ) to compress video data. The decoded image quality using this encoder is better on average in terms of PSNR than JPEG.

In wireless communication, the available bandwidth generally changes with time. Our PVQ encoder, therefore, adjusts the frame rate according to the available bandwidth. If a large bandwidth is available, we increase the frame rate, improving the video quality at the receiver. If the bandwidth is limited, we decrease the frame rate, which results in degraded video quality. This ability to dynamically vary the compression rate allows the encoder to adaptively vary the amount of video data transmitted to achieve the best image quality for a given available bandwidth.

To handle variable frame rates while consuming the absolute minimal power, which is critical in portable systems, we propose to use circuits whose speed/power consumption can be adjusted by actual encoder throughput requirements. Our approach is to design a power supply controller that can adjust the DC voltage to control the desired performance. At high frame rates or when large bandwidth is available, the encoder would operate at high voltages, and, therefore, higher frequencies, allowing more image pixels to be processed per second. If smaller bandwidth is available, the supply voltage need not operate at a high voltage and is decreased appropriately to allow efficient operation at the required throughput. The encoder, therefore, consumes the absolute minimal power necessary to meet the frame rate of the encoder.

II. Power-Supply Regulation

In order to provide a variable supply voltage as a function of the processing speed required, the voltage regulator must rapidly vary the supply voltage to meet the required throughput rate, while maintaining high power efficiency. We have designed a dc-dc switching regulator that

achieves efficiency in excess of 90% with a tracking speed of under 1 ms. The regulator supplies efficiently from a few milli-Watts to several hundred milli-Watts for all supply voltages of interest.

A. Introduction to Switching Regulator

The switching regulator works by chopping the input battery voltage to generate a wave of pulses. These pulses pass through a second-order low-pass filter, which reduce the ac component to an acceptable ripple. The chopping is accomplished by active devices, which are integrated on a single chip to meet the size and weight requirements in portable applications. The inductor and capacitor, which form the low-pass filter, cannot be integrated to standard CMOS process, unfortunately, because of their large inductance and capacitance values. Consequently, off-chip inductors and capacitors are used.

B. Low Power Techniques For Switching Regulators

The switching regulator can ideally achieve 100% efficiency. There are three main sources of dissipation which cause the conversion efficiency to be less than unity: conduction loss in the chopping transistors, switching loss due to parasitics, and gate drive loss.

To improve the conversion efficiency, we employ synchronous rectification and fixed pulse-width voltage modulation. A diode is typically placed between a ground and the input to the low-pass filter to drive the pulse to zero volt. For low-power applications, the voltage drop across the diode causes significant power loss compared to the power delivered. This conduction loss is minimized by replacing a diode with a gated NMOS, which reduces the conduction loss substantially. This use of NMOS is called *synchronous rectification.*

The output voltage is approximately equal to the input voltage multiplied by the duty factor. The duty cycle can be changed arbitrarily by varying the pulse-width or keeping the pulse-width constant and varying the operation frequency. Unlike most traditional switching regulators, we use the latter approach of modulating the output voltage. By keeping the pulse-width constant and varying the operation frequency, the size of the optimal chopping transistors remains relatively constant for varying operating conditions. The amount of energy delivered per pulse remains invariant to varying load sizes, allowing a PMOS transistor sizing that is optimal for all loading conditions.

C. The Feedback Loop

The chopping of the supply voltage makes the converter intrinsically a nonlinear system. Methods of approximating this non linearity to a linear system for a small region of operation and

performing appropriate feedback compensation techniques are well known. Since our encoder must operate at wide load conditions as well as operating voltages, the location of the poles and zeros move by substantial amounts. To maintain stability with a fast response time, the converter needs to track the large movements of poles and zeros and place the compensating poles appropriately. This complicates the controller, which increases power dissipation and lowers efficiency. A nonlinear feedback controller is, therefore, employed requiring only a few adders and comparators. This controller is shown to be stable for all operating regions of interest.

III. Low-Power PVQ Encoder

A real-time, low-power video encoder for pyramid vector quantization is estimated to dissipate only 2.1mW for video compression of images of 256x256 pixels at 30 frames per second in 0.8-micron CMOS technology with a 1.5V supply. Applying this quantizer to subband decomposed images, the quantizer performs better than JPEG on average. We achieve this high level of power efficiency with image quality exceeding that of variable rate codes through efficient algorithm-to-hardware mapping.

Pyramid vector quantization (PVQ) is a quantization technique first introduced by Fisher as a fast method of quantizing and coding Laplacian-like data. PVQ is a fixed rate coding technique with compression performance asymptotically equivalent to a uniform scalar quantizer with entropy coding. PVQ compression capabilities and its fixed rate property, which prevents catastrophic error propagation, are well suited for transmission over noisy, wireless channels.

Our PVQ encoder operates by grouping multiple independent and identically distributed subband coefficients into a vector and finding the index of the nearest lattice point on the surface of a 1-dimensional hyperpyramid. The regularity of a pyramidal shape in multi-dimensional space allows simple recursive equations to assign unique indices to each point on the pyramid. Computing codeword indices rather than employing a large look-up table stored in memory is critical in low-power architectures, since memory operations consume far more power than arithmetic computations, often by several factors for on-chip memory accesses, not to mention the power needed for off-chip memory access.

The original PVQ encoder algorithm was modified to provide more parallelism and pipelining in the architecture, allowing the encoder to efficiently quantize vectors with dimensions as large as 256. This was the key to achieving high compression efficiency while maintaining good image quality at very low power levels.

IV. Conclusion

The goal of this research was to study the energy-on-demand design methodology for implementing low-power video compression systems. The methodology introduced using our dynamic variable supply voltage, however, can be employed in various other digital signal processing applications, where the required throughput rates are time-variant. We are exploring other applications for this energy-on-demand design methodology.

JSEP Supported Presentations

1. E. K. Tsern "A Low-Power Video-Rate Pyramid VQ Decoder," presentation at 1996 IEEE International Solid-State Circuits Conference, February 1996.
2. T. H.-Y. Meng, "A Low-Power Encoder Architecture for Pyramid Vector Quantization of 2-D Subband Coefficients," presentation at International Conference on Image Processing, October 1995.
3. N. Chaddha, "Scalable Video Compression," presentation at International Conference on Image Processing, October 1995.
4. T. H. Meng, "Portable Video-on-Demand in Wireless Communication," invited seminar presentation at Princeton University, April 1995.
5. T. H. Meng, "Portable Video-on-Demand in Wireless Communication," invited seminar presentation at Rockwell Science Center, March 1995.

JSEP Supported Publications

1. W. Namgoong, N. Chaddha and T. H. Meng, "Low-Power Video Encoder/Decoder Using Wavelet/TSVQ With Conditional Replenishment," *Proceedings IEEE ICASSP*, Atlanta, Georgia, May 1996.
2. E. K. Tsern and T. H. Meng, "A Low-Power Video-Rate Pyramid VQ Decoder," *1996 IEEE International Solid-State Circuits Conference Digest of Technical Papers*, pp. 162-163, San Francisco, California, February 1996.
3. W. Namgoong and T. H. Meng, "A Low-Power Video Encoder for Pyramid Vector Quantization of Subband coefficients," submitted to *Journal of VLSI Signal Processing*, February 1996.
4. A. C. Hung, E. K. T. and T. H. Meng, "Error Resilient Pyramid Vector Quantization for Image Compression," submitted to *IEEE Transactions on Image Compression*, January 1996.

5. B. M. Gordon, E. K. Tsern, and T. H.-Y. Meng, "Design of a Low-Power Video Decompression Chip Set for Portable Applications," invited submission to *Journal of VLSI Signal Processing*, October 1995.

6. W. Namgoong, M. Davenport, T. H.-Y. Meng, "A Low-Power Encoder Architecture for Pyramid Vector Quantization of 2-D Subband Coefficients," *Proceedings of 1995 IEEE Workshop on VLSI Signal Processing*, pp. 391-400, Osaka, Japan, October 1995.

UNIT: 7

TITLE: Adaptive DFE for GMSK in Indoor Radio Channels

PRINCIPAL INVESTIGATOR: J. M. Cioffi

GRADUATE STUDENTS: R. D. Wesel and K. Jacobsen

I. Introduction

Point-to-multipoint transmission problems are finding increasing application in broadcast and data communication networks. Such problems were the main focus of the supported JSEP research. Two Ph.D. students are matriculating in 1996 in these areas, Richard Wesel and Krista Jacobsen. Both have significant results, as reported below, and several published or pending papers under this contract's support.

Super-redundancy - R.D. Wesel

Rick Wesel's work focused on broadcast coding methods. In this area, a single source of digital information sends the same information to may remote users, with no feedback path. The transmission paths may vary from user to user and with time for a particular user. Such a situation is characteristic of terrestrial or satellite broadcast networks.

Rick found that to optimize a transmission system fully, the channel characteristic must be known to both the transmitter and the receiver. The consequent optimal action of the transmission system is then a function of this known channel characteristic. In the broadcast case, each user has a different channel characteristic and all are unknown to the transmitter. However, the maximum data rate that could be achieved by each of these users is roughly the same that should achieve at least the worst-case capacity on all the channels. Rick found this rate can be achieved without having to use different codes/designs for the different user paths.

Rick's work then progressed to a search for such a robust code, and several have been found as well as a general search procedure. These codes and the search procedure are described in Section II.

Multipoint-to-point access protocol and analysis - K. Jacobsen

The main focus of Krista Jacobsen's research has been the mechanisms for upstream access in a point-to-multipoint transmission architecture. The specific architecture studied was tree-structured coaxial networks, but the results also apply to wireless and local-area networks.

This work has produced a number of protocols and contention resolution methods for multicarrier transmission with such networks. In particular, a combination of time and frequency division access are combined at the physical transmission layer to improve throughput versus latency trade-offs in such networks, as described in Section III.

A method for network synchronization and coordination was postulated for a multicarrier transmission system and reservation-based access protocols were investigated. Significant improvements in throughput and efficiency were obtained with respect to time-only multiplexing.

Both sets of work have resulted in a reasonable level of publication as reported in Sections II. and III.

II. Trellis Codes for Correlated Fading - Rick Wesel

The Problem

Consider transmission over one or more channels subject to fading in time or frequency such that the fading can be estimated at the receiver but is unknown to the transmitter. An important example of this is digital video broadcast as shown in Fig. 1. This scenario also occurs in single carrier modulation in the presence of flat fading and frequency hopped transmissions in the presence of frequency selective fading. Our work during this period has resulted in a trellis code design technique that provides reliable performance on a much wider class of fading patterns than previous fading channel coded modulation techniques.

Performance of an example code designed using the new technique demonstrates consistently good bit error rate performance over a wide range of fading behavior. It is well known that an Ungerboeck--style trellis code concatenated with a forward error correction code can give performance approaching the channel capacity of an additive white Gaussian noise channel. The new code design technique combined with a forward error correction code can approach capacity simultaneously for a whole class of frequency selective channels, within the limitations of a fixed transmitter power spectrum. Thus, the new design technique provides trellis

codes that are ideal for use in broadcast transmissions where a single transmission must work for a variety of different channels.

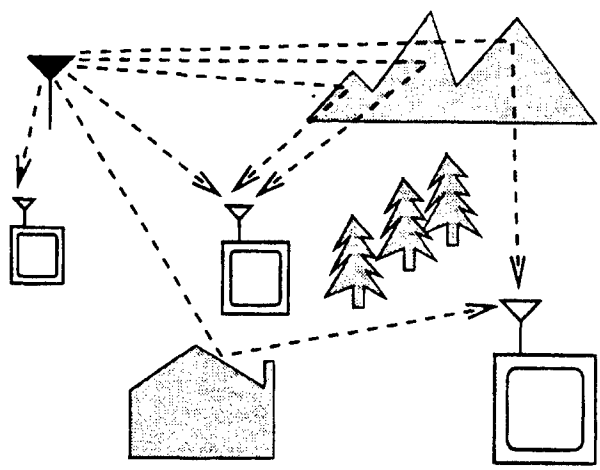

Figure 1: Digital Video Broadcast.

These new codes have already generated significant interest in industry. Telia Research, the Swedish telecommunications company, is exploring how these codes can be used to provide reliable wireless data links between a base station and a mobile user. Here again the transmitter cannot specialize the transmission to the particular fading. Unlike the broadcast situation, there is only one fading pattern. However, the transmitter does not know what that fading pattern is. Thus a robust code is required.

The Subchannel Decomposition

Regardless of whether the fading is in time or frequency, the overall subchannels with different SNRs are shown in Fig. 2. The new code design technique is based on two observations involving this subchannel decomposition. First, the number of coded bits transmitted per symbol needs to approach the subchannel capacities of the high capacity subchannels. Second, code distance must be carefully distributed to ensure that as many uncorrelated subchannels as possible can contribute to decoding.

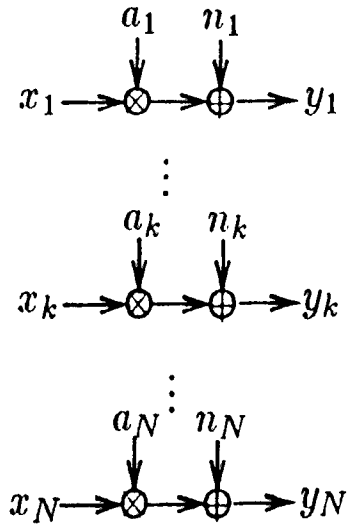

Figure 2: Overall subchannels with different SNRs.

Super-Redundancy

The first requirement, that the number of coded bits transmitted per symbol be large, implies that good fading--channel trellis codes will have a large amount of redundancy. This concept of super-redundancy can be contrasted with the additive white Gaussian noise channel, where it was shown that only one bit of redundancy is required [Ungerboeck]. In the fading environment, the subchannel capacities can vary by a large amount. To efficiently use the channel as a whole, each individual subchannel must be used efficiently. This requires that the number of coded bits be large enough that the high capacity subchannels can be fully utilized.

Code Distance Distribution and Correlation in Fading

It is well known that trellis codes designed for fading channels should distribute distance over as many codewords as possible. This concept of maximizing "effective code length" was formalized [Wilson and Leung] almost ten years ago. Our new code design technique takes this concept one step further. There is correlation between adjacent symbols in time or frequency, and our code design metrics consider the distance associated with groups of adjacent frequencies or time symbols together. This ensures that distance is not accidentally concentrated on a group of symbols which will experience correlated fading.

Previous techniques use interleaving to make the fading appear locally uncorrelated. This interleaving is combined with codes designed for fading assumed to be completely uncorrelated. Interleaving is still used in our new codes to allow short constraint lengths. However, unlike

previous techniques, the permuted correlation in the interleaved fading channel is a primary consideration the code design procedure.

To utilize this correlation information in a straightforward way, periodic interleaving is used. The interleaving period is chosen small enough that symbols within one period are essentially uncorrelated. Symbols separated by multiples of the interleaving period are extremely correlated. Thus symbol--error distances on symbols separated by multiples of the interleaving period provide exactly one "diversity branch".

The code design search procedure finds the trellis code that spreads code distance as evenly as possible on as many of these diversity branches as possible. The number of diversity branches in such a scheme is upper bounded by the period of the interleaver. However, if this period is chosen correctly, that is also the limit of the diversity present in the fading environment. Detailed discussions of the code design procedure can be found in the publications listed at the end of this section.

Performance of the New Codes

To see how well the new codes can perform we consider the example of multicarrier broadcast and consider the four different frequency responses shown in Fig. 3. A multicarrier system with 512 subcarriers in assumed and the desired information rate will be fixed at 1 bit per symbol. Our code design procedure produces a rate 1/4 convolutional code which is used to select points form a 16 QAM constellation. This code is compared with a standard code for multicarrier broadcast of 1 bit per symbol -- a rate 1/2 code used to select points from a 4 PSK constellation. Both codes have 64 states and thus require Viterbi decoders with the same complexity.

Figure 4 shows that the newly designed code provides consistent performance on all four of these channels. At a bit error rate of 10^6 the new code has all four performance curves within a band of 0.75 dB. The standard code performs 1 dB better on the Flat Channel (Channel 1). However, it's performance becomes unacceptable as the frequency selectivity become more pronounced. On the Step Channel (Channel 4), which is a step in the frequency response, the standard code has bit error rates close to 1/2 for the entire range of the plot.

Conclusion

The new codes produced by this research provide reliable performance over a wide variety of time/frequency fading patterns. This type of consistent reliability is unmatched by previous

techniques, and the new codes will find applications in numerous data communication applications including digital video broadcasting and wireless data networks.

III. Design and Analysis of Multipoint-to-point Discrete-Multitone-based Networks - Krista S. Jacobsen

The Problem

As the deployment of hybrid fiber-coax (HFC) networks by both cable television and telephone companies continues, efficient, cost-effective techniques to transmit digital multimedia signals both to and from the home must be developed. Transmission channels in the downstream direction (from the central site to the customer premise) are generally high-quality, and use of a single-carrier modulation in broadcast mode is probably sufficient for downstream transmission. However, the upstream bandwidth of HFC networks is often plagued by numerous transmission impairments, including passband ripple, spectral nulls, and radio-frequency ingress. Hence, a robust upstream modulation technique is required to ensure that effective communications can occur in the presence of these impairments. Furthermore, because HFC networks are generally configured in tree-and-branch topologies, as shown in Fig. 1, the return channel (upstream bandwidth) is shared among many users, potentially thousands. Consequently, use of the available upstream bandwidth must be coordinated somehow to ensure the channel is used efficiently.

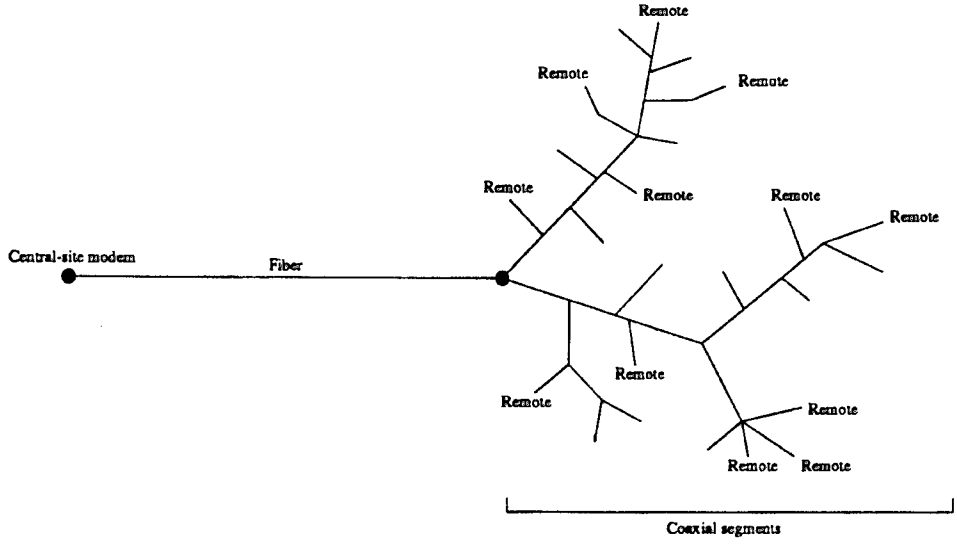

Figure 1: HFC network configuration.

Discrete-multitone (DMT), a type of multicarrier modulation, has been shown in previous JSEP-sponsored papers (i.e., [Jacobsen and Cioffi-a], [Jacobsen and Cioffi-b]) to offer significant advantages for upstream transmission in HFC channels, particularly because DMT can optimize the data rate on channels suffering from severe transmission impairments such as those prevalent in the HFC return channel. However, to exploit these advantages and achieve improvements in the overall network performance, an efficient multicarrier-based channel access protocol is required. Many general protocol alternatives can be adapted to control multicarrier-based remote units, but the challenge lies in developing a simple, easily managed protocol that separates, as much as possible, the modulation from the protocol without losing the benefits gained by using multicarrier transmission.

The goal of this work is to design and analyze DMT-based multipoint-to-point networks in general and HFC networks in particular. Issues addressed include the gains in spectral efficiency that can be realized by using DMT modulation rather than a single-carrier modulation with equalization; methods for installing, synchronizing, and training multiple DMT-based remote units [Jacobsen and Cioffi-c]; the performances of various channel access protocol alternatives for DMT-based networks; and the differences in overall system complexity of single-carrier-based and DMT-based HFC networks. In this document, recent work on the installation, synchronization, and training procedures is presented along with preliminary results on one channel access protocol designed specifically for multicarrier-based multipoint-to-point networks.

Procedure for Installing, Synchronizing and Training DMT-based Remote Units

Because HFC networks span large distances and must support a large number of remote units, at all times, including during installation, it is desired that communications from any particular remote unit to the central-site modem occur without disrupting in-progress data transmissions by other remote units. Thus, when it is first installed on the network, before a remote unit is synchronized it may only transmit while the other remote units are silent. First, the remote unit loop-times its local clock with the central-site model clock, which is broadcast in a downstream control channel. To enable remote unit installations, synchronization, and initial training, silent intervals of a predetermined length are observed periodically in the upstream data stream by all remote units on the network. The central unit transmitter constantly sends a trigger in a downstream control channel to instruct installing remote units to send their installation parameters. Upon receiving a valid installation signal during the silent period, the central-site controller compares the signal's symbol boundaries to those of symbols transmitted by the remote units currently operating. In general, there will be a difference in the symbol boundaries, and the controller computes and sends the time delay required of the synchronizing unit to correct the

misalignment. The remote unit then implements the requested sample delay and transmits a signal requesting verification that it is synchronized. If the remote unit transmission is indeed synchronous, the central unit controller sends a signal to that unit in the downstream channel to indicate that no further shifting is required, and that the remote unit may now communicate with the central-site modem incorporating the appropriate delay. Otherwise, the synchronization procedure is repeated until the central-site controller determines the remote unit is synchronized. After the initial symbol delay has been determined, unless a remote unit is moved or its connection to the network is terminated, it should not have to be resynchronized. Failing to synchronize the remote units to within a certain tolerance can result in interchannel interference, which can decrease the achievable bit rates on the affected subchannels.

After receiving and incorporating the required sample delay from the central-site modem, an installing remote unit transmits a wide-band signal during a specified number of upcoming silent periods to train the central unit receiver. Because the newly installed remote unit is now synchronized with respect to the other remote units, it can transmit using all of the symbols during the next several silent periods for channel analysis. All other remote units remain quiet while the remote unit transmits a training signal on the permissible subset of the subchannels allocated to it, and the central unit controller records the bit capacity and magnitude and phase of each subchannel from that remote unit. The bit capacities are used to determine subchannel assignments when the remote later requests either a constant data rate or a packet transmission. Because the controller allocates the subchannels to the various remote units every symbol period, it can apply the appropriate subchannel magnitude/phase inverse to each subchannel to demodulate the received signal. Hence, if the remotes are all properly synchronized, the signal arriving at the central unit receiver, which is actually an aggregate of transmissions from a number of different remote units, can be demodulated as though it were from a single remote modem, using the appropriate mixture of subchannel magnitude/phase inverses.

After a remote has been installed, it is periodically retrained during another silent interval reserved specifically for this purpose. As during the installation silent period, all remote units that are not training remain quiet to allow the central unit controller to update its settings for the training remote. Depending on the frequency of these silent intervals, the number of remotes on a particular network, and other system parameters, each remote could be retrained as often as many times per second or as infrequently as every few seconds.

Design and Analysis of the Reservation-Based Multicarrier (RBM) Protocol

After the remote units have been installed, synchronized, and trained, they are capable of transmitting without interfering with other remote units as long as they obey a channel access protocol. One alternative for controlling transmissions from remote units so that data is always transmitted collision-free is a reservation-based protocol. Under a generalized reservation-based protocol, to obtain permission to transmit data a remote unit must first transmit a reservation request. When a reservation has been granted, then the corresponding data message is guaranteed to be received intact (channel noise notwithstanding) by the central-site modem. If reservation requests are transmitted using the same bandwidth as data transmissions, then coordination of reservation requests is necessary to ensure they do not interfere with data transmissions.

The *Reservation-Based Multicarrier (RBM)* [Jacobsen and Cioffi-d] protocol has been developed for multicarrier-based multipoint-to-point networks (such as HFC) in which data transmissions scheduled by a central controller are desirable because remote units are unable to detect whether or not the upstream channel is in use, and data transmissions and reservation requests occupy the same bandwidth. Under the RBM protocol, each multicarrier symbol is marked by the central controller as either reserved for data transmissions or available for reservation requests. The controller, which resides at the central-site, broadcasts in a downstream control channel a binary-valued "channel status" signal during every symbol period to inform the remote units whether the channel will be in use for data transmissions during the subsequent symbol period. Based on the status of the next symbol, a remote unit with a data message ready for transmission either reschedules the request for a later time according to a nonpersistent algorithm, or it sends its reservation request during the next symbol period on a randomly-selected "frequency-domain slot." A frequency-domain slot is a set of subchannels in the frequency domain that together support, during one symbol period, a bit capacity equal to the number of bits required to transmit a "request for bandwidth" (RFB). Each RFB consists of at least the remote unit's address, and it may also indicate the size of forthcoming data messages, quality of service parameters, etc, depending on the network particulars. As an example of frequency-domain slot partitioning, if there are N B-bit subchannels in the multicarrier system, and RFBs consist of kb bits, then the subchannels are grouped into K sets of k subchannels. Because all remote units with data ready for transmission may send their RFBs during any symbol period not reserved for scheduled data transmissions, RFBs are subject to collisions with other RFBs. However, because RFBs are generally short, the collision probability is fairly low, and partitioning the subchannels into K sets ensures that collisions always overlap completely. A system allowing different numbers of bits on each subchannel may group a different number of subchannels into each of the K sets, but collisions still overlap completely, and the concept of frequency-domain slots still

holds. Regardless of what method is used to divide the subchannels into frequency-slots, the partitioning must be observed by all remote units.

After transmitting its RFB on one of the K subchannel sets, a remote unit waits a specified period of time, determined by the round-trip propagation delay of the channel and the central unit processing time, to ascertain whether or not its RFB arrived successfully at the receiver. If the waiting remote does not receive a grant message from the central controller within a certain period of time, which indicates that its RFB collided with another unit's RFB or was unintelligible to the receiver for some other reason, it reschedules the RFB for a later time according to a delay distribution. If the remote does receive a grant message before timing out, it begins to transmit its message using all subchannels during the symbol period corresponding to the index sent by the central controller. Figure 2 illustrates the protocol timing, channel status signal, and upstream channel activity when a successful RFB occurs and the minimum delay is incurred.

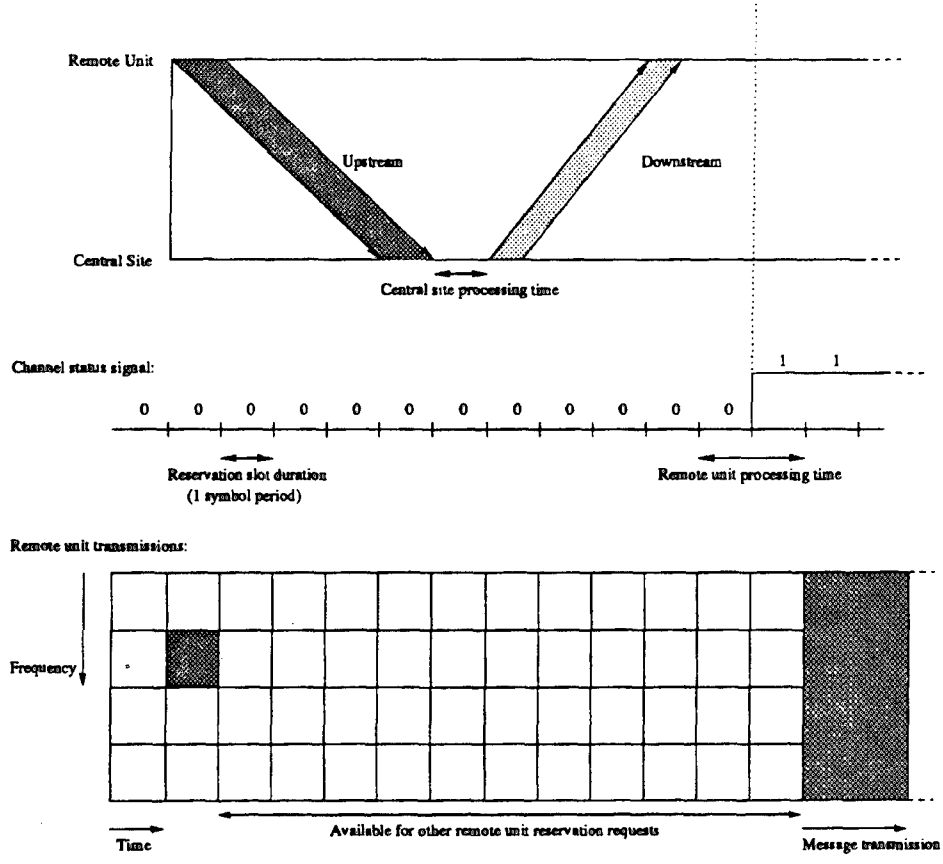

Figure 2: Illustration of protocol with K = 4.

To simplify protocol management, all multicarrier remote units are constrained to transmit using the same bit tables. In other words, for all remote units, the number of bits b_i on the i th subchannel is the same. Note that the number of bits supported by subchannel i need not equal the number supported by subchannel j, as long as b_i and bj are the same across all remote units on the network. Under the constraint of equivalent bit tables, the central unit receiver applies the same decoding procedure to every received symbol. Therefore, the receiver does not need to know in advance which of the remotes is transmitting an RFB or, for that matter, a message. Furthermore,

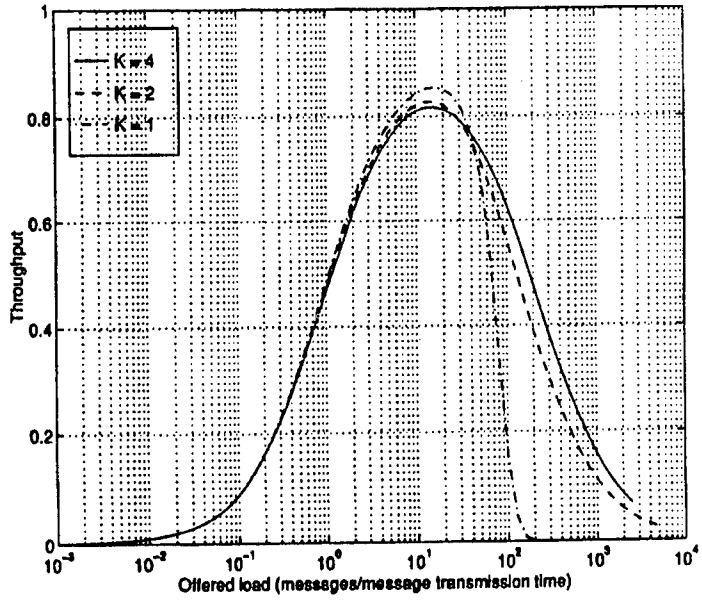

Figure 3: Achievable throughputs of 32-subchannel (K = 4), 16 subchannel (K = 2), and 8 subchannel (K = 1, slotted single carrier) RBM protocols: 256 bits/message, 2 bits/subchannel, 16 bits/RFB.

although RFBs are transmitted on only a few of the available subchannels, messages are transmitted using all subchannels in a symbol. Hence, if a symbol has been reserved for data transmission, only one remote unit transmits during that symbol. This restriction simplifies protocol management and enables the remote units to determine whether to transmit RFBs by checking only the binary channel status signal.

Of interest for evaluating the performance of a particular protocol is the expected *throughput* it enables at various loads. The throughput is defined as the percent of time the channel is used for data transmissions. Figure 3 shows the achievable throughputs of the RBM protocol with various numbers of subchannels as a function of offered load for a network with $a = 1$. A constant message length of 256 bits was used with 16 bits per RFB, and the available transmission

bandwidth was divided into 32 (K = 4), 16 (K = 2), and 8 (K = 1, slotted single-carrier) 2-bit subchannels. Hence, the time required to transmit each message is the same for each scenario, and the achievable throughputs for the various values of K may be compared without modification.

The figure illustrates that the throughput achieved by the RBM protocol is a function of the offered traffic load and the expected number of successful RFB transmissions during a message slot, which in turn is a function of the number of subchannel sets, K, available for simultaneous reservation requests. For loads in the range from $G = 0$ to $G = G_C$, where G_C is some critical value of the offered load, the slotted single-carrier version of the RBM protocol (K = 1) can achieve a slightly higher throughput than $K > 1$ versions, whereas the $K > 1$ versions perform significantly better when $G > G_C$. As a general rule, then, the throughput of networks with higher numbers of subchannels degrades less severely as the offered load increases. It is important to note that the offered load in a real system is likely to change significantly during operation. Hence, at times the network load will exceed G_C, especially if the remote unit traffic sources are bursty. The results presented imply that certain networks intended to support bursty traffic sources can benefit significantly from using multicarrier modulation in conjunction with the RBM protocol.

References

[Ungerboeck] G. Ungerboeck, "Channel Coding with Multilevel/Phase Signals," *IEEE Transactions on Information Theory*, **40**(5):1459-1473, September 1994.

[Wilson and Leung] S. G. Wilson and Y. S. Leung, "Trellis-Coded Phase Modulation on Rayleigh Channels," *Proceedings of ICC*-87, pages 739-742, June 1987.

[Jacobsen and Cioffi-a] K. S. Jacobsen and J. M. Cioffi, "An Efficient Digital Modulation Scheme for Multimedia Transmission on the Cable Television Network," in *Technical Papers, 43rd Annual National Cable Television Association (NCTA) Convention and Exposition,* New Orleans, LA , May 1994.

[Jacobsen and Cioffi-b] K. S. Jacobsen and J. M. Cioffi, "High-performance Multimedia Transmissions on the Cable Television Network," in *Proceedings 1994 International Conference on Communications*, New Orleans, LA, May 1994.

[Jacobsen and Cioffi-c] K. S. Jacobsen and J. M. Cioffi, "Synchronized DMT for Multipoint-to-point Communications on HFC Networks," in *Globecom '95 Proceedings*, Singapore, November 1995.

[Jacobsen and Cioffi-d] K. S. Jacobsen and J. M. Cioffi, "Achievable Throughput in Multicarrier-based Multipoint-to-point Networks Using a Reservation-based Channel Access Protocol," submitted to *Globecom '96.*

JSEP Supported Publications

1. R. D. Wesel and J. M. Cioffi, "Fundamentals of Coding for Broadcast OFDM," In *Proceedings of the 29th Asilomar Conference on Signals Systems & Computers*, November 1995.
2. R. D. Wesel and J. M. Cioffi, "A Transmission System Using Codes Designed for Transmission with Periodic Interleaving," U. S. Patent Pending.
3. R. D. Wesel and J. M. Cioffi, "Trellis Codes for Channels with Correlated Fading," in Preparation for Submission to *IEEE Transactions on Communications.*
4. K. S. Jacobsen and J. M. Cioffi, "An Efficient Digital Modulation Scheme for Multimedia Transmission on the Cable Television Network," in *Technical Papers, 43rd Annual National Cable Television Association (NCTA) Convention and Exposition,* New Orleans, LA , May 1994.
5. K. S. Jacobsen and J. M. Cioffi, "High-performance Multimedia Transmissions on the Cable Television Network," in *Proceedings 1994 International Conference on Communications,* New Orleans, LA, May 1994.
6. K. S. Jacobsen and J. M. Cioffi, "Synchronized DMT for Multipoint-to-point Communications on HFC Networks," in *Globecom '95 Proc.*, Singapore, Nov. 1995.
7. K. S. Jacobsen and J. M. Cioffi, "Achievable Throughput in Multicarrier-based Multipoint-to-point Networks Using a Reservation-based Channel Access Protocol," submitted to *Globecom '96.*

UNIT: 8

TITLE: Robust Estimation Methods for Adaptive Filtering

PRINCIPAL INVESTIGATOR: T. Kailath

GRADUATE STUDENTS: Y. C. Pati and B. Hassibi

1 Introduction

Our earlier JSEP-supported work was concerned with the use of spatial and temporal (signal) structure in smart antennas for mobile radio networks. The work done there gradually led us to consider, and to study, the *robustness* of the underlying algorithms with respect to model uncertainties and lack of statistical information. In particular, of interest were adaptive filtering algorithms which are widely used in communications (as well as in many other areas) for the identification and equalization of channels.

Classical methods for such problems require a priori knowledge of the statistical properties of the signals. In many applications, however, one is faced with model uncertainties and lack of statistical information. Therefore the aforementioned methods are not directly applicable. Moreover, it is not even clear what the behaviour of such estimation schemes might be if the assumptions on the statistics and distributions are not exactly met.

Adaptive filtering techniques are currently widely used to cope with such model uncertainties and lack of a priori knowledge. The methods currently used fall into the two general classes of least-squares-based algorithms (such as recursive-least-squares or RLS) and gradient-based algorithms (such as least-mean-squares or LMS). While the former class is derived from an explicit cost function, it is suspect whether their robustness properties are always desirable. On the other hand, the former methods are rather ad-hoc and do not follow from a rigorous framework. However, the gradient algorithms are by far the ones most used in applications. Our work now provides some analytic explanation of this fact.

In the last decade such problems have received great attention in control theory, where a so-called H^∞ approach has been extensively studied. It turns out, in particular, that the LMS algorithm is H^∞-optimal, thus establishing the observed robustness of this very widely used algorithm. We have also obtained some results on the robustness of least-squares-based adaptive filters. This framework is currently being used to explore new adaptive filtering algorithms for nonstationary scenarios.

2 Adaptive Filtering

The standard model assumed in adaptive filtering is the following:

$$d_i = h_i^T w + v_i, \qquad i \geq 0 \tag{1}$$

where $\{d_i\}$ is an observed output sequence (often called the reference signal), $\{h_i\}$ is a known input vector sequence, w is an unknown weight vector that we intend to estimate, and $\{v_i\}$ is an unknown disturbance, which may also include modeling errors. We shall make no assumptions on the statistics or distributions of the $\{v_i\}$.

We denote the estimate of the weight vector using all the information available up to time i by

$$w_i = \mathcal{K}(d_0, d_1, \ldots, d_i; h_0, h_1, \ldots h_i).$$

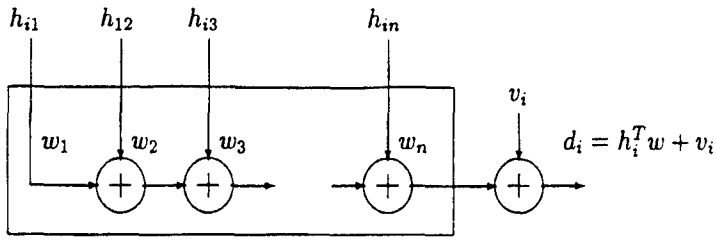

Figure 1: The model for adaptive filtering.

2.1 Least-Squares-Based Methods

There are a variety of choices for w_i, but the most widely used estimate w_i, is one that satisfies the following least-squares (or H^2 criterion):

$$\min_{w} \left[\mu^{-1}|w - w_{-1}|^2 + \sum_{j=0}^{i} |d_j - h_j^T w|^2 \right], \tag{2}$$

where w_{-1} is the initial estimate of w, and $\mu > 0$ represents the relative weight that we give to our initial estimate compared to the "sum of squared-error" term $\sum_{j=0}^{i} |d_j - h_j^T w|^2$. In the so-called *pure least-squares* problems one takes $\mu = \infty$, so that the first term in the cost function of (2) does not appear.

The *exact* solution to the above criterion is the RLS (Recursive Least Squares) algorithm:

$$w_i = w_{i-1} + k_{p,i}(d_i - h_i^T w_{i-1}) \quad , \quad w_{-1} \tag{3}$$

with $k_{p,i} = \frac{P_i h_i}{1+h_i^T P_i h_i}$ and $P_{i+1} = P_i - \frac{P_i h_i h_i^T P_i}{1+h_i^T P_i h_i}$, $P_0 = \mu I$.

RLS has certain stochastic optimality properties: if we assume in model (1) that the $w - w_{-1}$ and $\{v_i\}$ are zero mean independent Gaussian random variables with variances μI and 1 respectively, then the RLS algorithm yields the maximum likelihood estimate of w_i. In particular, it minimizes the expected *prediction error energy*:

$$E \parallel e_p \parallel_2^2 = E \sum_{j=0}^{i} |h_j^T w - h_j^T w_{j-1}|^2. \tag{4}$$

2.2 Gradient-Based Algorithms

In gradient-based algorithms instead of exactly solving the least-squares problem (2), the estimates of the weight vector are updated along the negative direction of the *instantaneous* gradient of the cost function appearing in (2). Two examples are the LMS (Least-Mean-Squares)

$$w_i = w_{i-1} + \mu h_i(d_i - h_i^T w_{i-1}) \quad , \quad w_{-1} \tag{5}$$

and normalized LMS

$$w_i = w_{i-1} + \frac{\mu}{1 + \mu h_i^T h_i} h_i(d_i - h_i^T w_{i-1}) \quad , \quad w_{-1} \tag{6}$$

algorithms. Note that in the case of LMS the gain vector $k_{p,i}$ in RLS (which had to be computed by propagating a Riccati equation) has been simply replaced by μh_i. Likewise if we compare normalized LMS with the RLS algorithm, we see that the difference is that instead of propagating the matrix P_i via the Riccati recursion we have simply set $P_i = \mu I$, for all i. Therefore the LMS and normalized LMS algorithms were long considered to be *approximate* least-squares solutions and were thought to lack a rigorous basis.

2.3 The Question of Robustness

We noted that under suitable stochastic assumptions, H^2-optimal adaptive filters have certain desirable optimality properties. However, a question that begs itself is what the performance of such filters will be if the assumptions on the disturbances are violated, or if there are modelling errors in our model so that the disturbances must include the modelling errors? In other words

- *is it possible that* **small** *disturbances and modelling errors may lead to* **large** *estimation errors?*

Obviously, a nonrobust algorithm would be one for which the above is true, and a robust algorithm would be one for which small disturbances lead to small estimation errors.

The problem of robust estimation is thus an important one. As we shall see in the next section, the H^∞ robust estimation formulation is an *attempt* at addressing this question. The idea is to come up with estimators that minimize (or in the suboptimal case, bound) the maximum energy gain from the disturbances to the estimation errors. This will guarantee that if the disturbances are small (in energy) then the estimation errors will be as small as possible (in energy), *no matter what the disturbances are.* In other words the maximum energy gain is minimized over *all possible* disturbances. The robustness of the H^∞ estimators arises from this fact. Since they make no assumption about the disturbances, they have to accomodate for all conceivable disturbances, and are thus over-conservative. So this is not necessarily the best solution and we are also exploring weaker criteria.

3 The H^∞ Approach

We now apply the H^∞ methodology to adaptive filtering (see [Hassibia] for details).

To this end, consider the following three types of estimation errors:

(i) The prediction error:

$$e_{p,i} = h_i^T w - h_i^T w_{i-1}.$$

(ii) The filtered error:

$$e_{f,i} = h_i^T w - h_i^T w_i.$$

(iii) The smoothed error:

$$e_{s,i} = h_i^T w - h_i^T w_N.$$

Any choice of estimation strategy $\mathcal{K}$ will induce a transfer operator from the disturbances to the above estimation errors. These we shall denote by

(i) $T_p(\mathcal{K})$: transfer operator from the disturbances $\{w - w_{-1}, v_i\}$ to the prediction errors $\{e_{p,i}\}$.

(ii) $T_f(\mathcal{K})$: transfer operator from the disturbances $\{w - w_{-1}, v_i\}$ to the filtered errors $\{e_{f,i}\}$.

(iii) $T_s(\mathcal{K})$: transfer operator from the disturbances $\{w - w_{-1}, v_i\}$ to the smoothed errors $\{e_{s,i}\}$.

Now for any choice of estimator, $\mathcal{K}$, and any given input disturbance sequence $\{w - w_{-1}, v_i\}$, that yields the prediction error, $\{e_{p,i}\}$, we may compute the energy gain

$$\frac{\|e_p\|_2^2}{\mu^{-1}|w - w_{-1}|^2 + \|v\|_2^2}, \tag{7}$$

where $\|a\|_2^2 = \sum_j |a_j|^2$ is defined as the energy of the sequence $\{a\}$ and μ is a positive constant. Thus (7) is a measure of the "amplification" of the noise given our choice of estimator $\mathcal{K}$. Now the ratio in (7) will clearly depend on the input disturbance, $\{w - w_{-1}, v_i\}$. however, if we consider *all* possible disturbance sequences $\{w - w_{-1}, v_i\}$, then we can find the largest energy gain in (7). This leads us to the definition of the H^∞ norm of a transfer operator T.

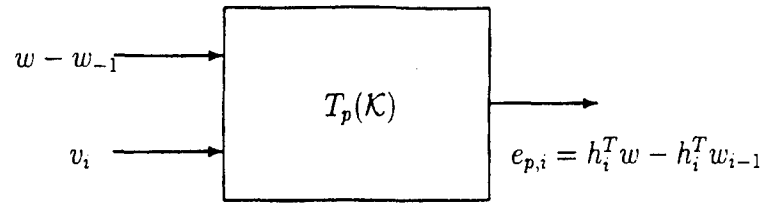

Figure 2: Transfer operator from the unknown disturbances $\{w - w_{-1}, v_i\}$ to the prediction errors $\{e_{p,i}\}$. Likewise for $T_f(\mathcal{K})$ and $T_s(\mathcal{K})$.

Definition 1 (The H^∞ Norm) *The H^∞ norm of a transfer operator T is defined as*

$$\|T\|_\infty = \sup_{x \in h^2, x \neq 0} \frac{\|Tx\|_2}{\|x\|_2} \tag{8}$$

where h^2 denotes the space of all square-summable causal sequences.

We now propose to choose the estimator $\mathcal{K}$ so as to minimize the H^∞ norms of $T_p(\mathcal{K})$, $T_f(\mathcal{K})$ and $T_s(\mathcal{K})$. To be more specific we have the following problem.

Problem 1 (H^∞ Adaptive Filtering Problem) *Find estimators $w_i = \mathcal{K}_p(d_0, \ldots, d_i; h_0, \ldots, h_i)$, that minimize the maximum energy gain from disturbances to estimation errors for each of the aforementioned errors,* i.e. , *find estimation strategies $\mathcal{K}_p$, $\mathcal{K}_f$ and $\mathcal{K}_s$ such that*

$$\gamma_p^2 = \inf_{\mathcal{K}_p} \sup_{w,v \in h_2} \frac{\|e_p\|_2^2}{\mu^{-1}|w - w_{-1}|^2 + \|v\|_2^2} \tag{9}$$

$$\gamma_f^2 = \inf_{\mathcal{K}_f} \sup_{w,v \in h_2} \frac{\|e_f\|_2^2}{\mu^{-1}|w - w_{-1}|^2 + \|v\|_2^2} \tag{10}$$

and

$$\gamma_s^2 = \inf_{\mathcal{K}_s} \sup_{w,v \in h_2} \frac{\|e_s\|_2^2}{\mu^{-1}|w - w_{-1}|^2 + \|v\|_2^2} \tag{11}$$

where $|w - w_{-1}|^2 = (w - w_{-1})^T(w - w_{-1})$ and $\mu > 0$ reflects a priori knowledge of how close w_{-1} is to w.

It turns out that nice solutions can be obtained for all three problems. The solutions to Prob. 1 are given below (see [Hassibia]), in which we have assumed that the input vectors $\{h_i\}$ are such that

$$\lim_{N \to \infty} \sum_{i=0}^{N} h_i^T h_i = \infty.$$

Solution to (i): If μ satisfies the bound

$$0 < \mu < \inf_i \frac{1}{h_i^T h_i} \tag{12}$$

then $\| T_p(\mathcal{K}) \|_\infty$ is minimized by the LMS algorithm with learning rate μ,

$$w_i = w_{i-1} + \mu h_i(d_i - h_i^T w_{i-1}) \quad , \quad w_{-1}$$

and the minimum H^∞ norm is given by

$$\gamma_p = 1.$$

Remarks:

(a) The fact that $\gamma_p = 1$ indicates that there is no amplification of the disturbances. Thus the prediction error energy will never exceed the disturbance energy.

(b) The above result is true only of the learning rate μ satisfies the bound (12). This is in accordance with the well-known fact that LMS behaves poorly of the learning rate is chosen too large.

Solution to (ii): $\| T_f(\mathcal{K}) \|_\infty$ is minimized by the normalized LMS algorithm

$$w_i = w_{i-1} + \frac{\mu}{1 + \mu h_i^T h_i} h_i (d_i - h_i^T w_{i-1}) \quad , \quad w_{-1}$$

and the minimum H^∞ norm is given by

$$\gamma_f = 1.$$

Remark: Note once more that there is no amplification of the noise. Now, however, we have no restriction on μ.

Solution to (iii): $\| T_s(\mathcal{K}) \|_\infty$ is minimized by the least-squares solution, and the minimum H^∞ norm is

$$\gamma_s = 1.$$

Remark: Thus least-squares algorithms are H^∞ optimal with respect to smoothing errors.

4 Robustness of Least-Squares Algorithms

Now that we have developed the H^∞ optimality of the LMS and normalized LMS algorithms with respect to prediction and filtered errors, it is natural to ask what the performance of the RLS algorithm will be with respect to these error criteria.

In order to answer the above question we need to compute the H^∞ norm of the RLS algorithm. Finding this H^∞ norm essentially amounts to finding the maximum singular value of a linear time-varying operator. Upper bounds on the H^∞ norm can be found by checking for the positivity of the solution of a certain time-varying discrete-time Riccati recursion. Although both approaches can be used in principle, they require knowledge of *all* the input data vectors $\{h_i\}$.

Since in adaptive filtering problems we are given, and are forced to process, the data in real time, we cannot store all the data and use the aforementioned methods to compute bounds for the H^∞ norm. Therefore the main effort in the results given below is to obtain bounds on H^∞ norm that use simple a priori knowledge of the $\{h_i\}$ and not their explicit values [Hassibib].

(i) For RLS, we can show

$$(\sqrt{R} - 1)^2 \leq \sup_{w, v \in h_2} \frac{\|e_p\|_2^2}{\mu^{-1}|w - w_{-1}|^2 + \|v\|_2^2} \leq (\sqrt{R} + 1)^2$$

or to give a "looser" bound

$$(\sqrt{1 + \mu \underline{h}^2} - 1)^2 \leq \sup_{w, v \in h_2} \frac{\|e_p\|_2^2}{\mu^{-1}|w - w_{-1}|^2 + \|v\|_2^2} \leq (\sqrt{1 + \mu \bar{h}^2} - 1)^2,$$

where

$$R = \max_i 1 + h_i^T P_i h_i \quad , \quad \bar{h}^2 = \max_i |h_i|^2 \quad , \quad \underline{h}^2 = \min_i |h_i|^2.$$

Remark: Note that for large μ, the H^∞ norm grows as μ. This shows that the pure least-squares problem (with $\mu = \infty$) is highly non-robust with respect to prediction errors.

(ii) For filtered errors we have

$$\sup_{w,v \in h_2} \frac{\|e_f\|_2^2}{\mu^{-1}|w - w_{-1}|^2 + \|v\|_2^2} \leq (\sqrt{1/r} + 1)^2 \leq 4,$$

where

$$r = \min_i 1 + h_i^T P_i h_i \geq 1.$$

Remarks:

(a) Note that, as with normalized LMS, the H^∞ norm does not depend on μ.

(b) The above result for filtered errors is an intermediate stage between the smoothing error case (where the H^∞ and H^2 optimal filters coincide) and the prediction error case (where the performance of LMS and RLS can be drastically different.)

5 Future Work

The H^∞ approach to adaptive filtering described in the previous section suggests several directions for future research. We mention a few here.

5.1 Time-Varying Problems

So far we have assumed that the weight vector, w, is constant in time. In many applications one needs to assume a time-varying, w, and must therefore devise algorithms that can track the time-variations of the weight vector.

In such cases, one approach is to use windowing. Two common windowing schemes are the following.

(i) **Exponential Window:** The exponential window gives (exponentially) larger weight to the more recent data. In particular, the prediction error and disturbance energies are computed as:

$$\sum_{j=0}^{i} \lambda^{-j} |e_j|^2 \quad \text{and} \quad \sum_{j=0}^{i} \lambda^{-j} |v_j|^2, \tag{13}$$

where $0 < \lambda < 1$ is the so-called forgetting factor that is chosen based upon a priori knowledge of how fast the weight vector varies with time.

(ii) **Finite-Memory Window:** In this case one only considers the last L data points so that the prediction error and disturbance energies are computed as

$$\sum_{j=i-L+1}^{i} |e_j|^2 \quad \text{and} \quad \sum_{j=i-L+1}^{i} |v_j|^2, \quad \text{respectively.} \tag{14}$$

L is often referred to as the window length.

It is therefore useful to consider the H^∞ filters that result from such "windowed" definitions of energy. The filters that are obtained in this fashion will have good tracking properties and, at the same time, be robust.

5.2 Mixed H^2/H^∞ Estimation

Fig. 5.2 shows the (squared) singular values of $\mathcal{T}_{p,rls}$ and $\mathcal{T}_{p,lms}$ (the transfer operators from disturbances to estimation errors for RLS and LMS) for $N = 50$ (where N is the number of observed data points) and $\mu = .9$, for a simple one-dimensional adaptive filtering problem. As can be seen the maximum singular value for $\mathcal{T}_{p,lms}$ is one, whereas for $\mathcal{T}_{p,rls}$ it is much larger. On the other hand, the RLS algorithm minimizes the Frobenius norm (the sum of the squared singular values) of the transfer operator $\mathcal{T}_K$ which can be visualized as the area under the curve of the (squared) singular values. Thus if we choose disturbances uniformly from the space $\mathcal{C}^{50}$, the RLS algorithm will have better average performance than LMS, although its worst-case performance is significantly worst.

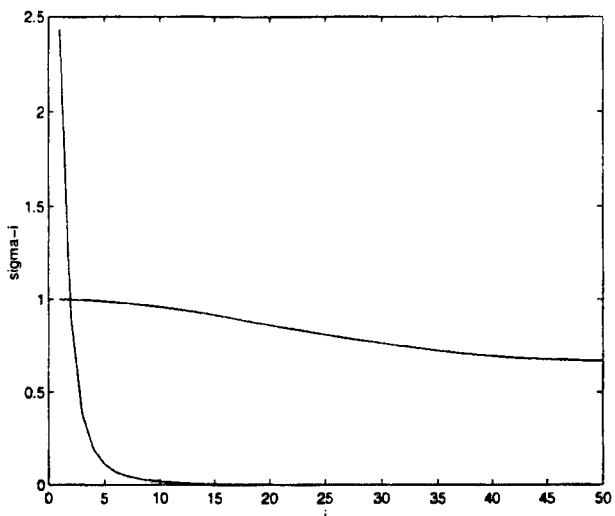

Figure 3: Singular values for $\mathcal{T}_{p,rls}$ and $\mathcal{T}_{p,lms}$ for $N = 50$ and $\mu = .9$.

Note, moreover, that although the LMS algorithm does not allow any amplification of the disturbances, it does not provide significant suppression of the disturbances, either. (The smallest squared singular value for $\mathcal{T}_{p,lms}$ which represents the minimum energy gain is roughly 0.65.) Since the H^∞ optimal filters are not unique (LMS is only the central solution), it is very interesting to study the possibility of choosing other H^∞ optimal filters to further reduce the Frobenius norm of $\mathcal{T}_K$. This will result in algorithms that have the best possible average behaviour while at the same time having the best possible worst-case performance. This framework is called the mixed H^2/H^∞ estimation framework and is an area that we intend to pursue.

References

[Hassibia] B. Hassibi, A.H. Sayed and T. Kailath. H^∞ Optimality of the LMS Algorithm. *IEEE Trans. on Signal Processing*, vol 44, pp. 267-281, February 1996.

[Hassibib] B. Hassibi and T. Kailath. H^∞ bounds for the recursive-least-squares algorithm. in *Proceedings of the 33rd IEEE Conference on Decision and Control*, pp. 3927-3929, Orlando. FL, Dec 1994.

UNIT: 9

TITLE: Efficient Data Compression

PRINCIPAL INVESTIGATOR: T. Cover

GRADUATE STUDENTS: E. Erkip, P. Fahn, G. Iyengar, D. Kimber, I. Kontoyiannis, A. Lapidoth and E. Ordentlich

AFFILIATED STUDENTS: V. Castelli and T. Jing

1 Scientific Objectives

We apply techniques of information theory to problems of efficiently compressing data, for the purpose both of storage and transmission of data. Our results concern compression schemes both for specific circumstances, such as specific noise profiles in communications channels, and for general circumstances, such as human "non-algorithmic" image compression. How much can be gained by customizing data compression to specific circumstances, as opposed to using the convenience of established, off-the-shelf algorithms? During the past year this work resulted in 9 supported papers and 1 Ph.D. thesis.

2 Summary of Research

One of the new innovations in this year's research on data compression is the work of G. Iyengar on the capacity of the voice channel. In most channels, one constructs waveforms that are invulnerable to noise. In the voice channel, we use an independent source of white noise to drive a filter which is chosen at the discretion of the speaker. The filter models the speaker's vocal tract. We ask how many distinguishable filters there are in the presence of additive white noise as heard by the listener. A solution of this problem will yield the capacity of the voice channel, a characterization of an optimal vocabulary, the role of feedback in speaking, models for languages, and finally, since we're able to model speech, the optimal method of data compression associated with the voice channel.

The results of a multiyear project on image compression are being summarized in a paper by T. Jing, T. Cover and R. Wesel and L. An. We have found that if humans are allowed to intervene in a legitimate image compression experiment substantial improved data compression can be achieved over existing JPEG standards. This is not a surprise because our experiment requires over 100 man hours of work per image to achieve the desired data compression. However, the magnitude of the improvement shows how far existing image compression algorithms have to go before they achieve their ultimate limits.

In other work by P. Fahn, we are investigating the quantum theoretic correlations in distributed measurements and observations. This leads naturally to questions of data compression for quantum theoretic systems, or by means of such systems. These data compression results will turn out to be nonclassical because the marginal distributions of measurements have been shown, via Bell's inequality, to be inconsistent with any multivariate distribution. In a sense, there is no underlying physical reality with which the observations are consistent.

3 Detailed Research Descriptions

3.1 Image Compression

Our experiment to compare the image compression abilities of humans and computers is in its final stages. Our goal is to estimate the minimal rate, in bits per pixel, at which an image can be compressed without incurring significant perceptible distortion. First, one experimental subject simplies a given image without significantly distorting it, and then another subject predicts the simplified image, pixel by pixel, as accurately as possible. The accuracy of the second subject's predictions can be quantified to yield an estimate of the entropy of the simplified image. Not only will our results be useful as a benchmark to researchers in the field, but the experimental framework itself may lead to a new algorithm for data compression. A paper detailing the results of the experiment is currently under preparation.

3.2 Voice Channel

The thrust of this research is to develop a characterization of the capacity and optimal coding vocabularies of voice channels, which are mathematical models intended to capture properties of human speech generation. This research area will provide guidance on data compression for a voice channel or other channels with similar characteristics.

Consider a communication system with a channel characterized by a linear filter g in an additive Gaussian noise environment, i.e., $y(t) = u(t) * g(t) + z(t)$, where $z(t)$ is white noise and $u(t)$ is the channel input. Instead of fixing the filter $g(t)$, which is the traditional approach, we fix the input signal $u(t)$ and attempt to choose a distribution on the space of linear, passive, causal filters $g(t)$ that maximizes the mutual information between the output and the filter. This model and its discrete-time analog are, we propose, an approximate model for the voice generation process

3.3 Feedback in Communication

It was recently shown by [Pombra and Cover] that the maximum achievable throughput (sum of rates of all users) of a Gaussian multiple access channel with feedback is at most twice that achievable without feedback. We prove [Ordentlich] a somewhat stronger result which establishes the factor of two bound not only for the total throughput but for the entire capacity region as well. Specifically, we show that the capacity region of a Gaussian multiple access channel with feedback is contained within twice the capacity region without feedback.

We have recently extended the factor of two bound on the capacity region of Gaussian multiple access channels to channels with inter-symbol interference (ISI). For single user Gaussian channels there is no information theoretic complication introduced by the addition of a causal linear filter at the transmitter. If the filter is invertible, the channel can be transformed into an ISI-free channel with an appropriately modified noise spectrum. For the multiple access channel, if the ISI filters are not identical for all transmitters, as is the case in practice, no such transformation is possible. This new result demonstrates that in wireless communications networks, once steady state has been reached via power control and channel learning, the maximum additional gain in capacity region afforded by receiver-to-transmitter feedback is limited to a factor of two, no matter how cleverly the feedback is used.

3.4 Robustness of Communication

Lapidoth, in a series of papers [Lapidoth 1], [Lapidoth 2], [Lapidoth 3], has considered the robustness of signaling in the presence of noise in an unknown environment. It is well known that Gaussian signals and matched filter decoding is optimal for signaling with a power constraint over an additive white noise Gaussian channel. This is the basis for much of the signaling which is done, say, in deep space communication or in mobile communication. Lapidoth is able to show that even if you fix the receiver to be a matched filter receiver and continue to use the same signals, the information will get through the channel no matter what the noise is, just so long as the total noise power is not increased. Specifically, if the distribution of the noise is changed from Gaussian and independent to non-Gaussian and arbitrarily time dependent, as long as the noise power is not increased, the channel will still work and the probability of error will be exponentially small. This shows the robustness of existing communication schemes to changes in the underlying assumptions on the model.

3.5 Universal lossless compression

We investigate the convergence properties of optimal data compression algorithms. The two major directions of this research are entropy (redundancy) estimation for text and images, and calculation of the exact distribution of codeword-lengths for large data sets.

In a series of papers [Kontoyiannis and Suhov 1], [Kontoyiannis and Suhov 2], [Kontoyiannis, Algoet and Suhov], we have investigated the convergence properties of several entropy estimation algorithms. These algorithms are suggested by optimal data compression schemes that are based on pattern-matching, such as the celebrated Lempel-Ziv algorithm for text compression. Our results prove the optimality of some existing methods and also suggest new algorithms for the efficient estimation of the redundancy withing any given data set.

The results along the second direction of this research provide a second-order analysis of the distribution of the size of losslessly encoded data. We prove a second-order refinement to Shannon's (lossless) Source Coding Theorem. In essence this result says that the distribution of the deviations of the compressed data size from its mean is, at best, Gaussian. The minimum variance of this Gaussian is a quantity characteristic of the source, and it provides a theoretical bound on the variance of the encoded data size.

3.6 Quantum Data Compression

As feature sizes on electronic devices continue to shrink, there is fear that quantum effects will become significant and hinder reliable functioning. A few researchers have started to realize, however, that the strange properties of quantum systems can be exploited to great advantage. A quantum bit is not restricted to the "classical" values 0 and 1, but can take values anywhere in a two-dimensional Hilbert space. If we can find practical methods to compress data using quantum bits, therefore, the efficiency achieved could greatly surpass the limits of classical data compression.

Of course if quantum bits are so efficient, they may be used throughout the computation and communication processes. Therefore we have been studying the possibilities for quantum data compression of quantum data as well as of classical data. If a quantum source generates data described by a density operator ρ, data compression limits can be established using the Von Neumann entropy $-k\mathrm{Tr}\rho\log\rho$, instead of the Shannon entropy used in traditional data

compression. Furthermore, one can compress partly entangled pairs of quantum particles into a small number of completely entangled pairs — the so-called Bell states — which can then be used for efficient communication of quantum data.

References

[Castelli and Cover] V. Castelli and T. Cover. On the Exponential Value of Labeled Samples. *Pattern Recognition Letters*, 16:105-111, January 1995.

[Cover and King] T. Cover and R. King. A Convergent Gambling Estimate of the Entropy of English. *IEEE Trans. on Information Theory*, IT-24(4):413–421, July 1978.

[Kontoyiannis and Suhov 1] I. Kontoyiannis and Yu. M. Suhov, Prefixes and the Entropy Rate for Long-range Sources, in *Probability Statistics and Optimization*, F. P. Kelly, ed. Chichester, England: Wiley, 1994, pp. 89–98.

[Kontoyiannis and Suhov 2] I. Kontoyiannis and Yu. M. Suhov, Stationary Entropy Estimation via String Matching, in *Proceedings of the Data Compression Conference*, Snowbird, Utah, April 1996.

[Kontoyiannis, Algoet and Suhov] I. Kontoyiannis, P.H. Algoet and Yu. M. Suhov, Two Consistent Entropy Estimates for Stationary Processes and Random Fields, in preparation to be submitted to *IEEE Transactions on Information Theory.*

[Lapidoth 1] S. Shamai and Amos Lapidoth. Bounds on the Capacity of a Spectrally Constrained Poisson Channel. *IEEE Transactions on Information Theory*, 39(1):19-29, January 1993.

[Lapidoth 2] Amos Lapidoth. On the Reliability Function of the Ideal Poisson Channel with Noiseless Feedback. *IEEE Transactions on Information Theory*, 39(2):491-503, March 1993.

[Lapidoth 3] Amos Lapidoth. The Performance of Convolutional Codes on the Block Erasure Channel Using Various Finite Interleaving Techniques. *IEEE Transactions on Information Theory*, 40(5):1459-1473, September 1994.

[Ordentlich] E. Ordentlich. A Class of Optimal Coding Schemes for Moving Average Additive Gaussian Noise Channels with Feedback. *Proceedings of the IEEE International Symposium on Information Theory*, p.467, June 1994.

[Pombra and Cover] S. Pombra and T. Cover. Non-White Gaussian Multiple Access Channels with Feedback, *IEEE Transactions on Information Theory*, 40(3):885-892, May 1994.

4 Publications Supported by JSEP

4.1 Ph.D. Theses Supported by JSEP

A. Lapidoth, "Mismatched Decoding of the Multiple-Access Channel and Some Related Issues in Lossy Source Compression," August 1995.

4.2 Published Papers Supported by JSEP

1. S. Pombra and T. Cover. Non-White Gaussian Multiple Access Channels with Feedback, *IEEE Transactions on Information Theory*, 40(3):885-892, May 1994.

2. Z. Zhang and T. Cover. On the Maximum Entropy of the Sum of Two Dependent Random Variables. *IEEE Transactions on Information Theory*, 40(4):1244-1246, July 1994.

3. V. Castelli and T. Cover. On the Exponential Value of Labeled Samples. *Pattern Recognition Letters*, 16:105-111, January 1995.

4.3 Papers Submitted for Publication

1. T. Cover and E. Ordentlich. Universal Portfolios with Side Information. To appear in *IEEE Transactions on Information Theory.*

2. P. Fahn. Maxwell's Demon and the Entropy Cost of Information. To appear in *Foundations of Physics.*

3. I. Kontoyiannis, P.H. Algoet and Yu. M. Suhov, Two Consistent Entropy Estimates for Stationary Processes and Random Fields, in preparation to be submitted to *IEEE Transactions on Information Theory.*

4. A. Lapidoth. Mismatched Decoding and the Multiple-Access Channel. *Stanford University Statistics Department Technical Report No.87*, February 1995. Under review by *IEEE Transactions on Information Theory.*

5. E. Ordentlich. On the Factor-of-Two Bound for Gaussian Multiple Access Channels with Feedback. Submitted to *IEEE Transactions on Information Theory.*

6. E. Ordentlich and T.M. Cover. Max-Min Optimal Investing. To appear in *Proceedings of 1996 IEEE/IAFE Conference on Computational Intelligence for Financial Engineering.*

DOCUMENT 5

Hierarchical Adaptive Microstructures: Smart Steels

AD-A318433

October 1996

Northwestern University

Evanston, IL

SF 298 MASTER COPY KEEP THIS COPY FOR REPRODUCTION PURPOSES

REPORT DOCUMENTATION PAGE

Form Approved OMB NO. 0704-0188

1. AGENCY USE ONLY *(Leave blank)*	2. REPORT DATE	3. REPORT TYPE AND DATES COVERED
	21 October 1996	Final, Sept 93 - 29 Aug 96

4. TITLE AND SUBTITLE

Hierarchical Adaptive Microstructures: Smart Steels

5. FUNDING NUMBERS

DAAH04-93-G-0471

6. AUTHOR(S)

Gregory B. Olson

7. PERFORMING ORGANIZATION NAMES(S) AND ADDRESS(ES)

Northwestern University
633 North Clark Street
Evanston,,IL 60208-1110

8. PERFORMING ORGANIZATION REPORT NUMBER

9. SPONSORING / MONITORING AGENCY NAME(S) AND ADDRESS(ES)

U.S. Army Research Office
P.O. Box 12211
Research Triangle Park, NC 27709-2211

10. SPONSORING / MONITORING AGENCY REPORT NUMBER

ARO 31576.1-MS

11. SUPPLEMENTARY NOTES

The views, opinions and/or findings contained in this report are those of the author(s) and should not be construed as an official Department of the Army position, policy or decision, unless so designated by other documentation.

12a. DISTRIBUTION / AVAILABILITY STATEMENT

Approved for public release; distribution unlimited.

12b. DISTRIBUTION CODE

13. ABSTRACT *(Maximum 200 words)*

Inspired by biomimetic concepts, a systems approach to materials design is extended to hierarchical adaptive microstructures undergoing a programmed dynamic evolution in both processing and service to achieve novel combinations of properties. Fundamental principles are developed to support rational design of (a) high-toughness ultrahigh-strength martensitic steels of interest for advanced armor and high performance gear applications, and (b) "smart composite" ferrous superalloys for damage tolerant high temperature applications in advanced tank propulsion systems. Theoretical modelling and high resolution microanalytical experiments in the martensitic alloys address control of autocatalytic coherent precipitation to achieve efficient strengthening without embrittlement, and the controlled precipitation of optimal stability metastable austenite for adaptive dilatant transformation plasticity tuned to crack-tip stress states for efficient interaction with strain localization processes in ductile fracture. Novel composite strategies address thermodynamically compatible shape-memory alloy reinforcement for pseudoelastic crack-bridge toughening of high temperature superalloys, combined with self-healing of low temperature damage by shape-memory-assisted crack rewelding at service temperatures.

14. SUBJECT TERMS	15. NUMBER IF PAGES
Materials Design, Hierarchical Structures, Smart Materials	49
	16. PRICE CODE

17. SECURITY CLASSIFICATION OR REPORT	18. SECURITY CLASSIFICATION OF THIS PAGE	19. SECURITY CLASSIFICATION OF ABSTRACT	20. LIMITATION OF ABSTRACT
UNCLASSIFIED	UNCLASSIFIED	UNCLASSIFIED	UL

HIERARCHICAL ADAPTIVE MICROSTRUCTURES: SMART STEELS

FINAL PROGRESS REPORT

G. B. OLSON

OCTOBER 21, 1996

U.S. ARMY RESEARCH OFFICE

GRANT NUMBER DAAH04-93-G-0471

NORTHWESTERN UNIVERSITY

Foreword: Materials as Hierarchical Systems

The late C. S. Smith [1] expounded a "systems" view of materials as hierarchical structures with properties governed by dynamic evolution in processing and in service. The Smith Philosophy has been developed into a methodology for rational design of complex materials, pioneered by the multi-institutional Steel Research Group (SRG) program centered at Northwestern University [2-4], demonstrating successful application in high toughness ultrahigh-strength alloy steels [4,5]. This view of a secondary-hardening martensitic alloy steel as a system is summarized in Figure 1 [2], depicting the hierarchy of microstructural subsystems controlling the required set of properties for desired performance, and the sequential processing subsystems which in turn control structure. Organized within this framework, basic research integrating materials science, applied mechanics and quantum physics has focused on key process/structure and structure/property relations, defining quantitative microstructural objectives expressible in thermodynamic terms (including scaling factors governing dynamic evolution), and the THERMOCALC thermochemical database and software system [6] has been applied as an integrative design tool predicting multicomponent alloy composition capable of achieving desired multiphase microstructures under prescribed processing conditions. The successful application of this approach in ultrahigh strength steels has made possible an undergraduate course in Materials Design [3], and the extension of thermodynamics-based systems design to ceramics and polymers is now being undertaken within the Department of Materials Science and Engineering at Northwestern [7].

C. S. Smith also emphasized the strong parallels between engineering materials and the hierarchical structures of the biological world [1,8]. The discovery that relatively primitive biological systems such as viruses and bacteria exploit such sophisticated materials technology as martensitic transformation plasticity and the shape memory effect [9] reinforces this parallelism. In response, an active area of current investigation is the field of biomimetics [10,11] in which complex biological systems are investigated to incorporate biological principles in the rational design of more sophisticated engineering materials. This has inspired the notion of extending materials structure to both higher levels of hierarchy and more dynamic character to achieve "adaptive" or "smart" microstructures programmed to evolve along predetermined pathways in response to a given stimulus to achieve novel properties. Such programming "brings to life" Smith's seminal vision of dynamic hierarchical materials.

The research reported here is aimed at extending the SRG systems design approach to higher levels of structural hierarchy, while incorporating more dynamic character in the form of adaptive system concepts via a synergistic integration of materials science and applied mechanics. The research addresses both the methodology of rational design at new levels of materials complexity, and the fundamental principles of specific materials behaviors necessary to support quantitative design. Research addresses adaptive multilevel microstructures in two broad areas for applications of advanced ferrous alloys:

(a) Gradient Systems with application in high performance gear technology and advanced armor, achieving novel strength/toughness combinations through control of coherent carbide precipitation in processing and tuned-stability cracktip transformation plasticity in service.

(b) Biomimetic Laminate Systems combining an oxidation resistant and high-temperature creep resistant matrix alloy with a thermodynamically compatible ductile reinforcement consisting of a shape memory alloy imparting biologically-inspired ductile-crack-bridge toughening via thermoelastic martensite pseudoelasticity at low temperatures,

and shape-memory-induced crack clamping for diffusional damage healing at high temperatures.

These areas are chosen both to represent challenging problems in hierarchical design and to respond to performance needs specific to Army applications which pose some of the most severe requirements for high performance ferrous alloys. Designed gradient systems offer the potential for a new generation of high power density gear systems exploiting the greatly increased fatigue strength of higher case hardness levels as well as the greater thermal stability of secondary hardening steels to allow both lighter weight gears and higher gear system operating temperatures desired for helicopter transmission systems. Tough high-hardness alloys offer a new generation of shatter-resistant ultrahard armor steels with higher V_{50} ballistic penetration resistance and greatly improved resistance to plastic shear localization, of particular interest for lighter aircraft armor systems and ballistically tolerant components. The especially challenging problem of the biomimetic laminates not only tests the limits of materials design, but holds promise for tank turbine applications such as the current AGT1500 which makes extensive use of ferrous superalloys. Sufficient improvement of creep-strength/ductility combinations in ferritic-based composites would allow exploitation of their superior thermal conductivity and lower thermal expansion to displace current austenitic alloys.

TABLE OF CONTENTS

LIST OF APPENDIXES, ILLUSTRATIONS AND TABLES

Research Progress

A. Problem Statement

While quantitative property objectives are important to obtain sufficient focus of basic research coordinated within an interdisciplinary systems design framework, the primary objectives of this research effort are the fundamental principles and basic data necessary to support rational design. This includes the principles of microstructural evolution during coherent carbide precipitation for efficient strengthening without embrittlement, the control of metastable austenite precipitation for optimal-stability transformation toughening, the behavior of pseudoelastic crack-bridge toughening, and the shape-memory-based healing of internal composite damage. The research emphasizes the dynamics of microstructural evolution in processing and in service, and the design methodology for control of multilevel dynamic hierarchical microstructures as programmed adaptive systems.

Specific property targets which guide the conceptual design of prototype materials for evaluation are a case hardness of R_c70 for the secondary hardening gear steels, offering the potential for a 60 pct. increase in contact fatigue strength. Desired core properties should maintain a K_{IC} toughness of >60 MPa$\sqrt{m}$ at R_c50 hardness to provide a critical flaw size superior to current aerospace gear steels, while maintaining thermal stability up to 400C. Armor steel objectives are a transformation toughened secondary hardening steel of R_c57 hardness with $K_{IC} > 80$ MPa$\sqrt{m}$ for shatter resistance. Specific operating temperature requirements for the shape-memory reinforced superalloy laminates would be 600-700C with a 10^5hr creep strength of 100 MPa.

B. Summary of Results

B.1 Gradient Systems

The system structure of Figure 2 represents our long-term goal in expanding our approach to high power density gear systems to higher levels of structural hierarchy. The approach considers not only the case/core gradient system of the gear steel itself, but the integrated design of compatible surface hard coatings and associated interfaces, ultimately incorporating design of gear shape to optimally exploit new material properties. Also represented are alternative processing routes to provide cost-effective manufacturing strategies for specific application areas. Research thus far has addressed the conventional forging and machining route appropriate to military helicopters, focussing on the case/core gear steel subsystem.

Before further discussion of the gradient gear steel, we next examine the underlying phenomena allowing the desired control of strength and toughness in such systems.

a) Strengthening

The first dynamic problem of interest in the systems of Figures 1 and 2 is the evolution of coherent carbide precipitation controlling strength. The pioneering work of Speich [12] established that good toughness in secondary hardening alloy steels demands near-completion of M_2C alloy carbide precipitation in order to dissolve transient cementite (Fe_3C) particles that otherwise contribute to microvoid nucleation during ductile fracture. The challenge to maintaining strength in such an overaged condition is to maintain a fine carbide particle size. A thorough electron microscopy study of M_2C precipitation in the commercial AF1410 steel [13] was performed in the doctoral research of J. S. Montgomery (now at ARL/MD) in conjunction with Small-Angle Neutron Scattering (SANS) studies by Weertman and coworkers [14],

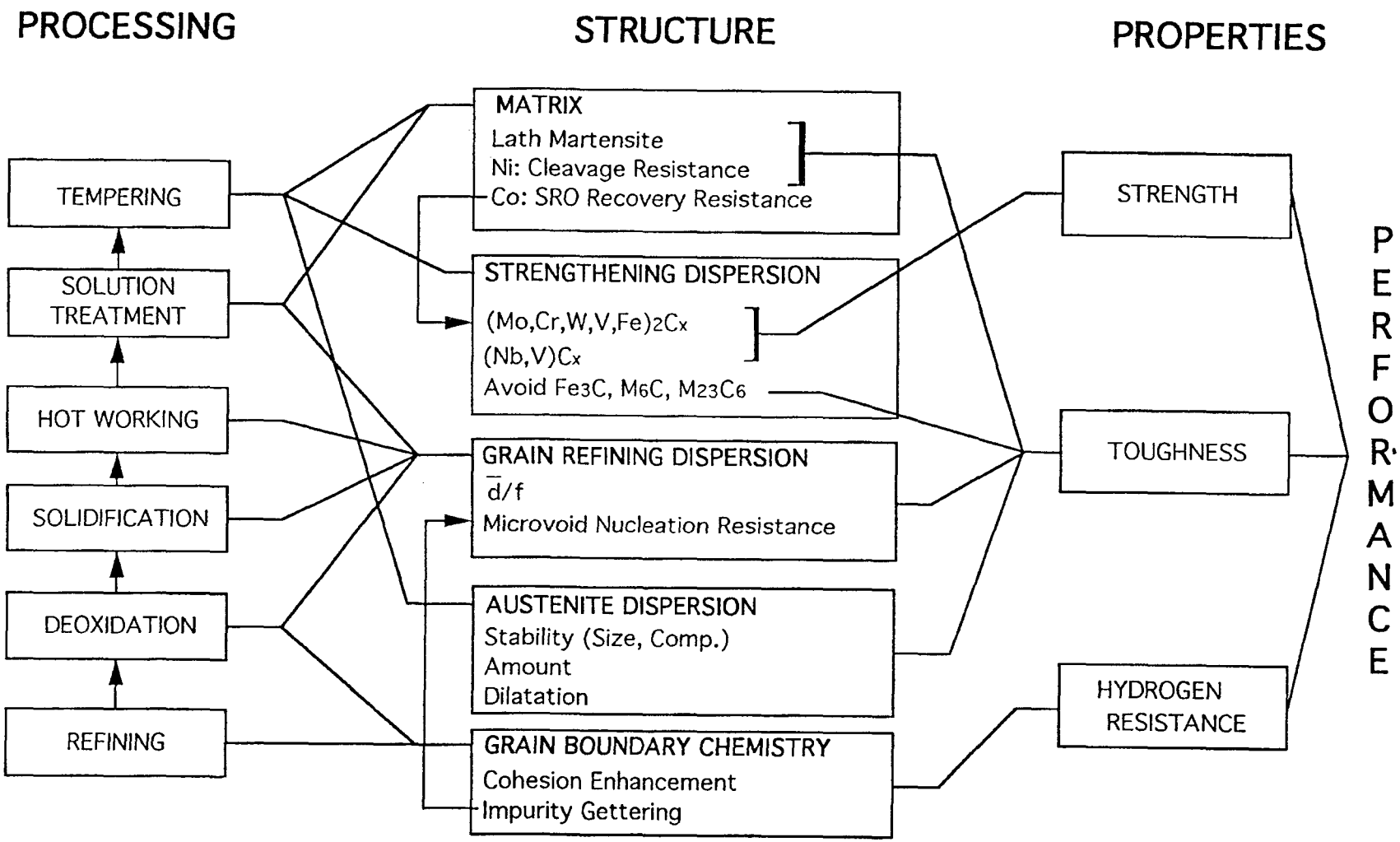

Figure 1. System structure of secondary hardening martensitic alloy steel.

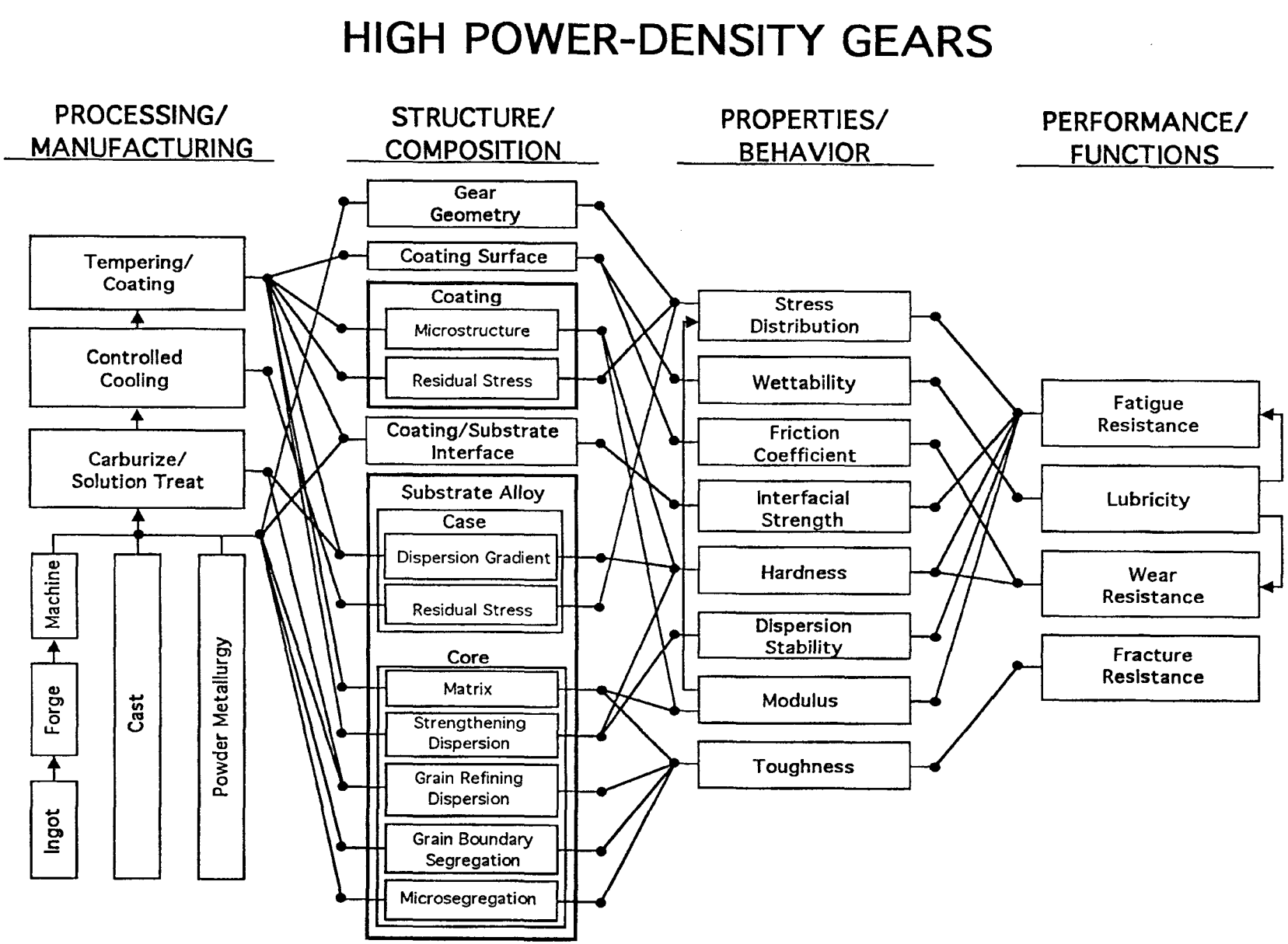

Figure 2. System structure of high power density gears.

demonstrating coherent precipitation behavior consistent with recent theory of precipitation at high supersaturations [15,16]. In this regime the fundamental scaling factor governing particle size (and thus alloy strength) is the initial critical nucleus size which scales inversely with the thermodynamic driving force for precipitation; the time scale of precipitation is governed by a diffusion time defined by the coarsening rate constant. To compute the thermodynamic driving force for coherent M_2C precipitation, the doctoral research of K. C. King with Professors T. Mura and P. Voorhees addressed the elastic self energy of the coherent carbides [17], and also explored the elastic interactions with dislocations during heterogeneous nucleation [18]. Incorporating the composition dependence of the carbide lattice parameters, the THERMOCALC chemical thermodynamic database was then modified to incorporate the additional elastic self energy contribution to the thermodynamics of coherent precipitation. To control the time scale of precipitation, theories of coarsening kinetics in multicomponent systems were developed by Kuehmann & Voorhees [19] and Umantsev [20] to define a multicomponent diffusional rate constant.

Our more recent work has tested model predictions in a series of 16Co-5Ni-0.24C steels with the Cr and Mo contents represented in Figure 3 displaying contour plots of predicted coherent precipitation driving forces and coarsening rate constants. An X-ray diffraction study of the precipitation hardening behavior of these alloys was initiated by Visiting Scientist S. Endo of NKK Japan and correlated with model predictions by Research Scientist C. J. Kuehmann [4]. Measured peak hardness shows a strong correlation with the coherent precipitation driving force, Figure 4, after taking into account the "paraequilibrium" condition of prior precipitation of cementite under carbon diffusion control. Figure 5 shows a good correlation of the measured precipitation half time and the predicted multicomponent coarsening rate constant calculated for a condition of 50% relative supersaturation. The models thus provide the basis for thermodynamic prediction of strengthening and precipitation rate with useful accuracy.

Toward improved precision of the M_2C coherent thermodynamics, the recently completed doctoral research of C. Knepfler [21], with ceramist Prof. K. Faber, has addressed the synthesis and characterization of $(Mo,Cr,V,Fe)_2C$ carbides in bulk form, measuring the composition dependence of lattice parameters, thermal expansion and isotropic elastic moduli as inputs into a more precise treatment of the composition and temperature dependence of the carbide elastic self energy. Measured lattice parameters of the $(Mo,Cr)_2C$ system are summarized in Figure 6. Measured elastic constants were also applied to an analysis of the critical particle size for the shear/bypass transition in precipitation strengthening of steels, and carbide heat capacity vs. temperature was measured defining Debye temperatures for a more precise description of the M_2C chemical thermodynamics.

The doctoral research of R-H. Liarng with Prof. Mura has incorporated Knepfler's measurements in refined calculations of the carbide elastic self energy in an iron-based matrix, taking into account the differing elastic constants of matrix and particle, and the role of particle shape. Figure 7 depicts computed elastic self energies vs. particle/matrix lattice parameter ratios for two particle shapes (prolate spheroids of aspect ratio 1 and 3) using typical values of the carbide shear modulus. Liarng also computed internal stresses on carbide shear systems relevant to coherency loss mechanisms, predicted solute distributions around coherent particles, and considered interparticle elastic interactions promoting autocatalytic nucleation. As the transformation eigenstrains for a coherent M_2C carbide in an Fe matrix are quite high, these linear elastic calculations are regarded as upper bound estimates of self energies and local stresses. To rationalize observed coherent nucleation conditions and coherent particle compositions measured by atom-probe microanalysis, it has been necessary to apply a correction factor of 1/3 to the computed self energies. Liarng has performed lower bound self energy estimates by excluding the energy density contributions of highly strained regions likely to be

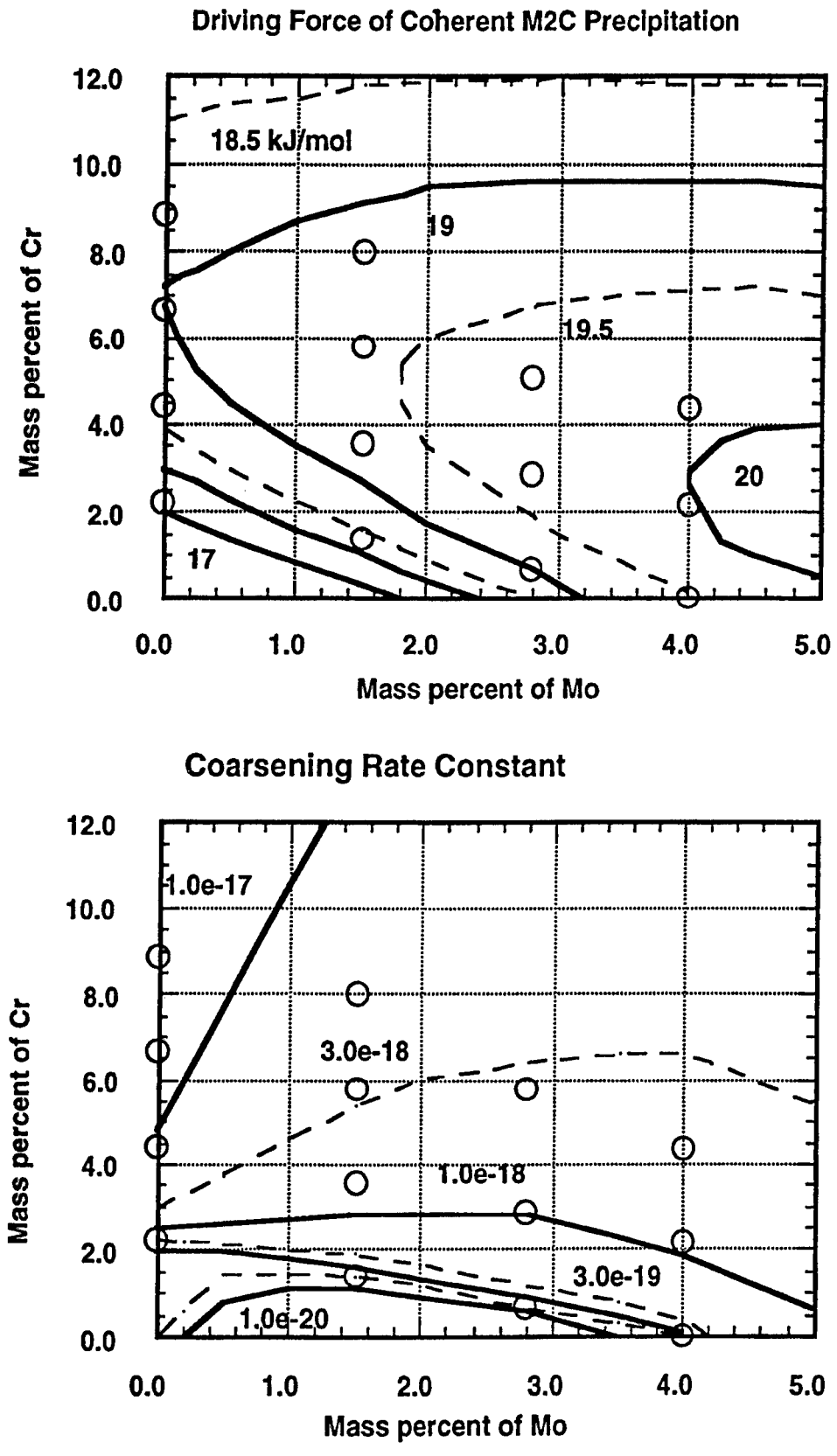

Figure 3. Contour plots of predicted coherent M_2C precipitation driving force and coarsening rate constant for 16Co-5Ni-0.24C steels at 510C vs. Cr and Mo content. Open points denote compositions of experimental alloy series.

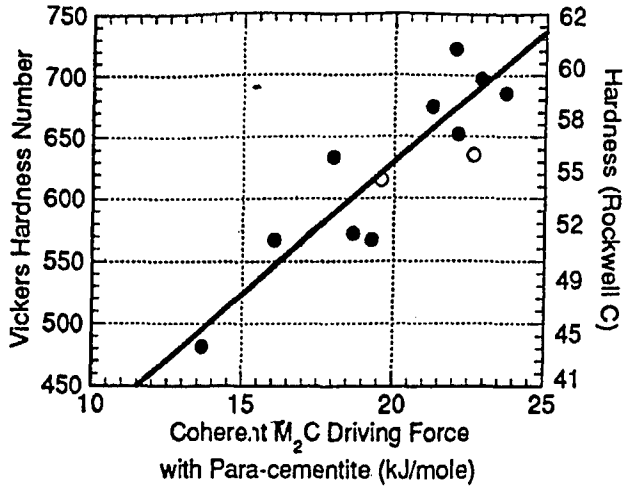

Figure 4. Correlation of Peak Hardness of alloys of Figure 3 with predicted coherent M_2C driving force after precipitation of paraequilibrium cementite [4].

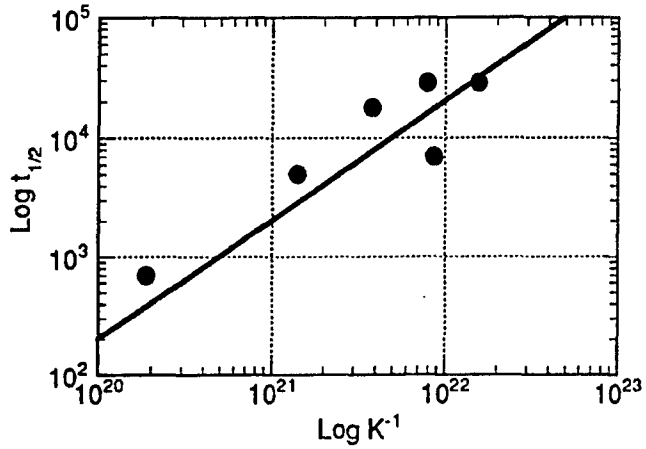

Figure 5. Correlation of precipitation half-completion time with predicted M_2C multicomponent coarsening rate constant [4].

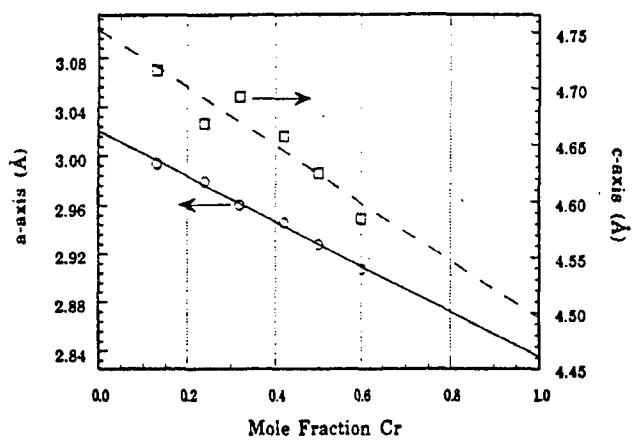

Figure 6. Measured composition dependence of a and c lattice parameters of $(Mo_{1-X}\ Cr_X)_2C$ carbides [21].

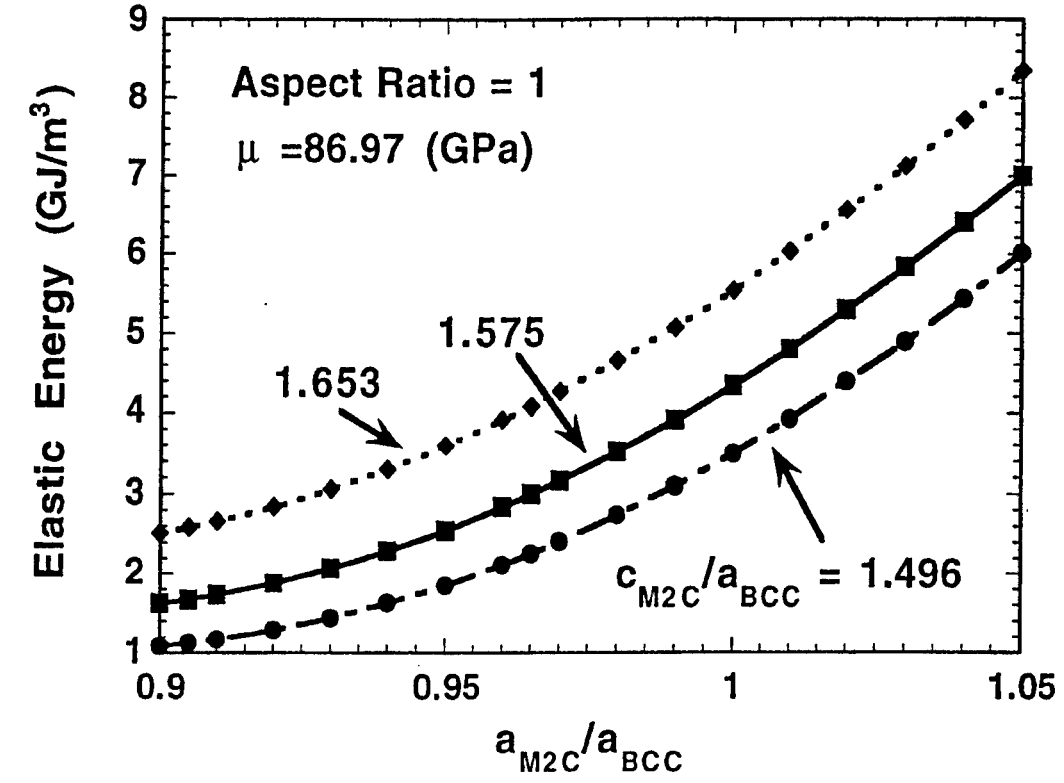

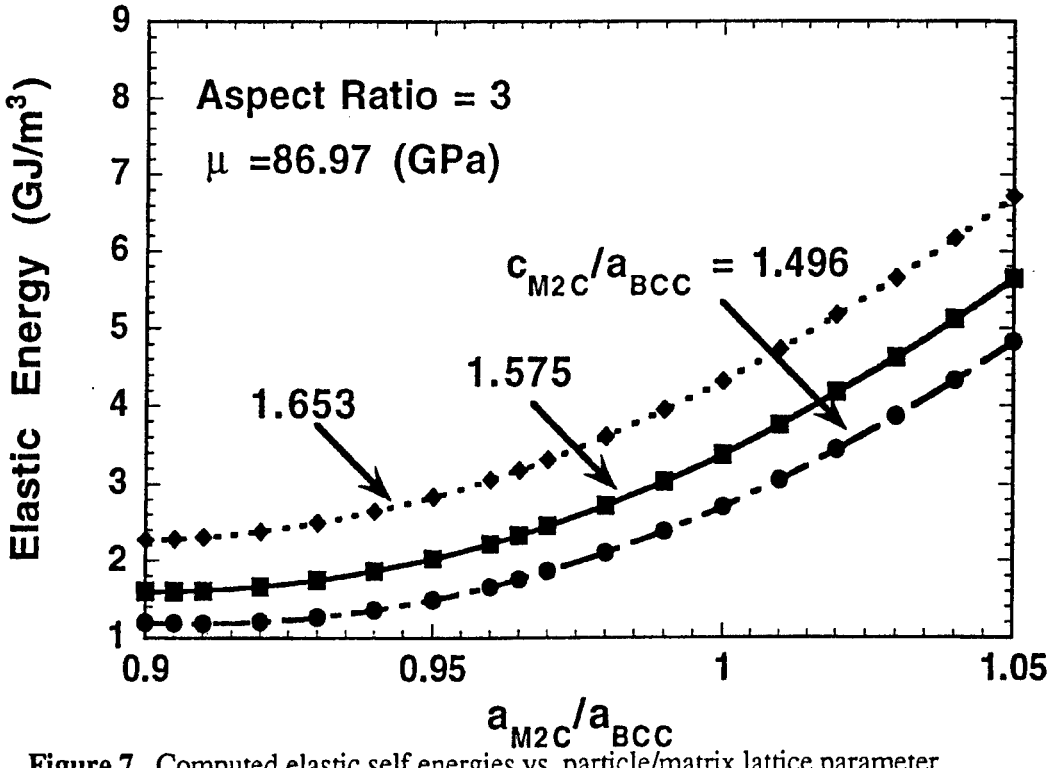

Figure 7. Computed elastic self energies vs. particle/matrix lattice parameter ratios for two shapes of coherent M_2C carbides in Fe matrix.

strongly nonlinear, similar to the dislocation core cutoff approximation, supporting correction factors of this magnitude.

Employing the more precise coherent thermodynamics provided by the improved elastic self energy estimates, the correlation of strength and thermodynamic driving force in Figure 4 can be modeled more precisely be relating driving force to particle size, and particle size to strength. The latter has been treated as part of the doctoral research of J. Wise. Figure 8 depicts the correlation of measured hardness with the Orowan-Ashby dislocation bypass strengthening equation for particles of radius R and mean spacing L, using a dislocation core size of r_o=b. The fit is based on the SANS data so far available for three of the 0.24C alloys in the series of Figure 3. The lower figure then predicts the dependence of hardness at completion of precipitation on alloy carbon content for various particle diameters, including the critical size d_c for the shear/bypass transition corresponding to a theoretical upper limit of strength. The trends are in good agreement with measured hardness and particle size in commercial and experimental alloys investigated.

b) Toughening

Early work under the SRG Program addressed toughening of UHS steels via (a) control of microvoid nucleating particle dispersions governing plastic shear localization [22-25], and (b) dispersed-phase transformation toughening by precipitation of optimal stability austenite particles [26,27]. A continuing effort under ONR support has defined requirement to resist intergranular fracture [28]. Guided by model predictions on microvoiding behavior, the recent doctoral research of C. J. Kuehmann under ARO support addressed optimization of the solution treatment of the commercial Aermet100 alloy to obtain a residual grain refining dispersion of fine TiC particles with improved resistance to microvoiding as attested by J_{IC} toughness measurements [29]. Kuehmann then explored optimization of multistep tempering treatments to achieve dispersed-phase transformation toughening in this alloy.

Our understanding of transformation toughening mechanisms has benefited from a parallel DOE-sponsored effort studying fully austenitic alloys, experimentally demonstrating the role of phase stability and dilatation [2,30-32] with numerical simulations defining the effect of transformation plasticity in enhanced resistance to plastic localization [33] and microvoiding processes [34]. ARO sponsored research has explored the application of this understanding to the control of dispersed-phase transformation plasticity in the secondary hardening martensitic steels. Our progress is summarized by the toughness-hardness plot of Figure 9. Early experiments guided by thermodynamic predictions of achievable austenite stability in the AF1410 composition boosted toughness to the AF1410-TT band employing multistep tempering to nucleate a fine dispersion of Ni enriched austenite while maintaining a sufficiently fine carbide dispersion for desired strength [26]. Our efforts to apply the same strategy to the higher strength Aermet100 alloy revealed a much tighter processing window due to the faster carbide precipitation kinetics associated with this higher Cr composition. Initial multistep tempering studies by Kuehmann [29] demonstrated transformation toughening, but at less than desired strength levels. A more thorough study was then undertaken by Visiting Scientist M. Srinivas from the Defence Metallurgical Research Laboratory, India, establishing first the detailed low temperature tempering kinetics for optimal strengthening, then interposing short intermediate temperature austenite nucleation treatments. Detailed measurement of toughness evolution was provided by relatively simple cracktip stretch-zone measurements followed by verification of promising treatments with J_{IC} tests. The results of optimal processing are represented by the Aermet100-TT and MTL1-TT band in Figure 9. These exceptional properties were obtained with both the Aermet100 composition and our V modified lower C prototype armor steel designated MTL1. The outstanding toughness and hardness combinations are seen to lie within the dashed box representing the original property objectives of the SRG program.

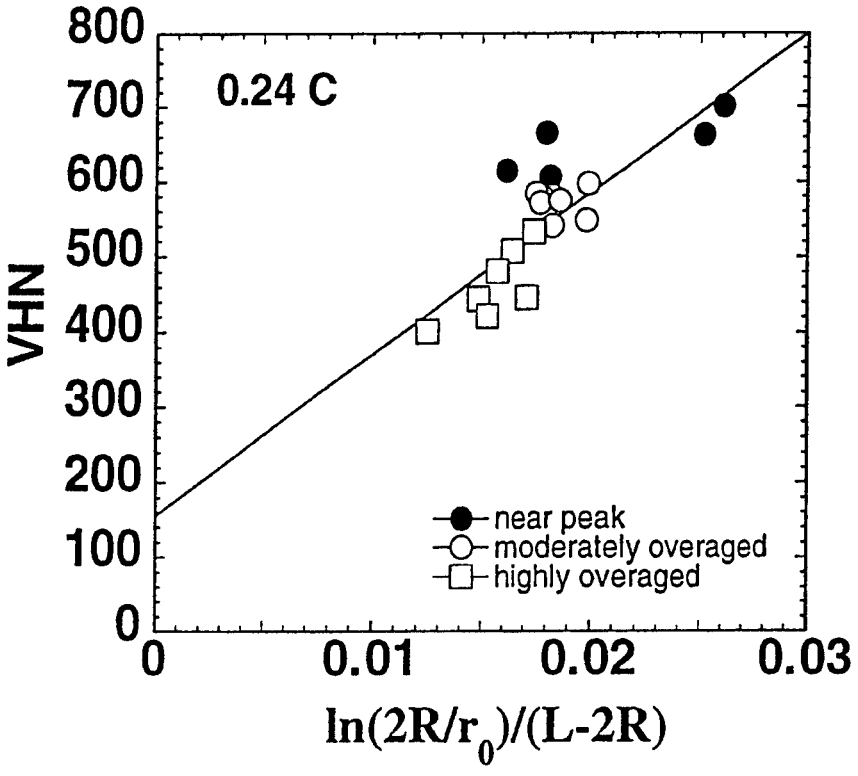

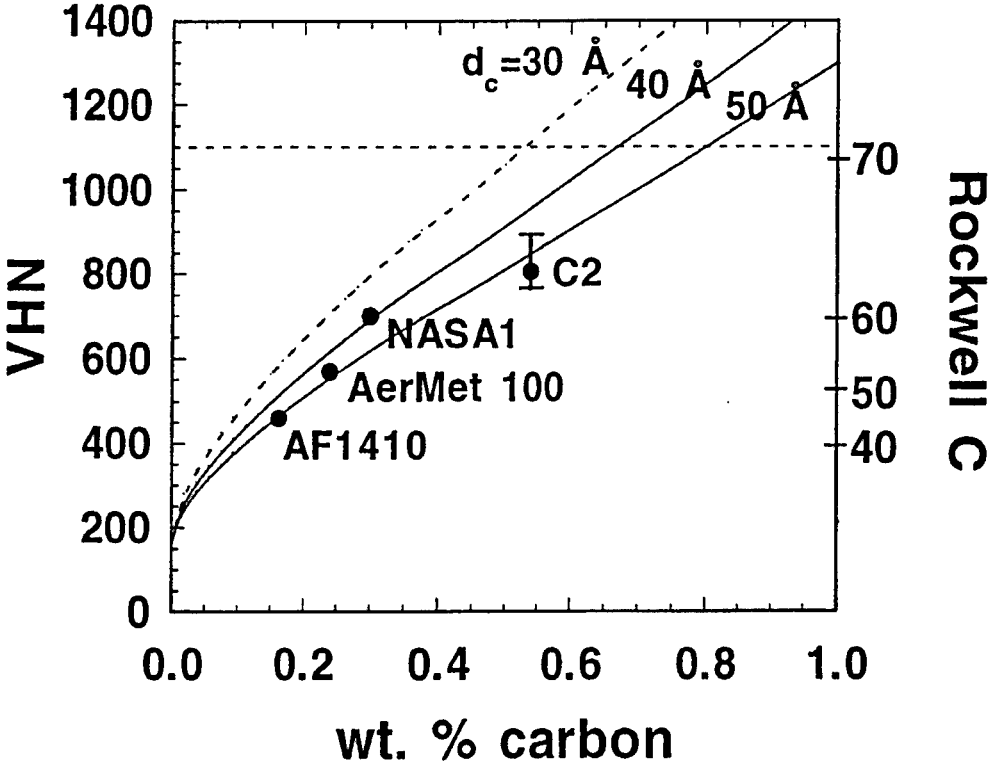

Figure 8. Correlation of measured hardness with Orowan-Ashby strengthening theory based on SANS data; predicted dependence of hardness at precipitation completion on alloy carbon content.

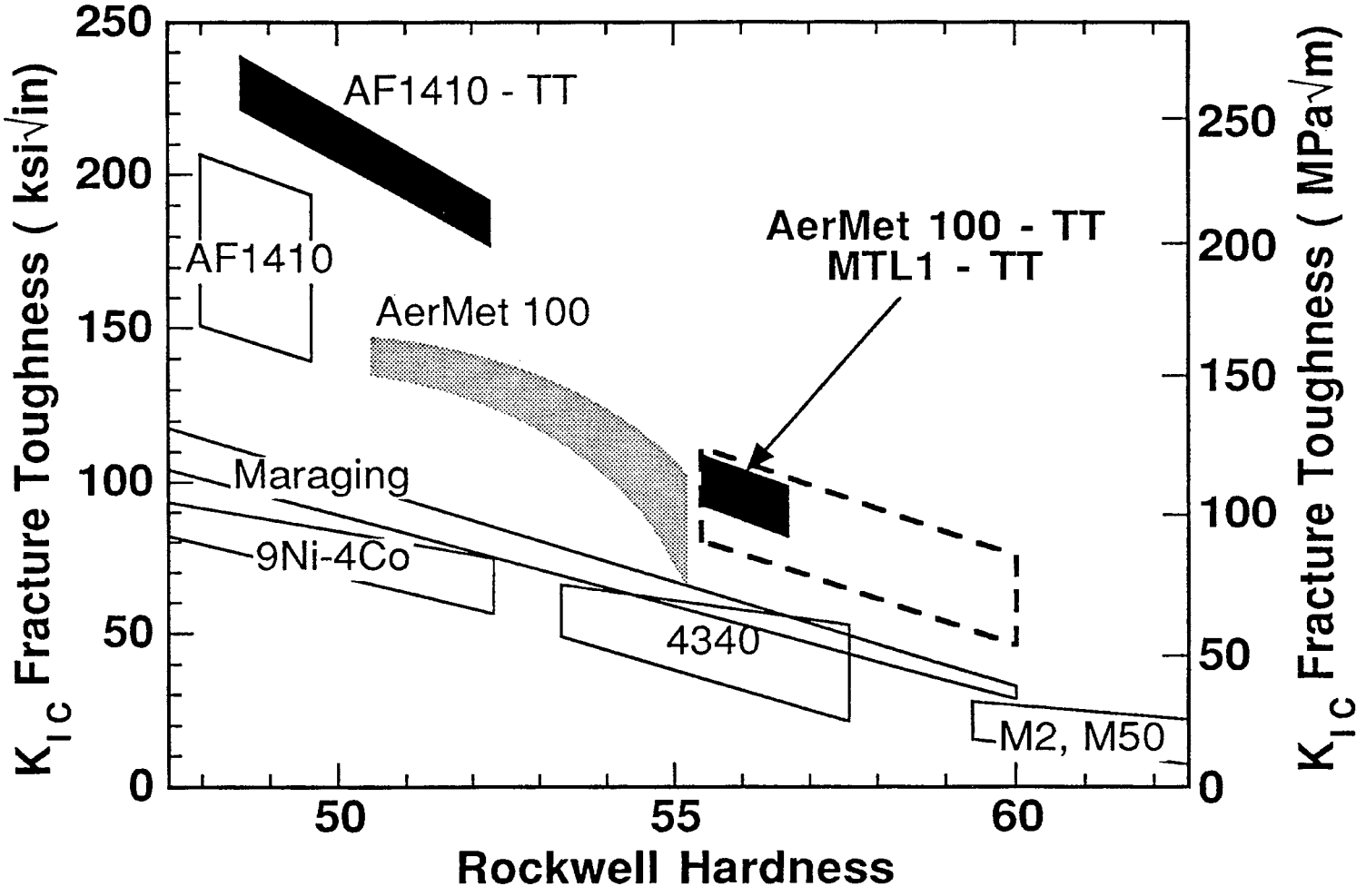

Figure 9. Toughness-hardness plot with dark bands denoting properties of transformation toughened (TT) materials; dashed box denotes original SRG objectives.

Austenite precipitation behavior in these alloys is being investigated by electron microscopy and microanalysis in the doctoral research of fellowship student H. Lippard cosupervised by Prof. V. Dravid. The dark-field micrograph of Figure 10 (using an 002_γ reflection) reveals two forms of precipitated austenite in the Aermet100-TT material of Figure 9. The microstructure is similar to our previous observations in AF1410-TT [26] in which slightly Ni enriched austenite discs at martensite lath boundaries (A) coexist with a fine dispersion of more Ni rich intralath precipitates (B); the lath boundary precipitation gives nonequilibrium austenite compositions while the composition of the fine intralath precipitates is in good agreement with equilibrium predictions. The high austenite stability responsible for toughening these UHS steels is attributed to the fine size and Ni enrichment of the latter. While the fine austenite in AF1410-TT had a particle size of 20nm, the fine particles of Figure 10 observed in Aermet100-TT are only 5nm, taxing the limits of high resolution electron microanalysis. In addition to the 200kV cold field emission Hitachi HF2000 analytical electron microscope at Northwestern, the samples have been analyzed with a Phillips CM20 at Gatan Laboratories (employing a Gatan Imaging Filter for EELS imaging with the Ni core loss L-edge) and the highest brightness 300kV cold field emission UHV VG603 STEM at Lehigh University. The apparent Ni enrichments of embedded austenite particles plotted in Figure 10 were obtained with the latter instrument, supporting the interpretation of the 5nm particles as austenite, but not allowing direct composition measurement due to extreme matrix overlap at ~100nm foil thickness.

c) Gradient Systems: Gear Steels

Case hardenable secondary hardening steels for the high power density gear systems of Figure 2 may represent the most promising area for application of the design models we are developing. This line of research originated as conceptual designs in Materials Design class projects performed in collaboration with a mechanical engineering design class who identified property objectives for a 50% weight reduction in gears. Preliminary designs comparing low temperature nitriding and high temperature carburizing led to selection of carburizing as the most promising processing route to achieve the 1mm-scale case depths needed in typical gear applications. Two generations of carburizable prototype compositions were designed and evaluated. An undergraduate project evaluating the second prototype alloy, designated C2, won 1st prize in the last TMS-AIME national student design competition [35].

Research on carburizable gradient systems for gear applications has continued in the doctoral research of J. Wise, initiated under seed funding from the Ford Motor Company. Precise treatment of the dynamics of gradient formation by carburizing has been made possible by the new DICTRA multicomponent diffusion code developed at the Royal Institute of Technology in Stockholm as an extension of the THERMOCALC system. The DICTRA system combines the thermodynamic database of THERMOCALC with a mobility database to compute the full multicomponent diffusivity matrix, and solves 1, 2, and 3 dimensional diffusion problems by a finite difference method. To apply the code to carburization of the complex multicomponent steels of interest, Wise conducted preliminary carburizing experiments on an Fe20Co10Ni alloy and determined the composition-dependent C diffusivity from measured C profiles, as summarized in Figure 11. Based on these measurements, it was found necessary to modify the DICTRA mobility database (mob4) through a Co-C interaction term to give the improved fit shown in the figure. The model was then validated by comparison with measured diffusion profiles in carburized Aermet100 steel as shown in Figure 12, demonstrating excellent agreement. Combining DICTRA diffusion simulations with the strengthening model of Figure 8 provides the basis for precise control of hardness profiles in these secondary hardening steels. The hardness profile so far obtained in the C2 prototype gear steel is compared in Figure 13 with that of a conventional gear steel. Maintaining an equivalent gradient depth, a substantial

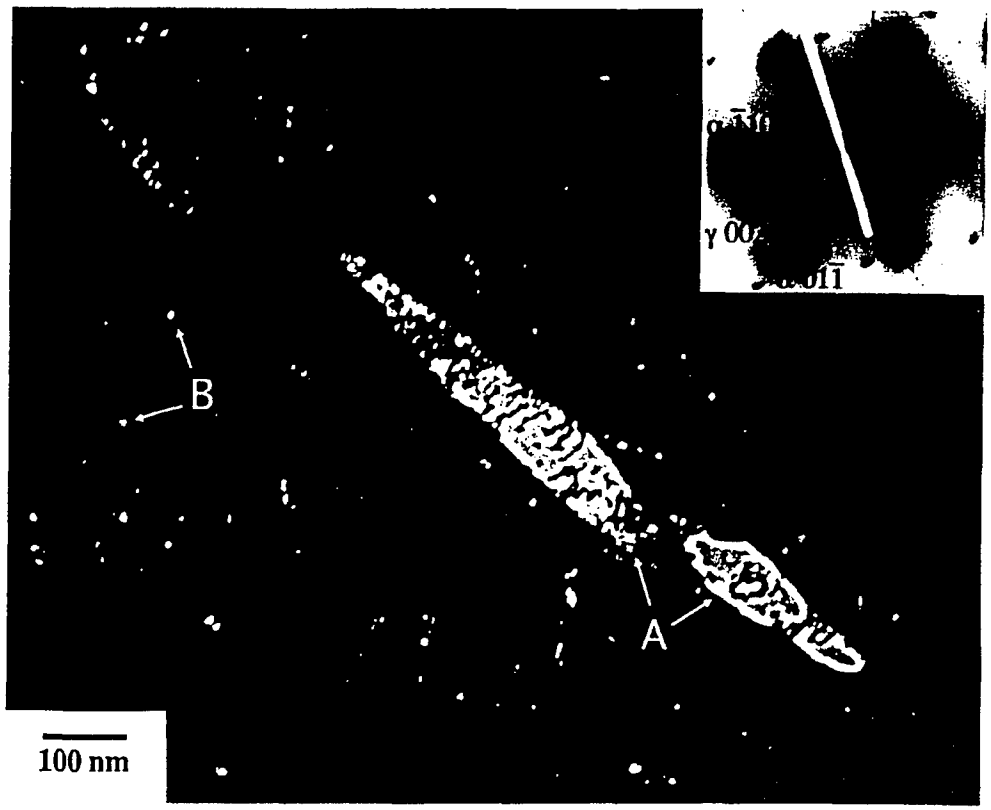

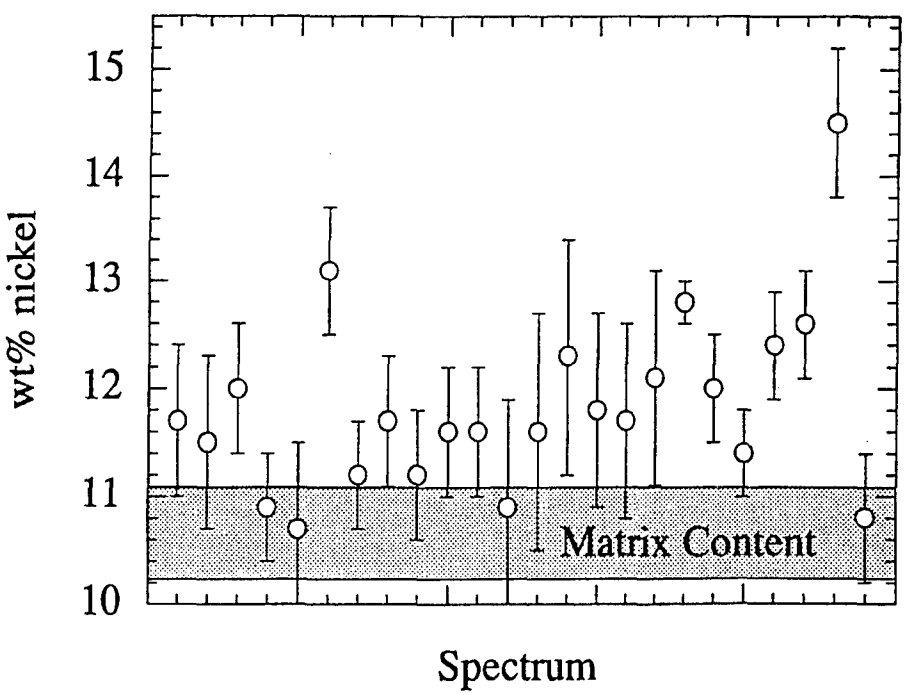

Figure 10. Dark field electron micrograph using 002_γ reflection to reveal large interlath (A) and fine (B) intralath precipitated austenite in transformation-toughened Aermet100 of Figure 9. Lower plot shows apparent Ni contents of various small B-type austenite particles using VG603 STEM microanalysis.

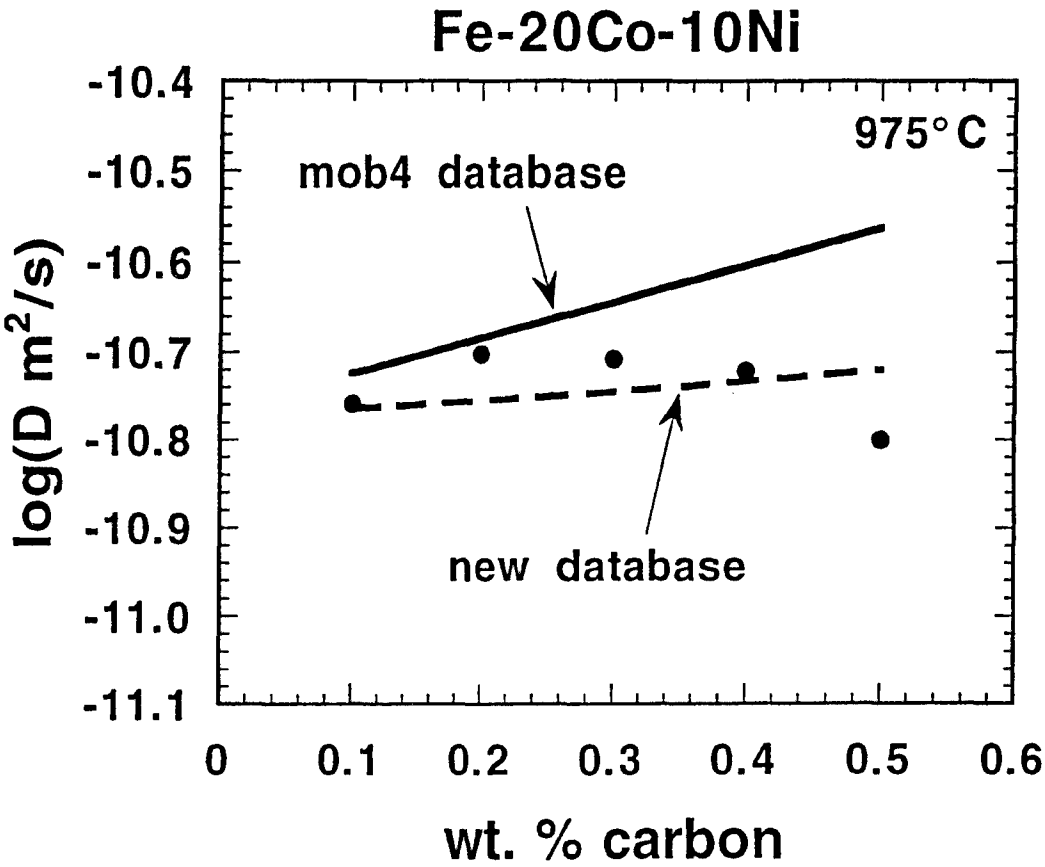

Figure 11. Carbon diffusivity determined from diffusion profiles in carburized Fe-20Co-10Ni, showing fit of new mobility database.

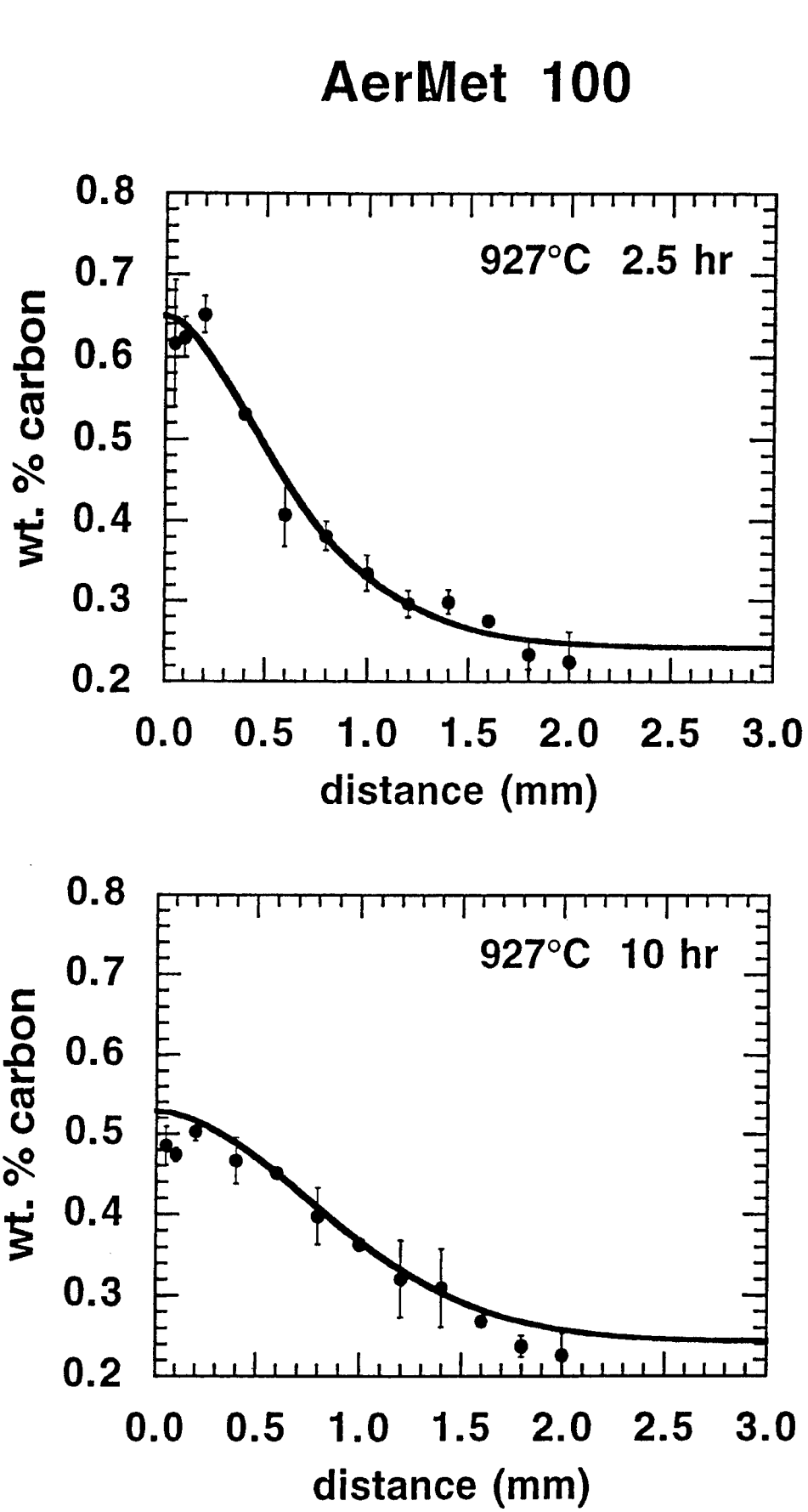

Figure 12. Comparison of measured C diffusion profiles in carburized Aermet100 steel with predictions of DICTRA simulations employing new mobility data.

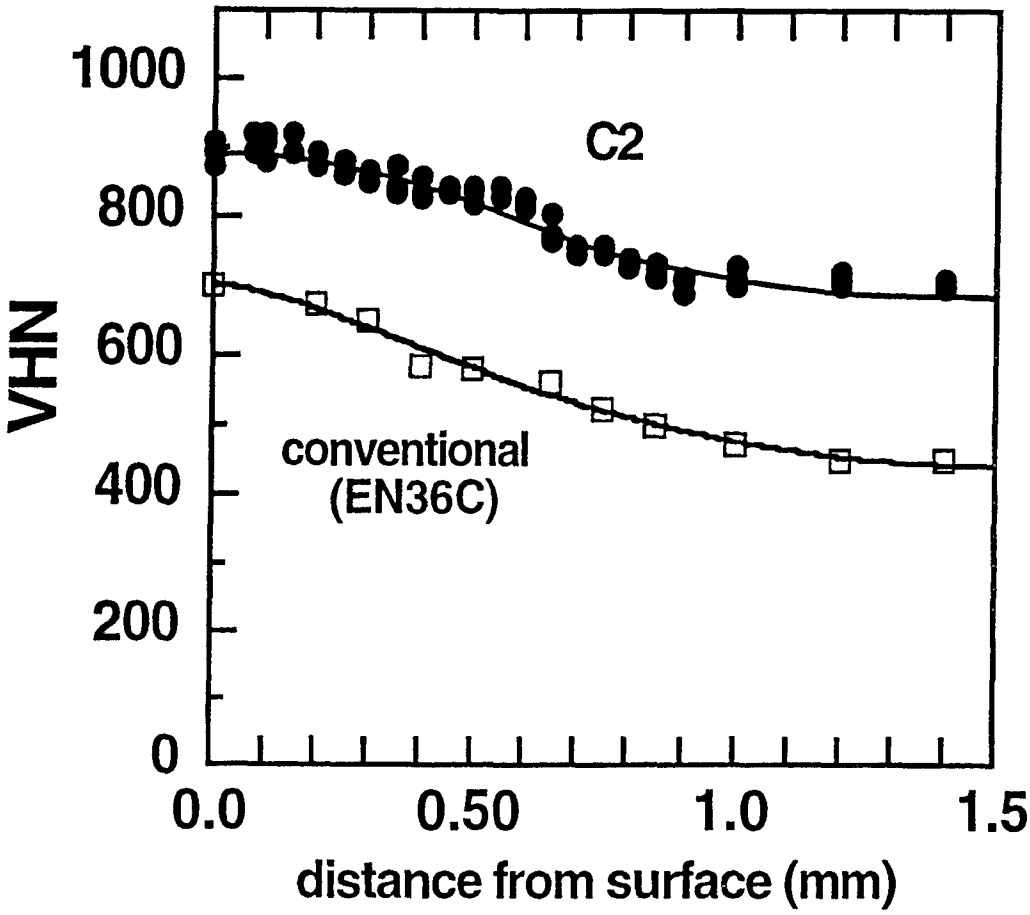

Figure 13. Hardness profile obtained in C2 prototype gear steel compared with conventional EN36C gear steel.

increment of hardness improvement has been demonstrated with a surface carbon content of 0.55C as also denoted in Figure 8.

d) High Hardness Armor Steels

Under a one-year contract from ARL/MD, formerly MTL, available SRG design tools were applied to the design of a prototype high hardness armor steel. This led to the alloy designated MTL1 in Figure 9, which was evaluated in the Masters thesis of J. Cho [29]. Employing a V addition to enhance strengthening efficiency, the alloy demonstrated properties equivalent to the Aermet100 alloy, but with lower C content (0.21C). Ballistic testing at ARL/MD demonstrated V_{50} levels at fixed plate thickness equivalent to the best monolithic armor steels. A higher carbon composition (0.25C) for higher hardness has been prepared for further evaluation at ARL/MD.

B.2 Biomimetic Laminates

Testing the limits of complexity in rational materials design incorporating biomimetic adaptive system concepts, the essential concepts of the self healing "smart steel" superalloy composite are summarized in the system chart of Figure 14. A ferritic (BCC) superalloy strengthened by a coherent dispersion of ordered B2 precipitates is reinforced by a thermodynamically compatible γ' strengthened austenitic (FCC) shape memory alloy in a laminate formed by hot rolling of a consolidated blend of prealloyed powders. The composite integrates two biomimetic concepts. At low temperatures the shape memory alloy reinforcement toughens the otherwise brittle ferritic alloy by bridging cracks via martensitic pseudoelasticity, mimicking the nonlinear polymer reinforcement of a brittle ceramic in the toughened laminate system of natural seashell [10,11]. Returning an internally damaged composite to the superalloy operating temperature, the bridges contract via the shape memory effect providing a crack clamping force to promote diffusional rewelding of cracks as a biomimetic self-healing mechanism. Thermodynamic compatibility demands that the BCC(α) and FCC (γ) alloys be in near-equilibrium with each other at hot working and solution treatment temperatures, and that the two 2-phase α+B2 and $\gamma+\gamma'$ alloys reside in an equilibrium 4-phase α+B2+$\gamma+\gamma'$ field at service temperatures. Matrix/reinforcement interfacial strength must be limited to promote crack bridging behavior, and the austenitic alloy must exhibit higher creep strength than the ferritic alloy to maintain crack clamping forces for damage healing.

The original conceptual design and preliminary feasibility calculations by an undergraduate Materials Design class project team won 2nd prize in the first TMS-AIME national student design competition [36]. Under AASERT support, the doctoral research of B. Files has investigated the realization of this concept, taking advantage of design data being generated under a ferritic superalloy project supported by EPRI. Work so far has emphasized refinement of thermodynamic models of the Fe-Ni-Al-Ti-Co-Mo system with explicit treatment of order/disorder transitions underlying miscibility gaps. The models have identified a suitable 4-phase α-B2-γ-γ' field at a service temperature of 600C in the basic Fe-Ni-Al-Ti system, as denoted by the solid points bounding the tie-tetrahedron represented within the composition tetrahedron of Figure 15. The alloy compositions denoted A and B in the figure correspond to α+B2 and $\gamma+\gamma'$ alloys with dispersion fractions of 20%. Based on a preliminary thermodynamic database, diffusion couples of A and B type alloys were prepared and reacted 24hrs at 1100C to investigate the diffusional interaction at solution temperatures where each alloy should be single-phase. The electron microanalysis data of Figure 16 (employing a Hitachi S-4500 FEG-SEM) demonstrates a sufficiently large diffusion distance of 50-100μm allowing accurate measurement of multicomponent diffusion composition trajectories. The larger diffusion distance of Al is consistent with its predicted higher diffusivity. The measured trajectories are represented in Figure 17, projected on the median Ti plane (3.3Ti) in (a) and the median Al plane (2.5Al) in (b). The S-shaped trajectory in (a) reflects the effect of the high Al diffusivity. Also represented are

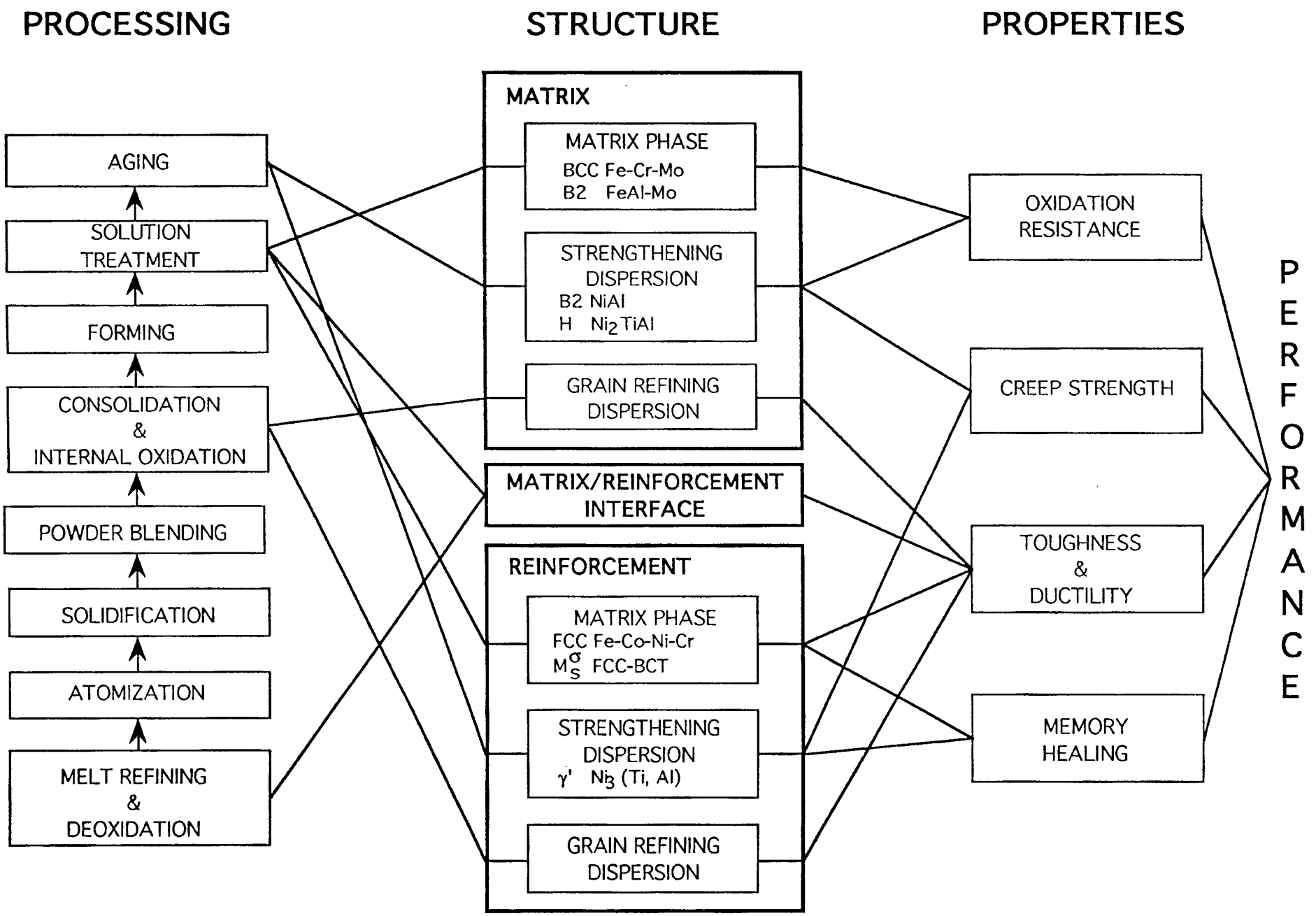

Figure 14. System structure of self-healing "smart steel" superalloy composite.

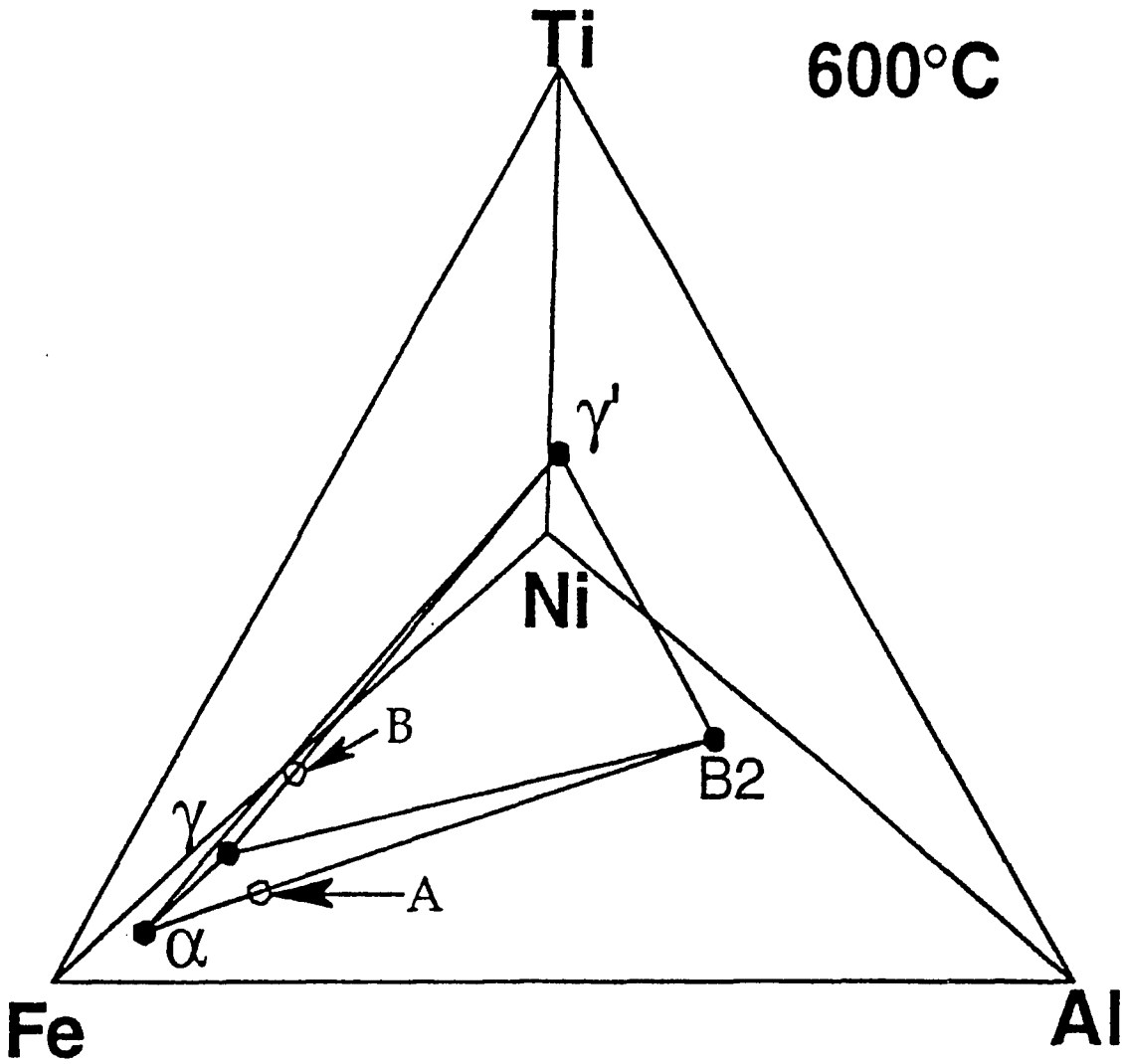

Figure 15. Computed 4-phase α-B2-γ-γ' field in Fe-Ni-Al-Ti system at 600C based on preliminary thermodynamic database. Compositions A and B represent α-B2 and γ-γ' alloys, respectively.

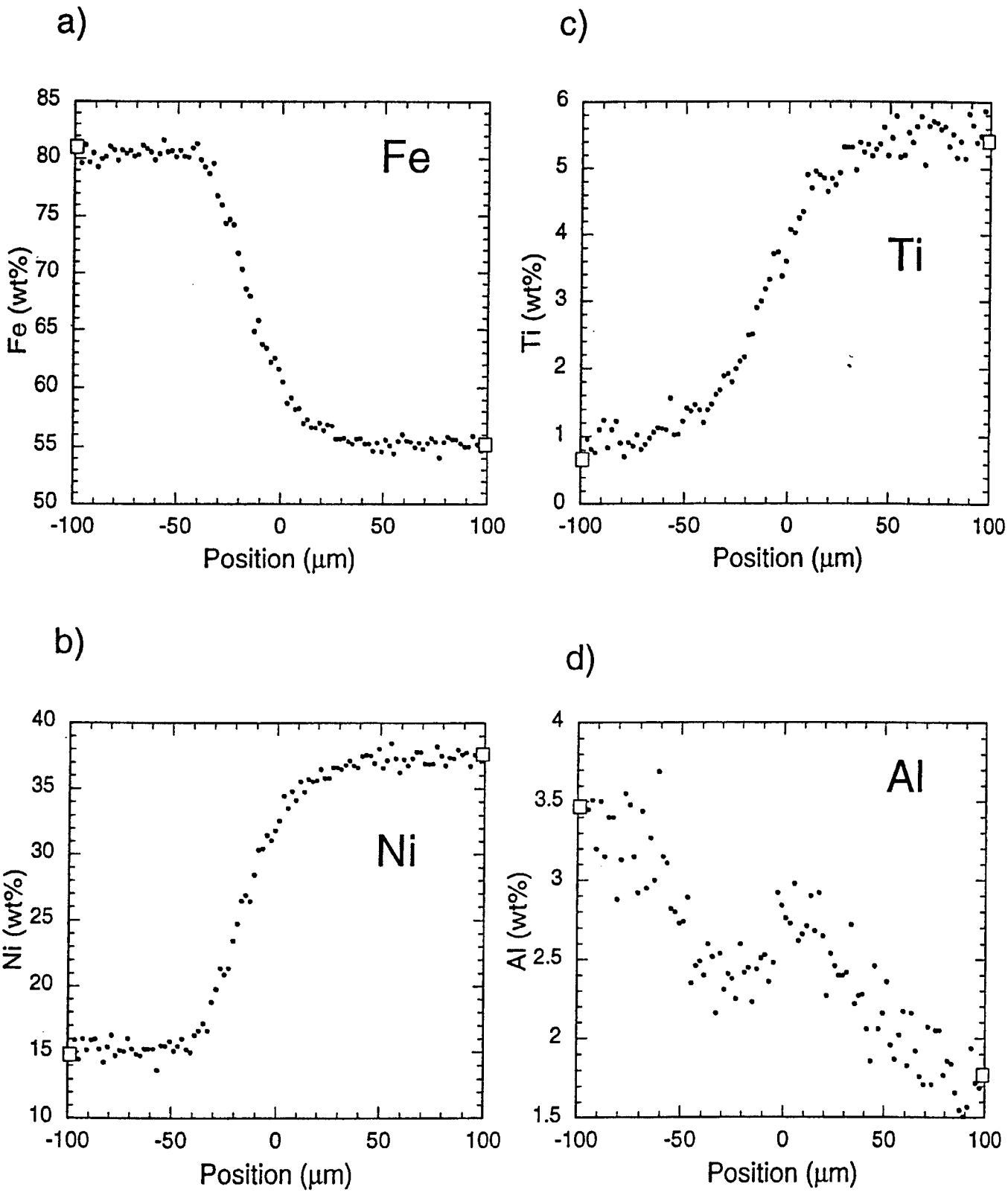

Figure 16. Measured composition profiles in diffusion couple of alloys A and B reacted 24hr at 1100C. Boxes denote bulk compositions measured far from couple interface.

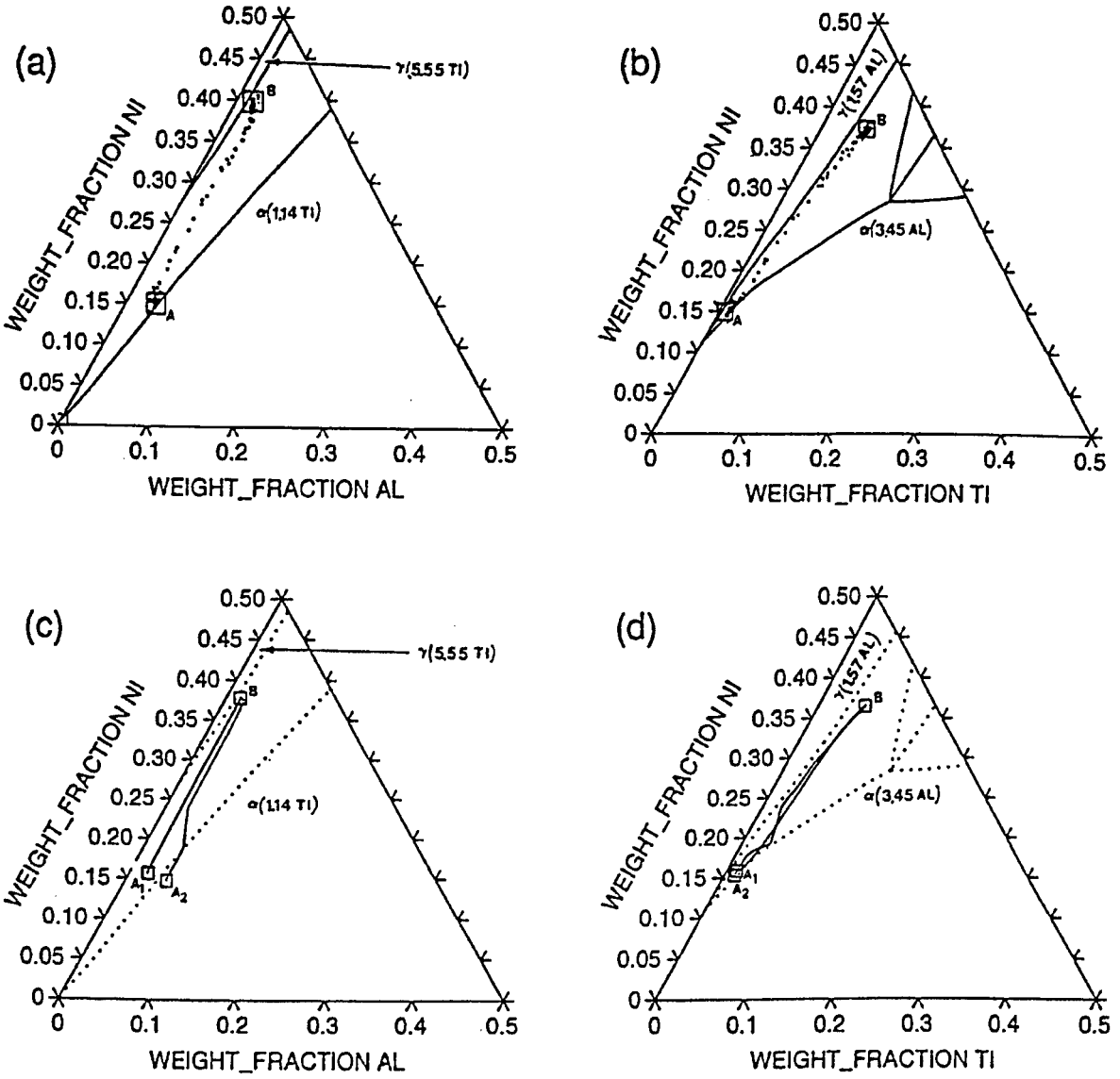

Figure 17. Measured diffusion composition trajectories in A-B couples projected on median Ti plane in (a) and median Al plane in (b). Corresponding DICTRA simulations for γ single-phase A1/B and α-γ two-phase A2/B couples in (c) and (d).

the computed boundaries of the single phase fields at the respective Ti and Al contents of alloys A and B, generated from our current database. These newer calculations indicate that alloy A is actually well within the two-phase $\alpha+\gamma$ field at 1100C. To simulate a couple between two single-phase alloys, DICTRA simulations were run modifying the A composition to the nearby single-phase α composition A2 giving the A2/B trajectories represented in (c) and (d). The "doglegs" in these projected trajectories reflect tie-lines crossing the $\gamma+\alpha$ two-phase field. Consistent with the absence of this feature in the experimental trajectories (and the lack of corresponding interface steps in Figure 16) microscopy revealed a martensitic structure in alloy A indicating the alloy was fully austenitic at 1100C. A DICTRA simulation of the interdiffusion of such a γ/γ couple is represented by that for nearby austenitic alloy A1 in (c) and (d). These preliminary couple experiments provide important input for refining the thermodynamic database to properly position the relatively narrow $\gamma+\alpha$ field in the region of interest, while also providing useful diffusivity information for further refinement of the DICTRA mobility database.

Electron micrographs in Figure 18 show that the microstructure of alloy A after aging 1 week at 600C exhibits a three-phase $\alpha+B2+\gamma$ structure with ~1μm γ particles shown in (a). The higher magnification dark field micrograph in (b) using a 100 B2 superlattice reflection shows the desired fine dispersion of coherent B2 in the α matrix. The presence of γ at 600C in this alloy, intended to be two-phase $\alpha+B2$, is in line with the finding at 1100C that the current thermodynamic database underestimates the stability of γ in this system. Further microanalysis of phase compositions will provide valuable information for refinement of the thermodynamics.

In parallel with the study of the Fe base alloys, a prototype system for testing bridging and healing concepts is being investigated mechanically using a low melting Sn-Bi alloy reinforced by TiNi shape memory alloy fibers. Blunt notch tensile specimens are employed to investigate internal cracking and healing behaviors. Experimental procedures thus developed will ultimately be applied to the Fe-base composites.

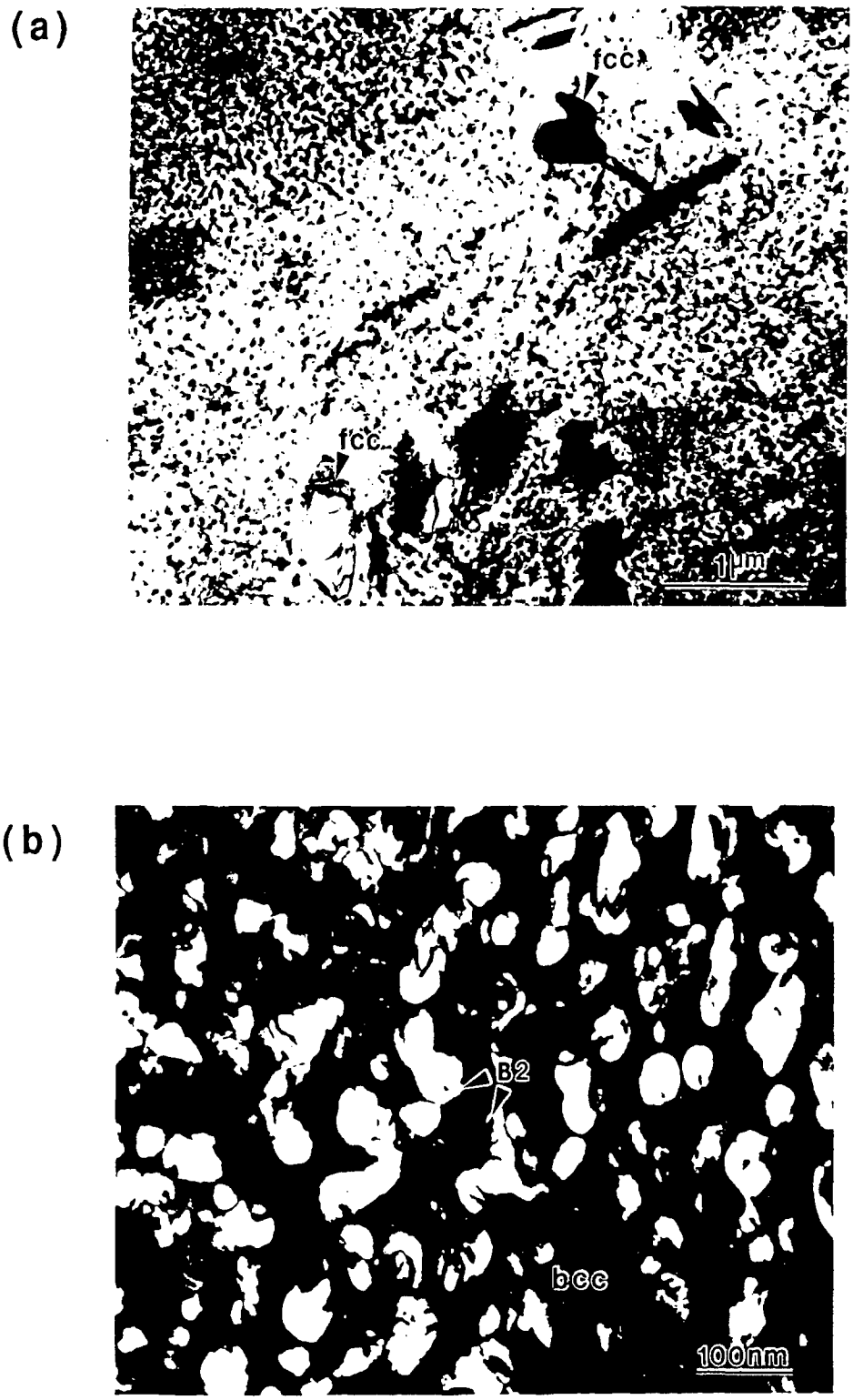

Figure 18. Electron micrographs of alloy A after aging 1 week at 600C; (a) bright field image of large γ particles in fine α-B2 matrix; (b) higher magnification dark field image using 100 B2 super-lattice reflection to reveal fine B2 dispersion in α.

C. Publications and Technical Reports

A Umantsev and G. B. Olson, "Ostwald Ripening in Multicomponent Alloys," Scripta Metall. Vol. 29 (1993) pp. 1135-1140.

C. J. Kuehmann, J. Cho, T. A. Stephenson, and G. B. Olson, "Systems Design of High Performance Steels," Metallic Materials for Lightweight Applications (40th Sagamore Army Materials Research Conference), eds. E. B. Kula and M. G. H. Wells, U.S. Government Printing Office, Washington, DC, Lake George, NY (1994) 337-355.

C. J. Kuehmann, G. B. Olson, "Computer-Aided Systems Design of Advanced Steels," Proc. International Symposium of Phase Transformations During the Thermal/Mechanical Processing of Steel - Honoring Professor Jack Kirkaldy, E. B. Hawbolt et al., eds., Metallurgical Society of the Canadian Institute of Mining, Metallurgy and Petroleum, Vancouver BC (1995) 345-356.

G. B. Olson, "Materials Design: Building a Better Martensite," to appear in Proc. C. M. Wayman International Conference on Displacive Phase Transformations and Their Applications in Materials Engineering, May 8-9, 1996, TMS-AIME.

C. J. Kuehmann and P. W. Voorhees, "Ostwald Ripening in Ternary Alloys," Met. Trans. A, 27A (1996) 937-943.

C. A. Knepfler, K. T. Faber, J. Weertman, G. B. Olson, C. R. Hubbard, O. B. Cavin, N. Packen, "High Temperature Stability and Thermal Expansion Behavior of Molybdenum-Chromium M_2C Carbides," J. Alloys & Compounds, in press.

D. Participating Scientific Personnel

Prof. Gregory B. Olson, Principle Investigator
Prof. Toshio Mura, Co-Investigator
Dr. Gautam Ghosh, Research Assistant Professor
Dr. Thomas J. Kinkus, Research Associate
Dr. Hossein Shodja, Research Associate
Dr. Alexander Umantsev, Research Associate
Shegiru Endo, Visiting Scientist
David Bergstrom, Research Assistant, Ph.D. 1995
Scott Danielson, Research Assistant, M.S./MMM 1995
Cynthia Hsieh, Research Assistant, M.S. 1994
Cheryl Knepfler, Research Assistant, Ph.D. 1994
Charles J. Kuehmann, Research Assistant, Ph.D. 1994
Ruoh-Huei Liarng, Research Assistant, Ph.D.
Henry Lippard, Research Assistant
Andrew McGeorge, Research Assistant, M.S. 1996
John Wise, Research Assistant

5. Report of Inventions

none

6. Bibliography

(*denotes papers acknowledging ARO support)

1. C. S. Smith, A Search for Structure, (1981) MIT Press: Cambridge MA

* 2. G.B. Olson, "Science of Steel," in Innovations in Ultrahigh-Strength Steel Technology, ed. G.B. Olson, M. Azrin, and E.S. Wright, Sagamore Army Materials Research Conference Proceedings: 34th (1990) 3-66.

* 3. G.B. Olson, "Materials Design: An Undergraduate Course," Morris E. Fine Symposium, eds. P.K. Liaw, J.R. Weertman, H.L. Markus, and J.S. Santner, TMS-AIME Warrendale, PA (1991) pp. 41-48.

4. C. J. Kuehmann and G. B. Olson, "Computer-Aided Systems Design of Advanced Steels," Proc. International Symposium of Phase Transformations During the Thermal/Mechanical Processing of Steel - Honoring Professor Jack Kirkaldy, E. B. Hawbolt et al., eds., Metallurgical Society of the Canadian Institute of Mining, Metallurgy and Petroleum, Vancouver BC (1995) 345-356.

5. T. A. Stephenson, C. E. Campbell, and G. B. Olson, "Systems Design of Advanced Bearing Steels," in Advanced Earth-to-Orbit Propulsion Technology 1992, eds. R. J. Richmond and S. T. Wu, NASA Conf. Pub. 3174, Vol. II (1992) pp. 299-307.

6. B. Sundman, B. Jansson and J. O. Andersson, "THERMOCALC: a Thermochemical Databank and Software System," CALPHAD 9 (1985) 153.

7. G. B. Olson, Materials Design Initiative, Dept. Materials Science and Engineering, Northwestern University, Evanston, IL.

8. C. S. Smith, "A History of Martensite: Early Ideas on the Structure of Steel," in Martensite, eds. G. B. Olson and W. S. Owen, ASM: Materials Park, OH (1992) pp. 11-20.

9. G. B. Olson and H. Hartman, "Martensite and Life: Displacive Transformations as Biological Processes," J. de Physique 43 (1982) C4-855.

10. M. Sarikaya and I. A. Aksay, "An Introduction to Biomimetics: A Structural Viewpoint," J. Mater. Sci. (1993).

11. M. Sarikaya and I. A. Aksay, "Nacre of Abalone Shell: a Natural Multifunctional Nanolaminated Ceramic-Polymer Composite Material," in Results and Problems in Cell Differentiation, ed. S. T. Case, Springer-Verlag: Berlin (1992) pp. 1-26.

12. G. R. Speich, "Secondary Hardening Ultrahigh-Strength Steel," in Innovations in Ultrahigh Strength Steel Technology, eds. G. B. Olson, M. Azrin and E. S. Wright, Sagamore Army Materials Research Conf. Proc.: 34th (1990) pp. 89-112.

* 13 J. S. Montgomery and G. B. Olson, "M_2C Carbide precipitation in AF1410," in Gilbert R. Speich Symp. Proc.: Fundamentals of Aging and Tempering in Bainitic and Martensitic Steel Products, eds. G. Krauss and P. E. Repas, ISS-AIME: Warrendale, PA (1992) pp. 177-214.

14. A. J. Allen, D. Gavillet and J. R. Weertman, "SANS and TEM Studies of Isothermal M_2C Carbide Precipitation in Ultrahigh Strength AF1410 Steels," Acta Metall. 41 (1993) 1869.

15. J. S. Langer and A. J. Schwartz, Phys. Rev. A21 (1980) 948.

16. R. Wagner and R. Kampmann, "Solid State Precipitation at High Supersaturations," in Innovations in Ultrahigh Strength Steel Technology, eds. G. B. Olson, M. Azrin and E. S. Wright, Sagamore Army Materials Research Conf. Proc.: 34th (1990) pp. 209-222.

* 17. K. C. King, P. W. Voorhees and G. B. Olson, "Solute Distribution Around a Coherent Precipitate in a Multicomponent Alloy," Metall. Trans. A 22A (1991) 2199-2210.

* 18. K. C. King, G. B. Olson and T. Mura, "Elastic Energy of Coherent Precipitation at Dislocations in an Anisotropic Matrix," Proc. ARO Workshop, Modern Theory of Anisotropic Elasticity and Applications, Ed. J. J. Wu, T. C. T. Ting, and D. M. Barnett, SIAM: Philadelphia, PA (1991) pp. 103-121.

* 19. C. J. Kuehmann and P. W. Voorhees, "Ostwald Ripening in Ternary Alloys," Met. Trans. A, 27A (1996) 937-943.

* 20. A Umantsev and G. B. Olson, "Ostwald Ripening in Multicomponent Alloys," Scripta Metall. Vol. 29 (1993) pp. 1135-1140.

21. C. Knepfler, "Synthesis and Characterization of Molybdenum-Based M_2C Carbides," Ph.D. thesis, Northwestern University Dept. Materials Science and Engineering, December, 1994.

22. A. Needleman, "A Numerical Study of Void Nucleation at Carbides," in Innovations in Ultrahigh-Strength Steel Technology, G. B. Olson, M. Azrin and E. S. Wright, eds., Sagamore Army Materials Research Conf. Proc.: 34th (1990) p. 331.

23. J. W. Hutchinson and V. Tvergaard, "Effect of Particle-Void Interaction on Void Growth in Tension and Shear," in Innovations in Ultrahigh-Strength Steel Technology, G. B. Olson, M. Azrin and E. S. Wright, eds., Sagamore Army Materials Research Conf. Proc.: 34th (1990) p. 347.

24. J. G. Cowie, M. Azrin and G. B. Olson, "Microvoid Formation During Shear Deformation of Ultrahigh-Strength Steels," Metall. Trans. A. 20A (1989) 143.

25. M. J. Gore, G. B. Olson and M. Cohen, "Grain-Refining Dispersions and Properties in Ultrahigh-Strength Steels," in Innovations in Ultrahigh Strength Steel Technology, eds. G. B. Olson, M. Azrin and E. S. Wright, Sagamore Army Materials Research Conf. Proc.: 34th (1990) pp. 425-442.

26. G. N. Haidemenopoulos, G. B. Olson, and M. Cohen, "Dispersed-Phase Transformation Toughening in Ultrahigh-Strength Steels," in Innovations in Ultrahigh Strength Steel Technology, eds. G. B. Olson, M. Azrin and E. S. Wright, Sagamore Army Materials Research Conf. Proc.: 34th (1990) pp. 549-596.

27. G.N. Haidemenopoulos, G.B. Olson, M. Cohen, and K. Tsuzaki, "Transformation Plasticity of Retained Austenite in Stage I Tempered Martensitic Steels," Scripta Metall. 23 (1989) 207-211.

28. D. Spaulding, G. B. Olson and Y-W. Chung, "Grain Boundary Cohesion and Segregation in Ultrahigh Strength Steels," submitted to Metall. Mater. Trans. A.

* 29. C. J. Kuehmann, J. Cho, T. A. Stephenson, and G. B. Olson, "Systems Design of High Performance Steels," Metallic Materials for Lightweight Applications (40th Sagamore Army Materials Research Conference), eds. E. B. Kula and M. G. H. Wells, U.S. Government Printing Office, Washington, DC, Lake George, NY (1994) 337-355.

30. C-C. Young, "Transformation Toughening in Phosphocarbide-Strengthened Austenitic Steels," Ph.D. Thesis, MIT Dept. Materials Science and Engineering, June 1988.

31. F. Stavehaug, "Transformation Toughening of γ' Strengthened Metastable Austenite Steels," Ph.D. Thesis, MIT Dept. Materials Science and Engineering, June, 1990.

32. D. Bergstrom, "Transformation Toughening in UHS Austenitic Steels," Ph.D. thesis, Northwestern University Dept. of Materials Science and Engineering, June, 1996.

33. R. G. Stringfellow and D. M. Parks, "Strain-Induced Transformation Toughening in Metastable Austenitic Steels," in Fracture Behavior and Design of Materials and Structures, Vol. 1, Ed. D. Firrao, EMAS Ltd., Warley, U.K., p. 400.

34. S. Socrate, "Mechanics of Microvoid Nucleation and Growth in High Strength Metastable Austenitic Steels", Ph.D. thesis, MIT, March, 1995.

35. D. Cook and G. Lewis, "High Performance Secondary-Hardening Gear Steel Design and Evaluation: The C2 Prototype," MSc C90 Materials Design project report, Northwestern University, June, 1994.

36. E. Chu, D. Fong, C. Klapperich and T. Yeh, "Terminator 3: Biomimetic Smart Steels," MSc C90 Materials Design project report, Northwestern University, June, 1993.

APPENDIX

Austenite Stability and Mechanical Properties of Austempered Ductile Iron

Abstract

The stability of austenite in Austempered Ductile Iron (ADI) has been quantified by measurement of the M_s^{σ} temperature, below which stress-assisted martensitic transformation controls yielding. In both the Grade 1 (115 ksi (800 MPa) yield stress) and Grade 3 (150 ksi (1030 MPa) yield stress), the M_s^{σ} temperature in uniaxial tension is near 100°C. Below this temperature the tensile yield stress shows a nonmonotonic temperature dependence indicative of isothermal martensitic transformation. Consistent with the usual stress-state sensitivity associated with the transformation dilatation, blunt notch tensile specimens with a stress-state ratio of $\Sigma = \sigma_h / \bar{\sigma} = 1.1$ demonstrate an increased M_s^{σ} near 190°C. From these stability measurements it is estimated that the temperature of maximum transformation toughening, corresponding to the M_s^{σ} for a crack-tip stress state of $\Sigma \approx 2.3$, would be greater than 300°C. Below room temperature the measured temperature dependence of the fracture toughness is dominated by the ductile / brittle transition, and it is obscured at higher temperatures by the high scatter associated with the distribution of graphite nodules. Although clear metallographic support could not be obtained, the measured stability indicates that the austenite should transform during fracture, but the stability is too low to give significant transformation toughening. Higher toughness at and above room temperature should then be

achievable by increasing austenite stability. However, the measured stress-strain curve shapes are consistent with a broad distribution of austenite stabilities, as indicated by the lack of sharp yielding at low temperatures. This suggests that the stabilities measured in this work represent the least stable austenite in the distribution, and that the breadth of the distribution limits the transformation toughening. The stress-strain curves also indicate enhanced strain hardening at temperatures above 200°C from possible stress-assisted bainitic transformation.

Introduction

Several investigations have shown that austempered ductile irons exhibit improved mechanical properties compared to conventional cast irons [1-5]. Much of their favorable combination of strength and ductility can be attributed to the presence of a significant amount of retained austenite. The stability of this austenite with respect to the formation of mechanically induced martensite depends sensitively on its carbon content, which can change significantly with slight changes in austempering time or temperature [6]. If the austenite stability could be optimized, the mechanical properties could be improved even more by the process of transformation toughening. It is well known that mechanically induced martensitic transformations can enhance ductility and fracture toughness if the austenite is of the proper stability [7]. This stability is quantified by the M_S^{σ} temperature. Defined as the temperature below which initial yielding is due to martensitic transformation, the M_S^{σ} is a strong function of the imposed stress state. Experimentally M_S^{σ} is determined as the temperature at which the temperature dependence of the measured yield stress reverses. The present study has been undertaken to determine the M_S^{σ} temperatures under different stress states and assess

the effect of transformation plasticity on the mechanical properties in two grades of an austempered ductile iron.

Materials and Procedures

One inch and half inch thick plates of ADI of weight percent composition, 3.7 C, 2.7 Si, 0.97 Ni, 0.87 Cu, 0.27 Mn, 0.057 Mg and 0.032 Cr, were received from the U.S. Army Research Laboratory Materials Directorate. The material had been heat treated according to ASTM standard A 897-90 [8] to produce at least one plate each of Grades 1 and 3 for both thicknesses. The heat treatments used are listed in Table 1. Uniaxial and blunt notched tensile tests and K_{IC} fracture toughness tests were performed at temperatures from -196°C to 350°C in order to determine the effect of austenite stability and stress state on the flow behavior and fracture toughness of these materials.

	Grade 1	Grade 3
Preheat Time & Temp.	105 min at 593°C (1100°F)	120 min at 593°C (1100°F)
Austenitizing Time & Temp.	100 min at 891°C (1635°F)	150 min at 885°C (1625°F)
Quench Time & Temp.	100 min at 327°C (620°F)	150 min at 316°C (600°F)
Quench Medium	Molten Salt	Molten Salt
Rockwell C Hardness	32.2	41.5

Table 1 Heat treatments applied to produce plates of Grades 1 and 3.

In the initial stages of this work, seventeen tensile specimens were made from each of the half-inch plates, in order to measure their uniaxial tension M_S^{σ} temperatures. Tensile tests were performed at temperatures from -196°C to 236°C. Below 20°C the tests were conducted in isopentane or methanol cooled by liquid nitrogen or in pure liquid nitrogen, from 20°C to 150°C they were conducted in air and above 150°C in vacuum. The tensile specimen geometry is shown in Figure 1a.

To determine how sensitive the martensitic transformation is to the triaxiality of the stress state, blunt-notched tensile specimens of the type shown in Figure 1b were made. Ten specimens were made from Grade 1, and five were made from Grade 3. They were strained to failure at temperatures from -196°C to 225°C in the same environments that were used for the uniaxial tensile tests.

K_{IC} fracture toughness tests were performed according to ASTM standard E 399-89 on compact tension specimens which were cut from the half-inch plates of each grade. Tests run below 20°C were in air cooled by nitrogen, those from 20°C to 150°C were run in air and those above 150°C were tested in vacuum.

Results and Discussion

The 0.2% offset yield stress versus temperature data from the uniaxial tension tests are plotted in Figure 2. As the figure shows, both grades have a very broad peak around 100°C. Because of the peak breadth and scatter, it is difficult to determine an exact M_S^{σ}, but there appears to be little difference in stability between the two grades. Figure 2 also shows the yield stress versus temperature curves for the blunt-notch tensile tests. Once again, both grades display broad peaks. However, as expected for

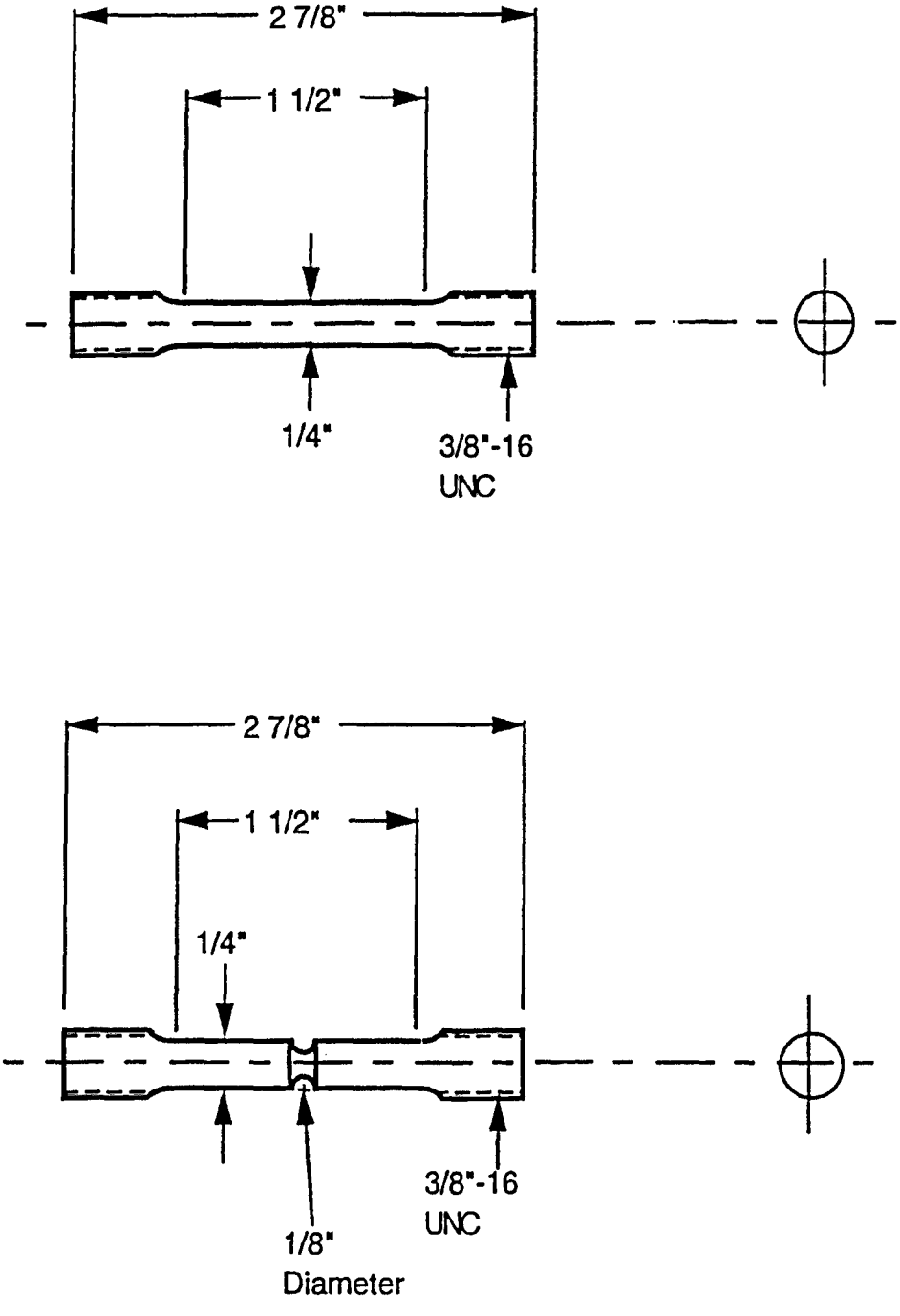

Figure 1 Uniaxial and blunt notch tensile specimens.

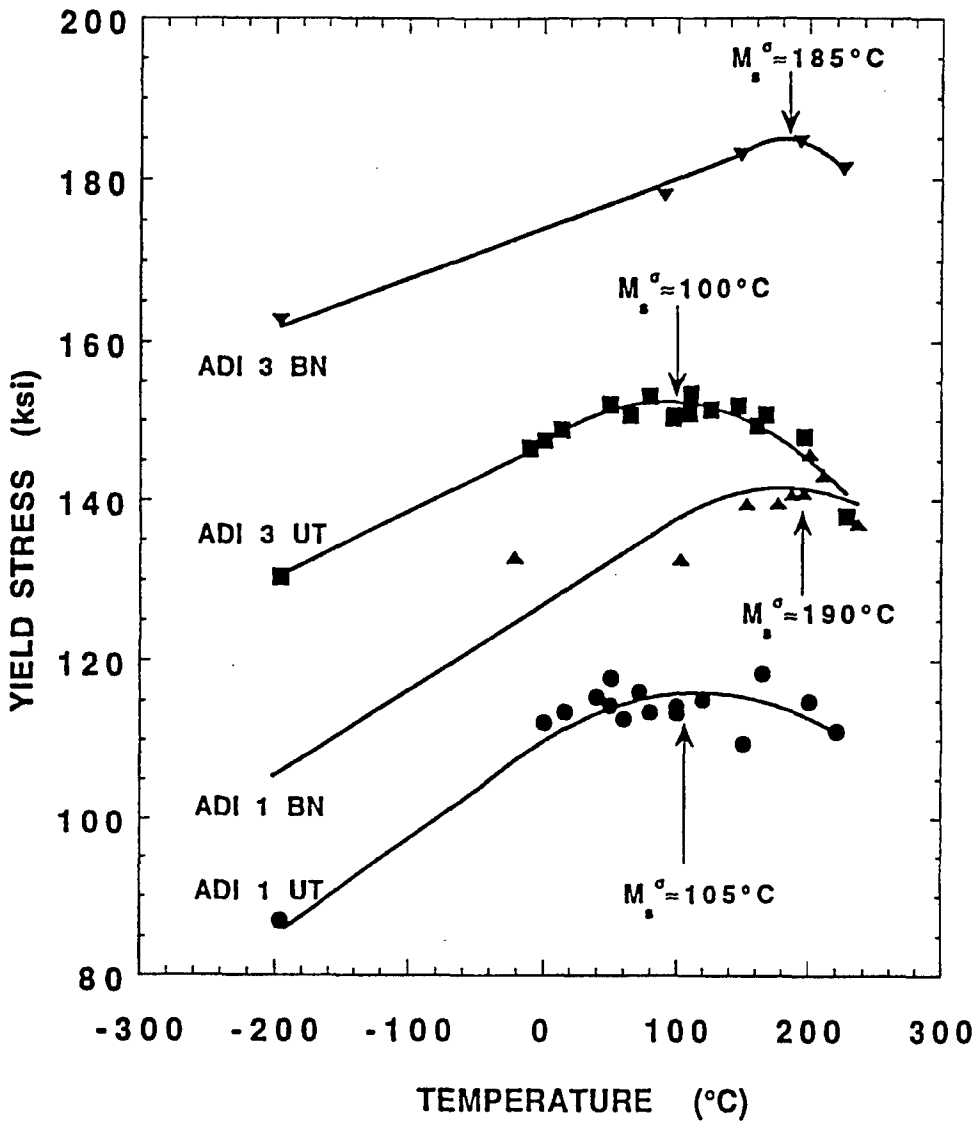

Figure 2 A plot of 0.2% yield stress versus temperature from uniaxial and blunt notch tensile tests on material from the 1/2 inch plates.

this more highly triaxial stress state, the M_S^{σ} temperatures are about 85° higher than in uniaxial tension.

Based on these observations and a parallel study by Matlock and Krauss [5], a more extensive study was made of the properties of the Grade 1 material in uniaxial tension. As this grade was shown to have nearly 10% more retained austenite [5], the effects of austenite stability on the mechanical behavior should be more apparent than in the Grade 3 material. Figure 3 shows the 0.2% yield stress, UTS and fracture strain of Grade 1 material from the 1 inch plate at temperatures from -196°C to 350°C, while Figure 4 shows stress-strain curves from these tests at selected temperatures.

The dip in 0.2% yield stress at very low temperatures is evidence of isothermal martensite formation. The fact that the curves do not exhibit a sharp stress plateau after the onset of transformation controlled yielding indicates that there is a range of austenite compositions in this material, likely associated with a distribution in carbon content. The stabilities measured by M_S^{σ} thus represent the least stable austenite in the distribution. The inflections in the stress strain curves for tests above 200°C suggest another change in structure is taking place, most likely the formation of stress assisted bainite. The maximum fracture strain and a local maximum in UTS (which is equal to the fracture stress, since there is no appreciable necking) occur at near 250°C in the temperature regime where this transformation occurs.

K_{IC} fracture toughness tests were performed on compact tension specimens of the type shown in Figure 5, which were cut from the half inch plates of each grade. The results of these tests are shown in Figure 6. These are provisional "K_Q" values because, except at room temperature, it was not possible to use our C.O.D. gage. However, when values obtained using the gage at room temperature were compared to those

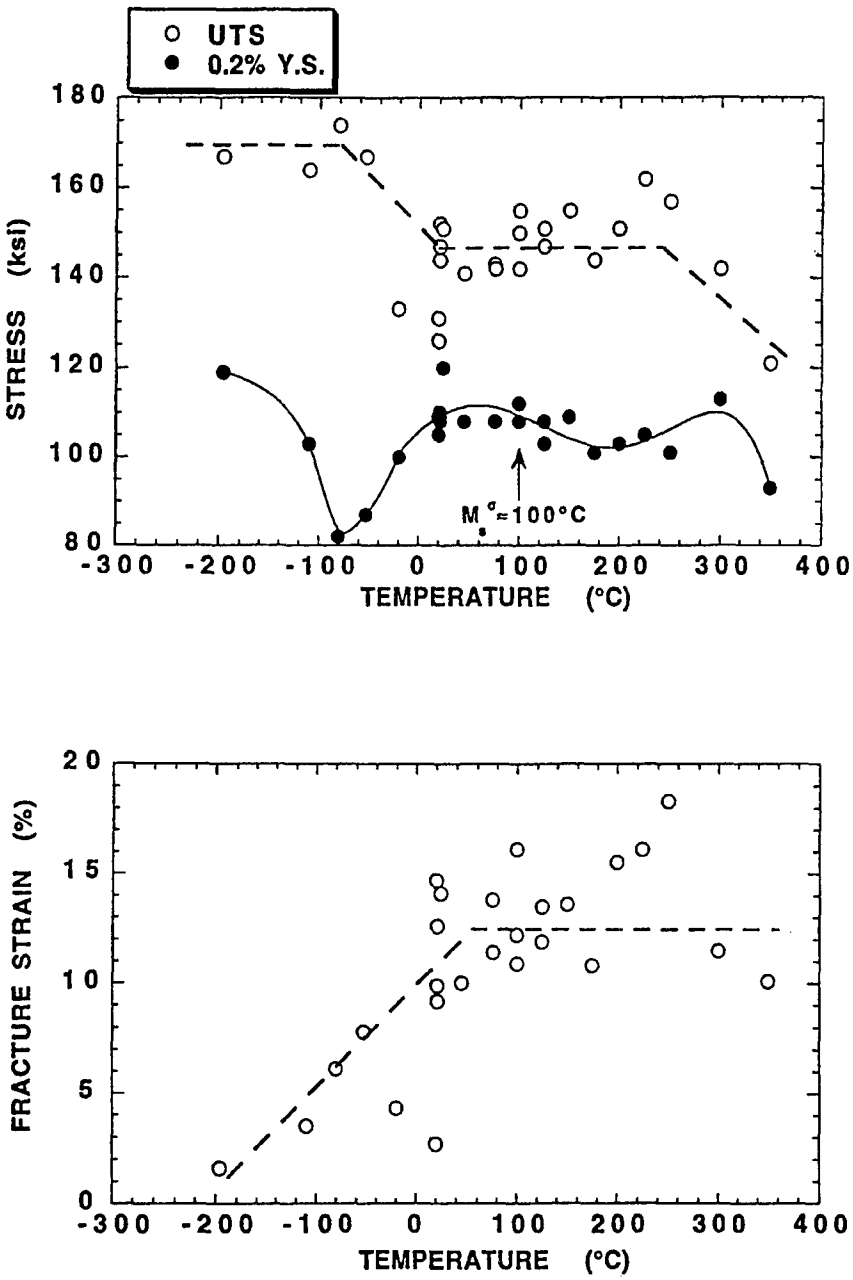

Figure 3 Plots of 0.2% yield stress and UTS (top) and fracture strain (bottom) versus temperature for Grade 1 material from the 1 inch plate.

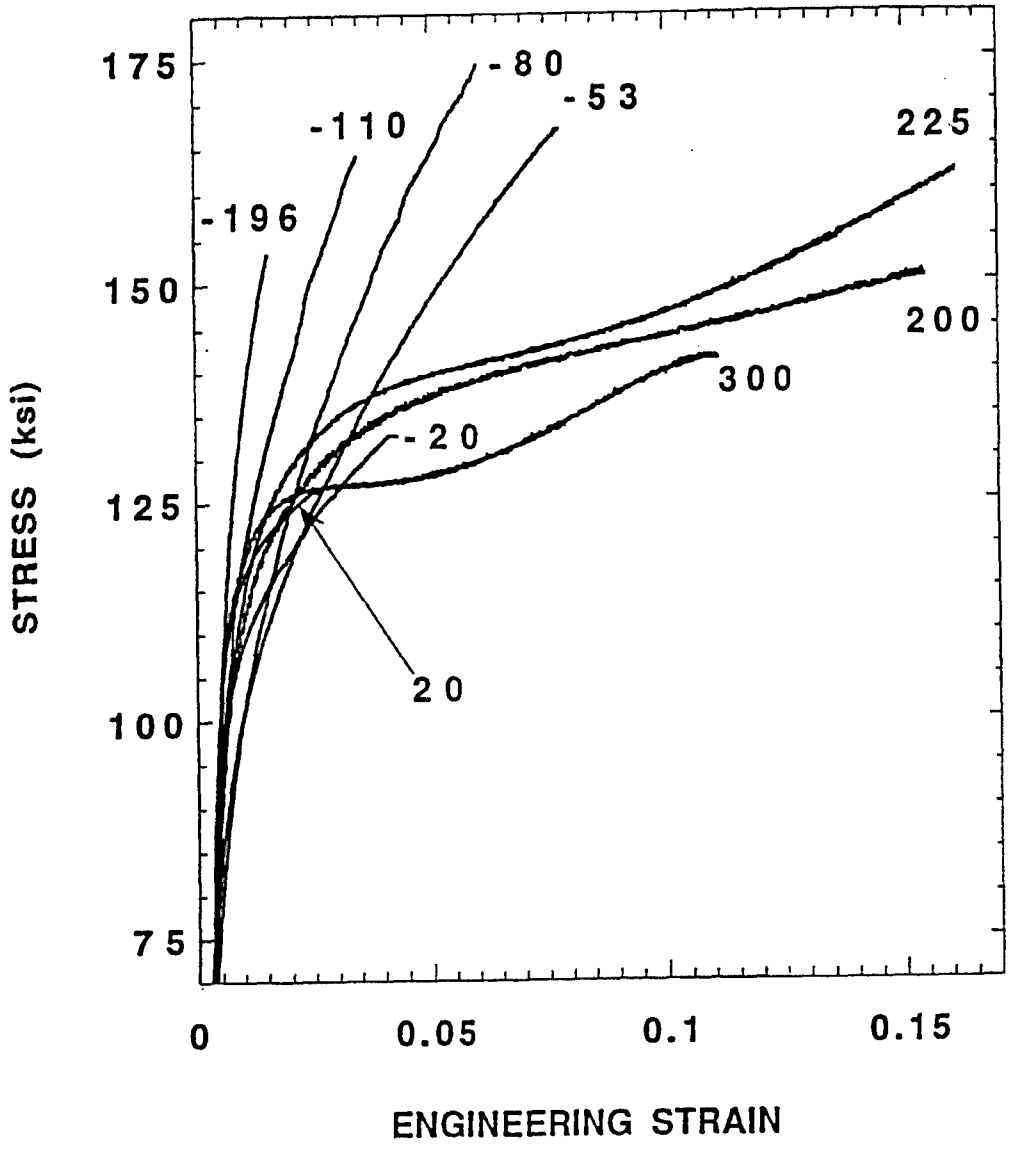

Figure 4 Stress-strain curves for Grade 1 specimens from the 1 inch plate in uniaxial tension at selected temperatures.

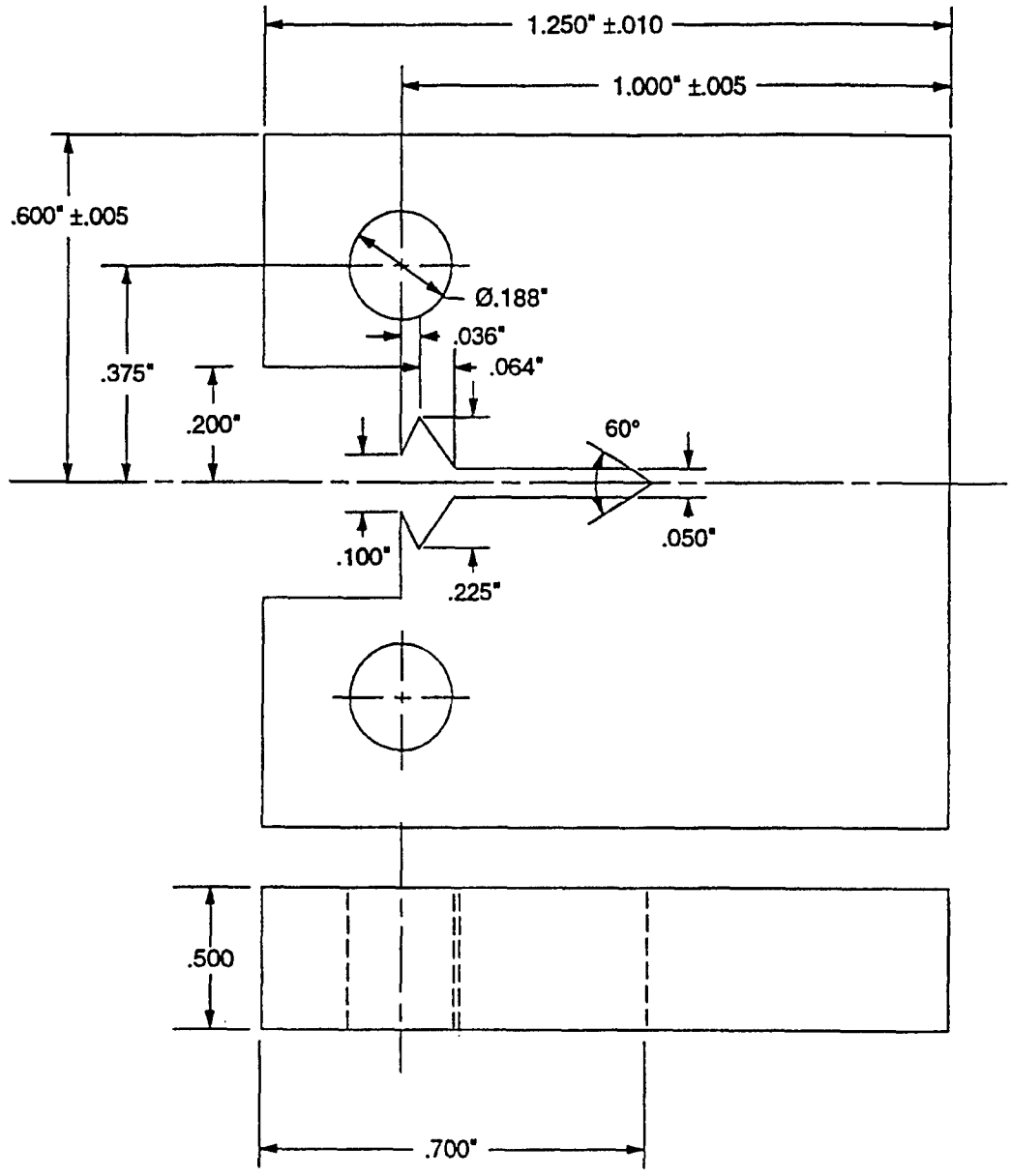

Figure 5 Compact tension fracture toughness specimen.

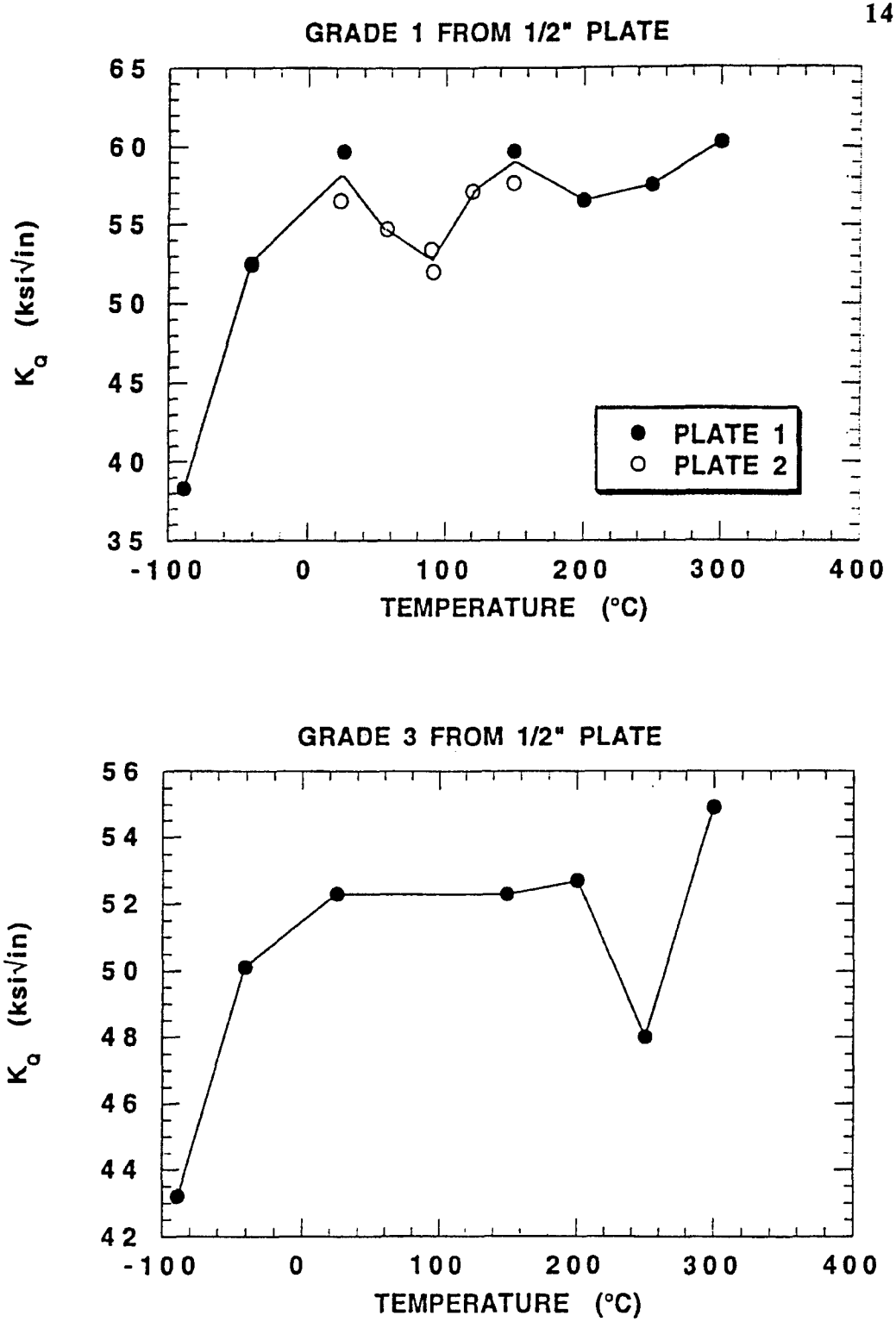

Figure 6 Plots of K_Q fracture toughness versus temperature for Grades 1 and 3 from the 1/2 inch plates.

calculated at the same temperature without using the gage, they were virtually the same. Therefore, the K_Q values should be a good approximation of K_{IC} at other temperatures.

As denoted in Figure 6a, specimens of the Grade 1 material were cut from two different plates. Although both plates were given the same heat treatment, the material from the first plate had a hardness of R_C 32 while those from the second plate measured R_C 34. Combining the data from the two plates, no clear peak in fracture toughness is evident.

The most noticeable feature of these tests is the significant embrittlement at low temperatures. As Figure 6 shows, the fracture toughness of each grade drops sharply as the temperature falls below 0°C. Between room temperature and -40°C, the fracture toughness decreases by over 10% (for Grade 1), while the uniaxial fracture strain drops by about 50% (Figure 3). Between room temperature and -80°C the fracture toughness drops by more than 30%. Above room temperature, K_Q remains relatively constant until it rises again above 250°C. Figure 7 shows the fracture surfaces of compact tension specimens tested at -90°C and 300°C. These images clearly demonstrate the change of fracture mode from ductile to brittle at low temperatures.

These tests indicate little difference in austenite stability among the grades and plate thicknesses. In uniaxial tension the M_S^{σ} temperatures were measured at about 100°C, while they were found to be near 190°C for blunt notch tension. Based on these values, the M_S^{σ} temperature for a crack-tip stress state was estimated to be in excess of 300°C. However, this could not be experimentally verified because it was too close to

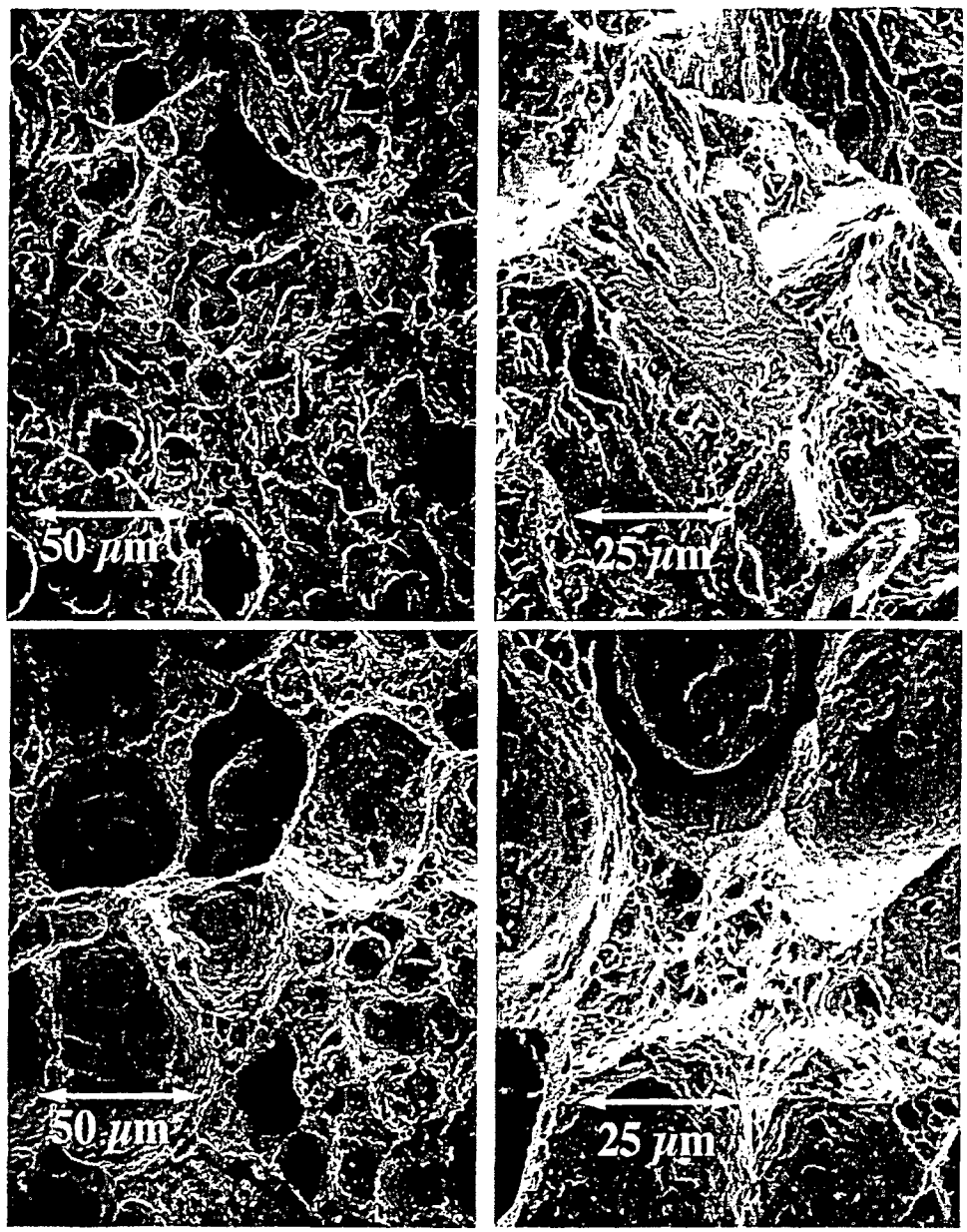

Figure 7 SEM micrographs of compact tension specimen fracture surfaces of Grade 1 material from the original 1/2 inch plate, fractured at -90°C (top) and 300°C (bottom).

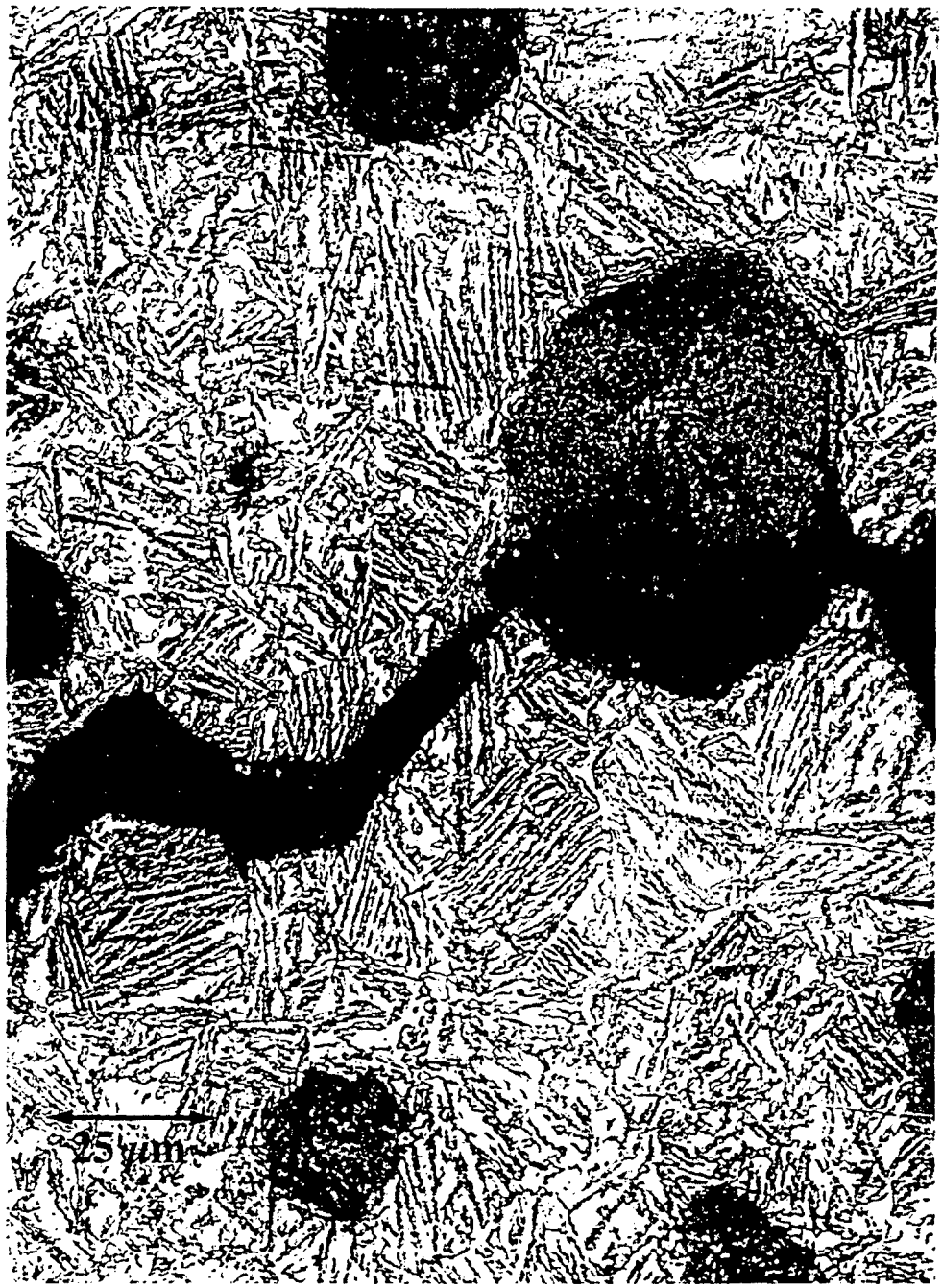

Figure 8 Optical micrograph of a uniaxial tension specimen of Grade 1 material from the 1/2 inch plate that was strained to failure at -196°C.

the austempering temperature. It should be noted again that the measured austenite stabilities likely represent the least stable of a range of compositions. It may be that this range of stabilities is too broad to show a well defined transformation toughening peak.

The presence of stress-assisted plate martensite is expected in the specimens tested below their M_S^{σ}. Several of these samples were examined using light and scanning electron microscopy in an attempt to confirm the presence of this martensite. Aranzabal *et al*. [1] saw stress-assisted martensite near a fracture surface using a 4% Nital etch, and Kovacs [9] reports that, after applying this same etchant, a four to eight hour heat tint at 500°F will cause any martensite to turn a deep blue. However, after trying both of these methods, no martensite could be distinguished, even in the specimen shown in Figure 8, which was strained to failure in liquid nitrogen.

Conclusions

The austenite stability has been measured in terms of the M_S^{σ} temperature under several states of stress for two grades of austempered ductile iron. For Grade 1 material, $M_S^{\sigma}(UT) \approx 105°C$ and $M_S^{\sigma}(BN) \approx 190°C$, while $M_S^{\sigma}(UT) \approx 100°C$ and $M_S^{\sigma}(BN) \approx 185°C$ for Grade 3 material. Based on these measurements, M_S^{σ} (CT) was estimated to be in excess of 300°C for both grades. Although, because of the complex microstructure, conclusive metallographic evidence of martensite formation was not found, these stability measurements are consistent with the occurrence of mechanically-induced martensitic transformation. Below these temperatures, the yield stress decreases in a manner indicative of stress-assisted martensitic transformation. Above M_S^{σ}, the effect of transformation on toughness is obscured by scatter due to the large volume fraction of graphite particles and the likelihood that compositional inhomogeneities

resulted in a wide distribution of austenite stabilities. At temperatures above 200°C the stress-strain curves show increased strain hardening, which may be evidence of stress-assisted bainite formation.

Below 20°C, both grades pass through the ductile to brittle transformation temperature and their toughness and ductility drop rapidly.

Acknowledgments

The author would like to thank the U. S. Army Research Laboratory for sponsorship of this work and Dr. Martin G. H. Wells of ARL for his assistance.

Appendix References

1. J. Aranzabal, I. Gutierrez, J.M. Rodriguez-Ibabe, and J.J. Urcola, "Influence of Heat Treatments on Microstructure and Toughness of Austempered Ductile Iron," *Mat. Sci. and Tech.*, **8** (1992) 263-73.

2. K.B. Rundman, D.J. Moore, K.L. Hayrynen, W.J. Dubensky and T.N. Rouns, "The Microstructure and Mechanical Properties of Austempered Ductile Iron," *J. Heat Treat.*, **5** (1988) 79-95.

3. N. Darwish and R. Elliot, "Austempering of Low Manganese Ductile Irons," *Mater. Sci. Technol.*, **9** (1993) 572-585.

4. B.V. Kovacs, "Austempered Ductile Iron: Fact and Fiction," *Modern Casting*, **90** (1990) 38-41.

5. D.K. Matlock and G. Krauss, " Mechanical Performance of Austempered Ductile Iron," *Report submitted to U. S. Army Research Laboratory Materials Directorate,* December, 1993.

6. K.B. Rundman and R.C. Klug, "An X-Ray and Metallographic Study of an Austempered Ductile Cast Iron," *AFS Trans.* **91** (1983) 499-508.

7. G. B. Olson and M. Cohen, in : *Mechanical Properties and Phase Transformation in Engineering Materials*, S. D. Antolovich, R. O. Ritchie and W. W. Gerberich, eds., TMS-AIME, Warrendale, PA (1986) 367.

8. "E 897-90 : Standard Test Method for Plane-Strain Fracture Toughness of Metallic Materials," in : *1992 Annual Book of ASTM Standards, American Society for Testing and Materials*, Philadelphia, PA (1992) 557-562.

9. B.V. Kovacs, "A Simple Technique to Identify Various Phases in Austempered Ductile Iron," *Modern Casting*, **77** (1987) 34-35.

Electronic References

INTERNET LOCATIONS

Note: The following URLs are current as of the date of publication

It's a Small, Small, Small World - ***http://web.mit.edu/afs/athena/org/t/techreview/www/articles/fm97/merkle.html***

It's a Small, Small, Small, Small World By Ralph C. Merkle Ralph C. Merkle is a research scientist at Xerox Palo Alto Research Center (PARC), where he is pursuing research in computational nanotechnology. He chaired the Fourth Foresight Conference on Molecular Nanotechnology, and will chair the next such conference, to be held in November. Before concentrating on nanotechnology, Merkle specialized in cryptography; he is the co-inventor of public key encryption.

Weiss Group's Useful Sites - ***http://stm1.chem.psu.edu/OtherSites.html***

Pennsylvannia State University 's collection of Surface Chemistry, Surface Physics, and Nanotechnology related sites.

Institute of Microtechnology, University of Neuchatel, Switzerland - ***http://www-imt-dr.unine.ch/***

Institute of Microtechnologies features a publications database and an icon for research activities in the Department of Microelectronics, sensors and actuators.

Minnesota Microtechnology Laboratory - ***http://www.ee.umn.edu/groups/mtl/indexNT.html***

Current research activities being explored in the miniaturization of microelectronic devices.

Center for Microelectronics and Optoelectronics (CMO) - ***http://www-phys.llnl.gov/H_Div/CMO/cmo.html***

Lawrence Livermore National Laboratory's competency in microelectronics and optoelectronics is seen as a major element in the Lab's future mission.

Lawrence Livermore National Laboratory: LLNL - ***http://www.llnl.gov/***

Includes a laboratory research section and publications database.

Nanotechnology - ***http://nano.xerox.com/nano***

Everything you wanted to know regarding nanotechnology. Publications, books, newsletters and organizations.

Foresight Institute - ***http://www.foresight.org/***

Foresight Institute's goal is to guide emerging technologies to improve the human condition. Foresight focuses its efforts upon nanotechnology, the coming ability to build materials and products with atomic precision, and upon systems that will enhance knowledge exchange and critical discussion, thus improving public and private policy decisions.

Small is Beautiful - ***http://science.nas.nasa.gov/Groups/Nanotechnology/links.html***

The purpose of this page is to help facilitate access to information on the emerging science of nanotechnology.

Welcome to The Institute of Physics - ***http://www.iop.org/***

Electronic Journals on smart materials and structures, nanotechnology. Includes the table of contents, forthcoming articles and preprints.

News and Alerting Services - ***http://www.iop.org/Physics/Resources/phnews.htm***

From the Institute of Physics.

Sites Related to Superconducting Electronics - ***http://www.physics.iastate.edu/htcu/othersites.html***

Superconductivity and Superconducting Electronics -Institute of Physics

The High-Tc Update - ***http://www.physics.iastate.edu/htcu/htcu.html***

Published for the Division of Materials Sciences, Office of Basic Energy Sciences, USDOE, under Contract W-7405-eng-82 with the Ames Laboratory, Iowa State University. Funded by DMS/BES/USDOE, ARPA, ONR, NSF, EPRI, and other agencies, organizations, and individuals.

Research centres - ***http://www.iop.org/Physics/Resources/phcent.html***

Institute of Physics listing of research centers.

Preprint databases - ***http://www.iop.org/Physics/Resources/phprepr.html***

Includes locations of preprint publications. such as LANL collection on physics, mathematics- Institute of Physics

American Institute of Physics - ***http://www.aip.org/publications.html***

American Institute of Physics Home Page features AIP publications,magazines and newsletters.

Physics Related Resources on the Internet - ***http://www.aps.org/phys.html***

The American Physical Society has put together this comprehensive listing of Physics related sites.

Materials Related Links - ***http://www.mrs.org/related/government.html***

The Materials Research Society list of materials related links including the Argonne National Laboratory Brookhaven National Laboratory Department of Energy Environmetal Protection Agency Ernesto Orlando Lawrence Berkeley National Laboratory Fermi National Accelerator Laboratory and many others.

IEEE Home Page - ***http://www.ieee.org/***

The Institute of Electrical and Electronics Engineers, Inc.

IEEE Society Reports on Emerging Technologies - ***http://www.ieee.org/newtech/reports/index.html***

MIT Microsystems Technology Laboratories - ***http://www-mtl.mit.edu/***

Professional Organizations and Government labs for Electrical Engineers - ***http://www.ee.umr.edu/orgs/***

Long list of sites including academic and government research centers.

The Semiconductor Subway - ***http://www-mtl.mit.edu/semisubway.html***

The Semiconductor Subway provides links to all manner of semiconductor and microsystems related information, including fabrication facilities, research activities, standards work, etc.

LETI-Laboratory Of Electronics Technology and Instrumentation - *http://www-dta.cea.fr/wwwcea/leti/uk/leti.htm*

This laboratory is a part of CEA (Commissariat a l' energie atomique) French Atomic Energy Commission. It is one of the most important European Applied Research Laboratories in Electronics. Research on Microsensors, microconnectors and microsystems.

UCI's Technology Outreach Program - *http://www.top.uci.edu/top.htm*

This is the Home page for the University of California, Irvine Technology Outreach Program. Current research programs emphasize microelectronics, biomedical electronics, digital electronics, MEMs, ans sensors.

Unbounding the Future: The Nanotechnology Revolution - *http://www.foresight.org/UTF/Unbound_LBW/index.htm*

Unbounding the Future, by K. Eric Drexler, Chris Peterson and Gayle Pergamit (Quill 1991) provides a non-technical discussion of what nanotechnology should let us do, using technically feasible scenarios to clearly illustrate the possibilities..

Additional References

Note: Refer to the order form following the bibliographies for ordering information

AD NUMBER: A324529

MASSACHUSETTS INST OF TECH LEXINGTON LINCOLN LAB

(U) HANDBOOK OF PHOTONICS/MINIATURE SOLID-STATE LASERS,

1997 73P
PERSONAL AUTHORS: ZAYHOWSKI, J. J.; HARRISON, J.

UNCLASSIFIED REPORT

ABSTRACT: (U) This chapter presents fundamental concepts and formulas for designing and utilizing miniature solid state lasers. Diode pumped, miniature, monolithic, solid state lasers offer an efficient, compact, and robust means of generating diffraction limited, single frequency radiation. In addition, their diminutive size results in high speed tuning capabilities and short pulsed operation unmatched by larger devices. Applications areas are as Diverse as communications, spectroscopy, remote sensing, nonlinear optics, projection displays, and micromachining.

DESCRIPTORS: *SOLID STATE LASERS, LASER PUMPING, Q SWITCHING, REPRINTS, NONLINEAR OPTICS, GAIN, QUANTUM ELECTRONICS, MINIATURE ELECTRONIC EQUIPMENT.

AD NUMBER: A321560

HIGH PERFORMANCE MATERIALS INC HERMANN MO

(U): ADVANCED COMPOSITE SOLDERS FOR MICROELECTRONICS. PHASE 2.

FEB 97 109P

UNCLASSIFIED REPORT

ABSTRACT: (U) The objectives of the phase 2 work were (1) increase Solder Powder production capacity of the rpm production facility from 10 lb/batch to 500 lbs/batch for the production of Conventional 63 sn-37 pb Solder Powders, ternary and quaternary 63sn-37 pb-x(x=ni,cu,ag,sb,in or bi) Solder Powders, and lead free Sn-based Solder Powders; and (2) perform a comprehensive study of the physical, mechanical and solderability/wettability properties of the solder powders.

DESCRIPTORS: *MICROELECTRONICS, *SOLDERING ALLOYS, SHEAR PROPERTIES, MICROSTRUCTURE, FATIGUE LIFE, TENSILE PROPERTIES, EXTRUSION, FRACTURE(MECHANICS), PRODUCTION CONTROL, CREEP, THERMAL FATIGUE, POWDER METALLURGY, THERMAL CYCLING TESTS, FATIGUE TESTS(MECHANICS), CYCLIC LOADS, EUTECTICS, LEAD ALLOYS, TIN ALLOYS.

IDENTIFIERS: SBIR(SMALL BUSINESS INNOVATION RESEARCH)

AD NUMBER: A321085

INSTITUTE FOR POSTDOCTORAL STUDIES SCOTTSDALE AZ

(U): MICROELECTRONICS AND NANOMETER STRUCTURES
PROCESSING, MEASUREMENT, AND PHENOMENA.

DEC 96 845P
PERSONAL AUTHORS: SCHULTE, C. R.

UNCLASSIFIED REPORT

ABSTRACT: (U) The Twenty-Third Annual Conference on the Physics and Chemistry of Semiconductor Interfaces was held in Lajolla, California and the enclosed report contains papers presented.

DESCRIPTORS: *SEMICONDUCTORS, *MICROELECTRONICS, *NANOTECHNOLOGY, SCANNING ELECTRON MICROSCOPES, SYMPOSIA, SILICON DIOXIDE, PLASMAS(PHYSICS), ELECTRON SCATTERING, CHARGE CARRIERS, NITRIDES, ELECTRON BEAMS, ANISOTROPY, VACUUM APPARATUS, MASS SPECTROMETERS, X RAY SPECTROSCOPY, BIPOLAR TRANSISTORS, SILICONES, PHOTOLITHOGRAPHY, GALLIUM ARSENIDE LASERS, MOLECULAR BEAM EPITAXY.

AD NUMBER: A319391

STATE UNIV OF NEW YORK AT STONY BROOK

(U): FUTURE TRENDS IN MICROELECTRONICS: REFLECTIONS ON THE ROAD TO NANOTECHNOLOGY.

NOV 96 418P
PERSONAL AUTHORS: LURYI, SERGE; XU, JIMMY; ZASLAVSKY, ALEX

UNCLASSIFIED REPORT

DESCRIPTORS: *NANOTECHNOLOGY, GALLIUM ARSENIDES, TUNNELING(ELECTRONICS), VERY LARGE SCALE INTEGRATION, FABRICATION, INTEGRATED CIRCUITS, MONTE CARLO METHOD, LASER APPLICATIONS, MICROELECTRONICS, QUANTUM ELECTRONICS, RELIABILITY(ELECTRONICS), ELECTRONIC SWITCHING.

2IDENTIFIERS: QUANTUM DOTS

AD NUMBER: A315842

TEXAS UNIV AT AUSTIN COLL OF ENGINEERING

(U): MICROELECTRONICS AND MATERIALS RESEARCH EQUIPMENT.

MAR 96 19P
PERSONAL AUTHORS: KLEIN, DALE E.

UNCLASSIFIED REPORT

ABSTRACT: (U) This report summarizes the actions and progress in equipping the Microelectronics and Materials Research Programs at the University of Texas at Austin. The Department of Defense provided $6,000,000 towards research equipment purchases for the completion of the research facilities. The University of Texas at Austin had already invested $34 million to build a new 135,000 square foot facility and partially equipped it using $10 million. The $6.0 million of DoD funds completed the acquisition of the equipment necessary to fully utilize the new facility.

DESCRIPTORS: *MATERIALS, *MICROELECTRONICS, *LABORATORY EQUIPMENT, METALS, DEPARTMENT OF DEFENSE, POLYMERS, PROCESSING, STRUCTURES, THIN FILMS, CHEMICAL VAPOR DEPOSITION, EPITAXIAL GROWTH, MICROWAVES, AMORPHOUS MATERIALS, HEAT, IMPEDANCE, MOLECULAR BEAM EPITAXY.

IDENTIFIERS: NANOHETEROGENEOUS, SPIN VALVE,

♦AD NUMBER: A313700

STANFORD UNIV CA STANFORD ELECTRONICS LABS

(U): JSEP ANNUAL REPORT.

FEB 96 72P
PERSONAL AUTHORS: HARRIS, JAMES S JR

UNCLASSIFIED REPORT

ABSTRACT: (U) This is the annual report of the research conducted at the Stanford Electronics Laboratories under the sponsorship of the Joint Services Electronics Program from March 1, 1995 through February 29, 1996. This report summarizes the areas of research, identifies the most significant results and lists the dissertations and publications sponsored by contract DAAHO4-94-G-OO58.

DESCRIPTORS: *QUANTUM ELECTRONICS, *ELECTRONICS LABORATORIES, PORTABLE EQUIPMENT, REPORTS, THIN FILMS, EPITAXIAL GROWTH, SUBSTRATES, FIELD EFFECT TRANSISTORS, FIELD EMISSION, ADAPTIVE FILTERS, N TYPE SEMICONDUCTORS,

IDENTIFIERS: MSK(GAUSSIAN FILTERED MINIMUM SHIFT KEYING), QUANTUM DOTS.

♦Included in *The DTIC Review*, September 1997

♦AD NUMBER: A313593

ADVANCED FUEL RESEARCH INC EAST HARTFORD CT
(U): HTS JOSEPHSON TECHNOLOGY ON SILICON WITH APPLICATION TO HIGH SPEED DIGITAL MICROELECTRONICS. PHASE 1.

AUG 96 32P
PERSONAL AUTHORS: ROSENTHAL, PETER A.; HAMBLEN, DAVID G.; COSGROVE, JOSEPH E.; GURVITCH, MICHAEL; TOLPYGO, SERGEY

UNCLASSIFIED REPORT

ABSTRACT: (U) The goal of this program was to develop ultra-fast superconducting digital technology based on HTS Josephson Junctions on silicon substrates. Working Josephson Junctions and Squid's were successfully fabricated on silicon, and an yttrium-barium-copper-oxide rsfq rs flip-flop with 14 junctions and i/o test structures was successfully designed, fabricated, and tested. The kinetic inductance and london penetration depth of the films on silicon were determined from measurements of squids on silicon. Minimizing kinetic inductance through the use of thicker films will be required in future devices.

DESCRIPTORS: *JOSEPHSON JUNCTIONS, STRESSES, DIGITAL SYSTEMS, FABRICATION, EPITAXIAL GROWTH, SUBSTRATES, COEFFICIENTS, SILICON, MICROELECTRONICS, BONDING, FLIP FLOP CIRCUITS, WAFERS, HIGH TEMPERATURE SUPERCONDUCTORS, INDUCTANCE, ELECTRONIC SWITCHES. IDENTIFIERSSQUIDS(SUPERCONDUCTING QUANTUM INTERFERENCE DEVICES)

AD NUMBER: A311740

MATERIALS RESEARCH SOCIETY PITTSBURGH PA

(U): SYMPOSIUM PROCEEDINGS POLYMERIC/INORGANIC INTERFACES II HELD IN SAN FRANCISCO, CALIFORNIA ON 18-20 APRIL 1995. VOLUME 385.

JUN 96 252P
PERSONAL AUTHORS: BALLANCE, JOHN B.

UNCLASSIFIED REPORT

ABSTRACT: (U) This volume addresses various aspects of polymer/inorganic interfaces. Such as surface preparation and treatment. Characterization, and performance of interfaces. In addition, it also discusses applications where the interface and its properties play a significant role, such as biointerfaces. Microelectronics, Polymer composites, and interpenetrating polymer networks.

DESCRIPTORS: *INTERFACES, *POLYMERS, *INORGANIC MATERIALS, SYMPOSIA, PREPARATION, NETWORKS, COMPOSITE MATERIALS, SURFACES, MICROELECTRONICS.

IDENTIFIERS: BIOINTERFACES, INTERPENETRATING

♦Included in *The DTIC Review*, September 1997

AD NUMBER: A311553

NAVAL POSTGRADUATE SCHOOL
MONTEREY CA

(U): DESIGN OF A SATELLITE-BASED MICROELECTRONIC RADIATION TESTING EXPERIMENT.

MAR 96 255P
PERSONAL AUTHORS: MOONEY, CHRISTOPHER S.

UNCLASSIFIED REPORT

ABSTRACT: (U) In this research, an electronic daughterboard to be used on the microelectronics and photonics test bed satellite was designed. A printed circuit board with radiation-hardened components was laid out to test various families of static ram Chips and an experimental gallium arsenide integrated circuit. Computer aided design tools produced by cadence design systems were used to logically and physically design the experiment. Output from the cadence software provides the information necessary to fabricate, assemble, and test the board.

DESCRIPTORS: *TEST BEDS, *PRINTED CIRCUIT BOARDS, *RADIATION HARDENING, COMPUTER AIDED DESIGN, GALLIUM ARSENIDES, THESES, CHIPS(ELECTRONICS), RANDOM ACCESS COMPUTER STORAGE, MICROELECTRONICS, SPACECRAFT COMPONENTS.

IDENTIFIERS: CADENCE COMPUTER PROGRAMS, SINGULAR EVENT UPSET

AD NUMBER: A310747

AIR FORCE INST OF TECH WRIGHT-PATTERSON AFB OH

(U): STRUCTURES AND TECHNIQUES FOR IMPLEMENTING AND PACKAGING COMPLEX, LARGE SCALE MICROELECTROMECHANICAL SYSTEMS
USING FOUNDRY FABRICATION PROCESSES.

JUN 96 479P
PERSONAL AUTHORS: COMTOIS, JOHN H.

UNCLASSIFIED REPORT

ABSTRACT: (U) Microelectromechanical Systems, or 'Mems' is a broad new field of research into devices that range in size from a few microns to a few millimeters. Much of the technology supporting Mems research is borrowed from the microelectronics industry; so Mems holds out the promise of batch fabrication of microminiaturized machines that can be easily integrated with electronics. This dissertation research investigated structures and methods for implementing and packaging complex, large scale Microelectromechanical devices and systems using commercially available foundry fabrication processes.

DESCRIPTORS: *ELECTROMECHANICAL DEVICES, *INDUSTRIAL ENGINEERING, THERMAL PROPERTIES, OPTICAL EQUIPMENT, THESES, FABRICATION, STEPPER MOTORS, DIES, MICROELECTRONICS, PACKAGING,
MACHINES, ACTUATORS, DISTORTION, BATCH PROCESSING, FOUNDRIES, MICROMINIATURIZATION.

IDENTIFIERS: MICROELECTROMECHANICAL SYSTEMS

AD NUMBER: A310359

VIXEL INC BROOMFIELD CO

(U): LOW-RESISTANCE, HIGH-POWER-EFFICIENCY VERTICAL CAVITY MICROLASERS.

MAY 96 15P
PERSONAL AUTHORS: JEWELL,

UNCLASSIFIED REPORT

ABSTRACT: (U) The purpose of this project was to improve the total Power efficiency of vertical cavity Microlasers to further the Commercialization of large arrays of semiconductor lasers integrated on single chips. Vertical cavity surface emitting lasers are tiny semiconductor lasers, typically about 10 micrometers in diameter, whose optical cavities and electrical injection schemes are radically different from conventional edge emitting semiconductor lasers. The vcssel geometry emits high quality beams perpendicular to the face of the chip, rather than out the edge of the chip, and can be readily fabricated in one and two dimensional arrays. A preliminary demonstration of the modulation doped approach was made. The resuit was a record low threshold voltage of 1.7 volts for vcsels. Previously, vcsels required a minimum of about 2.5 volts for thresholed or had very high current thresholds

DESCRIPTORS: *SEMICONDUCTOR LASERS, LASER CAVITIES, EDGES, THRESHOLD EFFECTS, ARRAYS, EFFICIENCY, CHIPS(ELECTRONICS), ELECTRICAL PROPERTIES, MINIATURE ELECTRONIC EQUIPMENT.

IDENTIFIERS: VCSEL(VERTICAL CAVITY SURFACE EMITTING LASERS), MICROLASERS,

AD NUMBER: A310337

ARIZONA UNIV TUCSON DEPT OF ELECTRICAL AND COMPUTER ENGINEERING

(U): INVESTIGATION OF RADIATION EFFECTS IN MICROELECTRONICS.

JUN 96 320P
PERSONAL AUTHORS: GALLOWAY, KENNETH F.; SCHRIMPF, RONALD D.; JOHNSON, GREGORY H.

UNCLASSIFIED REPORT

ABSTRACT: (U) Electronic components implemented in space borne and Military applications are often required to operate in a hostile Radiation Environment, and are therefore subject to the degradation and failure mechanisms associated with such environments. This report discusses radiation effects research in the areas of (1) Single event burnout of power Mosfets (2) single event gate rupture of power Mosfets; (3) total dose degradation of power Mosfets (including mobility degradation, cryogenic operation, 1/f noise, and termination structures); and (4) total-dose gain degradation of bipolar junction transistors.

DESCRIPTORS: *MOSFET SEMICONDUCTORS, *RADIATION DAMAGE, SIMULATION, DEGRADATION, SPACE ENVIRONMENTS, ELECTRONIC EQUIPMENT, GATES(CIRCUITS), BURNOUT, MICROELECTRONICS, DOSAGE,

IDENTIFIERS: SEU(SINGLE EVENT UPSET), 1/F NOISE,

AD NUMBER: A323968

AIR FORCE INST OF TECH
WRIGHT-PATTERSON AFB OH

(U) A MICROMECHANICAL SILICON OSCILLATING ACCELEROMETER.

APR 97 105P
PERSONAL AUTHORS: GIBBONS, KEVIN A.

UNCLASSIFIED REPORT

ABSTRACT: (U) This thesis describes the design and testing of a silicon oscillating accelerometer (SOA). The SOA is a silicon, micromechanical, oscillating beam accelerometer. The accelerometer is configured with two silicon tuning fork oscillators that are electrostatically driven and sensed in their out of phase vibrational resonance. The oscillators move on flexure beams which are configured to have one end anchored and the other end fixed to a shared seismic mass. When the seismic mass experiences an input acceleration, one oscillator's vibrating beams are loaded in tension while the other oscillator's beams are loaded in compression. This loading causes an increase and decrease in the respective oscillator's natural frequency. This change in frequency is proportional to the input acceleration. Automatic gain control electronics regulate the oscillation amplitude at resonance. The two oscillator's frequency outputs are differenced to exploit common mode error rejection. The SOA has been fabricated from single crystal silicon using a bulk dissolved wafer on glass micromachining process. It is vacuum packaged in a leadless ceramic chip carrier to achieve high quality factor and thus a sharp resonance. Results of both closed form and finite element analyses are described and are in good agreement sensors were fabricated and experimental data including quality factor, input acceleration sensitivity or scale factor, and oscillator temperature sensitivity results are presented. An oscillator frequency of 27 kHz, A G factor over 100,000, a scale factor of 4 Hz per g, and an oscillator temperature sensitivity of 0.4 Hz per degree Celsius have been achieved. The experimental data is shown to be in agreement with analysis results.

DESCRIPTORS: (U) *ACCELEROMETERS, *CRYSTAL OSCILLATORS, OSCILLATORS, ELECTRONICS, MACHINING, EXPERIMENTAL DESIGN, FINITE ELEMENT ANALYSIS, THESES, CHIPS(ELECTRONICS), SINGLE CRYSTALS, AUTOMATIC GAIN CONTROL, DIFFERENCE FREQUENCY.

IDENTIFIERS: SILICON OSCILLATING ACCELERONMETER

AD NUMBER: A322842

MASSACHUSETTS INST OF TECH
LEXINGTON LINCOLN LAB

(U) SOLID STATE RESEARCH.

AUG 96 80P
PERSONAL AUTHORS: SHAVER, DAVID C.

UNCLASSIFIED REPORT

ABSTRACT: (U) This report covers in detail the research work of the Solid State Division at Lincoln laboratory for the period 1 May-31 July 1996. The topics covered are electrooptical devices, quantum electronics, materials research, submicrometer technology, high speed electronics, microelectronics, and analog device technology. Funding is provided primarily by the AIR FORCE, with additional support provided by the ARMY, DARPA, NAVY, BMDO, NASA, and NIST.

DESCRIPTORS: (U) *SOLID STATE PHYSICS, ELECTRONICS, AIR FORCE RESEARCH, ELECTROOPTICS, MATERIALS, MICROELECTRONICS, QUANTUM ELECTRONICS, ANALOG SYSTEMS.

♦AD NUMBER: A322246

SFA INC LANDOVER MD

(U) MICROELECTRONIC RADIATION HARDENING PROCESS AND DESIGN DEVELOPMENT, TEST, AND EVALUATION.

MAR 97 49P

PERSONAL AUTHORS: MCMARR, PATRICK; REVESZ, AKOS; LAWRENCE, REEK

UNCLASSIFIED REPORT

ABSTRACT: (U) Radiation induced charge trapping versus buried oxide (box) thickness on various separation by implantation (simox) buried oxides has been determined. An inflection point has been observed in the voltage shift vs. Buried oxide thickness relationship. As such, the radiation induced voltage shifts for Thin Buried Oxides are greater than what could be expected from a Simple Square Law relationship. These results can be explained by the location and magnitude of the radiation induced oxide charge Centroid and its relationship to the box thickness. The location of the Centroid for trapped positive charge is dependent on the Radiation induced hole mobility, which is related to Simox Processing as well as on geometry and charge saturation. Photoinjection was used to study the charge trapping properties of High Temperature Oxidation (HITOX) Simox Buried Oxides, provided by two independent vendors. After electron injection, the electron trapping per area for both HITOX material sources was found to be larger than their respective standard (CONTROL) Simox structures. Photo injection, buried oxide, oxide charge Centroid, electron capture cross section, high temperature oxidation, separation by implantation of oxygen.

DESCRIPTORS: (U) *ION IMPLANTATION, *SOLID STATE CHEMISTRY, *RADIATION HARDENING, THIN FILMS, TRAPPING(CHARGED PARTICLES), CROSS SECTIONS, MICROELECTRONICS, SEPARATION, ELECTRON CAPTURE, SILICON ON INSULATOR.

IDENTIFIERS: HITOX(HIGH TEMPERATURE OXIDATION), BOX(BURIED OXIDES

AD NUMBER: A321966

CASE WESTERN RESERVE UNIV CLEVELAND OH DEPT OF MACROMOLECULAR SCIENCE

(U) TWENTIETH ASILOMAR CONFERENCE ON POLYMERIC MATERIALS,

FEB 97 22P

PERSONAL AUTHORS: BAER, ERIC

UNCLASSIFIED REPORT

ABSTRACT: (U) The 1997 Asilomar Conference on Polymeric Materials focused on Electroactive Polymer Systems. New directions were probed for use of such materials in power sources. The implications in biological integration of such systems were also explored. An attempt was made to understand and predict structure-property relationships by using hierarchical paradigms to describe these complex materials systems. Special emphasis were on the modeling of such Polymers using advanced computer methods, and on the design and synthesis of new Eelectroactive Polymeric Materials based on the predictions elucidated from these computational advances. As in previous years, this conference addressed the problems and opportunities that are arising with the emergence of a hierarchical approach to the design of new materials systems. Focus was on important questions such as the factors that gave rise to relatively discrete organizational levels of structure, the interactions between such levels and the synthesis of new active Polymers with functional designs aimed at the efficient and selective transport of energy. The Twentieth Asilomar Conference focused particularly on new Polymers with unusual properties, on Polymers with switching characteristics, and on Macromolecular Neural Networks for image processing.

DESCRIPTORS: (U) *POLYMERIC FILMS, *POLYMORPHISM, SYMPOSIA, GRAFT POLYMERIZATION, COPOLYMERS, AMORPHOUS MATERIALS, CRYSTALLIZATION, MACROMOLECULES, MOLECULAR STRUCTURE, MICROANALYSIS, NUCLEOTIDES, NANOTECHNOLOGY.

AD NUMBER: A321589

NOTRE DAME UNIV IN

(U) COLLECTIVE COMPUTATIONAL ACTIVITY IN SELF- ASSEMBLED ARRAYS OF QUANTUM DOTS: A NOVEL NEUROMORPHIC ARCHITECTURE FOR NANOELECTRONICS,

OCT 96 13P
PERSONAL AUTHORS: ROYCHOWDHURY, VWANI P.; JANES, DAVID B.; BANDYOPADHYAY, SUPRIYO; WANG, XIAODONG

UNCLASSIFIED REPORT

ABSTRACT: (U) We describe a new class of Nanoelectronic Circuits which exploits the charging behavior in resistively/capacitively linked arrays of Nanometer-Sized Metallic Islands (Quantum Dots), self-assembled on a resonant tunneling diode, to perform neuromorphic computation. These circuits produce associative memory effects and realize the additive short-term memory (stm) or content addressable memory (cam) models of neural networks without requiring either large-area/high-power operational amplifiers, or massive interconnectivity between devices. Both these requirements had seriously hindered the application of neural networks in the past. Additionally, the circuits can solve np-complete optimization problems (such as the traveling sales-man problem) using single electron charge dynamics, exhibit rudimentary image-processing capability, and operate at room temperature unlike most quantum devices. Two-dimensional (2d) processors, with a 100 x 100 pixel capacity, can be fabricated in an area of 10-8 cm2 leading to unprecedented functional density. Possible routes to synthesizing these circuits, employing self-assembly, are also discussed.

DESCRIPTORS: (U) *QANTUM ELECTRONICS, *NANOTECHNOLOGY, IMAGE PROCESSING, REPRINTS, NEURAL NETS, COMPUTATIONS, TUNNELING(ELECTRONICS), MEMORY DEVICES, ASSOCIATIVE PROCESSING, NONLINEAR PROGRAMMING.

IDENTIFIERS: QUANTUM DOTS, RESONANT TUNNELING, CAM(CONTENT ADDRESSABLE MEMORY), TRAVELING SALESMAN PROBLEMS

AD NUMBER: A321584

NOTRE DAME UNIV IN

(U COMPUTATIONAL PARADIGMS IN NANOELECTRONICS: QUANTUM COUPLED SINGLE ELECTRON LOGIC AND NEUROMORPHIC NETWORKS,

JUN 96 14P

UNCLASSIFIED REPORT

ABSTRACT: (U) We describe a new class of nanoelectronic circuits Where circuit functions are derived from cooperative, quantum Mechanical interactions between single electrons confined in arrays of quantum dots. Two specific architectures are examined: (i) quantum coupled logic in which boolean logic functions are implemented by quantum mechanical spin-spin interactions between single electrons in arrays of quantum dots, and (ii) quantum neuromorphic networks that exploit the complex spatial and temporal evolution of discrete charge in an ensemble of nonlinearly interacting quantum dots to elicit collective computational behavior. The first class of circuits includes combinational and sequential digital systems. Both logically irreversible elements such as half adders, s-r flip flops, shift registers, ring counters, etc., and reversible feynman gates for quantum computation have been designed in this paradigm. These circuits can be endowed with the required 'unidirectional' (non-reciprocal) character that previous (flawed) designs of similar circuits lacked. The second class of circuits comprises discrete hopfield networks which utilize single electron tunneling events in arrays of metallic islands to perform neuromorphic computation. They can solve np-complete optimization problems (such as the traveling salesman problem), produce associative memory effects and also exhibit rudimentary image-processing capability.

DESCRIPTORS: (U) *ELECTROOPTICS, *QUANTUM ELECTRONICS, *NANOTECHNOLOGY, IMAGE PROCESSING, REPRINTS, NEURAL NETS, TUNNELING(ELECTRONICS), QUANTUM EFFICIENCY, LOGIC CIRCUITS, ASSOCIATIVE PROCESSING, SPIN STATES, PHASE LOCKED SYSTEMS, BOOLEAN ALGEBRA, SHIFT REGISTERS.

IDENTIFIERS: QUANTUM DOTS, SPIN SPIN INTERACTIONS, HOPFIELD NETWORKS, MAGNETIC SPINS, SPIN POLARIZATION

AD NUMBER: A321364

AIR FORCE INST OF TECH WRIGHT-PATTERSON AFB OH

(U) MICROELECTROMECHANICAL ISOLATION OF ACOUSTIC WAVE RESONATORS.

DEC 96 107P
PERSONAL AUTHORS: REID, JAMES R., JR

UNCLASSIFIED REPORT

ABSTRACT: (U) Microelectromechainical Systems (mems) is a rapidly expanding field of research into the design and fabrication of actuated mechanical systems on the order of a few micrometers to a few millimeters. Mems potentially offers new methods to solve a variety of engineering problems. A large variety of mems systems including flip-up platforms, scanning micromirrors, and rotating micromirrors are developed to demonstrate the types of mems that can be fabricated. The potential of mems for reducing the vibration sensitivity of surface acoustic wave and surface transverse wave resonators is then evaluated. A micromachined vibration isolation system is designed and modeled. A fabrication process utilizing two sided anisotropic etching of ? 110 ilicon wafers is developed. The process utilizes standard microelectronic fabrication equipment to batch fabricate the isolation systems. The fabricated systems are only 1 cm by 1 cm by 1 mm. Several oscillators are fabricated using commercially fabricated stw resonators mounted on the isolation systems. The resonators are driven by their standard oscillator circuit. Incorporating the isolation system into the oscillator does not result in an appreciable increase the size or the weight of the oscillator. Testing of the oscillators shows that the isolators successfully function as passive vibration isolation systems.

DESCRIPTORS: (U) *ACOUSTIC RESONATORS, *MICROELECTRONICS, COMPUTER AIDED DESIGN, MACHINING, ACCELERATION, VIBRATION ISOLATORS, THESES, TRANSVERSE WAVES, COMPUTER AIDED MANUFACTURING, WAFERS, SURFACE ACOUSTIC WAVES, FREQUENCY SHIFT, CRYSTAL OSCILLATORS.

IDENTIFIERS: MEMS (MICROELECTROMECHANICAL SYSTEMS), MICROMACHINING

AD NUMBER: A321224

PRINCETON UNIV NJ

(U) SMART MATERIALS SYSTEMS THROUGH MESOSCALE PATTERNING,

1996 13P
PERSONAL AUTHORS: AKSAY, I. A.; GROVES, J. T.; GRUNER, S. M.; LEE, P. C.; PRUD'HOMME, R. K.

UNCLASSIFIED REPORT

ABSTRACT: (U) We report work on the fabrication of smart materials with two unique strategies: (1) self-assembly and (2) laser stereolithography. Both methods are akin to the processes used by biological systems. The first one is ideal for pattern development and the fabrication of miniaturized units in the submicron range and the second one in the 10 micrometers to 1 mm size range. By using these miniaturized units as building blocks, one can produce smart material systems at larger length scales such as smart structural components. We have chosen to focus on two novel piezoceramic systems: (1) high-displacement piezoelectric actuators, and (2) piezoceramic hydrophone composites processing negative poisson ratio matrices. High-displacement actuators are essential in such applications as linear motors, pumps, switches, loud speakers, variable-focus mirrors, and laser deflectors. Arrays of such units can potentially be used for active vibration control of helicopter rotors as well as the fabrication of adaptive rotors. In the case of piezoceramic hydrophone composites, we utilize matrices with a negative poisson's ratio in order to produce highly sensitive, miniaturized sensors. We envision such devices having promising new application areas such as monitoring fluid pressures in constrained volumes using small, sensitive hydrophones. Negative poisson ratio materials have promise as robust shock absorbers, air filters, and fasteners, and hence, can be used in aircraft and land vehicles.

DESCRIPTORS: (U) *MATERIALS, *CERAMIC MATERIALS, *PIEZOELECTRIC MATERIALS, *PATTERNS, LINEAR SYSTEMS, CONTROL, VIBRATION, AIRCRAFT, COMPOSITE MATERIALS, SHOCK ABSORBERS, ARRAYS, FABRICATION, MODULAR CONSTRUCTION, SENSITIVITY, LITHOGRAPHY, SCALE, PRESSURE, ADAPTIVE SYSTEMS, MINIATURIZATION, STRUCTURAL COMPONENTS, SWITCHES, POISSON RATIO,.

IDENTIFIERS: *SMART MATERIALS, *MESOSCALE PATTERNING, *PIEZOCERAMIC MATERIALS, STEREOLITHOGRAPHY,

AD NUMBER: A321180

NATIONAL AIR INTELLIGENCE CENTER
WRIGHT-PATTERSON AFB OH

(U) RESEARCH ON GYRO ACCELEROMETER OUTPUT DEVICE,

OCT 96 14P
PERSONAL AUTHORS: CHANGZHI, XU; WEI, WANG; CAIFAN, ZHAO

UNCLASSIFIED REPORT

ABSTRACT: (U) To design a new gyro accelerometer output device, this paper advances a miniaturized high-speed and high-precision dynamic oniometric system plan and discusses the engineering realization of this plan. In fact, this goniometric system has already been successfully applied to a static pressure liquid-floated gyro accelerometer.

DESCRIPTORS: (U) *ACCELEROMETERS, FOREIGN TECHNOLOGY, TRANSLATIONS, MINIATURE ELECTRONIC EQUIPMENT, MINIATURIZATION, GYROSCOPES, CHINA, CHINESE LANGUAGE, GONIOMETERS.

IDENTIFIERS: FOREIGN REPORTS

AD NUMBER: A321118

YALE UNIV NEW HAVEN CT
DEPT OF ELECTRICAL ENGINEERING

(U) OFFICE OF NAVAL RESEARCH FINAL TECHNICAL REPORT FOR GRANT: N00014-94-1-0267.

JAN 97 10P
PERSONAL AUTHORS: REED, M. A.

UNCLASSIFIED REPORT

ABSTRACT: (U) This work is intended to provide new materials and methods for systems with micrometer and nanometer dimensions that will contribute to microelectronics design and manufacturing. The major components of the programs are: (1) self-assembly, which provides a way of making highly perfect structures with minimal cost and high quality (2) self-assembled monolayers (sams), system of materials that provides a high level of control over the properties of surfaces, and that are also functional in various ways (3) soft lithography, which provides a technology for patterning in the plane of the surface that is complementary to current photolithography. (4) electronically functional devices from conjugated organic oligomers of precise length and constitution for utilization as interconnects and devices.

DESCRIPTORS: (U) *SOLID STATE ELECTRONICS, *NANOTECHNOLOGY, LITHOGRAPHY, PRECISION, MICROELECTRONICS, OLIGOMERS, PHOTOLITHOGRAPHY.

IDENTIFIERS: SOFT LITHOGRAPHY

AD NUMBER: A320629

MASSACHUSETTS INST OF TECH LEXINGTON LINCOLN LAB

(U) SOLID STATE RESEARCH.

MAY 96 58P
PERSONAL AUTHORS: SHAVER, DAVID C.

UNCLASSIFIED REPORT

ABSTRACT: (U) This report covers in detail the research work of the solid state division at Lincoln Laboratory for the period 1 February-30 April 1996. The topics covered are electrooptical devices, quantum electronics, materials research, submicrometer technology, high speed electronics, microelectronics, and analog device technology. Funding is provided primarily by the Air Force, with additional support provided by the Army, DARPA, Navy, BMDO, NASA, and MST.

DESCRIPTORS: (U) *QUANTUM ELECTRONICS, *SOLID STATE PHYSICS, SOLID STATE LASERS, ELECTROOPTICS, EPITAXIAL GROWTH, ETCHING, ELECTROMECHANICAL DEVICES, MICROELECTRONICS, ANALOG SYSTEMS.

IDENTIFIERS: MICROMECHANICAL,

AD NUMBER: A319998

CORNELL UNIV ITHACA NY MATERIALS SCIENCE CENTER

(U) ATOMIC MECHANISMS OF FLOW AND FRACTURE AT METAL-CERAMIC INTERFACES AND THEIR ROLE IN THE DESIGN OF METAL MATRIX COMPOSITES

NOV 96 25P
PERSONAL AUTHORS: RAJ, RISHI

UNCLASSIFIED REPORT

ABSTRACT: (U) This report describes new and significant results that can be applied in the microstructure design for optimum mechanical performance of metal-ceramic composites and laminates. There are three elements to these recommendations: (1) the design of the atomic structure of metal-ceramic interfaces, (2) identification of the critical length scale in the two phase microstructure, and (3) prediction of the microstructural conditions under which the thermal conductivity of the composite becomes significantly influenced by the thermal boundary resistance of interfaces. In the first topic we show that the beneficial effect of titanium interlayers at a copper/alumina interface is accomplished with only about one monolayer; with further increase in the titanium interlayer thickness having an insignificant effect on the interfacial strength. In the second topic we show that the metal ligament size is the key microstructural parameter in controlling the flow stress, the fracture stress and the fracture toughness of metal-ceramic composites. The metal ligament size is important because dislocation activity in the metal, which produces pile ups against the interface, is the critical event in flow and fracture of composites. In the third area we show that the interfacial thermal boundary resistance plays a dominant role in the overall thermal conductivity of the composite when the microstructural scale becomes smaller than about 1um.

DESCRIPTORS: (U) *CERAMIC MATRIX COMPOSITES, *METAL MATRIX COMPOSITES, *FRACTURE(MECHANICS), *PLASTIC FLOW, PLASTIC DEFORMATION, MICROSTRUCTURE, STRESS ANALYSIS, ALUMINUM ALLOYS, LAMINATES, COPPER ALLOYS, TOUGHNESS, OXIDATION, ALUMINUM OXIDES, THERMAL CONDUCTIVITY, TITANIUM, DUCTILITY, THERMAL BOUNDARY LAYER, GRAIN BOUNDARIES, THERMAL RESISTANCE, CREEP STRENGTH, NANOTECHNOLOGY.

AD NUMBER: A319052

AIR FORCE INST OF TECH WRIGHT-PATTERSON AFB OH

(U) DEMONSTRATING OPTICAL ABERRATION CORRECTION WITH A MEMS MICRO-MIRROR DEVICE.

DEC 96 104P
PERSONAL AUTHORS: HICK, SHAUN R.

UNCLASSIFIED REPORT

ABSTRACT: (U) This research conducted the first demonstrated use of a micro-electro-mechanical structure (mems) mirror array to correct a static optical aberration. A well developed technique in adaptive optics imaging systems uses a deformable mirror to reflect the incident wave front to the imaging stage of the system. By matching the surface of the deformable mirror to the shape of the wave front phase distortion, the reflected wave front will be less aberrated before it is imaged. Typical adaptive optics systems use piezo-electric actuated deformable mirrors. This research used an electrostatically actuated, segmented mirror array, constructed by standard mems fabrication techniques, to investigate its performance as a deformable mirror. The relatively cheap cost of mems fabrication promises new adaptive optics applications if a suitable design can be found. In the demonstration, the point spread function (psf) of the corrected and uncorrected aberrated image were compared. A 43 percent improvement in the peak intensity of the psf was noted in the corrected image.

DESCRIPTORS: (U) *IMAGE PROCESSING, *MICROELECTRONICS, *ADAPTIVE OPTICS, FOURIER TRANSFORMATION, MIRRORS, OPTIMIZATION, ELECTROOPTICS, THESES, OPTICAL IMAGES, IMAGE INTENSIFICATION, SYSTEMS ANALYSIS, FOCAL PLANES, OPTICAL PROCESSING, PLANE WAVES, ELECTROSTATICS, PHASE DISTORTION, DIFFRACTION ANALYSIS, WAVEFRONTS, OPTICAL FILTERS.

IDENTIFIERS: MEMS(MICROELECTROMECHANICAL SYSTEMS)

AD NUMBER: A318864

AIR FORCE INST OF TECH WRIGHT-PATTERSON AFB OH
SCHOOL OF ENGINEERING

(U) MODELING AND SIMULATION OF OPTICAL CHARACTERISTICS OF MICROELECTROMECHANICAL MIRROR ARRAYS.

DEC 96 152P
PERSONAL AUTHORS: ROBERTS, PETER C.

UNCLASSIFIED REPORT

ABSTRACT: (U) Mems (micro-electro-mechanical systems) micromirror devices can be used to control the phase of a propagating light wavefront, and in particular to correct aberrations that may be present in the wavefront, due to either atmospheric turbulence or any other type of fixed or time and space varying aberrations. In order to shorten the design cycle of mems micromirror devices, computer software is developed to create, from mems micromirror device design data, a numerical model of the mems device. The model is then used to compute the far field diffraction pattern of a wavefront reflected from the device, and to predict the effectiveness with which it can be used to correct an aberrated wavefront. For validation, the computed far field diffraction pattern is compared to that measured using a real mems micromirror device, with a reasonable match between the two being found. The model is designed for maximum flexibility and can be easily adapted to new designs of mems micromirror devices.

DESCRIPTORS: (U) *MIRRORS, *ELECTROMECHANICAL DEVICES, *ADAPTIVE OPTICS, MATHEMATICAL MODELS, COMPUTERIZED SIMULATION, SOFTWARE ENGINEERING, IMAGE PROCESSING, OPTICAL PROPERTIES, AIR FORCE RESEARCH, COMPUTER AIDED DESIGN, ARRAYS, THESES, TURBULENCE, ATMOSPHERIC MOTION, OPTICAL IMAGES, OPTICAL ANALYSIS, APPROXIMATION(MATHEMATICS), MICROELECTRONICS, PLANE WAVES, DIFFRACTION ANALYSIS, WAVEFRONTS, FOURIER ANALYSIS.

IDENTIFIERS: MEMS(MICROELECTROMECHANICAL SYSTEMS)

AD NUMBER: A318441

WASHINGTON STATE UNIV PULLMAN DEPT OF PHYSICS

(U) SMART OPTO MECHANIC POLYMER DEVICES.

NOV 96 15P
PERSONAL AUTHORS: KUZYK, MARK G.

UNCLASSIFIED REPORT

ABSTRACT: (U) We have demonstrated that polymer optical fiber can be built into smart photomechanical devices that have the ability to sense strain and to make mechanical adjustments accordingly. The first bulk device demonstrated is an all optical vibration stabilizer that is capable of keeping the position of a mirror fixed to within one part in 10(exp 8). This device is unique in that no electronics are used: light powers the device; light acts as the sensing medium; light carries the information; the information is processed by light; and the light is used to move the material by photomechanical action. We have also demonstrated that such a device can be miniaturized to sub-millimeter dimensions and that all the functions of the bulk device can be simultaneously imparted to one physical part of the device. Such devices can be connected in series or parallel to make ultrasmart associations that can be built into smart composite materials. Our devices have been patented and the technology is being transferred to industry.

DESCRIPTORS: (U) *ADAPTIVE CONTROL SYSTEMS, *ELECTROOPTICS, *VIBRATION ISOLATORS, FIBER OPTICS, MECHANICAL PROPERTIES, POLYMERS, COMPOSITE MATERIALS, STRAIN(MECHANICS), MINIATURIZATION, STABILIZATION SYSTEMS.

IDENTIFIERS: *PHOTOMECHANICS, SMART MATERIALS

AD NUMBER: A315763

EQUINOX CORP BALTIMORE MD

(U) PHASE I STTR: POLARIZATION IMAGER TECHNOLOGY.

AUG 96 27P
PERSONAL AUTHORS: WOLF, LAWRENCE B.

UNCLASSIFIED REPORT

ABSTRACT: (U) The first section of this report motivates the unique capabilities afforded by polarization imagers and the second section discusses the need and design for the next generation of polarization imager technology along with the critical advantages of this new technology. The third section discusses the technical hurdles needed to be transcended to make this new technology a reality. The fourth section describes the feasibility objective for phase i and the corresponding actual results. The fifth section describes some of the low level technical development details, and section six is a brief conclusion.

DESCRIPTORS: (U) *IMAGE CONVERTERS, *CHARGE COUPLED DEVICES, POLARIZATION, CHIPS(ELECTRONICS), PHOTOMASKING, NANOTECHNOLOGY.

AD NUMBER: A311822

MASSACHUSETTS UNIV AMHERST
DEPT OF MECHANICAL ENGINEERING

(U) FINITE ELEMENT MODELING AND ANALYSIS OF MCM HIGH DENSITY INTERCONNECT VIAS.

JUN 96 100P
PERSONAL AUTHORS: GROSSE, I.; DITOMASSO, J.

UNCLASSIFIED REPORT

ABSTRACT: (U) Failure modes of vias within a chip's first multi-chip module are studied using several two and three-dimensional families of finite element models. The models study both the global strains of the entire module and local strains of a single via under uniform temperature loading between -65 deg c and 120 deg c. The accuracy of the models was verified by comparing different families of models with each other, with analytical beam theory, and with empirical data generated by electron beam moire strain data taken by NIST on a test specimen. Global finite element analysis results revealed that the strains within the high density interconnect layer have only a 10% effect upon the local via strains. A simple analytical method was developed to obtain displacement boundary conditions to be applied to local via finite element models, thereby precluding the need for global finite element analysis of the entire module. For a local via analysis, the axisymmetric and three-dimensional finite element models were found to predict the location of via failures, which agrees with failure locations observed under accelerated test conditions. A number of via design factors were identified that affect the strain concentration in the via wall. However, the dielectric/epoxy intermaterial boundary was not found to be the cause of the strain concentration in the via wall.

DESCRIPTORS: (U) *STRESS ANALYSIS, *FINITE ELEMENT ANALYSIS, *CHIPS(ELECTRONICS), *MODULES(ELECTRONICS), STRESS STRAIN RELATIONS, MATHEMATICAL MODELS, DIELECTRICS, CRACK PROPAGATION, THERMAL EXPANSION, MICROELECTRONICS, NONLINEAR ANALYSIS, RELIABILITY(ELECTRONICS), THERMAL STRESSES, FAILURE(ELECTRONICS), STRESS CONCENTRATION.

IDENTIFIERS: MULTICHIP MODULES, PLANE STRAIN

AD NUMBER: A311553

NAVAL POSTGRADUATE SCHOOL
MONTEREY CA

(U) DESIGN OF A SATELLITE-BASED MICROELECTRONIC RADIATION TESTING EXPERIMENT.

MAR 96 255P
PERSONAL AUTHORS: MOONEY, CHRISTOPHER S.

UNCLASSIFIED REPORT

ABSTRACT: (U) In this research, an electronic daughterboard to be used on the microelectronics and photonics test bed satellite was designed. A printed circuit board with radiation-hardened components was laid out to test various families of static ram chips and an experimental gallium arsenide integrated circuit. computer aided design tools produced by cadence design systems were used to logically and physically design the experiment. Output from the cadence software provides the information necessary to fabricate, assemble, and test the board.

DESCRIPTORS: (U) *TEST BEDS, *PRINTED CIRCUIT BOARDS, *RADIATION HARDENING, COMPUTER AIDED DESIGN, GALLIUM ARSENIDES, THESES, CHIPS(ELECTRONICS), RANDOM ACCESS COMPUTER STORAGE, MICROELECTRONICS, SPACECRAFT COMPONENTS.

IDENTIFIERS: CADENCE COMPUTER PROGRAMS, SINGULAR EVENT UPSET

AD NUMBER: A310359

VIXEL INC BROOMFIELD CO

(U) LOW-RESISTANCE, HIGH-POWER-EFFICIENCY VERTICAL CAVITY MICROLASERS.

MAY 96 15P
PERSONAL AUTHORS: JEWELL,

UNCLASSIFIED REPORT

ABSTRACT: (U) The purpose of this project was to improve the total power efficiency of vertical cavity microlasers to further the commercialization of large arrays of semiconductor lasers integrated on single chips. Vertical cavity surface emitting lasers are tiny semiconductor lasers, typically about 10 micrometers in diameter, whose optical cavities and electrical injection schemes are radically different from conventional edge emitting semiconductor lasers. The vcssel geometry emits high quality beams perpendicular to the face of the chip, rather than out the edge of the chip, and can be readily fabricated in one and two dimensional arrays. A preliminary demonstration of the modulation doped approach was made. The result was a record low threshold voltage of 1.7 volts for vcsels. Previously, vcsels required a minimum of about 2.5 volts for thresholed or had very high current thresholds. This demonstration destroyed the then widely held micsconception that vcsels inherently were high resistance and high voltage devices.

DESCRIPTORS: (U) *SEMICONDUCTOR LASERS, LASER CAVITIES, EDGES, THRESHOLD EFFECTS, ARRAYS, EFFICIENCY, CHIPS(ELECTRONICS), ELECTRICAL PROPERTIES, MINIATURE ELECTRONIC EQUIPMENT.

IDENTIFIERS: VCSEL(VERTICAL CAVITY SURFACE EMITTING LASERS), MICROLASERS

AD NUMBER: A310337

ARIZONA UNIV TUCSON DEPT OF ELECTRICAL AND COMPUTER ENGINEERING

(U) INVESTIGATION OF RADIATION EFFECTS IN MICROELECTRONICS.

JUN 96 320P
PERSONAL AUTHORS: GALLOWAY, KENNETH F.; SCHRIMPF, RONALD D.; JOHNSON, GREGORY H.

UNCLASSIFIED REPORT

ABSTRACT: (U) Electronic components implemented in space borne and military applications are often required to operate in a hostile radiation environment, and are therefore subject to the degradation and failure mechanisms associated with such environments. This report discusses radiation effects research in the areas of (1) single event burnout of power mosfets (2) single event gate rupture of power mosfets; (3) total dose degradation of power mosfets (including mobility degradation, cryogenic operation, 1/f noise, and termination structures); and (4) total-dose gain degradation of bipolar junction transistors. Experiment details and modeling and simulation results are given in these areas. This work is intended to (1) facilitate selection of appropriate components for radiation environments; (2) provide design techniques to improve the radiation hardness of power mosfets and bipolar junction transistors; and (3) advance the technical base with new physical insights in radiation effects in microelectronics.

DESCRIPTORS: (U) *MOSFET SEMICONDUCTORS, *RADIATION DAMAGE, SIMULATION, DEGRADATION, SPACE ENVIRONMENTS, ELECTRONIC EQUIPMENT, GATES(CIRCUITS), BURNOUT, MICROELECTRONICS, DOSAGE, MILITARY APPLICATIONS, CRYOGENICS, BIPOLAR TRANSISTORS, RADIATION HARDENING, UNCTION TRANSISTORS, FAILURE(ELECTRONICS), SPACEBORNE.

IDENTIFIERS: SEU(SINGLE EVENT UPSET), 1/F NOISE

AD NUMBER: A305195

ARMY RESEARCH LAB ABERDEEN PROVING GROUND MD

(U) PRELIMINARY DESIGN OF A RANGE CORRECTION MODULE FOR AN ARTILLERY SHELL.

MAR 96 26P
PERSONAL AUTHORS: HOLLIS, MICHAEL S.

UNCLASSIFIED REPORT

ABSTRACT: (U) With the advances in microelectronics, miniature motor technology, and sensor technology, the reality of a low cost competent munition (lccm) trajectory correction module is conceivable. The U.S. Army Research Laboratory (ARL) and the U.S. Army Armament Research, Development, and Engineering Center (ARDEC) have been working on various lccm concepts. The lccm concept dictates that the design of a trajectory correction module will fit into an artillery shell like any of the fuzes used by NATO. This report represents an initial design process to identify potentially critical problems in the mechanical design of a trajectory control device. The design process will concentrate on the current level of technologies and the electro-mechanical requirements for a d-ring range correction module. The d-ring correction module is a one-dimensional, self-correction device concept for providing sufficient change in drag, to achieve the needed correction, given the constraints of size, power, and other necessary components and technologies. An lccm range correction module appears to be a very viable concept without requiring aggressive technologies or high-risk approaches. The efficient use of the available volume for electrical and mechanical components will he crucial.

DESCRIPTORS: (U) *FIRE CONTROL SYSTEMS, *PROJECTILE TRAJECTORIES, *ARTILLERY AMMUNITION, NATO, MECHANICAL PROPERTIES, MILITARY REQUIREMENTS, ARMY RESEARCH, DETECTORS, RISK, LOW COSTS, EFFICIENCY, ELECTROMECHANICAL DEVICES, MICROELECTRONICS, RANGE FINDING, DRAG, MOTORS, MINIATURIZATION, ELECTRICAL EQUIPMENT, CORRECTIONS, MECHANICAL COMPONENTS.

IDENTIFIERS: LCCM(LOW COST COMPETENT MUNITION)

AD NUMBER: A304367

ARMY RESEARCH LAB ABERDEEN PROVING GROUND MD

(U) APPLICATION OF AN INERTIAL RETICLE SYSTEM TO AN OBJECTIVE PERSONAL WEAPON.

FEB 96 30P
PERSONAL AUTHORS: VON WAHLDE, RAYMOND; KREGEL, MARK; HAUG, TOM; BROSSEAU, TIM

UNCLASSIFIED REPORT

ABSTRACT: (U) The Inertial Reticle System (IRS) is a novel fire control system that improves the accuracy of direct-fire weapons by stabilizing the aim point rather than the weapon. Miniature inertial sensors measure weapon motion and drive an electronically generated reticle in opposition so that it appears to remain fixed relative to the target. The system senses when the actual aim point will cross the inertial reticle and then fires the weapon. The U.S. Army Research Laboratory (ARL) has equipped small-caliber weapons such as an m16 and a sniper rifle with the IRS. An IRS on a pistol- sized Objective Personal Weapon (OPW) would help achieve the OPW accuracy goals by reducing weapon pointing error. In addition, by enabling a shooter to preselect an aim point and maintain it despite weapon motion, the IRS would reduce collateral damage and aid in immediate incapacitation. An Opw, equipped with inertial sensors and a video sight, might function much like the current IRS. The target could be viewed on a weapon or helmet-mounted display. Miniaturization of components is the greatest technical barrier to fitting the IRS on an OPW. However, progress in electronics and work in micromachines make application of the IRS to an OPW feasible.

DESCRIPTORS: (U) *SMALL ARMS AMMUNITION, *FIRE CONTROL SYSTEMS, WEAPONS, LINE OF SIGHT, ELECTRONICS, ARMY RESEARCH, DETECTORS, SNIPERS, MOTION, ACCURACY, ERRORS, BARRIERS, SIGHTS, AIMING, INERTIAL SYSTEMS, VIDEO SIGNALS, RIFLES, MINIATURIZATION, SENSES(PHYSIOLOGY), HELMET MOUNTED DISPLAYS, INCAPACITATION, RETICLES, FITTINGS.

AD NUMBER: A323754

NEBRASKA UNIV LINCOLN

(U) INVESTIGATION OF MICROSCOPIC MECHANISMS OF FAILURE OF ELECTRONIC SMART MATERIALS/SYSTEMS.

SEP 96 12P
PERSONAL AUTHORS: JIANG, QING

UNCLASSIFIED REPORT

ABSTRACT: (U) The development of ferroelectric ceramics is driven by the needs of functional ceramics for various applications, such as sensors, transducers and actuators, and these functional ceramics account for more than 60% of the total high technology ceramics market worldwide. Owing to their strong electromechanical coupling effect and the prompt response to applied electric fields, ferroelectric ceramics have been increasingly used in designing smart actuators for active control applications, such as large flexible space trusses (Crawley and de Luis 1987), fixed wing and helicopter rotary blades (Sprangler and Hall 1990, Samak and Chopra 1993 & 1994, Giurgiutiu, Chaudhry and Rogers 1994) and automotive suspensions (Thirupathi and Naganathan 1992). The most commonly used ferroelectic ceramics for transducer and actuator applications are the oxides of lead zirconium titanium, pb(zr(x), ti(1-x)o3, also known as pzt ceramics, because of their strong electromechanical coupling effect and relative low cost for massive production. The actuation force, or the actuation displacement equivalently, is determined by a material parameter, named the remnant polarization which is related to the electromechanical coupling effect of polycrystalline ferroelectric ceramics. The remnant polarization of pzt ceramics deteriorates after many cycles of applied electric field (Jiang, Cao and Cross 1994) and, consequently, the actuation force or the actuation displacement diminishes. This project focused on the microscopic mechanisms of electric fatigue of ferroelectric ceramics.

DESCRIPTORS: (U) *MICROSTRUCTURE, *CERAMIC MATERIALS, *FATIGUE(MECHANICS), *FERROELECTRIC MATERIALS, *MICROCRACKING, POLARIZATION, ELECTROMECHANICAL DEVICES, TRANSDUCERS, ACTUATION.

IDENTIFIERS: REMNANT POLARIZATION, SMART MATERIALS

♦AD NUMBER: A322992

GEORGIA INST OF TECH ATLANTA SCHOOL OF MECHANICAL ENGINEERING

(U) A TECHNIQUE FOR ACHIEVING 4000 MICROSTRAIN FROM HARD PZT.

MAR 97 57P

PERSONAL AUTHOR: LYNCH, CHRISTOPHER S.

UNCLASSIFIED REPORT

ABSTRACT: (U) The year 1 effort was split between laboratory development and research. A smart materials laboratory was developed for research on the mechanics of electro-mechanical coupled materials. The laboratory includes sample preparation, test facilities, and failure analysis tools as described below. There are presently four graduate students working on this research, one at the Masters level and three at the PH.D. level. There have been two conference proceedings articles and one journal article submitted. This will substantially increase in the coming year. The PI has made four presentations of research results and will make an invited presentation in July, 1997. The PI is presently working on several related programs described below. Departmental support from Georgia Tech is being used to perform work in excess of the original scope of this project.

DESCRIPTORS: (U) *STRAIN(MECHANICS), *ELECTROMECHANICAL DEVICES, *PIEZOELECTRIC MATERIALS, *FERROELECTRIC MATERIALS, MICROSTRUCTURE, STRESS ANALYSIS, ELECTRIC FIELDS, FRACTURE(MECHANICS), CERAMIC MATERIALS, RELIABILITY, CRACK PROPAGATION, LEAD COMPOUNDS, FAILURE(MECHANICS), MICROMECHANICS, TITANATES, ELECTRICAL LOADS.

IDENTIFIERS: PZT(LEAD ZIRCONATE TITANATE)

♦Included in *The DTIC Review*, September 1997

AD NUMBER: A321073

PRINCETON UNIV NJ

(U) DESIGN OF MATERIALS WITH EXTREME THERMAL EXPANSION USING A THREE-PHASE TOPOLOGY OPTIMIZATION METHOD

MAY 96 40P
PERSONAL AUTHORS: SIGMUND, OLE; TORQUATO, SALVATORE

UNCLASSIFIED REPORT

ABSTRACT: (U) Composites with extremal or unusual thermal expansion coefficients are designed using a three-phase topology optimization method. The composites are made of two different material phases and a void phase. The topology optimization method finds the distribution of material phases optimizing an objective function (e. g., Thermoelasticity) subject to certain constraints, such as elastic symmetry or volume fractions of the constituent phases, within a periodic base cell. The effective properties of the material are found using numerical homogenization based on finite element discretization of the base cell. To benchmark the design method we first consider two-phase designs. Our optimal two-phase microstructures agree well with rigorous bounds and so-called vigdergauz microstructures that realize the bounds. For three phases, the optimal microstructures are compared with new rigorous bounds and again it is shown that the method yields designed materials with thermoelastic properties close to the bounds. The three-phase design method is illustrated by designing materials having maximum directional thermal expansion (thermal actuators), zero isotropic thermal expansion (thermal actuators), zero isotropic thermal expansion, and negative isotropic thermal expansion. It is shown that materials with effective negative thermal expansion coefficients can be obtained by mixing two phases with positive thermal expansion coefficients and void.

DESCRIPTORS: (U) *MATERIALS, *THERMAL EXPANSION, THERMAL PROPERTIES, MICROSTRUCTURE, OPTIMIZATION, CELLS, FINITE ELEMENT NALYSIS, NUMERICAL ANALYSIS, ELASTIC PROPERTIES, VOIDS, PHASE, TOPOLOGY, ISOTROPISM, SYMMETRY, YIELD, MIXING, ACTUATORS, TEMPERATURE COEFFICIENTS, TWO PHASE FLOW, HOMOGENEITY, DIRECTIONAL, DENMARK, THERMOELASTICITY.

♦AD NUMBER: A318433

NORTHWESTERN UNIV EVANSTON IL

(U) HIERARCHICAL ADAPTIVE MICROSTRUCTURES: SMART STEELS.

OCT 96 50P
PERSONAL AUTHORS: OLSON, GREGORY B.

UNCLASSIFIED REPORT

ABSTRACT: (U) Inspired by biomimetic concepts, a systems approach to materials design is extended to hierarchical adaptive microstructures undergoing a programmed dynamic evolution in both processing and service to achieve novel combinations of properties. Fundamental principles are developed to support rational design of (a) high-toughness ultrahigh-strength martensitic steels of interest for advanced armor and high performance gear applications, and (b) 'smart composite' ferrous superalloys for damage tolerant high temperature applications in advanced tank propulsion systems. Theoretical modelling and high resolution microanalytical experiments in the martensitic alloys address control of autocatalytic coherent precipitation to achieve efficient strengthening without embrittlement, and the controlled precipitation of optimal stability metastable austenite for adaptive dilatant transformation plasticity tuned to crack-tip stress states for efficient interaction with strain localization processes in ductile fracture. Novel composite strategies address thermodynamically compatible shape-memory alloy reinforcement for pseudoelastic crack-bridge toughening of high temperature superalloys, combined with self-healing of low temperature damage by shape-memory-assisted crack rewelding at service temperatures.

DESCRIPTORS: (U) *MICROSTRUCTURE, *STEEL, *ADAPTIVE SYSTEMS, *HIERARCHIES, CONTROL, ARMOR, LOW TEMPERATURE, STABILITY, OPTIMIZATION, STRATEGY, DAMAGE, INTERACTIONS, DYNAMICS, MATERIALS, HIGH TEMPERATURE, COMPUTER PROGRAMMING, EMBRITTLEMENT, ALLOYS, HIGH RESOLUTION, STRENGTH(MECHANICS), FRACTURE(MECHANICS), AUSTENITE, PROPULSION SYSTEMS, PRECIPITATION, PLASTIC PROPERTIES, SYSTEMS APPROACH, IRON ALLOYS, DUCTILITY, GEARS, METASTABLE STATE, TRANSFORMATIONS, SUPERALLOYS, MARTENSITE, MICROANALYSIS.

IDENTIFIERS: *SMART MATERIALS, BIOMIMETIC, HIERARCHICALSTRUCTURES

♦Included in *The DTIC Review*, September 1997

AD NUMBER: 315582

CLARKSON UNIV POTSDAM NY

(U) MANUFACTURING & OPTIMIZATION PROBLEMS OF ELECTROMAGNETIC DEVICES.

JUN 96 80P
PERSONAL AUTHORS: BAROUCH, E. J.

UNCLASSIFIED REPORT

ABSTRACT: (U) During the duration of this project, we have developed several new algorithms for simulation of microstructures, devices, and fabrication methods for ic technology. We have interacted extensively with both industrial and government labs and collaborated with personnel of both. We have developed algorithms for imaging of microstructures, investigated the effects of off-axis illumination and finite-thickness effects on mask imaging. Furthermore, we have investigated the effects of post-exposure baking on chemically amplified resists, optimized stepper parameters, as well as proximity effects on mask making. Last, but not least, we developed new visualization algorithms that allow multiple viewing of the microchip processes.

DESCRIPTORS: (U) *PRODUCTION ENGINEERING, *INTEGRATED CIRCUITS, ALGORITHMS, MICROSTRUCTURE, OPTIMIZATION, PARAMETERS, CHIPS(ELECTRONICS), FABRICATION, MAGNETIC DEVICES, MASKS.

IDENTIFIERS: STEPPER PARAMETERS, OPTICAL PROXIMITY CORRECTIONS

AD NUMBER: A313705

YALE UNIV NEW HAVEN CT

(U) LOW TEMPERATURE NEAR-FIELD SCANNING OPTICAL MICROSCOPE FOR CHARACTERIZATION OF SEMICONDUCTOR MICROSTRUCTURES.

AUG 96 6P
PERSONAL AUTHORS: GROBER, ROBERT

UNCLASSIFIED REPORT

ABSTRACT: (U) This Durip Grant funded the capital equipment for a project to design and build a low-temperature, high magnetic field, near-field scanning optical microscope for the purpose of characterizing semiconductor nanostructures. All of the equipment necessary to build and operate this microscope has been purchased. The microscope has been completely designed, machined, and assembled. The need for robust, low-temperature, inertial motion has motivated us to invent a new kind of inertial motion motor. A prototype motor has been produced and is robust enough (i.e. drive voltage less than 5 v at room temperature) for low temperature operation. The 15/17 t superconducting magnet and cryogenic housing has been delivered and the facility to support this system is complete. We expect oxford instruments to perform a final installation during the month of August.

DESCRIPTORS: (U) *LOW TEMPERATURE, *MICROSTRUCTURE, *SEMICONDUCTORS, *MICROSCOPES, *OPTICAL SCANNING, *NEAR FIELD, OPTICAL EQUIPMENT, MAGNETIC FIELDS, MOTION, VOLTAGE, ROOM TEMPERATURE, INSTALLATION, INSTRUMENTATION, INERTIAL SYSTEMS, MAGNETS, MOTORS, CRYOGENICS, SUPERCONDUCTIVITY.

IDENTIFIERS: NEAR FIELD SCANNING, INERTIAL MOTION

Products and Services Order Form

MAIL Orders:
DTIC-BRR
Defense Technical Information Center
8725 John J. Kingman Rd., STE 0944
Ft. Belvoir, VA 22060-6218

CALL-IN Orders:
DTIC-BRR
Defense Technical Information Center
(703) 767-8274/(DSN) 427-8274
1-800-225-DTIC (3842)
(Menu selection 1, Option 1)

FAX Orders:
DTIC-BRR
Defense Technical Information Center
(703) 767-9070/(DSN) 427-9070

E-MAIL Orders:
msorders@dtic.mil
rp-orders@dtic.mil

INTERNET Orders:
http://www.dtic.mil/dtic/docorderform.html

Requesting Organization Information

User Code |___|___|___|___|___|___|

Contract Number (last six digits) |___|___|___|___|___|___|

Organization _____

Point of Contact _____

Phone Number _____

Method of Payment

Note: All Credit Card Types Must Be Preregistered

☐ Deposit Account Number |___|___|___|___|___|-|___|

☐ VISA ☐ MasterCard ☐ American Express

Account Number _____

Cardholder's Name _____

Expiration Date _____

DTIC does not accept cash, checks, or COD.

Type of Service Codes

R = Regular Service

Priority Services *(Must be called in or faxed)*

P = Picked Up Next Business Day ($10.00 surcharge/document)

M = Mailed Next Business Day ($10.00 surcharge/document)

E = Express - Mailed Next Business Day (Guaranteed Delivery in 2 Business Days) ($20.00 surcharge/document)

Document Orders

Type of Service Code	AD Number	Requested by	Quantity Hard Copy	Quantity Microfiche
	/JAA			
	/JAA			
	/JAA			
	/JAA			
	/JAA			
	/JAA			
	/JAA			
	/JAA			
	/JAA			
	/JAA			
	/JAA			
	/JAA			
	/JAA			
	/JAA			

Order
The DTIC Review
as a subscription product and Save!

Only $85/year for quarterly updates

(Available to DTIC Registered Users)

For more **information** call:
Phone: (703) 767-8266/DSN 427-8266
Fax: (703) 767-9070/DSN 427-9070
Email: bibs@dtic.mil

To **order** a single copy for $25, contact DTIC's Reference and Retrieval Services Branch at:
1-800-225-3842 (menu selection 1, option 1)
Phone: (703) 767-8274/DSN 427-8274
Fax: (703) 767-9070/DSN 427-9070
Email: msorders@dtic.mil or rp-orders@dtic.mil

To **subscribe** call:
1-800-225-3842 (menu selection 2, option 2)
Phone: (703) 767-8272/DSN 427-8272
Fax: (703) 767-8228/DSN 427-8228
Email: reghelp@dtic.mil